Studies on Corrosion, Fouling and Durability of Advanced Functional Nonwetting Surfaces

S.M. Ali Mousavi

Dissertation submitted to the Faculty of the
Virginia Polytechnic Institute and State University
in partial fulfillment of the requirements for the degree of

Doctor of Philosophy
In
Mechanical Engineering

Ranga Pitchumani, Chair
Michael Ellis
Roop L. Mahajan
Amanda Morris

September 22, 2021
Blacksburg, Virginia

Keywords: non-wetting, hydrophobic, superhydrophobic, lubricant-infused, corrosion inhibition, anti-fouling, corrosion modeling, fouling modeling

Studies on Corrosion, Fouling and Durability of Advanced Functional Nonwetting Surfaces

S.M. Ali Mousavi

Abstract

Superhydrophobic and lubricant-infused porous surfaces are two classes of non-wetting surfaces that are inspired by the adaptation of natural surfaces such as *lotus* leaves, *pond skater* legs, *butterfly* wings, and *Nepenthes* pitcher-plant. This dissertation focuses on fabrication and in-depth study of bioinspired functional metallic surfaces for applications such as power plant condensers and marine applications. Toward that, first, facile and scalable methods are developed for the fabrication of superhydrophobic surfaces (SHS) and lubricant-infused surfaces (LIS).

Second, the corrosion inhibition mechanism of SHS was systematically studied and modeled via electrochemical methods to elucidate the role of superhydrophobicity and other parameters on corrosion inhibition. The anti-corrosion properties of SHS and LIS were systematically studied over a range of temperatures (23°C–90°C) to simulate an actual condenser environment. Moreover, the environment of application often involves using harsh cleaning chemicals. The fabricated non-wetting surfaces were examined over a wide range of acidity and basicity ($pH = 1$ to $pH = 14$). Third, the durability of SHS and LIS is systematically assessed using a set of testing protocols including water impingement tests, scratch wear tests, and accelerated chemical corrosion tests. Considering that industrial environments of application are often turbulent, in addition to static long-term corrosion tests, long-term dynamic durability was studied in a simulated turbulent condition. Fourth, the performance of the fabricated nonwetting surfaces was systematically studied against calcium sulfate scaling in turbulent conditions and different temperatures. An analytical relationship based on the Hill-Langmuir model is proposed for the prediction of fouling on nonwetting and conventional surfaces alike in dynamic conditions.

Overall 1048 individual samples were studied via over 3000 measurements in this dissertation to establish a comprehensive fundamental knowledge base on fabrication and anti-fouling characteristics of metallic nonwetting surfaces, which profoundly helps to design appropriate surfaces and fabrication methods based on the use environment.

Studies on Corrosion, Fouling and Durability of Advanced Functional Nonwetting Surfaces

S.M. Ali Mousavi

General Audience Abstract

Metallic surfaces such as copper, brass, and aluminum are everywhere in our daily lives. From tumblers, household pipes to the bank of tubes in power plants condensers. Fouling of these surfaces has significant performance and economic impact. Scaling is a type of crystallization fouling like the familiar limescale everyone is familiar to see around the surface of a house kettle. Corrosion is another type of fouling and is detrimental to metallic surfaces. For example, 50% of water consumption in the U.S. is being used in thermo-electric power plants where fouling of metallic surfaces will impede the flow of working fluid, therefore increasing power needed for pumping, decrease efficiency, and decrease ultimate lifetime. One study in 2019 shows corrosion costs 3% of the gross national products of China and it is already known to be similar for other major economies like the USA, which is a hefty cost.

Nature has inspired a lot of solutions for mankind. In this work, inspired by natural surfaces such as *lotus* leaves, *butterfly* wings, and *pond skater* legs, a class of superhydrophobic surfaces (SHS) was fabricated. Moreover, a closer look at how the complex human body puts everything in order exposes one of its most striking and essential characteristics: how wet and lubricated its interfaces are. Our lungs, eyes, joints, intestine, bones; either hairy or porous, all are lined wet surfaces that work as fouling inhibitors and defect-free surfaces. This also have been observed elsewhere such as on Nepenthes pitcher-plant. Inspired by these, another class of non-wetting surfaces, lubricant-infused surfaces (LIS) was fabricated. This dissertation for the first time investigates a rational methodology in the fabrication of metallic SHS and LIS and their anti-scaling and anti-corrosion properties in different environments of application, including a range of temperature (23°C–90°C), various solutions ($pH = 1$ to $pH = 14$), and long-term static and dynamic (turbulent condition) durability. It is believed that this work would profoundly help to identify appropriate nonwetting metallic surfaces based on the intended use environment.

Acknowledgments

It is easy to see the tip of an ice-burg, but there are a great number of people that have paved my way to this point with their wisdom, supports, and guidance, before and during my graduate education. I cannot show my gratitude and appreciation equal to their true value but I would try my best.

First, my sincere appreciations go to my advisor Professor Ranga Pitchumani for giving me the opportunity and providing me the means to work in this field. From our first engaging meeting at Arlington to the times where my research efforts hit the ground in the lab, he was available all the time, weekend or holiday, with valuable advice and a keen and open mind to let me try new ways. I have also had the tremendous honor of learning from and being mentored by a number of outstanding faculty members at VriginiaTech. Of particular note, is my thesis committee, Professors Amanda Morris, Michael Ellis, and Roop Mahajan. I am thankful for all their feedbacks and advice for this dissertation. Besides that Prof. Morris's class helped me a lot to further advance myself in the electrochemistry field. Prof. Ellis's interim advisory and his generosity in borrowing equipment helped kick off the work. I am also grateful to Prof. Mahajan for supports in tough times and engaging research discussion. I like to appreciate Dr. Zheng Li for his teachings and for allowing me to gain valuable lab management skills. I would also like to thank Prof. Scott Turn my master's advisor at Hawaii Natural Energy Institute who supported me to go toward Ph.D., and also Prof. Lloyd Hihara for introducing me the first into electrochemistry at the University of Hawai'i at Manoa which I never thought one day would steer me to where I am now.

At the end, I would like to thank my parents, Mehdi and Razie for their amazing unconditional love, caring, and supports besides their tremendous patience throughout these long years of not being able to see them. Mehdi's sharp acumen in engineering, leadership, and management manifested in building factories was probably a motivation for me to walk the path of engineering, but growing and seeing his diligence to bring together the success of the project and the satisfaction of numerous personnel was a live life school to me. Razie's patience as a teacher was probably a motivation for me to walk the path of a Ph.D., but her compassion toward sharing knowledge was a big lesson for me. I would also like to thank my wonderful brothers Yaser, Saleh, and Kazem whom I could not finish this path without their unconditional love and supports. All the family was my teacher that taught me to seek and see life beyond matters and materials.

This dissertation was supported by the United States Department of Energy under Award Number DE-FE0031556.

Contents

List of Figures

List of Tables

Chapter 1. Introduction

Nature-inspired water repellency has been studied on various engineered materials for potential applications such a self-cleaning [1], anti-icing [2], anti-fouling [3–5], energy-efficient fluid transport [6–11], oil-water separation [12,13] and enhanced phase change heat transfer [14,15]. Superhydrophobic and lubricant-infused porous surfaces are two classes of non-wetting surfaces that are inspired by the adaptation of natural surfaces such as *lotus* leaves [16], *pond skater* legs [16], *butterfly* wings [17] and *Nepenthes* pitcher-plant [18].

Water affinity to any surface is characterized by the water contact angle (CA) and roll-off angle. Generally, a hydrophobic surface is defined as a surface with $90^{o} < CA < 150^{o}$ while a surface with $CA > 150^{o}$ and roll-off angle $< 10^{o}$ is called a superhydrophobic surface (SHS). Apparent water contact angle on lubricant-infused surfaces (LIS) is typically in a range of 80–140° with a sliding angle $< 20^{o}$. A droplet on a rough hydrophobic/superhydrophobic surface is supported partially by the solid surface and mostly by the trapped air in the micro/nano hierarchical structure of the surface. This composite interface (the trinary contact phase between the liquid, surface, and the trapped air in the roughness features) facilitates the easy shedding of the droplet and is classified as heterogeneous wetting state or Cassie-Baxter state [19]. On the other hand, on a rough wettable surface, the droplet penetrates the micro/nano hierarchical structure of the surface and stays in the so-called homogeneous wetting state or Wenzel state [20]. Unlike hydrophobic/superhydrophobic surface that owes its self-cleaning/non-wetting effect due to partial detachment of the water droplet from the surface (the air pockets) [21], a lubricant-infused surface provides such property by low bonding energy between the droplet molecules and the infused liquid molecules on the surface, which facilitates the droplet slipping off the surface at a very low angle [22]

Fabrication of such surfaces involves three steps of texturing, functionalization, and lubricant infusion (in the case of LIS). Texturing steps are divided into two general categories: *additive* and *removal* approaches. The lubricants are generally divided into two groups of *PFPEs* and *PDMS*. Copper is widely used in industries ranging from marine to power production. Two methods of surface texturing—electrodeposition (an additive process) and etching (a material removal process)—which both are scalable and facile, are juxtaposed for the first time in this work to bring further insight into the effect of fabrication method on performance of non-wetting surfaces.

With the rapid growth of industrialization of every corner of the world, corrosion is an omnipresent problem that imposes economic and environmental costs all over the world. Direct and indirect cost of corrosion of metallic surfaces that costs equal to 3-5% of the global gross national products [23,24]. While corrosion cannot be eliminated, various methods such as cathodic protection, anodic passivation, electrolyte inhibition or the combination have been pursued in order to slow down the corrosion kinetic. From a theoretical standpoint, adsorption of corrosive ions and species on a surface can be deterred by minimizing the wetted solid-electrolyte contact area and thereby lowering the corrosion rate. Corrosion characteristics of the fabricated surfaces were measured using electrochemical impedance spectroscopy as well as the linear polarization technique to elucidate insights into the corrosion mechanism on superhydrophobic surfaces. In chapter 2, systematic studies are conducted to quantify the effects of functionalization time (t_f), corrosivity of the immersion medium, immersion time, and temperature on the corrosion performance of as-purchased copper and textured electrodeposited superhydrophobic copper surfaces. The corrosion characteristics are investigated over the range of extremes of corrosivity, from a harsh acid medium with a pH of 1 to a harsh alkaline medium, pH = 14, including a 3.5% NaCl as a simulation for the marine environment. The study also reports corrosion measurements for long immersion time in a harsh environment via an in situ linear polarization method. Additionally, corrosion studies are presented, for the first time, on a range of temperatures in the range of $23°C–90°C$, from which an Arrhenius model is developed for the temperature-dependent corrosion rate of the superhydrophobic surfaces.

Applications of superhydrophobic (SHS) and lubricant infused surfaces (LIS) involve exposure to corrosive environments from the acidic to the basic, at a range of temperatures, that are not fully characterized. In Chapter 3, systematic corrosion studies are conducted using potentiodynamic polarization to quantify the corrosion inhibition of SHS and LIS over a range of temperatures above room temperature from which a relationship between corrosion rate and temperature is derived, for the first time, for SHS and LIS on copper. At the low temperature, electrodeposited SHS and etched SHS and LIS exhibited a $50-70$ fold reduction in corrosion rate while electrodeposited LIS reduced corrosion rate by two orders of magnitude. At the higher temperature, SHS reduced corrosion by a factor of $2–3$, whereas LIS was characterized by corrosion rate that was an order of magnitude lower than the bare copper surface. Microstructural

evaluation of LIS before and after corrosion testing is used to demonstrate the durability of the surface to corrosion. Finally, the performance of LIS in harsh acidic ($pH = 1$) and basic ($pH = 14$) environments is examined through electrochemical impedance spectroscopy measurements, for the generalized applicability of the surfaces developed in this study.

Fabrication of bioinspired SHS and LIS has been studied extensively on a variety of materials. In contrast, the durability of the surfaces exposed to harsh mechanical and chemical environments has been the subject of little attention. Chapter 4, considers the mechanical and chemical durability of SHS and LIS copper surfaces fabricated via facile electrodeposition and chemical etching methods. The as-fabricated surfaces demonstrate excellent non-wetting characteristics with water contact angle of 160° and sliding angle below 5°. The surfaces are subject to mechanical wear through scratch test and water jet impingement at 15 psi and 20 psi as well as accelerated corrosion following the ASTM E407 standard. The performance of the electrodeposited and etched non-wetting surfaces is systematically assessed in terms of contact and sliding angles and corrosion rate in a simulated marine environment. All surfaces are shown to be robust to mechanical wear after scratch test, with excellent stability of contact and sliding angles, and up to two orders of magnitude reduced corrosion rate compared to bare copper surface. SHS retained steadfast non-wetting characteristics under high-pressure water jet tests compared to the other surfaces while LIS, regardless of texturing method, showed one to two orders of magnitude reduced corrosion rate compared to bare copper surface throughout water jet impingement and chemical durability tests. The study presents for the first time a systematic comparison of durability of SHS and LIS through a common set of fabrication and testing protocols and helps identify appropriate nonwetting surfaces and fabrication methods based on the use environment.

There has been increasing attention to corrosion inhibition property of SHS and LIS in static or limited to laminar flow conditions [25–28], however, the environment of application is often turbulent. There is a conspicuous lack of corrosion study of SHS and LIS in the environment of the application, especially turbulent flow conditions and higher temperatures. In light of the knowledge gap, chapter 5, offers a very comprehensive approach in the rational design and a systematic study of both copper SHS and LIS. Two facile texturing processes: electrodeposition and etching are proposed to cover both additive and removal methods. Moreover, two different functionalization agents were selected along with two types of lubricant, one from the PFPEs group

and one from the PDMS group. For the first time, the long-term stability of the non-wetting surface was studied at both static and dynamic turbulent conditions. The dynamic tests were done in a novel yet simple in-house built setup. This setup allows electrochemically measuring corrosion inhibition properties whereas the laminar flow test in literature often used weight method, which suffers from precision. SHS and LIS may experience weight change due to loss of material which is not necessarily the result of added/removed material from corrosion reactions. Additionally, an Arrhenius model is developed for the corrosion rate of as-fabricated non-wetting surfaces over a range of temperatures, 23 °C-90 °C. All in all, this study with 234 tested surfaces and over 1,021 measurements provide for the first time a comprehensive view of the SHS and LIS by juxtaposing a rational selection over a gamut of texturing method, functionalization agents, lubricants, and tests in various conditions. This is believed to provide a multifacet perspective to the emerging non-we tting surfaces and valuable insight into their advancement for various applications.

Fouling occurs in two major categories, biological fouling and crystallization fouling. The latter is also called scaling which occurs due to the crystallization of the salt ions onto a surface. The excessive scaling of soluble salts in the process fluid on heat transfer surfaces impose performance degradation and maintenance cost. Phosphate, sulfates, and carbonate of calcium are among the salts that usually causes scaling. Calcium sulfate (gypsum) is one of the most common founded scaling compounds. It has been reported in various industries such as seawater desalination facilities [29], geothermal power plants working with brine [30], nanofiltration technology [31], heat exchanger [32], and condensers [33]. Consequently, there has been a lot of attention to understand and discover the underlying mechanism of crystallization [34,35] in general, and calcium sulfate scaling in particular [36–38].

Surfaces modification has drawn attention as a preventive approach against scaling. In specific, enhanced non-wetting surfaces have been fabricated via physical and chemical modifications namely hydrophobic surfaces (HS), superhydrophobic surfaces (SHS), and lubricant-infused surfaces (LIS) for different applications including anti-scaling, and has been studied at static conditions. Despite all, there is a shortage of studies exploring the extent of these surfaces against scaling at a dynamic condition that mimics the flow condition. To address this, in chapter 6, the effect of flow speed on the extent of scaling on the modified non-wetting surfaces as well as the control sample was studied by mimicking the turbulent flow condition in pipe via rotating-Couette

flow regime. A simple yet novel dynamic test was designed using a rotating drum and controlled temperature solution tank where the test coupons were mounted at the outer side of the rotating drum. The nucleation theory along with the crystallization theory and rotating-Couette flow regime theory was briefed. Furthermore, the experimental results were presented for parametric tests beginning with the effect of flow speed. After that effect of temperature was discussed over a set of experimental parametric tests. The performance of various in house fabricated enhanced surfaces was studied against scaling. Both superhydrophobic, as well as slippery surfaces, showed superior anti-scaling performance at all ranges of variables. With the help of briefed theories, it was discussed that the scale-inhibition effect of the fabricated surfaces is due to their built-in enhanced properties rather than solely changes in external conditions. Furthermore, a Langmuir-Hill relationship is adopted to model the scaling results and the accuracy of the model is explored against the experimental data. The application of Langmuir-Hill model for scaling application is explored and presented here for the first time. Despite all, as noted before in the literature regard the high uncertainty in the fouling experimentation, the experimental results were very well fitted via a proposed model, and a high accuracy was achieved.

Chapter 7 visits the nucleation theory from a comprehensive approach, by doing systematic studies on the controllable parameters including both surfaces related parameters and working fluid related parameters. Metallic surfaces with different roughness, relatively rough (Brass) and smooth (Aluminum), were chosen as the base material for dynamic scaling experiments. A facile etching method was employed for the fabrication of non-wetting enhanced HS and SHS and LIS on the metallic surfaces. Systematic dynamic scaling experiments on the five different types of surfaces were performed at three flow levels and two temperature levels. Finally, a comprehensive analysis was done on aggregated data to map the efficacy of different metallic surface modifications against scaling. We envision this rationale as an important step for the research and industrial community to pave the way toward robust and stable enhanced anti-scaling surfaces in the future.

The dissertation is written in manuscript format, with each succeeding chapter reflecting an article that has been published or submitted to a peer-reviewed journal. The dissertation ends with final word and suggestion for future works in chapter 8.

REFERENCES

[1] P. Ragesh, V. Anand Ganesh, S. V. Nair, A.S. Nair, A review on "self-cleaning and multifunctional materials," J. Mater. Chem. A. 2 (2014) 14773–14797. https://doi.org/10.1039/c4ta02542c.

[2] M.J. Kreder, J. Alvarenga, P. Kim, J. Aizenberg, Design of anti-icing surfaces: Smooth, textured or slippery?, Nat. Rev. Mater. 1 (2016) 1–15. https://doi.org/10.1038/natrevmats.2015.3.

[3] M. Cui, B. Wang, Z. Wang, Nature-Inspired Strategy for Anticorrosion, Adv. Eng. Mater. 21 (2019). https://doi.org/10.1002/adem.201801379.

[4] E. Vazirinasab, R. Jafari, G. Momen, Application of superhydrophobic coatings as a corrosion barrier: A review, Surf. Coatings Technol. 341 (2018) 40–56. https://doi.org/10.1016/j.surfcoat.2017.11.053.

[5] R. Deng, T. Shen, H. Chen, J. Lu, H.C. Yang, W. Li, Slippery liquid-infused porous surfaces (SLIPSs): A perfect solution to both marine fouling and corrosion?, J. Mater. Chem. A. 8 (2020) 7536–7547. https://doi.org/10.1039/d0ta02000a.

[6] S. Hatte, R. Pitchumani, Analytical model for drag reduction on liquid-infused structured non-wetting surfaces, Soft Matter. 17 (2021) 1388–1403. https://doi.org/10.1039/d0sm01272f.

[7] S. Hatte, R. Pitchumani, Fractal Model for Drag Reduction on Multiscale Nonwetting Rough Surfaces, Langmuir. 36 (2020) 14386–14402. https://doi.org/10.1021/ACS.LANGMUIR.0C02790.

[8] S. Hatte, R. Pitchumani, Analysis of Laminar Convective Heat Transfer Over Structured Non-Wetting Surfaces, Int. J. Heat Mass Transf. 167 (2021) 120810. https://doi.org/10.1016/J.IJHEATMASSTRANSFER.2020.120810.

[9] S. Hatte, R. Pitchumani, Analysis of convection heat transfer on multiscale rough superhydrophobic and liquid infused surfaces, Chem. Eng. J. 424 (2021) 130256. https://doi.org/10.1016/J.CEJ.2021.130256.

[10] K. Kant, R. Pitchumani, Laminar drag reduction in microchannels with liquid infused textured surfaces, Chem. Eng. Sci. 230 (2021) 116196. https://doi.org/10.1016/J.CES.2020.116196.

[11] C. Cottin-Bizonne, J.L. Barrat, L. Bocquet, E. Charlaix, Low-friction flows of liquid at nanopatterned interfaces, Nat. Mater. 2 (2003) 237–240. https://doi.org/10.1038/nmat857.

[12] S. Rasouli, N. Rezaei, H. Hamedi, S. Zendehboudi, X. Duan, Superhydrophobic and superoleophilic membranes for oil-water separation application: A comprehensive review, Mater. Des. 204 (2021) 109599. https://doi.org/10.1016/j.matdes.2021.109599.

[13] M.A. Gondal, M.S. Sadullah, T.F. Qahtan, M.A. Dastageer, U. Baig, G.H. McKinley, Fabrication and Wettability Study of WO3 Coated Photocatalytic Membrane for Oil-Water Separation: A Comparative Study with ZnO Coated Membrane, Sci. Rep. 7 (2017) 1–10. https://doi.org/10.1038/s41598-017-01959-y.

[14] R. Stoddard, K. Nithyanandam, R. Pitchumani, Steam condensation heat transfer on lubricant-infused surfaces, IScience. 24 (2021) 102336. https://doi.org/10.1016/j.isci.2021.102336.

[15] M. Edalatpour, L. Liu, A.M. Jacobi, K.F. Eid, A.D. Sommers, Managing water on heat transfer surfaces: A critical review of techniques to modify surface wettability for applications with condensation or evaporation, Appl. Energy. 222 (2018) 967–992. https://doi.org/10.1016/j.apenergy.2018.03.178.

[16] X. Feng, L. Jiang, Design and creation of superwetting/antiwetting surfaces, Adv. Mater. 18 (2006) 3063–3078. https://doi.org/10.1002/adma.200501961.

[17] Y. Zheng, X. Gao, L. Jiang, Directional adhesion of superhydrophobic butterfly wings, Soft Matter. 3 (2007) 178–182. https://doi.org/10.1039/b612667g.

[18] 2004_Bohn (pitcher lant)_ Insect aquaplaning Nepenthes pitcher, (n.d.).

[19] A.B.D. Cassie, S. Baxter, Wettability of porous surfaces, Trans. Faraday Soc. 40 (1944) 546–551.

[20] R.N. Wenzel, Resistance of solid surfaces to wetting by water, Ind. Eng. Chem. 28 (1936)

988–994. https://doi.org/10.1021/ie50320a024.

[21] D. Wang, Q. Sun, M.J. Hokkanen, C. Zhang, F.Y. Lin, Q. Liu, S.P. Zhu, T. Zhou, Q. Chang, B. He, Q. Zhou, L. Chen, Z. Wang, R.H.A. Ras, X. Deng, Design of robust superhydrophobic surfaces, Nature. 582 (2020) 55–59. https://doi.org/10.1038/s41586-020-2331-8.

[22] X. Chen, G. Wen, Z. Guo, What are the design principles, from the choice of lubricants and structures to the preparation method, for a stable slippery lubricant-infused porous surface?, Mater. Horizons. 7 (2020) 1697–1726. https://doi.org/10.1039/d0mh00088d.

[23] B. Hou, X. Li, X. Ma, C. Du, D. Zhang, M. Zheng, W. Xu, D. Lu, F. Ma, The cost of corrosion in China, Npj Mater. Degrad. 2017 11. 1 (2017) 1–10. https://doi.org/10.1038/s41529-017-0005-2.

[24] J. Kruger, Cost of metallic corrosion, in: Uhlig's Corros. Handb., 2011: pp. 15–20.

[25] S. Khodakarami, H. Zhao, K.F. Rabbi, N. Miljkovic, Scalable corrosion-resistant coatings for thermal applications, ACS Appl. Mater. Interfaces. 13 (2021) 4519–4534. https://doi.org/10.1021/acsami.0c19683.

[26] A. Masoudi, P. Irajizad, N. Farokhnia, V. Kashyap, H. Ghasemi, Antiscaling Magnetic Slippery Surfaces, ACS Appl. Mater. Interfaces. 9 (2017) 21025–21033. https://doi.org/10.1021/ACSAMI.7B05564.

[27] J.S. Wexler, I. Jacobi, H.A. Stone, Shear-Driven Failure of Liquid-Infused Surfaces, Phys. Rev. Lett. 114 (2015) 168301. https://doi.org/10.1103/PhysRevLett.114.168301.

[28] J.S. Wexler, I. Jacobi, H.A. Stone, Shear-Driven Failure of Liquid-Infused Surfaces, Phys. Rev. Lett. 114 (2015) 168301. https://doi.org/10.1103/PhysRevLett.114.168301.

[29] J. Zhao, M. Wang, H.M.S. Lababidi, H. Al-Adwani, K.K. Gleason, A review of heterogeneous nucleation of calcium carbonate and control strategies for scale formation in multi-stage flash (MSF) desalination plants, Desalination. 442 (2018) 75–88. https://doi.org/10.1016/J.DESAL.2018.05.008.

[30] J. Song, M. Liu, X. Sun, Model analysis and experimental study on scaling and corrosion

tendencies of aerated geothermal water, Geothermics. 85 (2020) 101766. https://doi.org/10.1016/J.GEOTHERMICS.2019.101766.

[31] P.S. Goh, W.J. Lau, M.H.D. Othman, A.F. Ismail, Membrane fouling in desalination and its mitigation strategies, Desalination. 425 (2018) 130–155. https://doi.org/10.1016/J.DESAL.2017.10.018.

[32] F.L. Wang, Y.L. He, S.Z. Tang, Z.X. Tong, Parameter study on the fouling characteristics of the H-type finned tube heat exchangers, Int. J. Heat Mass Transf. 112 (2017) 367–378. https://doi.org/10.1016/J.IJHEATMASSTRANSFER.2017.04.107.

[33] M. Kamalipour, S.A.M. Dehghani, A. Naseri, S. Abbasi, Role of agitation and temperature on calcium sulfate crystallization in water injection process, J. Pet. Sci. Eng. 151 (2017) 362–372. https://doi.org/10.1016/J.PETROL.2016.12.039.

[34] T.H. Chong, R. Sheikholeslami, Thermodynamics and kinetics for mixed calcium carbonate and calcium sulfate precipitation, Chem. Eng. Sci. 56 (2001) 5391–5400. https://doi.org/10.1016/S0009-2509(01)00237-8.

[35] J.G. Lee, Y. Jang, L. Fortunato, S. Jeong, S. Lee, T.O. Leiknes, N. Ghaffour, An advanced online monitoring approach to study the scaling behavior in direct contact membrane distillation, J. Memb. Sci. 546 (2018) 50–60. https://doi.org/10.1016/J.MEMSCI.2017.10.009.

[36] S. Tang, Y. Ji, K. Ge, Crystallization Kinetics and Mechanisms of Calcium Sulfate Dihydrate: Experimental Investigation and Theoretical Analysis, Ind. Eng. Chem. Res. 59 (2020) 21676–21684. https://doi.org/10.1021/ACS.IECR.0C04220.

[37] K.S. Song, J. Lim, S. Yun, D. Kim, Y. Kim, Composite fouling characteristics of CaCO3 and CaSO4 in plate heat exchangers at various operating and geometric conditions, Int. J. Heat Mass Transf. 136 (2019) 555–562. https://doi.org/10.1016/J.IJHEATMASSTRANSFER.2019.03.032.

[38] F. Alimi, A. Gadri, Kinetics and morphology of formed gypsum, Desalination. 166 (2004) 427–434. https://doi.org/10.1016/J.DESAL.2004.06.097.

Chapter 2. A Study of Corrosion on Electrodeposited Superhydrophobic Copper Surfaces

The work reported in this chapter is the basis for the following journal publication:

S.M.A. Mousavi, and R. Pitchumani. "A study of corrosion on electrodeposited superhydrophobic copper surfaces." *Corrosion Science* 186 (2021): 109420.

2.1. ABSTRACT

This study considers the corrosion characteristics of superhydrophobic copper surfaces with multiscale asperities formed inherently on a copper substrate, fabricated using a facile, low energy, electrodepostion method. A systematic study is presented for the first time on the effect of surface functionalization time for long-term immersion in a wide range of corrosive environments from the extremely acidic to the extremely alkaline. The corrosion resistance is also reported for the first time as a function of temperature in the range 23–85°C. The superhydrophobic surfaces are shown to enhance corrosion resistance by up to four orders of magnitude compared to bare copper.

KEYWORDS: superhydrophobicity; electrodeposition; copper; corrosion; salt solution; acidic and basic solution.

2.2. INTRODUCTION

With the rapid growth of industrialization, corrosion is an omnipresent problem that imposes economic and environmental costs all over the world. While corrosion cannot be eliminated, various methods such as cathodic protection, anodic passivation, electrolyte inhibition or the combination have been pursued in order to slow down the corrosion kinetics. From a theoretical standpoint, adsorption of corrosive ions and species on a surface can be deterred by minimizing the wetted solid-electrolyte contact area and thereby lowering the corrosion rate. Inhibiting corrosion on copper, as a material of interest for many applications, has drawn attention for decades and there are several methods used in practice. For instance, utilizing heterocyclic compounds (such as azole derivatives) [1], organic inhibitors [2], and conjugated double bonds [3] are among some of the methods, but their toxicity poses serious risks to humans and environmental life. Alternative methods based on coatings, such as electroactive conducting polymer coatings, are

susceptible to water permeability, and the use of self-assembled monolayers to prevent copper corrosion generally suffers from poor durability [4].

The presence of an air cushion in the inter-asperity regions of a solid surface can produce a non-wetting characteristic [5, 6] that can mitigate surface corrosion. Nature, throughout years of evolution, has already mastered such effect by creating superhydrophobic surfaces where the water-solid contact area is minimized [7-10], which has helped them survive the aggressive environment of their habitat. It is, therefore, of interest to explore the corrosion behavior of practical materials with engineered superhydrophobicity. In general, hydrophobicity is attributed to surfaces with a water contact angle above 90 and below 150 degrees, whereas superhydrophobicity is achieved when surfaces exhibit sustained water contact angles above 150 degrees and contact angle hysteresis below 10 degrees. Studies in the literature have identified two surface modifications to be responsible for producing the superhydrophobic effect: the first is the surface roughness, with structures ranging from micro- to nano-scales, and the second is a chemical coating with low surface energy molecules. Generally, chemical groups are ordered in decreasing order of surface energy as CH_2, CH_3, CF_3, CH_2F, CF_3, and even with CF_3 or other low surface energy materials as the coating on a smooth surface, the highest water contact angle reported does not exceed 130 degrees [11, 12]. This suggests that chemical modification alone is insufficient in providing superhydrophobicity in applications. Use of superhydrophobic surfaces, created through a combination of structural and chemical modification via different methods, has been studied in the literature for their corrosion inhibition characteristics. Various methods are used for the creation of roughness, such as templating, sol-gel method [13-15], electrospinning [16], laser etching [17], hydrothermal synthesis [18], anodization [19], plasma techniques [20, 21], and electrodeposition [22-24]. However, not all the approaches are suitable for large-scale fabrication. For example, the hydrothermal method, despite using environmentally friendly chemicals in the process (such as H_2O or dilute H_2O_2) [25], has to be done under high temperatures and pressures, raising the cost and complexity of fabrication. Etching, on the other hand, is a relatively simple process, but one that involves a mixture of harsh etchants (such as HCl, HF, etc.) [26, 27]. Among the fabrication methods, electrodeposition has been widely used [28] due to its low cost of fabrication, scalability regardless of surface size and shape, simplicity of the fabrication process at atmospheric pressure and room temperature [29-31], and the controllability of the resulting surface morphology [32].

The preparation of the superhydrophobic surface on various metallic and non-metallic surfaces via different methods including different electrodeposition approaches has been an active area of research in recent years. For a broader discussion on different methods and different substrates, the reader is referred to recent reviews [33, 34]. Herein, keeping with the present focus, the literature on fabrication of superhydrophobic copper surfaces using the constant potential electrodeposition method is reviewed. There have been a number of studies on characterizing electrodeposited superhydrophobic coating on a copper surface in a corrosive environment such as seawater. He et al. [29] electrodeposited zinc on copper at -1.35 V overpotential for 25 minutes, followed by 60 minutes of annealing at 190°C, and reported a superhydrophobic surface. The anticorrosion behavior of the surface was studied in 3.0% NaCl solution at room temperature, and was reported to exhibit a lower corrosion current and more cathodic corrosion potential compared to bare copper sample. Liu et al. [35] fabricated superhydrophobic copper surface via electrodeposition in cerium chloride and myristic acid electrolyte at atmospheric condition after applying 20V DC overpotential for 30 minutes. The prepared surfaces showed anticorrosion behavior compared to bare copper sample in terms of a lower corrosion current and a more noble corrosion potential. The stability of contact angle after 10 hours of immersion in different pH (1-14) solutions was also reported. Liu et al. [36] fabricated multiscale roughness via nucleating copper sulfate on top of a copper substrate by immersion of the substrate in the electrolyte mixture at 60°C for 1.5 hours, followed by modification of the samples with 0.5 wt.% stearic acid for 0.5 hours to achieve superhydrophobicity. The corrosion current on the surface was reported to decrease about two orders of magnitude in 3.5 wt.% NaCl solution and the corrosion potential was shown to shift 50 mV toward nobility compared to a bare copper sample. The stability in different pH environment was characterized by contact angle measurements in the range of pH between 2 and 12. The fabricated surfaces were reported to withstand 24 hours of long-term immersion but deteriorate after 48 hours in 3.5 wt.% sodium chloride solution.

Su et al. [31] electrodeposited nickel on a copper substrate at a constant current density of 0.75 $A.cm^{-2}$ at 50°C for 1 hour, followed by 2 hours of drying at 80°C, and surface treatment with AC-FAC at 110°C for 1 hour. The chemical stability was measured in terms of the contact angle of droplets with different pH ranging from 1 to 13 on the as-fabricated superhydrophobic surface. The corrosion resistance was shown to improve in 3.5% NaCl solution by means of a lower

corrosion current density relative to a bare copper sample. Wang et al. [37] electrodeposited copper on steel substrate at 10 V overpotential for 5 hours and reported good stability of the surfaces with regard to CA for 3 days of immersion in 3.5% NaCl solution. Wang et al. [38] used electrochemically grown laurylamine copper complex on copper substrate at 50V for 1 hour to fabricate superhydrophobic surfaces, which lowered corrosion current density in a 3.5% NaCl solution but degraded the contact angle below 150 after 4 days immersion in 3.5% NaCl solution. Liu et al. [39] fabricated superhydrophobic copper samples via electrodeposition at 20 V for 0.5 hour in myristic acid and cerium chloride mixed with ethanol as the electrolyte. The corrosion inhibition test showed about two orders of magnitude decrease of corrosion current compared to bare copper in 3.5% NaCl solution.

From the foregoing discussion, it is evident that the corrosion studies in the literature on electrodeposited non-wetting surfaces with constant potential method are based on fabrication using relatively high voltages, 5 to 20 volts, for a minimum duration of 0.5 h to 5 h. However, a drawback of such methods is that higher overpotentials and longer process durations lead to an increased system and energy cost. Furthermore, a systematic corrosion study of non-wetting surfaces over a range of harsh chemical environments is lacking. Moreover, with regard to stability, there is a shortage of information on corrosion performance in a harsh corrosive environment that exceeds an hour, as needed in many applications. Finally, most of the studies have focused on corrosion at room temperature, whereas the performance of such surfaces in corrosive environments at higher than room temperature is not reported.

The goal of the present study is to address the aforementioned limitations by considering the fabrication and corrosion performance of superhydrophobic copper surface. A facile, rapid process of electrodeposition of copper is presented with fabrication times less than 5 minutes at a very low overpotential of –1.1 volt that reduces the energy requirement for fabrication. The as-fabricated cauliflower shaped multiscale textured surfaces were chemically modified (functionalized) using stearic acid, an environmentally benign fatty acid. Corrosion characteristics of the fabricated surfaces were measured using electrochemical impedance spectroscopy as well as the linear polarization technique to elucidate insights into the corrosion mechanism on superhydrophobic surfaces. Systematic studies are conducted to quantify the effects of functionalization time (t_f), corrosivity of the immersion medium, immersion time, and temperature on the corrosion

performance of as-purchased copper and textured superhydrophobic copper surfaces. The corrosion characteristics are investigated over the range of extremes of corrosivity, from a harsh acid medium with a pH of 1 to a harsh alkaline medium, pH = 14, including a 3.5% NaCl as a simulation for the marine environment. The study also reports corrosion measurements for long immersion time in a harsh environment via an in situ linear polarization method. Additionally, corrosion studies are presented, for the first time, on a range of temperatures in the range of 23°C–90°C, from which an Arrhenius model is developed for the temperature-dependent corrosion rate of the superhydrophobic surfaces.

The article is organized as follows: the experimental methods of fabrication and characterization are described in the next section. The results of the study are presented and discussed in Section 3 in terms of the corrosion parameters as function of surface functionalization time, pH of the immersion environment, immersion time and immersion temperature. The principal conclusions of the study are summarized in Section 4.

2.3. EXPERIMENTAL METHODS

2.3.1. **Materials and reagents.**

Plain multipurpose copper sheet was purchased from McMaster, USA. Analytical-grade copper sulfate ($CuSO_4$, 99+%), sulfuric acid (H_2SO_4), acetone (99.5+%), methanol (99.8+%), and stearic acid ($CH_3(CH_2)_{16}CO_2H$, 97%) were purchased from Fisher Scientific, (Pittsburgh, PA, USA) and used as received without any further purification. For the preparation of aqueous solutions, deionized (DI) water with 14MΩ.cm resistance was purchased from CQ Concept (Illinois, IL, USA).

2.3.2. **Fabrication of copper superhydrophobic surfaces.**

A three-electrode electrochemical experiment setup, shown schematically in Figure 2.1, was used for the facile electrodeposition of copper on the copper substrate [32]. As purchased copper sheets were used as working and reference electrodes, while a platinum mesh was used as the counter electrode. An AUTOLAB PGSTAT128N potentiostat (ECO Chemie, Utrecht, The Netherlands) was used for all electrodeposition experiments. Using a mixture of 1M $CuSO_4$ and 0.5M H_2SO_4 as the electrolyte, electrodeposition was done over one side of the working electrode

while the other side was covered from electrodeposition with 3M® painting tape. All the surfaces used in the electrodeposition experiments were sonicated in acetone for 10 minutes, rinsed with DI water and dried in a nitrogen stream. Before each electrodeposition, the electrolyte was de-aerated by bubbling pure nitrogen gas for at least 20 minutes.

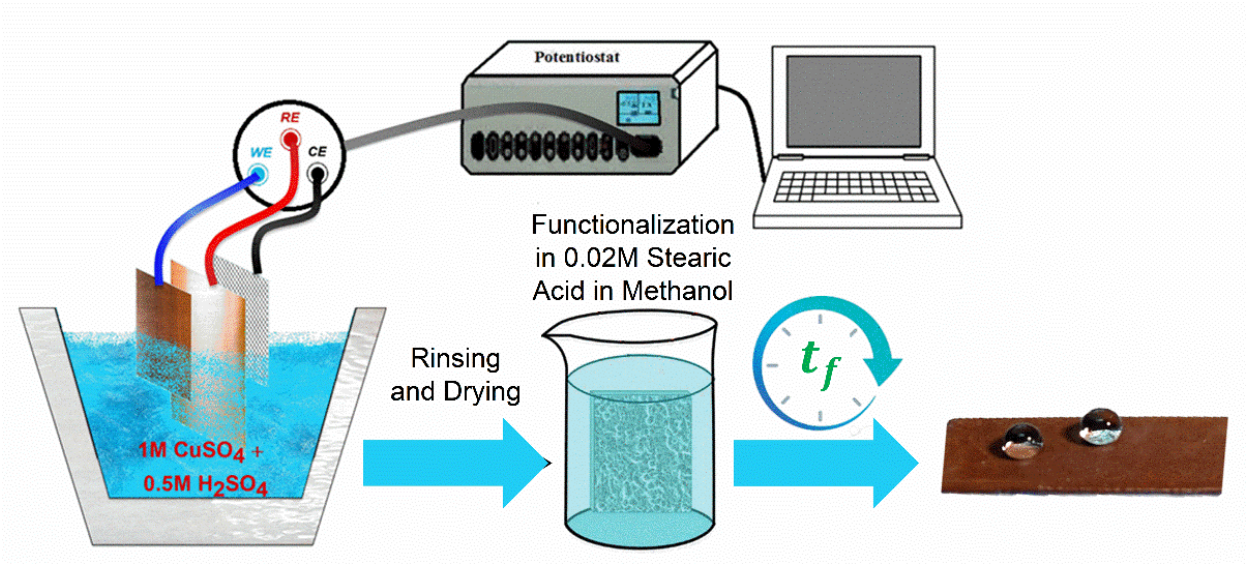

Figure 2.1. Schematic of the electrodeposition setup for fabrication of superhydrophobic surfaces.

The distance between the working and the reference electrodes was set to 0.5 cm. Negative overpotentials ranging from -0.5 V to -1.1 V in steps of -0.2 V were used for electrodeposition. For cases of -0.9 V and -1.1 V, which lead to an aggressively multiscaled texture of the deposited layer, a second deposition was conducted right after the first electrodeposition by applying -0.15 V for 10 seconds. The second deposition helps adhere the multiscale electrodeposited layers together and prevent them from peeling off the surface [32]. The electrodeposition time at each overpotential voltage was calculated to obtain about 30-micrometer deposition thickness (h) as per the relationship: $h = \frac{QM}{nF\rho A}$, where F is the Faraday constant, A is the surface area of the deposition, ρ is the density of the deposited copper, Q is the charge transferred in coulomb throughout the deposition ($Q = i.dt$), M is the molar weight of copper, and n is the number of transferred electrons in the copper reduction reaction, $Cu^{2+} + 2e^- \rightarrow Cu$.

After each electrodeposition run, the as-fabricated sample was rinsed with acetone and DI water and dried in a pure nitrogen stream. The fabricated samples were then vacuum dried at room temperature for 24 hours before the surface modification step to lower the surface energy. The electrodeposited textured surfaces were functionalized by immersing the samples in a solution of 0.02 M stearic acid (STA), an environmentally benign fatty acid, in methanol at room temperature, as depicted in Figure 2.1. The functionalizing time was varied between 1 h to 72 h as part of the systematic study to determine its influence on the corrosion behavior. in modification solution at room temperature. The fabricated superhydrophobic surfaces demonstrated excellent water repellency with high contact angle, as seen in Figure 2.1.

2.3.3. **Morphology, chemical composition analysis, and wettability characterization.**

The surface chemical composition was analyzed in a VersaProbe III Scanning XPS Microprobe (Physical Electronics, U.S.A.), using a monochromatic AlKα X-ray source (1486.6 eV) at 100 W. Images of the deposited surface morphologies and the elemental analysis of the surfaces were obtained with a field-emission scanning electron microscope (SEM) (JEOL 2100, Japan), operating at an acceleration voltage of 15 kV connected to energy dispersive x-ray analyzer (OXFORD, UK). The intrinsic wettability of water on the surfaces was characterized by measuring contact angle using a goniometer (ramé-hart model 590, NJ USA), at five different positions on each sample. The roll-off angle was measured by the same apparatus with 25 µl DI-water and tilting cradle method. For wettability characterization after each immersion test, the coupons were first slightly washed using a hand-squeezed laboratory DI-water bottle and left to dry in room atmosphere overnight before the contact angle measurement.

2.3.4. **Corrosion inhibition characterization.**

All the samples studied for corrosion inhibition were fabricated at -1.1 V overpotential and functionalized in 0.02 M stearic acid solution. Electrochemical three-electrode tests were carried out to measure and characterize the corrosion inhibition properties of the samples. Ag/AgCl (NaCl saturated) served as a reference electrode placed a distance of less than 3 mm from the sample surface (working electrode) in order to minimize the effect of solution resistance. A Pt mesh placed equidistant to the two other electrodes was used as a counter electrode. Potentiodynamic polarization (PDP) curves, electrochemical impedance spectroscopy (EIS) test and linear

polarization (LP) test data were recorded with a potentiostat device Solarton Inc. (model 1240 PA, USA) equipped with a frequency response analyzer. A scan range of -300 mV to +300 mV with respect to open circuit potential and a scan rate of 1 mV/s was used for the PDP test, while a 1/6 V/h scan rate, as per ASTM G3-14 (2019) standard [40], was used for the LP tests. Impedance spectra were registered in a range of 0.05 Hz to 100 kHz with sinusoidal signals of 10 mV amplitude with respect to the open circuit potential.

It is known that the open circuit potential (OCP) needs an initial time for stabilization and that this time is specific to the environment and the studied metal alloy [41]. Since corrosion is based on redox reactions happening at the surface, the very surface chemistry undergoes changes over time causing possible potential drift. To determine the stabilization time, the open circuit potential (OCP) was recorded in 3.5% NaCl solution at room temperature for bare copper, as the control sample, and the superhydrophobic copper surfaces. A higher relative potential fluctuation was seen in the first 10 minutes for the superhydrophobic copper samples that stabilized after about 20 minutes. Furthermore, the bare copper control sample potential drifted lower with a higher gradient after about 60 minutes, which was sought to be avoided. Based on these observed variations of the OCP with time, a 30-minute stabilization time in the electrolyte was selected before conducting each of the corrosion tests.

The data obtained from PDP scans were used to construct Tafel plots for determination of the corrosion potential, E_{corr}, corrosion current density, j_{corr}, and the corrosion resistance, R_{corr}. The EIS data were analyzed by constructing an equivalent electrical circuit model from which the charge transfer resistance, R_{ct}, was calculated using the Zview® software (Scribner Associates, Inc., NC, USA). The analysis of the obtained data is discussed in detail in the following section. The corrosion tests were conducted to systematically study and quantitatively assess the effects of the functionalization time, corrosivity of the environment in terms of pH, long term immersion time, and temperature as discussed in the next section.

2.4. RESULTS AND DISCUSSION

The results of the study are presented and discussed in this section, in terms of the morphology and wettability of the fabricated superhydrophobic surfaces, the chemical

composition of the functionalized surface of the superhydrophobic surfaces, and the corrosion inhibition characteristics of the superhydrophobic surfaces relative to a bare copper surface.

2.4.1. **Morphology, wettability, and chemical composition.**

The surface morphology of the electrodeposited surfaces before functionalization is depicted in Figure 2.2(a)–(d), for deposition voltages ranging from -0.5 V to -1.1 V, where a clear trend in the development of multiscale asperities with respect to the electrodeposition overpotential is evident. At a low overpotential voltage of 0.5 V, Figure 2.2(a), the deposition is relatively smooth with little surface roughness. An increase in the deposition overpotential to 0.7 V reveals the emergence of semi-spherical asperities on the surface, as seen in the SEM image of Figure 2.2(b). At higher overpotentials, 0.9 V and 1.1 V, the growth rate of deposition increased significantly. Figure 2.2(c) and 2(d) show the multiscale, cauliflower-shaped asperities deposited on to the copper surface at 0.9 V and 1.1 V, respectively.

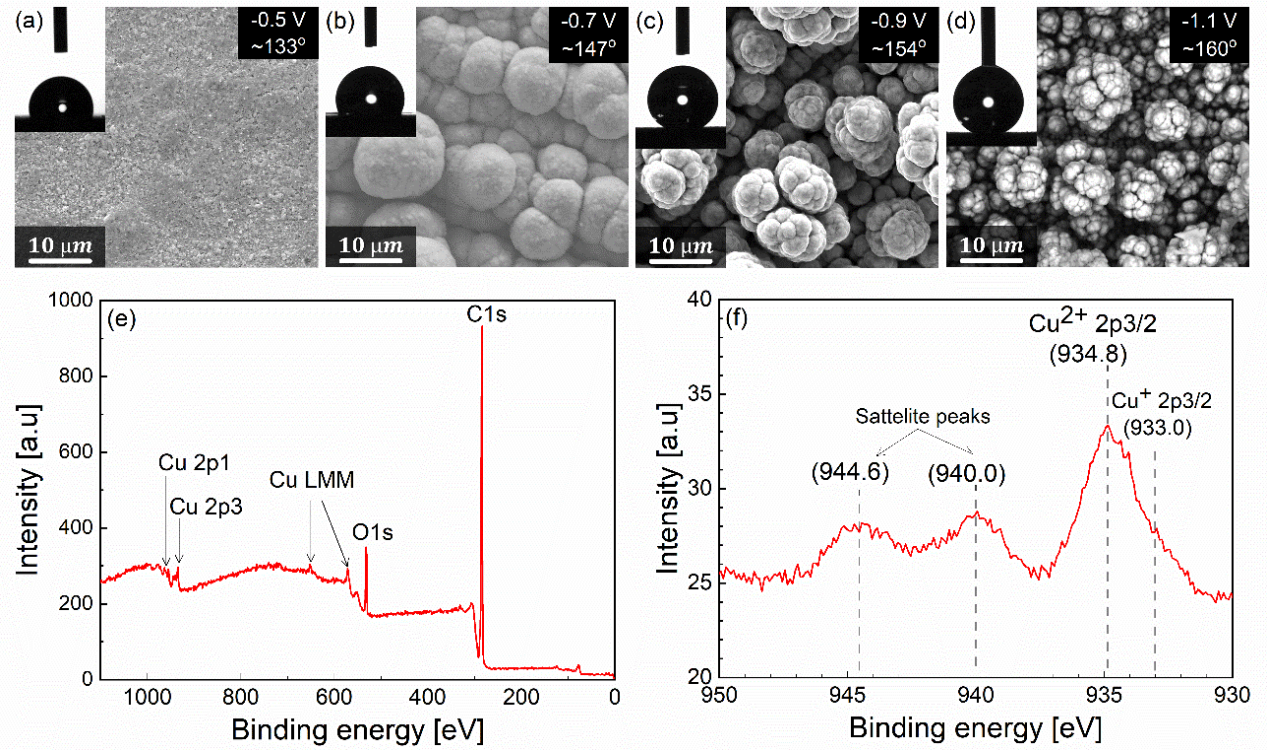

Figure 2.2. (a-d) SEMs of surfaces fabricated via electrodeposition at different voltages showing progressively increasing multiscale features and corresponding hydrophobicity or

superhydrophobicity; (e) XPS survey spectra and (f) XPS high resolution spectra of superhydrophobic copper surface fabricated via electrodeposition at -1.1 V and functionalized for 24 h in stearic acid.

As discussed earlier, theoretically, the two factors which play the major role in turning a surface to a hydrophobic or superhydrophobic surface are the surface roughness and the surface energy. The surface energy of the electrodeposited samples was lowered by functionalization them in a 0.02 M stearic acid solution in methanol for 1 hour. After that, the surfaces were characterized for their wetting contact angle with respect to a 10 μl DI-Water sessile drop, as depicted in the insets in Figure 2.2(a)–(d) which reveal the interplay between the roughness, functionalization and the non-wetting characteristic of the surface. Figure 2.2(a) shows a contact angle of 133 degrees for the surface electrodeposited at 0.5 V; with the emergence of the semi-spherical asperities at 0.7 V overpotential, the contact angle is seen to increase by about 14 degrees to 147 degrees in Figure 2.2(b). Surfaces fabricated at an overpotential of over 0.9 V reveal distinct superhydrophobicity with static contact angle larger than 150° and up to 160° for an overpotential of 1.1 V in Figure 2.2(d). In the 0.9 V and 1.1 V overpotential cases, the measured contact angle hysteresis was below 5° signifying excellent non-wettability of the fabricated surfaces. Moreover, the roll-off angle test showed a high average roll-off angle of 41 ± 30 and 36 ± 27 degrees for the 0.5 V case 0.7 V cases, respectively, while this value was below 5° for 0.9 V and 1.1 V cases. Figure 2.2(a)–(d) clearly demonstrate the combined role of the multiscale asperities and low surface energy in causing superhydrophobicity, that either alone will not produce.

In order to identify the main chemical composition of the superhydrophobic copper surface, X-ray photoelectron spectroscopy (XPS) scans were recorded on the samples fabricated at an overpotential of -1.1 V with a functionalization time, t_f, of 24 h in 0.02 M stearic acid solution in methanol. 24 h functionalization time was selected as a sample with a substantial coating material for XPS analysis. Figure 2.2(e) shows the XPS trace, from which carbon, oxygen, and copper are identified as the main components of the surface. The carbon and oxygen peaks indicate the successful reaction and bonding of stearic acid with the rough copper surface. Figure 2.2(f) highlights the variation in the range of 930–950 eV and shows a broad Cu 2p 3/2 feature which can be deconvoluted into two peaks at 932.6 and 934.8 eV (E_b), and a characteristic satellite feature

for Cu (II) at 940-945 eV. The minor peak at 932.6 eV can be assigned to Cu_2O, while the major peak at 934.8 eV can be assigned to $Cu(OH)_2$ [42]. The Cu $L_3M_{45}M_{45}$ Auger feature exhibits a single peak with a kinetic energy of 915.0 eV (E_k). The Modified Auger Parameter of 1849.8 eV ($E_b + E_k$) for the major peak at 934.8 eV is in good agreement with the value of $Cu(OH)_2$ (1851.3 eV) [42], confirming the major presence of $Cu(OH)_2$ on the surface. Since the minor 932.6 eV peak was not observed after the first sweep and accumulated after repeated sweeps, Cu_2O species could be resulted from reduction of $Cu(OH)_2$ after prolonged X-ray exposures. All these mean that the Cu is primarily in the form of CuO or $Cu(OH)_2$, suggesting $Cu_2O + 2CH_3(CH_2)_{16})COOH \rightarrow 2Cu[CH_3(CH_2)_{16}COO] + H_2O$ as a possible reaction mechanism for chemisorption of stearic acid with the surface cupreous oxide [18].

2.4.2. **Effect of functionalization time on corrosion.**

Parametric tests were done to investigate the effect of functionalization time, t_f, on the corrosion inhibition behavior of superhydrophobic copper surfaces immersed in solutions ranging from the extremely acidic (pH = 1) through the near-neutral 3.5% NaCl solution ($pH \approx 7$) to the extremely alkaline (pH = 14). The solutions with extreme acidity (pH = 1) and extreme alkalinity (pH = 14) were prepared by hydrolysis of sulfuric acid and sodium hydroxide in DI-water, respectively. In each case, the functionalization time in the fabrication of the superhydrophobic surfaces was varied in the range of $t_f = 1$ h to $t_f = 72$ h and, for comparison, bare copper samples were also immersed in the solutions. The static contact angles of DI-Water on the 1.1 V overpotential electrodeposited copper surfaces with 1 hour functionalization time and beyond was 160 ± 4.1 degrees with roll-off angles below 5 degree. For the bare copper, the static contact angle and roll-off angle was measured as 88.7 ± 5.7 and 48.0 ± 5.5, respectively. Note that unfunctionalized electrodeposited copper surfaces has shown superhydrophilicty with a low contact angle The studies in this parametric set were conducted at a temperature of 23°C (the actual room temperature in the laboratory) and consisted of potentiodynamic polarization tests as well as electrochemical impedance spectroscopy, as discussed below.

Potentiodynamic polarization (PDP)

Figure 2.3(a) shows the potentiodynamic polarization (PDP) data recorded for bare copper and superhydrophobic copper surfaces with six different functionalization time, at a temperature of

23°C. It is seen that, in general, the corrosion current density decreases with increasing functionalization time, and that all of the functionalized samples have a distinctly lower current density compared to bare copper, as evident in the progression of the curves from (a) to (g) in Figure 2.3. In order to quantitatively deduce the corrosion parameters from the measured PDP data, a Tafel extrapolation method was used, where the slope of the linear part of the cathodic region (β_{cat}) and anodic region (β_{an}), in mV/decade, were determined as illustrated in Figure 2.3(a) for the case of bare copper. From these slope measurements, the corrosion voltage, E_{corr}, and current density, j_{corr} ($\mu A \cdot cm^{-2}$) were derived from the intersection of the two linear asymptotes, and the corrosion resistance, R_{corr} ($\Omega \cdot cm^2$) was estimated from the parameters extrapolated from the Tafel plots by the Stern-Geary equation, $R_{corr} = \frac{\beta_{an} \cdot \beta_{cat}}{2.303 \cdot (\beta_{an} + \beta_{cat}) \cdot j_{corr}}$ [43]. Note that the validity of the Stern-Geary relationship is dependent on the anodic and cathodic reactions kinetics where both follow Tafel kinetics. Even though the Stern-Geary equation has been used to analyze copper foil and superhydrophobic surfaces [44, 45], in view of the limitation above, the R_{corr} values have not been used as the basis of the corrosion inhibition analysis rather as an estimate and relative comparison in parametric tests. Moreover, the estimated value of R_{corr} is shown later in the article to correlate closely to the charge transfer resistance measured from electrochemical impedance spectroscopy methods.

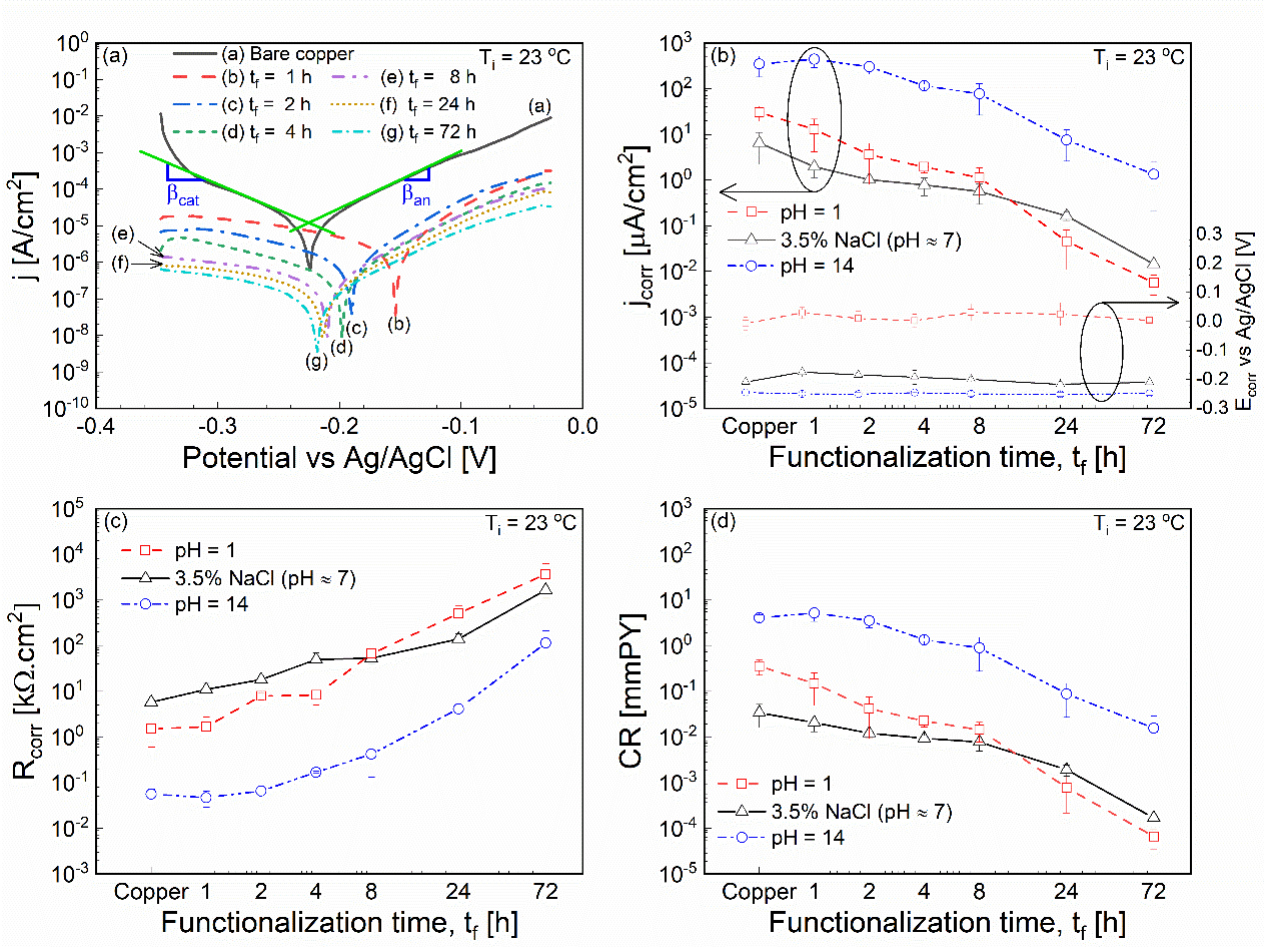

Figure 2.3. (a) Tafel plots from corrosion potentiodynamic polarization (PDP) test in 3.5 % NaCl (pH ≈ 7) solution at 23 °C. Variation of corrosion parameters-(b) corrosion current,j_{corr}, and corrosion potential, E_{corr}, (c) corrosion resistance, R_{corr}, and (d) corrosion rate, CR-with functionalization time, t_f, for superhydrophobic copper surfaces at 23 °C at different pH solutions.

The corrosion current density, j_{corr}, corrosion voltage, E_{corr}, corrosion resistance, R_{corr}, and the corrosion rate, CR, calculated from the PDP measurements are summarized in Figure 2.3(b)–(d). Figure 2.3(b) presents the variation of the corrosion current density, j_{corr}, and the corrosion voltage, E_{corr}, with functionalization time for superhydrophobic surfaces and for bare copper, as reference, for the three different solutions studied (pH values of 1, ≈ 7 (3.5% NaCl), and 14). For each pH value considered, the corrosion current is decreases from bare copper to the superhydrophobic surface and decreases monotonically with increasing functionalization time for

the superhydrophobic surfaces. The corrosion voltage, E_c, however, is seen to increase slightly from bare copper to superhydrophobic surfaces, but remains relatively insensitive to the functionalization time among the superhydrophobic surfaces. The corrosion inhibition effect of the fabricated superhydrophobic surfaces is evident in Figure 2.3(b) in two ways. First, the positive shift in the corrosion potential and second, the decrease in the corrosion current density which together correspond to a lower corrosion rate. For example, for immersion in the 3.5% NaCl solution, it is seen that E_{corr} increases +75.12 mV (-0.229 mV to -0.154 mV) for the sample functionalized for 1 h compared to the bare copper control sample. As the functionalization time increased, a net change of +10.29 mV ($E_{corr} = -0.219$ mV) is observed for the 72 h functionalized sample relative to the bare copper surface. Overall, the superhydrophobic surfaces exhibit a noble potential compared to the copper control samples, over the entire range of solution pH values.

On the other hand, for the 3.5% NaCl solution, the corrosion current density is seen to decrease significantly to 6.55 $\mu A.cm^{-2}$ for 1 h functionalization time—about one third of the current density value of 1.96 $\mu A.cm^{-2}$ for the bare copper control sample. Figure 2.3(b) further reveals that the current density decreases dramatically with an increase in functionalization time: about one order of magnitude reduction in j_{corr} of 0.48 $\mu A.cm^{-2}$ is achieved for the samples functionalized for 4 h, and the current density is as low as 0.15 $\mu A.cm^{-2}$ for the 72 h functionalization time. More dramatic reduction in the current density by three to four orders of magnitude is also seen in Figure 2.3(b) for the samples immersed in $pH = 1$ and 14: the current density decreases from 8.85 $\mu A.cm^{-2}$ (bare copper) to 0.0027 $\mu A.cm^{-2}$ (72 h functionalization) for immersion in an extremely acidic, $pH = 1$, solution, and from 404 $\mu A.cm^{-2}$ (bare copper) to 0.028 $\mu A.cm^{-2}$ (72 h functionalization) for immersion in an extremely alkaline, $pH = 14$, solution. Such low corrosion current density values clearly indicate the effective anti-corrosive nature of the fabricated superhydrophobic surfaces.

Expectedly, therefore, the corrosion resistance, R_{corr}, increases for the superhydrophobic surface compared to the bare copper surface in Figure 2.3(c), and with the functionalization time among the superhydrophobic surfaces, for all the solution pH studied. The resistance is seen to increase over 287-fold to 1658 $k\Omega \cdot cm^2$ for the superhydrophobic sample with 72 h functionalization immersed in 3.5% NaCl solution, compared to the 5.77 $k\Omega \cdot cm^2$ for a bare

copper surface immersed in the same solution concentration. For $pH = 1$ and $pH = 14$, the corresponding resistance increase is seen to be from 1.50 $k\Omega \cdot cm^2$ to 3,688 $k\Omega \cdot cm^2$ and from 0.06 $k\Omega \cdot cm^2$ to 114.32 $k\Omega \cdot cm^2$. The two- to four-orders of magnitude decrease in the current density noted in Figure 2.3(b) of superhydrophobic copper surfaces can be attributed to multiple mechanisms. The fabricated superhydrophobic surfaces include a chemisorbed functionalization layer which prevents the electrolyte, including the halide anions (Cl^-), from reaching the copper surface and acts as a physical barrier to avert oxidation of the surface. In addition, the superhydrophobicity of the samples ensures the presence of air bubbles trapped in the interasperity regions of the multiscale surface microstructures that serve to cushion the electrolyte further away from the surface, thereby limiting the potential for corrosion. Corrosion is a surface phenomenon in nature that begins from microcavities which have higher local current densities, which, combined with the water repellency effect of the SHS, can explain the trend in the improvement of the corrosion inhibition of the prepared samples with an increase in functionalization time. As the time of immersion in stearic acid solution increases, the number of micro-size defects, defined in terms of deviation from homogeneous chemisorption of the stearic acid, decreases. Therefore, there are fewer possible pairs of reduction and oxidation sites available to the electrolyte on the surface with an increase in functionalization time.

In a general metal anodic corrosion reaction, $M \rightarrow M^{n+} + n \cdot e^-$, the rate of corrosion can be calculated by relating the current flow to mass of metal being corroded, m, in terms of the Faraday constant (F), as: $Q = nF(m/A_w)$, where Q is the transferred charge, n is the number of electrons transferred per molecule or atom of metal and A_w is the atomic weight of the metal. By defining an equivalent weight (EW) as $\frac{A_w}{nF}$ and taking the time derivative of the expression for Q, the corrosion rate ($CR = \frac{1}{\rho A} \cdot \frac{dm}{dt}$) in mm/y (denoted as mmPY) is obtained as $CR = 3276.6 j_{corr} E_w/\rho$ where $j_{corr} = \frac{1}{A} \cdot \frac{dQ}{dt}$ is the current density, ρ is the metal density and A is the metal surface area being corroded. Figure 2.3(d) presents the variation of the corrosion rate with the functionalization time of the superhydrophobic surfaces in comparison to the corrosion rate of bare copper surface, in the three different pH solutions. The corrosion rate curves follow the same variation as that of the current density in Figure 2.3(b), and decrease significantly as the functionalization times increases. This decrease is observed to be about two to four orders of magnitude for $pH = 1$ and

$pH = 14$, for the samples with a functionalization time of 24 h and above. For the samples immersed in 3.5% NaCl ($pH \approx 7$) the corrosion rate decreases by nearly two decades. In all the cases, the distinct corrosion inhibition benefit of the superhydrophobic surfaces is evident relative to bare copper surface, which may be quantified further in terms of a corrosion inhibition efficiency, defined as $\eta_c = \left(1 - \frac{j^{SH}}{j^0}\right) \times 100\%$, where j^0 and j^{SH} are the corrosion current density for the bare copper and the superhydrophobic surfaces, respectively. In all the three solution pH studied, the samples with 8 h functionalization time had >90% corrosion inhibition efficiency. This value is over 99% for pH = 1 and pH = 14, and over 95% for 3.5%NaCl (pH ~ 7) solution for samples with functionalization time of 24 h and above. The dynamic polarization curve extrapolated information including β_{an}, β_{cat}, j_{corr}, E_{corr}, η are summarized and tabulated in Table 2.1.

Electrochemical impedance spectroscopy (EIS).

The corrosion of bare copper and superhydrophobic copper samples functionalized at the six different times, were also studied using the electrochemical impedance spectroscopy (EIS) technique, for immersion in 3.5% NaCl and solutions of $pH = 1$ and $pH = 14$, at a temperature of 23°C. Figure 2.4 presents the measured data on corrosion in 3.5% NaCl, as the various markers, in terms of the Nyquist plots for the bare copper sample (Figure 2.4(a)) and the superhydrophobic samples (Figure 2.4(b)), as well as the Bode plot (Figure 2.4(c)) and the phase plot (Figure 2.4(d)) for all the samples studied. The Nyquist plots for the functionalized superhydrophobic copper surfaces (Figure 2.4(b)) are distinctly different in shape and size compared to the bare copper surface (Figure 2.4(a)), which correspond to a difference in the corrosion mechanism between the two. The Nyquist plot for the bare copper sample shows a semicircle at the high-frequency region and a linear variation with a slope of ~45 degrees in the low-frequency region. The semicircular head of the plot is an indicator of charge transfer at the surface and the linear tail is an indicator of the presence of mass transfer (diffusion) attributed to either of the following transports: (1) the diffusion of anions produced from the reduction of the copper in the presence of the electrolyte, which diffuses halide copper complexes, namely $CuCl_2^-$ or $CuCl_4^{2-}$, into the bulk solution or (2) the diffusion of the dissolved oxygen toward oxidation corrosion sites on the surface [7,8]. In contrast, the mass transport region at the low frequency is absent for the superhydrophobic surfaces in Figure 2.4(b) suggesting an absence of or an insignificant transport of redox species.

Furthermore, among the superhydrophobic surfaces in Figure 2.4(b), the diameter of the capacitive loop increases with an increase in functionalization time indicative of a significant lower charge transfer for these surfaces in comparison to the bare copper surface.

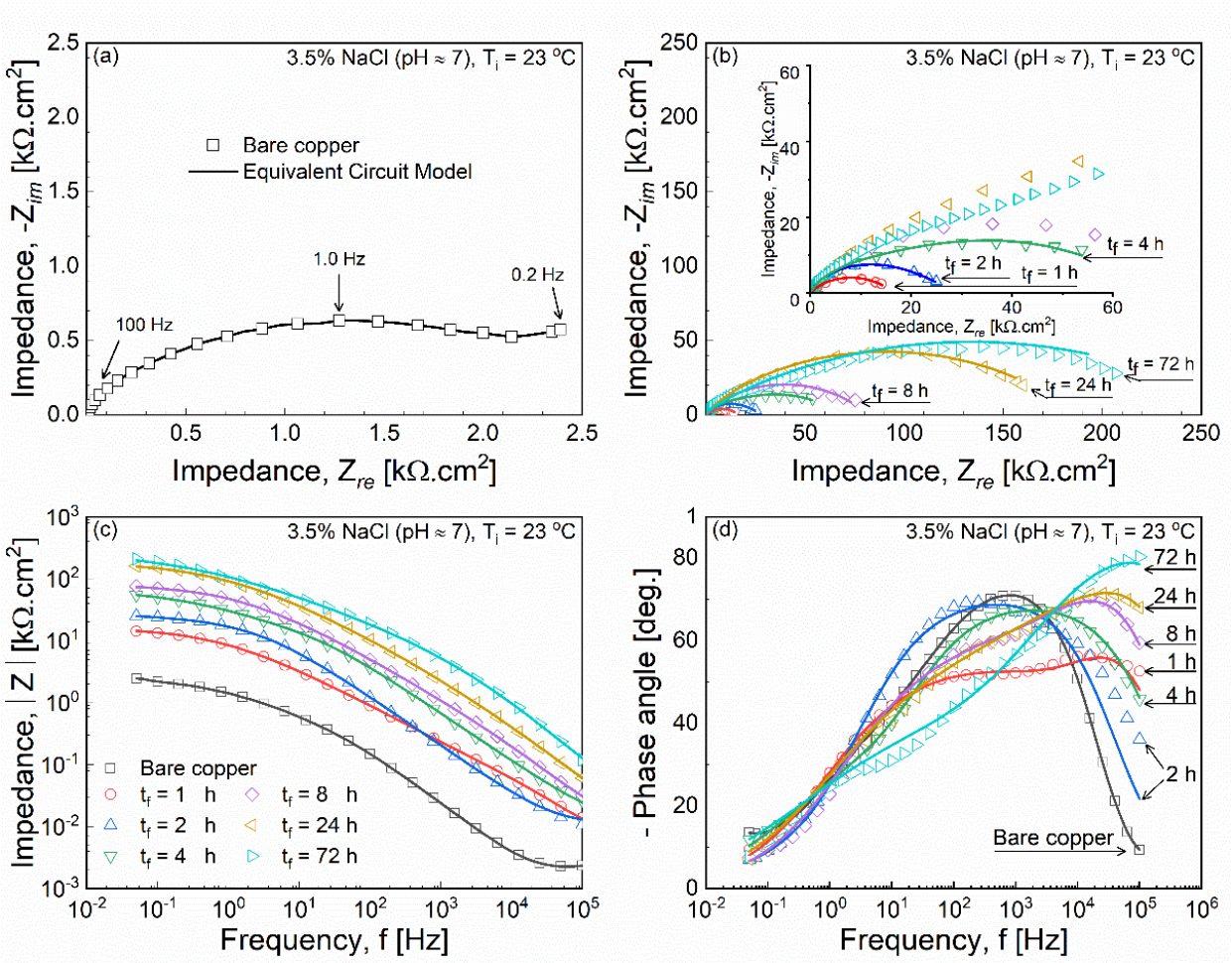

Figure 2.4. EIS data curves showing the effects of functionalizing time at 23 °C in 3.5 % NaCl (pH ≈ 7) solution: Nyquist plots of (a) bare copper as reference, and (b) superhydrophobic surfaces (SHS); (c) Bode plots of bare copper control sample and SHS, and (d) Phase diagrams of bare copper control sample and SHS.

The Bode diagram in Figure 2.4(c) provides further evidence of the corrosion behavior among the bare and the superhydrophobic samples. It is seen that the Bode plots shift toward higher a impedance modulus over the entire scanned frequency range for the superhydrophobic surfaces compared to bare copper, with generally increasing values with functionalization time among the

various superhydrophobic samples studied. It has been reported that the impedance modulus value in the low-frequency region of the Bode diagram may be regarded as an indicator of the corrosion inhibition behavior [10,11]. The impedance magnitude at a frequency of 0.05 Hz, for the superhydrophobic sample functionalized for 1h is seen to be about an order of magnitude larger than the corresponding value for the bare copper sample. With increasing functionalization time from 24 h to 72 h, the impedance value is seen to increase by a further order of magnitude, resulting in a two-orders of magnitude increase for the superhydrophobic surface with 72 h functionalization relative to bare copper.

Collectively, the Nyquist and the Bode plots in Figure 2.4(a)-(c) confirm a greater corrosion inhibition in the case of the functionalized superhydrophobic surfaces, and an increasing corrosion resistance with increasing functionalization time. Additionally, the phase plot in Figure 2.4(d) presents the variation of the negative of the phase angle with frequency for all the samples considered. In general, the variations exhibit a nonmonotonic trend with a peak phase angle at certain frequencies. The peak angle is larger and shifts to the higher frequencies for the longer functionalization times. Of further note in Figure 2.4(d) is the presence of two capacitive peaks for the functionalized samples that are especially evident in the case of the longer functionalization times.

Electrochemical impedance spectroscopy (EIS) data recorded on immersion of bare copper and superhydrophobic copper surface functionalized for 24 h in solutions with $pH = 1$ and $pH = 14$ are presented in Figure 2.5 along with the data for the 3.5% NaCl solution, redrawn from Figure 4 for comparison. In the Nyquist plots of Figure 2.5(a,b), the imaginary axis to the real axis scale ratio is kept to 3 for each pH value, for clarity of the shape of the curves. The data correspond to a temperature of $23°C$. For immersion of bare copper in the extremely acidic and the extremely alkaline solutions, the Nyquist plot in Figure 2.5(a) does not show a distinguishable diffusion tail (a slope of approximately 45° near the origin) in the low-frequency region that is evident for the data on the 3.5% NaCl solution. For the 24 h functionalized samples in all the pH cases, Figure 2.5(b) shows that the capacitive loops corresponding to the double-layer capacitance are much larger in magnitude and extend longer than the respective data for the bare copper control sample in Figure 2.5(a). This indicates excellent corrosion inhibition performance of the superhydrophobic surfaces over the entire range of pH values. Furthermore, the Bode plots in Figure 2.5(c) show

that the impedance magnitude is consistently at least a decade larger for the superhydrophobic surface over the entire frequency range and for all pH values. At the frequency of 0.05 Hz, the one, two and three orders of magnitude increase in the impedance magnitude for pH = 14, $pH \sim 7$ (3.5%NaCl), and pH = 1, respectively, offer evidence of the great corrosion inhibition characteristics of the superhydrophobic surfaces. The phase plots in Figure 2.5(d) show similar characteristics to that seen for the 3.5% NaCl solution in Figure 2.5(d), in the presence of a peak phase angle for immersion of bare copper in $pH = 1$ and $pH = 14$ solutions, with the latter demonstrating a double peak. For the superhydrophobic surface, the peak angle is shifted to larger frequencies, uniformly for all solution pH values. Furthermore, a twin capacitive peak is evident for immersion in all the solutions.

The observations in Figure 2.4 and 5 and are used to construct an equivalent circuit model for the corrosion of the bare and superhydrophobic surfaces, in order to determine the parameters describing the corrosion of the surfaces in the different pH solutions. Before constructing the equivalent circuit model, the validity of the EIS measurement was tested via Kramers-Kronig (K-K) analysis [46] to ensure that the EIS data represent the physical processes of the electrochemical system studied [47]. The Nyquist and the phase plots for bare copper (Figure 2.4(a), 5(a) and 4(d), 5(d)) suggest the use of a Warburg diffusion element in the circuit. Moreover, the semi-circular arcs in the Nyquist plots (Figure 2.4(a), (b) and 5(a), (b)) for both functionalized and bare copper samples suggest the use of a capacitor in parallel with a resistor. However, as seen in the phase diagram, Figure 2.4(d) and 5(d), the peaks do not reach the –90 degree value, the phase angle of an ideal capacitor. The depressed semi-circles in Figure 2.4(a), 5(a) and 4(b), 5(b) are known to be due to the dispersing effect [48] and may be effectively modeled by a constant phase element (CPE), instead of a pure capacitor, in parallel to a resistor. The use of CPE is well established in the literature and serves to compensate for the non-homogeneity of the systems arising from such factors as roughness, porosity, reactivity, potential, and current distribution attributed to the interface or the electrode geometry [49, 50]. Furthermore, the presence of two capacitive peaks in the phase plots for the superhydrophobic surfaces, Figure 2.4(d) and 5(d), justifies the use of two CPEs in the equivalent circuit model. Experimental observations and the measured data suggest the existence of a concentrated layer of dissolved corrosion redox species in the vicinity of the bare copper surface in the electrolyte, which has been treated as a film in its correspondent

equivalent circuit. Likewise, a Warburg element was used in series with the charge transfer resistor to compensate for the diffusion effect and the observed low-frequency tail.

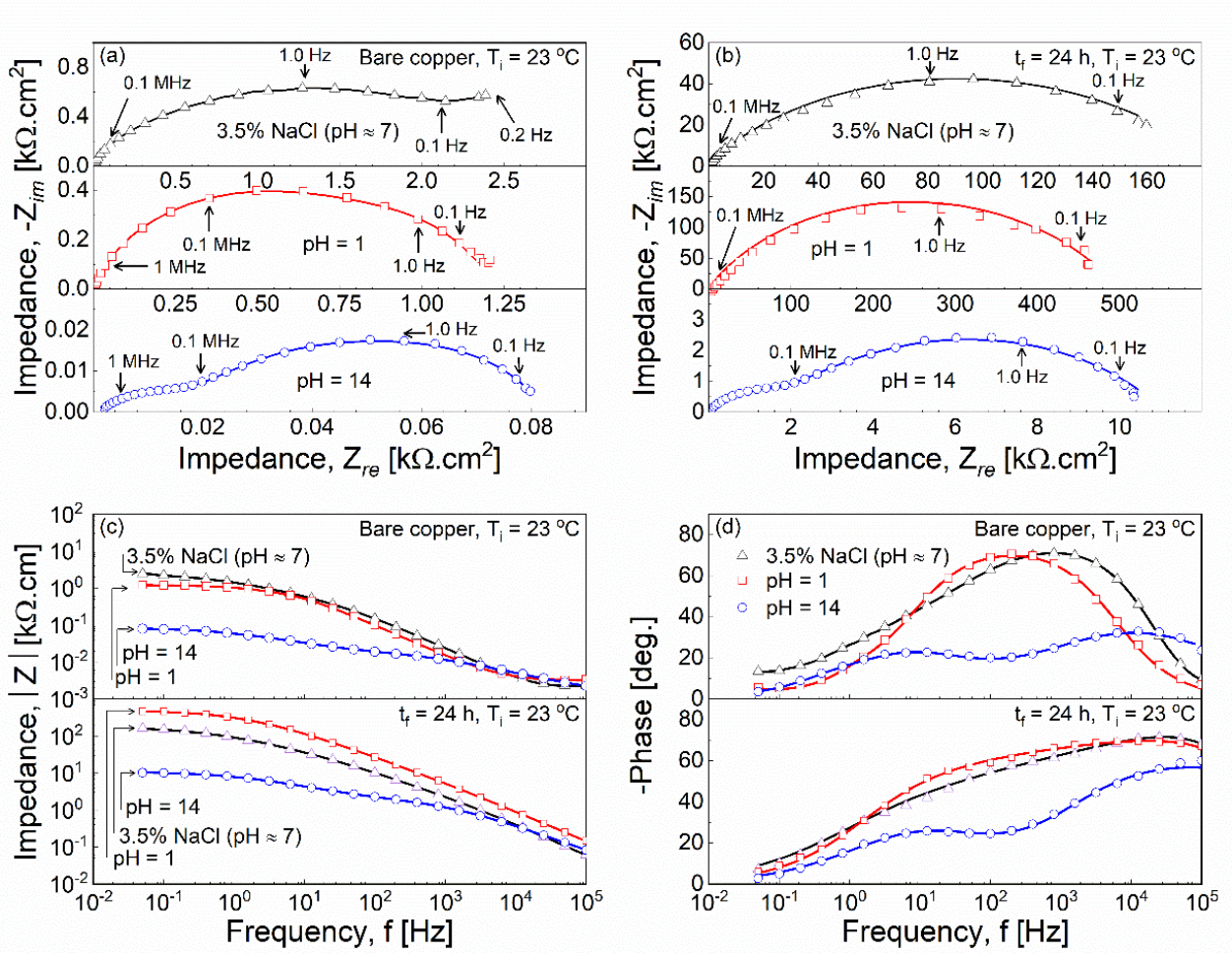

Figure 2.5. EIS data curves showing the effect of pH solution at 23 °C: Nyquist plots of (a) bare copper as reference and (b) superhydrophobic surfaces (SHS); (c) Bode plots of bare copper control sample and SHS; (d) Phase diagrams of bare copper control sample and SHS.

With the foregoing considerations, equivalent resistive and capacitive circuits are constructed for the bare copper and the superhydrophobic copper surfaces, as presented in Figure 2.6(a) and 6(b) for the bare copper and superhydrophobic surfaces, respectively. The equivalent circuits comprise the following elements: R_s representing the solution resistance, R_f denotes the surface film resistance to corrosion, R_{ct} is the charge transfer resistance corresponding to corrosion inhibition resistivity of the surface, and CPE_f and CPE_{dl} as the constant phase elements for the

film and double layer, respectively, defined as $CPE_i = \frac{1}{Q_i(j\omega)^{n_i}}$, where j is the imaginary number ($= \sqrt{-1}$), ω is angular frequency, the subscript i denotes either the surface film (f) or the double layer (dl), and Q_i and n_i are the magnitude of the capacitance and the phase exponent in the respective layer, such that a capacitor is an ideal CPE with a phase exponent of 1. The experimental data measured using EIS for immersion of the bare and the superhydrophobic samples (with the different functionalization times) in the three solutions were fit to the respective equivalent circuits, as shown by the solid lines in Figure 2.4 and 5. The corresponding calculated circuit element parameters, tabulated in Table 2.2 and 3, demonstrated the following salient features:

(1) the Q_f values for the superhydrophobic surfaces (0.006–0.02 for $t_f = 72$ h, for example) were generally one to three orders magnitude smaller than the corresponding values for bare copper (14.36–678.54), for all solution pH values. A higher Q_f means a higher level of penetration of the corrosive solution into the film cavities, and a constant decrease was seen in this value with an increase in the functionalization time.

(2) the Q_f values were all lower than Q_{dl} values for all surfaces, and for all solution pH values, implying that the charge double layer effect is a dominant corrosion phenomenon.

(3) the Q_{dl} values for superhydrophobic surfaces functionalized for 72 h were 0.4 ($pH = 1$), 2.75 (3.5% NaCl) and 1.37 ($pH = 14$), which were at least three decades lower than the corresponding values of 711.81, 167.07, and 3,211.10 for the bare copper surface. This trend is consistent with the expectation of less penetration of the solution into the double layer for the superhydrophobic surfaces. Furthermore, Q_{dl} for the bare copper immersed in extremely acidic and the extremely alkaline conditions are significantly higher values compared to the near-neutral 3.5% NaCl solution, reflecting the fact that a harshly acidic or alkaline condition can increase the penetration of the solution. However, with functionalization, the Q_{dl} for the superhydrophobic surface decreases signifying a protection.

(4) The values of the film resistance, R_f, which can be interpreted as a physical barrier against corrosion, ranged from 0.01–540.00 kΩ · cm^2 and were much smaller than the R_{ct} values of 0.04–1930.00 kΩ · cm^2, for both bare copper and superhydrophobic surfaces alike, and in all pH environments. The relative magnitude of the two resistances is consistent with the

observation from the PDP studies that the main contributor to corrosion inhibition is the superhydrophobicity effect rather than the physical barrier mechanism.

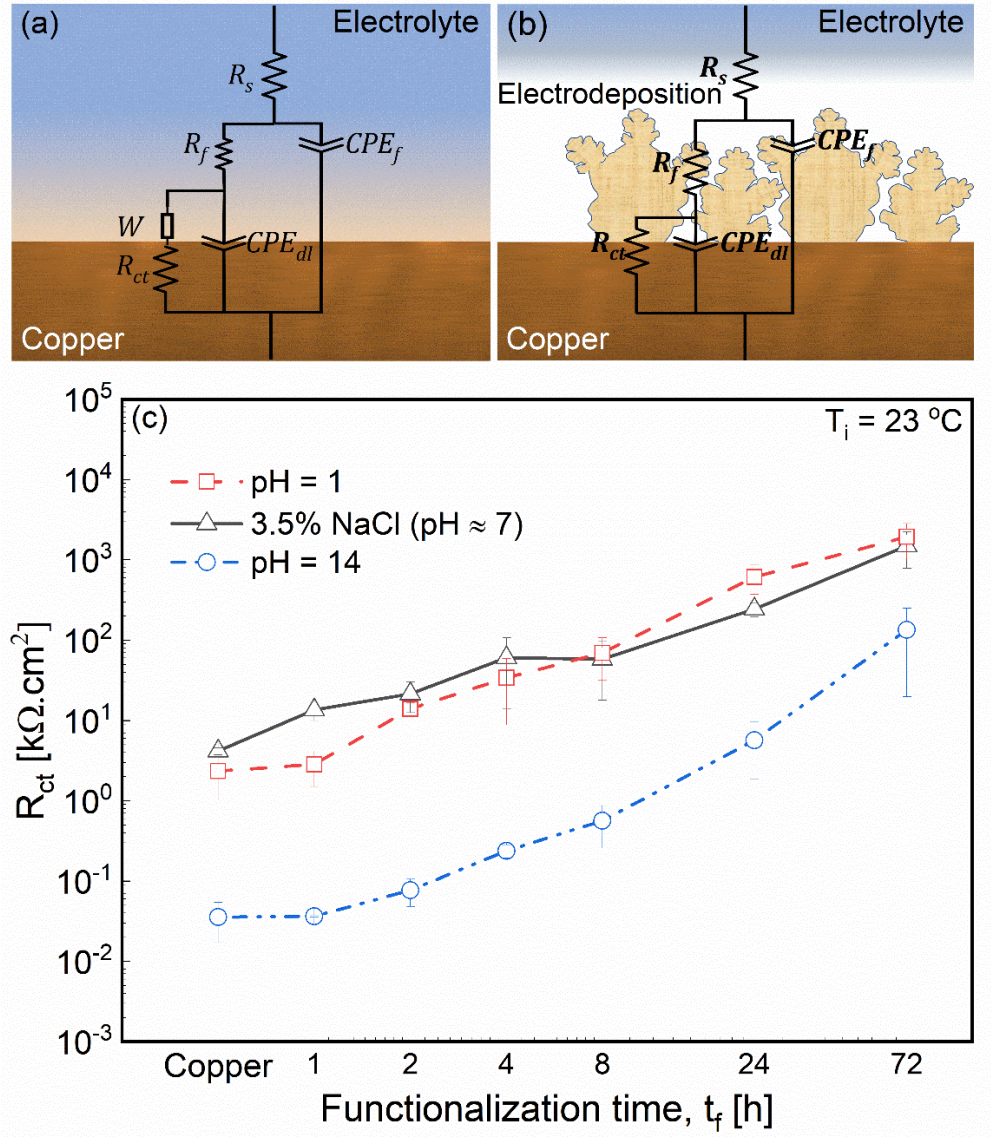

Figure 2.6. Schematic of the equivalent circuit model of EIS data for (a) bare copper control sample and (b) superhydrophobic surfaces; (c) variation of the charge transfer resistance, R_{ct}, derived from the equivalent circuit model for bare copper control sample and superhydrophobic surfaces with functionalization time, t_f, in three different pH solutions.

Figure 2.6(c) presents the variation of the charge transfer resistance (R_{ct}) values of the equivalent circuits for the bare copper and the superhydrophobic surfaces as a function of the functionalization time. The charge transfer resistance R_{ct} is seen to increase from the bare copper to the superhydrophobic surface, and further, increases monotonically with the functionalization time. Among the three different pH environments studied, the resistance is nearly independent of pH for $pH \lesssim 7$, but decreases with further increase in pH from 7 to 14. Of particular note is that the R_{ct} values for the different surfaces and the solution pH values closely match the corresponding R_c values derived from potentiodynamic test results, as presented in Figure 2.3(c), and follows the trend well. The close correspondence of the R_{ct} and R_{corr} values provides validation of the developed equivalent circuit model, which may be used for a deeper insight into the corrosion inhibition mechanism of the studied surfaces.

The corrosion inhibition seen in Figure 2.3–6 is explained by three phenomena [51, 52]. First is the passivation of the active corrosion sites by the chemisorbed functionalization agent molecules acting as physical barrier preventing the redox cations and anions from reaching the metallic surface. The second mechanism is the existence of excessive similar charge on the surface which presents repulsive forces that retard the diffusion of the corrosion redox species toward the surface. The pH effect on surface charge on superhydrophobic surfaces may provide insight into the second corrosion inhibition mechanism. It is shown experimentally in multiple studies that the interface of air/electrolyte on hydrophobic surfaces is basic at pH above the isoelectric point (IEP), the pH at which particular molecules carries no net electric charges in the solution [53-55]. For hydrophobic surfaces, the IEP is $pH = 2\ to\ 4$ [53, 55]. Further, it is also known that the OH^- ions have the highest absorption energy toward the water/SHS interface followed by Cl^- and H^+ [53], independent of the existence of multivalent anions in the electrolyte such as$CuCl_3^{2-}$ or Cu^{2+}[54, 55]. The second mechanism for the pH cases studied have been detailed as follow:

- For $pH = 1$, the $pH < IEP$ and the electrolyte/SHS interface is positively charged. Due to abundance of hydronium ions at this pH, the cathodic corrosion reduction reaction in the acidic environment follows the $O_2 + 4H^+ + 4e^- \rightarrow 2H_2O$ pathway rather than $O_2 + 2H_2O + 4e^- \rightarrow 4OH^-$. The positive charge at the interface exerts a repulsive electrostatic force retarding H^+ from diffusion to the interface and hence improves the corrosion resistance.

- For $pH \sim 7$, 3.5% NaCl solution, the $pH > IEP$ and the electrolyte/SHS interface carries OH^- static electric charge. In the presence of sodium chloride the anodic corrosion reaction follows one of the (I) $Cu + Cl^- \rightarrow CuCl + e^-$ or (II) $CuCl + Cl^- \rightarrow CuCl_2^-$ pathways. Therefore, the negative excessive charge retards the corrosion redox reaction and act as an anti-corrosion mechanism specific to hydrophobic surfaces.
- For $pH = 14$, the $pH > IEP$ and the electrolyte/SHS interface is negatively charged. The $O_2 + 4H^+ + 4e^- \rightarrow 2H_2O$ cathodic corrosion pathway is less favorable in this case, and the electrolyte is deprived of hydronium (or H^+) by 13 orders of magnitude compared to the basic case ($pH = 1$) and by 7 orders of magnitude compared to the chlorine case ($pH \sim 7$). Contrary to the other two cases, the excessive charge, therefore, neither retards nor accelerates corrosion on the surface. As a result, the corrosion resistance is generally lower in the harshly basic environment compared to the acidic environment in Figure 2.6(c).

The third and the most important corrosion inhibition mechanism that plays the major role compared to the other two, namely physical barrier and surface charge, is the existence of an air/electrolyte interface. The stable air bubbles between the multiscale porous structure of the superhydrophobic and the electrolyte, forms a cushion of air, with which reduces the number of the available redox reaction pair sites for corrosion to initiate.

2.4.3. **Long term immersion and corrosion inhibition stability.**

The results reported so far were for bare copper and superhydrophobic surfaces immersed in the different pH solutions for 30 min. In order to characterize the stability of the corrosion inhibition of the fabricated superhydrophobic surfaces, immersion tests were conducted for relatively longer durations of up to 800 min (referred to as "long term" in this study, which differs from the studies in the literature that refer to long term in duration of several days) in extremely acidic ($pH = 1$), near-neutral halide (3.5% NaCl, $pH \approx 7$) and extremely alkaline ($pH = 14$) solutions at room temperature ($23°C$). Linear polarization tests were performed intermittently at periodic intervals during the course of the immersion duration to derive the corrosion parameters, E_{corr}, j_{corr}, R_{corr}, and the corrosion rate (CR). With overpotential of ±20 mV with respect to open circuit potential, that are about 12 times smaller than the overpotential in a potentiodynamic polarization test, linear polarization tests are relatively nondestructive in nature. The corrosion potential, E_{corr}, is obtained as the intersection of the $j = 0$ A/cm^2 line and the measured voltage-

current density data. A linear line was fit to the data at ±10 mV of the E_{corr} The slope of the fitted line is the corrosion resistance, R_{corr}. The anodic and cathodic slopes, β_{an} and β_{cat}, were estimated by fitting Tafel relationship to the measured data, and the corrosion current was derived from the Stern-Geary relationship. There was not a significant dissolution of copper found for superhydrophobic samples, however, it should be noted that the corrosion resistance values derived from Stern-Geary equations are an estimate and are only used relatively for comparison as discussed in section 3.2.

The corrosion resistance and the corrosion rate are summarized in Figure 2.7 for the long-term immersion tests in the three pH solutions, where the solid markers correspond to bare copper and the open markers denote the parameters for a superhydrophobic surface with a functionalization time of 24 h. Figure 2.7(a) shows that the corrosion resistance for the superhydrophobic surface is stable throughout 800 minutes of immersion time and is consistently higher than the values for bare copper in all the three pH environments. For $pH = 14$, a reduction in the corrosion resistance is noted with the immersion duration, although the corrosion resistance of the superhydrophobic surface remains higher than that for bare copper throughout the duration of the test. Figure 2.7(b) presents the variation of the corrosion rate with immersion time and demonstrates excellent stability, that may be examined in terms of a corrosion inhibition efficiency, as defined in section 3.2. The corrosion inhibition efficiency stays at over 99% throughout the test for the 3.5% NaCl solution; for $pH = 1$ the corrosion efficiency begins at 99.9% efficiency and drops slightly to 96% by the end of the test, which is still an excellent corrosion inhibition compared to bare copper surface. For $pH = 14$, the corrosion inhibition efficiency remains stable at about 95%. Note that since the corrosion rate is a linear function of j_{corr}, the trends in Figure 2.7(b) on the corrosion rate may equivalently be interpreted to be the same as that in the corrosion current density.

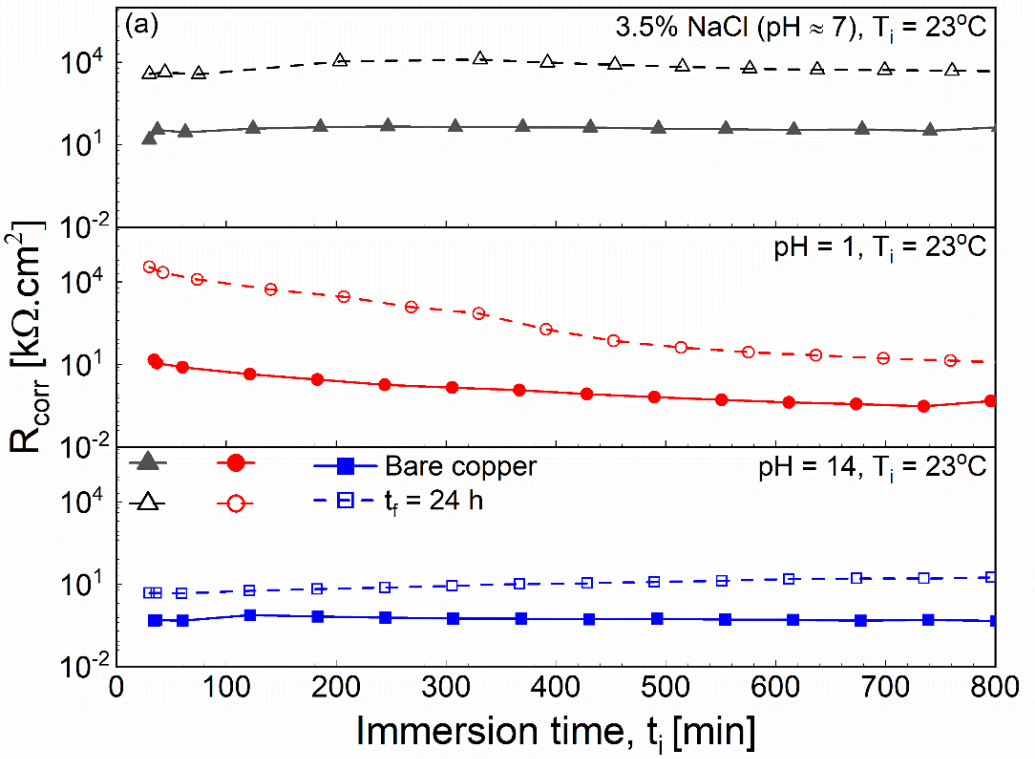
(a)
3.5% NaCl (pH ≈ 7), T_i = 23°C
pH = 1, T_i = 23°C
pH = 14, T_i = 23°C
Bare copper
t_f = 24 h
R_corr [kΩ.cm²]
Immersion time, t_i [min]

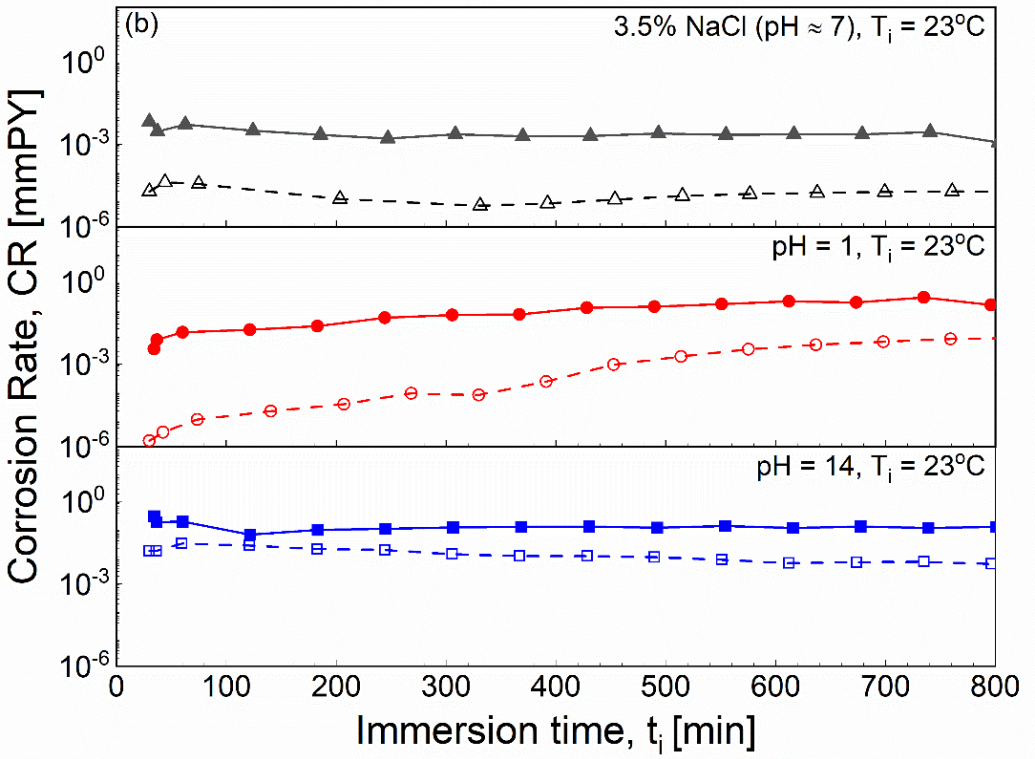
(b)
3.5% NaCl (pH ≈ 7), T_i = 23°C
pH = 1, T_i = 23°C
pH = 14, T_i = 23°C
Corrosion Rate, CR [mmPY]
Immersion time, t_i [min]

Figure 2.7. Variation of (a) corrosion resistance, R_{corr}, and (b) corrosion rate, CR, with immersion time, t_i, for bare copper control sample and superhydrophobic surfaces in three different pH of the immersion solution at T_i = 23 ℃.

The impact of the long-term corrosion of the samples was further assessed by means of scanning electron microscopy (SEM) imaging of the surfaces, composition analysis using energy dispersive x-ray (EDX) technique, and contact angle measurements as presented in Figure 2.8. Figure 2.8(a)–8(c) show the SEM images of the superhydrophobic surface with a functionalization time of 24 h, at three different magnifications, prior to the long term corrosion test. Figure 2.8(d)–8(f) present the surface SEM micrographs of the surface after the 800 minute immersion in 3.5% NaCl, $pH = 1$ and $pH = 14$, respectively, and in all three cases, demonstrates no surface morphology degradation compared to the surface image (Figure 2.8(c) at the same magnification) prior to the long term corrosion tests. Figure 2.8(g) summarizes the surface composition data obtained from EDX spectra collected at a low magnification of 500X on superhydrophobic samples immersed in the three pH solutions. As seen in the XPS data discussed earlier (section 3.1), the modification agent (stearic acid) comprises carbon and oxygen, whereas the corrosive environment contains chlorine (for NaCl case), sulfur ($pH = 1$), and sodium ($pH = 14$). There is almost no change in carbon, oxygen, and copper content of the surfaces after long term corrosion tests for all three cases, which confirms the surface composition stability along with the morphology stability shown by SEM analysis. Moreover, the absence of Cl, Na, and S in the collected EDS spectra of the test samples after the long term corrosion test implies absence of any residual corrosion footprint on the surface. This is evidence of the outstanding superhydrophobicity and slipperiness of the surface that effectively shields the base metal substrate from the invasive corrosive elements in the solutions. As further evidence of the integrity of the surfaces following long term corrosion, Figure 2.8(h) presents the contact angle measurements before and after the long term corrosion tests in the three solutions. It is seen that the surfaces remained strongly superhydrophobic with contact angle above 150 degrees in all the cases and, furthermore, no significant change is seen before and after long term corrosion tests in saline, harshly acidic, and harshly alkaline corrosive environments. The results in Figure 2.7and 8 sturdily demonstrate the excellent anti-corrosion performance and stability of the electrodeposited superhydrophobic copper surfaces.

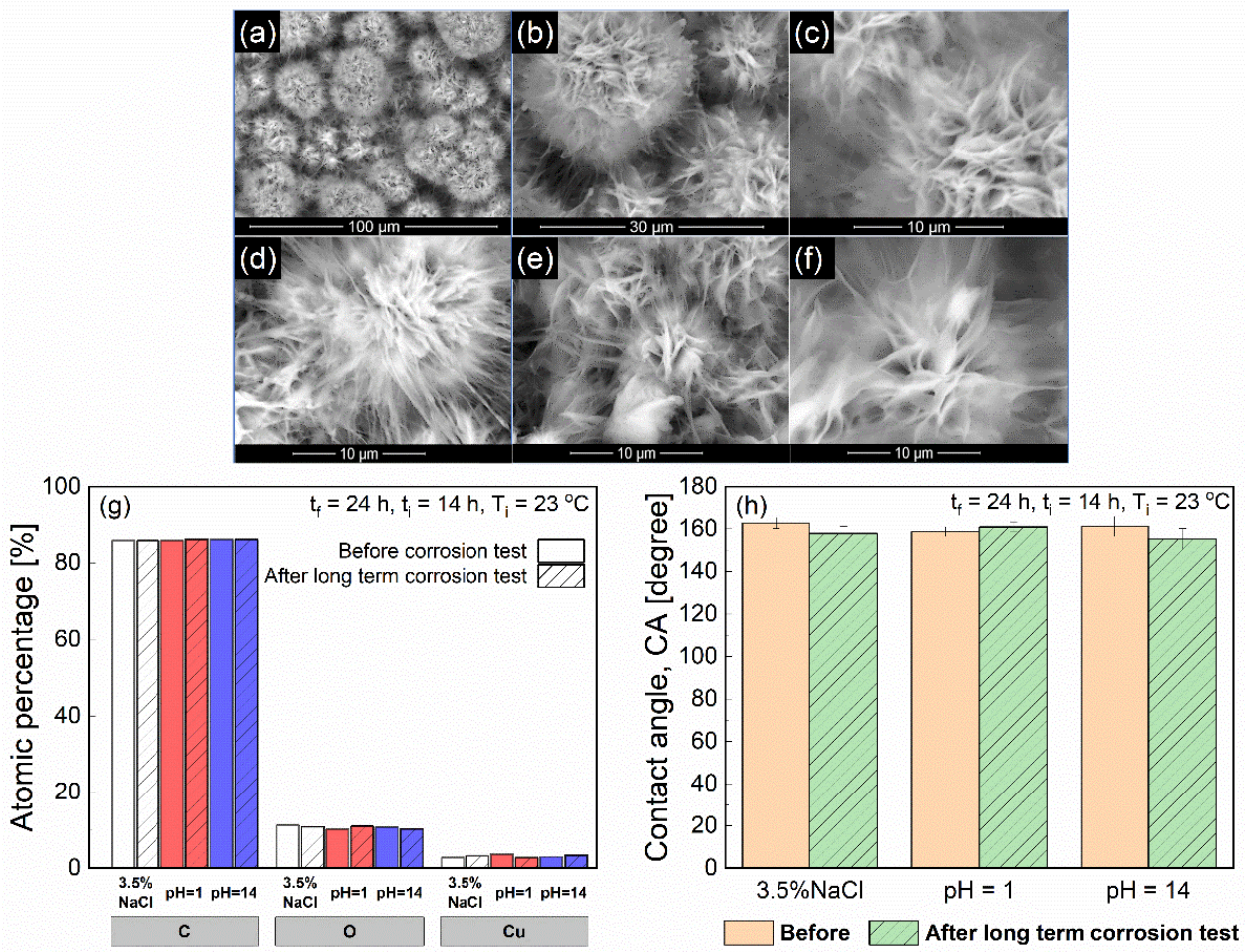

Figure 2.8. SEM images of superhydrophobic surface (SHS) at three different magnifications, (a–c) before the long term corrosion test and after long term corrosion test in (d) 3.5% NaCl (pH ~7), (e) $pH = 1$ and (f) $pH = 14$ aqueous solutions; (g) summary of surface relative atomic perc entage of detected elements and (h) contact angle of 10µl DI-water droplet on the surfaces before and after long term corrosion test in different pH solutions at temperature T_i = 23℃.

2.4.4. **Effect of temperature on corrosion.**

It is well known that the corrosion mechanisms are accelerated at the higher temperatures. Most of the studies in the literature have focused on corrosion performance of non-wetting surfaces at lower temperatures. In order to assess the temperature-dependent corrosion characteristics, corrosion measurements were made at a higher temperature of 50°C on bare copper and the fabricated superhydrophobic surfaces immersed in the three pH solutions. The corrosion resistance and the corrosion rate, derived as described in section 3.2, are presented for bare copper

and superhydrophobic surfaces with varying functionalization time in Figure 2.9(a) and 9(b), respectively. It is seen that the corrosion resistance drops below that for bare copper for superhydrophobic surfaces functionalized for less than 8 h in the case of immersion in 3.5% NaCl and for less than 24 h in the case of immersion in solutions with $pH = 1$ or $pH = 14$. Corresponding trends of increase in corrosion rate are noted in Figure 2.9(b) for the smaller functionalization times. For a functionalization time of 72 h, however, the corrosion resistance and the corrosion rate are about an order of magnitude improved compared to bare copper, in the case of immersion in 3.5% NaCl, and about a factor of 3 better in the case of immersion in extremely acidic or extremely alkaline environments. This suggests that superhydrophobic surfaces with longer functionalization times are warranted for applications to high temperature.

A comparison between the study at 50℃ and room temperature, Figure 2.9(a) and Figure 2.3(c) respectively, shows the acidic solution to have the highest change in corrosion resistance. followed by pH~7 (3.5% NaCl solution) and the basic solution. Corrosion is a chemical reaction in nature, where an increase in temperature increases the number of species that have sufficient energy to overcome the corrosion redox reaction activation energy barrier. The main anodic oxidation pathway in the presence of high concentration of the hydronium ion in case of $pH = 1$ is the H^+ reduction reaction rather than oxygen reduction reaction. The higher available energy in the system, because of the higher temperature, and the hydronium reduction pathway both contribute to the increased corrosion rate for the case of pH = 1. Unlike oxygen, the concentration of halide anions (Cl^-) does not decrease with increase in the temperature and for the case of pH~7 (3.5% NaCl) the anodic oxidation reaction rate increases, and thus the corrosion rate. For $pH = 14$, the concentration of the hydronium ($or\ H^+$) is insignificant, being 13 and 7 orders of magnitude less compared to $pH = 1$ and 7, respectively, and the corrosion mechanism follows the anodic oxygen reduction pathway. Since less oxygen is soluble at 50℃ compared to room temperature, the corrosion rate increases less intensely compared to the two other cases.

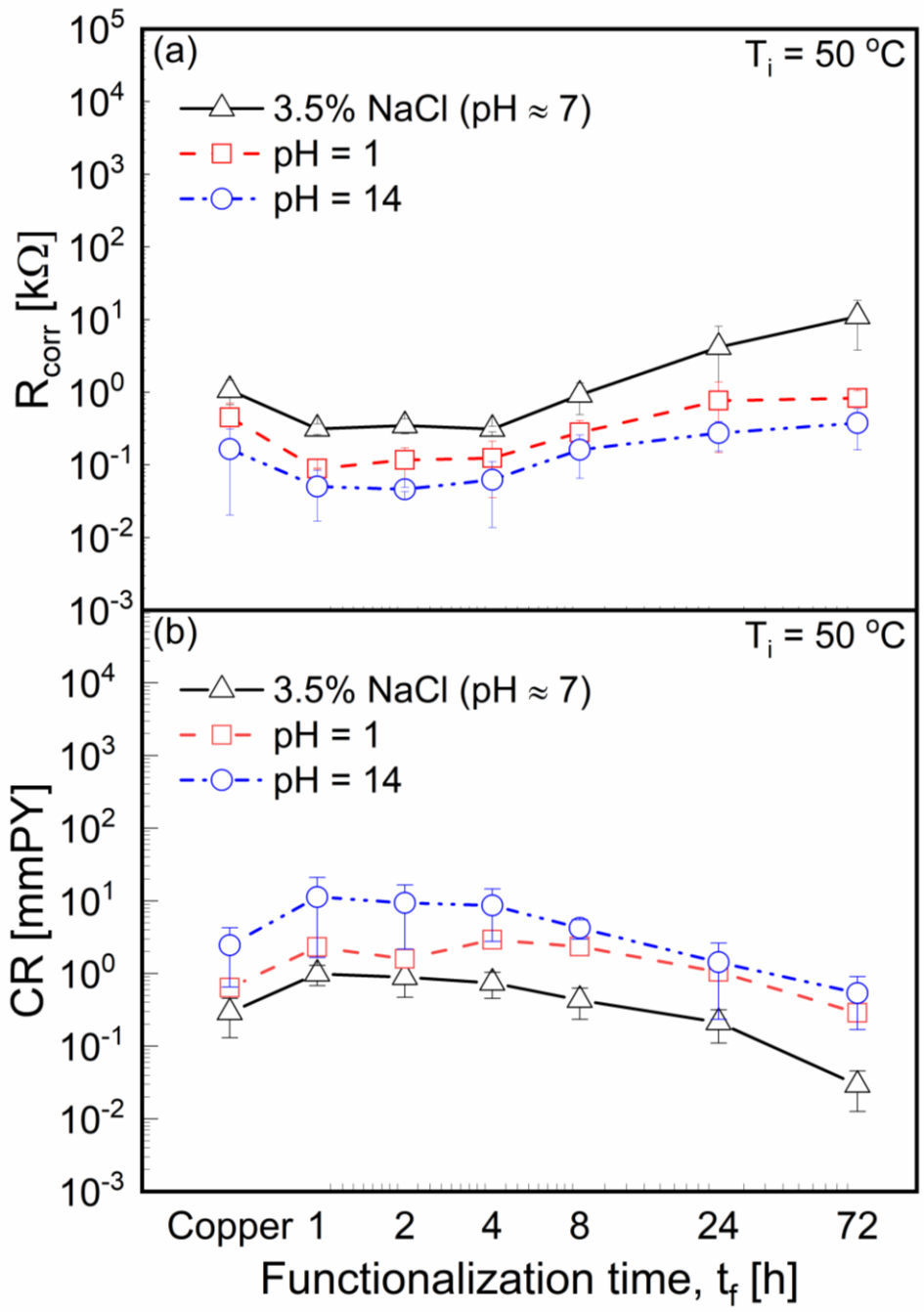

Figure 2.9. Variation of (a) corrosion resistance, R_{corr} and (b) corrosion rate, CR, for bare cop per control sample and superhydrophobic surfaces showing the effect of immersion time, t_i , and pH of the immersion solution at T_i = 50°C.

The higher corrosion resistance of bare copper compared to surfaces with functionalization time below 24 hours can be attributed to the readiness of the bare copper surface to corrosion at

the OCP resting period before the polarization test begins. This period has given the bare copper sample enough time to develop a relatively passive diffusive film at the vicinity of the surface. On the other hand, it is worth noting that for the calculation of the current densities apparent surface area of the test samples has been considered, which is less than the actual surface area in case of rough superhydrophobic surfaces and identical to actual surface area for case of bare copper.

The influence of corrosion at the higher temperature in the case of a superhydrophobic surface functionalized for 24 h is examined in Figure 2.10, in terms of the surface morphology using SEM (Figure 2.10(a)–(f)), chemical composition using an EDX analysis (Figure 2.10(g)), and the water contact angle before and after the corrosion test at 50°C (Figure 2.10(h)). Figure 2.10(a)–(c) present the morphology of the surface at three different magnifications, prior to the corrosion test, while Figure 2.10(d)–(f) show the surface morphologies after the corrosion test at in 3.5% NaCl (Figure 2.10(d)), harshly acidic, $pH = 1$, solution (Figure 2.10(e)) and harshly alkaline, $pH = 14$, solution (Figure 2.10(f)). The effect of the increased temperature is to lower the surface tension of the corrosive liquid, causing more contact with the solid surface. This clearly explains the sparse salt particles on the surface after immersion in 3.5% NaCl solution in Figure 2.10(d) and the presence of sodium peak in the EDX spectrum Figure 2.10(g). Likewise, the slight deformation of the surface morphology in Figure 2.10(e), and the presence of sulfur even though in trace quantity in Figure 2.10(g), is attributed to the same effect after the corrosion test in the harshly acidic aqueous solution of H_2SO_4 with $pH = 1$ at 50°C.

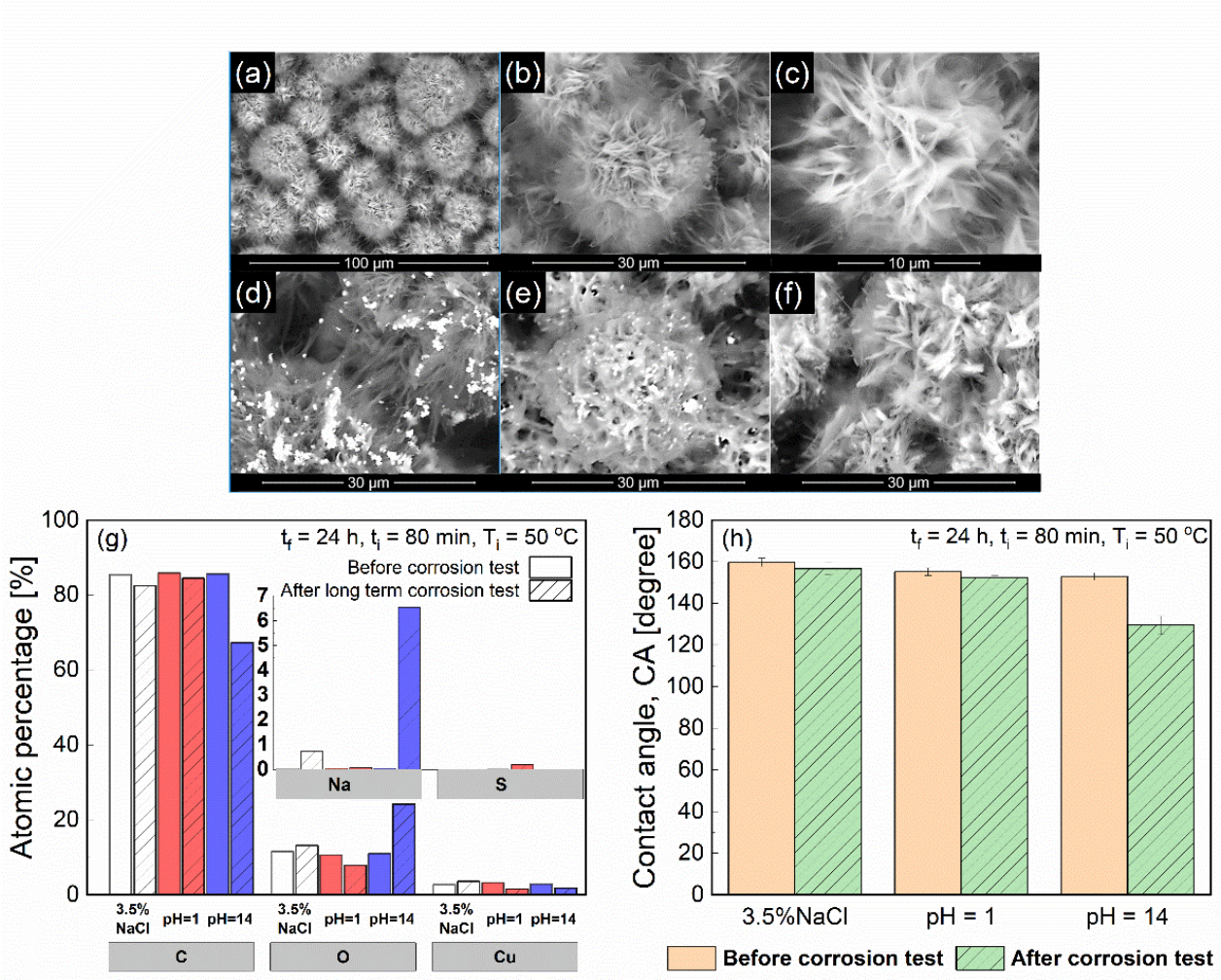

Figure 2.10. SEM images of superhydrophobic surface (SHS) at three different magnification s, (a–c) before the long term corrosion test and after long term corrosion test in (d) 3.5% NaCl (pH~7), (e) $pH = 1$ and (f) $pH = 14$ aqueous solutions; (g) summary of surface relative atomic p ercentage of detected elements and (h) contact angle of 10µl DI-water droplet on the surfaces bef ore and after long term corrosion test in different pH solutions at temperature T_i = 50℃.

Figure 2.10(f) does not show a detectable morphology change for the case of $pH = 14$ solution except sparse particles. The $pH = 14$ was obtained by hydrolysis of NaOH in DI-water. This observation is in agreement with the smaller contact angle measured after immersion in $pH = 14$ compared to the post-immersion contact angles measured for $pH = 1$ and 3.5% NaCl in Figure 2.10(h). Since the disassociation constant (pKa) of stearic acid is 10.15 [56, 57], the

functionalization agent on the surface behaves like an acid in contact with a $pH = 14$ solution and shows basic behavior in contact with $pH = 1$ corrosive solution. Besides, the electrode reduction potential table [58] suggests reactivity of H_2SO_4 and non-reactivity of NaOH with copper. Considering all these factors, besides the high solubility of copper sulfate in water clearly explains the relatively high intensity of the Na peak for the sample immersed in a $pH = 14$ (strongly alkaline) solution, whereas the S concentration in the case of $pH = 1$ (strongly acidic) is relatively small. The residual sodium on the surface after corrosion test for the case of $pH = 14$ is most likely in the form of precipitated NaOH after the sample dried in air, similar to the NaCl crystals distinguishable in the SEM image of 3.5% NaCl in Figure 2.10(d).

Figure 2.10(h) presents the change in the water contact angle before and after the high temperature corrosion tests, in the three solutions. In general, Figure 2.10(h) demonstrates that the superhydrophobic surfaces retain their non-wetting character after corrosion test in 50°C, with water contact angle of 156.74 ± 2.95 and 152.32 ± 1.23 degrees, respectively, after immersion in saline and extremely acidic ($pH = 1$) solutions. It has been reported in the literature that superhydrophobic surfaces tend to degrade in their water contact angle after immersion in harshly acidic and harshly alkaline solutions at room temperature [35]. In contrast, the superhydrophobic surfaces studied here not only showed almost no change in water contact angle after long term immersion in all the cases at room temperature (Figure 2.8) but also showed rejuvenated superhydrophobic behavior after corrosion test in 50°C for two cases of saline and acidic corrosive environments, as seen in Figure 2.10(h). The roll-off angle after long term test at 23°C was measured as 4.0 ± 1.4, 3.0 ± 1.5, and 3.2 ± 0.8 for $pH = 1$, $pH \sim 7$ (%3.5 NaCl), and $pH = 14$, respectively, which is not a significant change to the 3.0 ± 0.5 value before the test. Similarly, the roll-off angle after immersion in harsh acidic environment ($pH = 1$) and saline solution ($pH \sim 7$) at 50°C was measured as 8.2 ± 2.6 and 6.8 ± 3.2 degrees, respectively, while pinning was observed for the case of harsh alkaline solution. The drop in the water contact angle after immersion in the $pH = 14$ solution is attributed to the change in the degree of hydrophobicity due to the sodium contained molecules leftover on the surface.

The discussion so far pertained to one specific high temperature value, and it is of interest to consider the corrosion behavior over a range of temperatures. To this end, considering the case of immersion in 3.5% NaCl of a superhydrophobic surface functionalized for 72 h, the corrosion rate

was also measured using PDP method explained in section 2.4 for temperature values of 23°C to 35°C, 50°C, 70°C, and 85°C. 72 h functionalization was selected for this mean based on the functionalization parametric study. For statistical significance, the tests were repeated three times at each temperature. Figure 2.11presents the variation of the corrosion rate with the inverse of the absolute temperature (in Kelvin) on a semi-log plot. The decrease in the standard deviation of measured corrosion rate values at higher temperatures is attributed to the increase in homogeneity of the porous rough superhydrophobic surfaces. Corrosion is a surface phenomenon that begins at surface defects, as the temperature increases the randomly formed needle-like modification agent atop the multiscale electrodeposited layer tend to soften to a less rough and more homogenous structure. The linear nature of the variation in the semi-log plot suggests an Arrhenius relationship between the corrosion rate and the temperature, where the slope is the activation energy in the exponential term and the intercept on the ordinate is the pre-exponential factor. Based on a least-squares linear regression fit through the data, the following equation is derived for the temperature-dependent corrosion rate of the superhydrophobic surface in 3.5% NaCl solution.

$$\mathrm{CR} = 4.227 \times 10^{11} \cdot \exp\left(-\frac{9797.18}{T}\right)$$

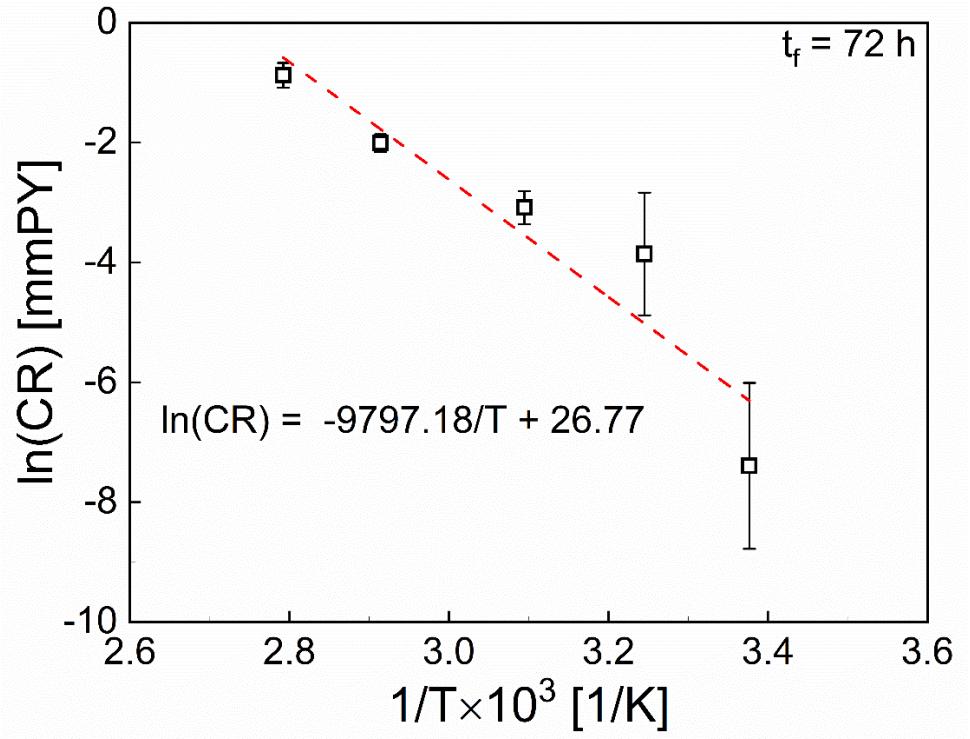

Figure 2.11. Arrhenius plot of the natural logarithm of the corrosion rate in terms of the recip rocal of absolute temperature for electrodeposited superhydrophobic samples, t_f = 72 h, in 3.5% NaCl aqueous solution

The Arrhenius equation serves to investigate corrosion of the superhydrophobic surfaces presented in this article in saline environment at any temperature of interest in the range of 23–85°C. Note that the Arrhenius relationship was developed here for a functionalization time of 72 h and 3.5% NaCl, based on the result in Figure 2.9 that showed this functionalization time to yield the greatest corrosion inhibition for the entire range of pH values. A similar relationship may be derived for other functionalization times and other pH values following the methodology presented.

2.4.5. **Chemical stability over a wide range of pH and salinity.**

The results so far in this section demonstrated the excellent corrosion inhibition performance of the superhydrophobic surfaces in two extreme values of pH namely, the strongly acidic ($pH = 1$) and the strongly basic ($pH = 14$). It was seen that hydrophobicity is the major contributor to

the corrosion inhibition effect. To demonstrate the durability of the superhydrophobic surface in corrosive environments the contact angle of aqueous solutions with various pH values ranging continuously from $pH = 1$ to $pH = 14$ was studied, as shown in Figure 2.12(a). The highest contact angle value was recorded as 161.35 ± 1.58 degrees for $pH = 7$ and an average contact angle over 158 degrees was observed for all the other pH values. The lowest contact angle of 153.38 ± 3.15 degrees was measured for $pH = 14$. Moreover, the roll-off angles for pH values between 2 and 12 was recorded to be less than 5 degrees and less than 10 degrees for $pH = 1$ and 12, respectively, and were measured as 15.8 ± 3.5 and 22.0 ± 4.7 degrees for $pH = 13$ and 14, respectively. The variation in contact angle in Figure 2.12(a) is well aligned with the corrosion performance studied in various pH solutions, where superhydrophobic surfaces had the least corrosion resistance in the extremely alkaline ($pH = 14$) solution compared to immersion in the 3.5% NaCl and the extremely acidic ($pH = 1$) solutions.

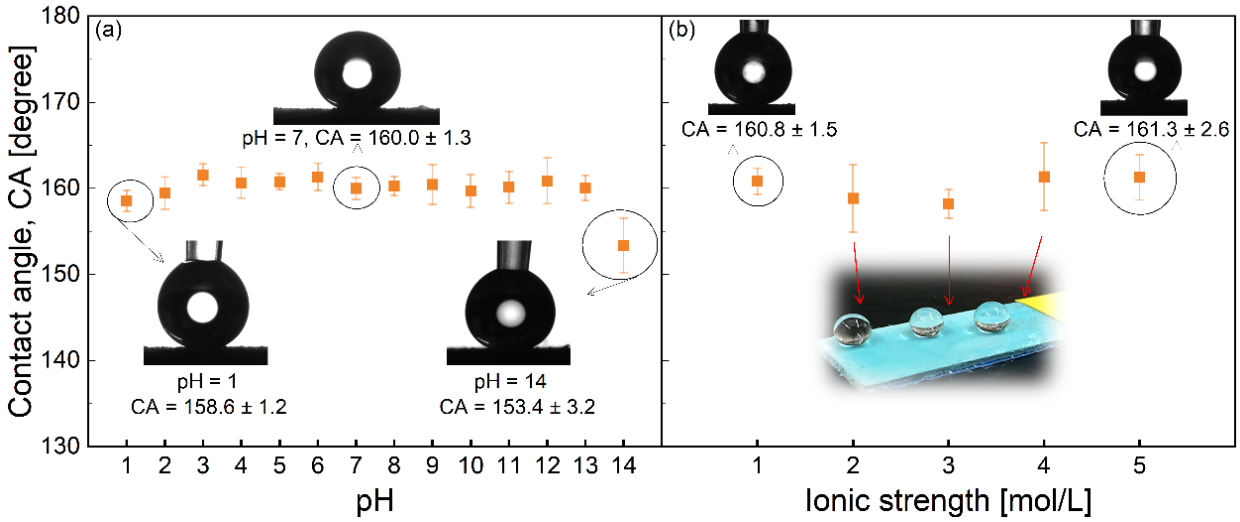

Figure 2.12. Effect of (a) pH and (b) ionic strength (salinity) on the droplet contact angle for electrodeposited samples, t_f = 72 h, at room temperature. Note a 3.5% NaCl aqueous solution corresponds to 0.6 M.

The corrosion studies reported in this section considered a simulated marine environment with a salinity of 3.5% NaCl, which corresponds to 0.6 M sodium chloride. The hydrophobicity of the surface exposed to various ionic strength of the aqueous halide solutions was also investigated, as summarized in Figure 2.12(b). The water contact angle variation with the ionic strength clearly

demonstrates the stability of the superhydrophobic surfaces in solutions with high ionic strength. In all the cases, the halide solution droplet showed an average contact angle of 158 degrees or higher, with contact angles as high as 161.3 degrees and average roll-off angle of 5.8 ± 1.2 degrees. The contact angle and roll-off angle values reported in this section are summarized in Table 2.4.

The corrosion inhibition mechanism was discussed to be divided into three major mechanisms: I) physical barrier effect of the coating, II) the repulsion force due to excessive charge at the water/SHS interface, III) air cushion due to heterogeneous wetting regime of the SHS. Based on EIS analysis, detailed in section 3.2, the first mechanism is not significant compared to the others with $Q_f < Q_{dl}$ and $R_f < R_{ct}$. Furthermore, the insignificant change of CA values with increasing the ionic strength, Section 3.5 Figure 2.12(b), indicates that the second mechanism should not be the major contributor as well. With that all, it was seen that hydrophobicity is the major contributor to the corrosion inhibition effect.

The results in this section collectively offer evidence of the robustness of the superhydrophobic surfaces fabricated by the electrodeposition method in a wide range of corrosive environments in practice. While the focus of this paper was on superhydrophobic surfaces, a companion class of liquid infused surfaces also offer non-wetting properties. Corrosion characteristics of liquid infused porous surfaces will be considered in a future work in comparison the results presented in this article. Furthermore, the corrosion durability of the non-wetting surfaces subject to abrasive and other harsh mechanical environments are also of significance in the design of the surfaces in practice, and will be considered in a future study.

2.5. CONCLUSIONS

A facile method was presented for the fabrication of multiscale textured surfaces on copper via electrodeposition. The fabrication time was less than five minutes and with low power consumption in comparison to similar methods presented in the literature. The fabricated surfaces, functionalized with an environmentally benign stearic acid, demonstrated water contact angle over 155 degrees, roll-off angle below 3 degrees, and contact angle hysteresis below 5 degrees. The fabricated superhydrophobic surfaces were systematically studied for their corrosion inhibition performance in a range of corrosive environments from the extremely acidic ($pH = 1$) to saline

3.5% NaCl solution to mimic the marine environment, and an extremely alkaline ($pH = 14$) environment. The corrosion inhibition was shown to increase with increase in functionalization time, and corrosion inhibition efficiency of over 99% was demonstrated at room temperature in all the harsh corrosion environments studied. The superhydrophobic surfaces were shown to inhibit corrosion by two to four orders of magnitude compared to bare copper. Long-term immersion studies demonstrated the excellent stability of the surfaces in all corrosive environments, and corrosion at higher temperatures suggested the need for a longer duration functionalization for application of the superhydrophobic surfaces to elevated temperature environments. An Arrhenius relationship was developed for the temperature-dependent corrosion rate of the superhydrophobic surface in 3.5% NaCl solution. Overall, the superhydrophobicity of the surface was found to be a major contributing factor to the corrosion resistance, and the superhydrophobicity was shown to be robust in a range of pH and ionic strength of aqueous halide solutions.

ACKNOWLEDGMENT AND DISCLAIMER

The material reported in this publication is based upon work supported by the U.S. Department of Energy under Award Number DE-FE0031556. This publication was prepared as an account of work sponsored by an agency of the United States Government. Neither the United States Government nor any agency thereof, nor any of their employees, makes any warranty, express or implied, or assumes any legal liability or responsibility for the accuracy, completeness, or usefulness of any information, apparatus, product, or process disclosed, or represents that its use would not infringe on privately owned rights. Reference herein to any specific commercial product, process, or service by trade name, trademark, manufacturer, or otherwise does not necessarily constitute or imply its endorsement, recommendation, or favoring by the United States Government or any agency thereof. The views and opinions of the authors expressed herein do not necessarily state or reflect those of the United States Government or any agency thereof.

REFERENCES

[1] E.-S.M. Sherif, Effects of 2-amino-5-(ethylthio)-1, 3, 4-thiadiazole on copper corrosion as a corrosion inhibitor in 3% NaCl solutions, Applied surface science, 252 (2006) 8615-8623.

[2] D.-q. Zhang, L.-x. Gao, G.-d. Zhou, Inhibition of copper corrosion in aerated hydrochloric acid solution by heterocyclic compounds containing a mercapto group, Corrosion science, 46 (2004) 3031-3040.

[3] E. Abelev, D. Starosvetsky, Y. Ein-Eli, Enhanced copper surface protection in aqueous solutions containing short-chain alkanoic acid potassium salts, Langmuir, 23 (2007) 11281-11288.

[4] Y. Qiang, S. Fu, S. Zhang, S. Chen, X. Zou, Designing and fabricating of single and double alkyl-chain indazole derivatives self-assembled monolayer for corrosion inhibition of copper, Corrosion Science, 140 (2018) 111-121.

[5] R.N. Wenzel, Resistance of solid surfaces to wetting by water, Industrial Engineering Chemistry, 28 (1936) 988-994.

[6] A. Cassie, S. Baxter, Wettability of porous surfaces, Transactions of the Faraday society, 40 (1944) 546-551.

[7] D.L. Hu, B. Chan, J.W. Bush, The hydrodynamics of water strider locomotion, Nature, 424 (2003) 663.

[8] Z. Sun, T. Liao, K. Liu, L. Jiang, J.H. Kim, S.X. Dou, Fly-Eye Inspired Superhydrophobic Anti-Fogging Inorganic Nanostructures, Small, 10 (2014) 3001-3006.

[9] S. Wang, Z. Yang, G. Gong, J. Wang, J. Wu, S. Yang, L.J. Jiang, Icephobicity of penguins spheniscus humboldti and an artificial replica of penguin feather with air-infused hierarchical rough structures, The Journal of Physical Chemistry C, 120 (2016) 15923-15929.

[10] J. Ju, H. Bai, Y. Zheng, T. Zhao, R. Fang, L. Jiang, A multi-structural and multi-functional integrated fog collection system in cactus, Nature communications, 3 (2012) 1247.

[11] J. Genzer, K.J.S. Efimenko, Creating long-lived superhydrophobic polymer surfaces through mechanically assembled monolayers, 290 (2000) 2130-2133.

[12] T. Nishino, M. Meguro, K. Nakamae, M. Matsushita, Y. Ueda, The lowest surface free energy based on− CF3 alignment, Langmuir, 15 (1999) 4321-4323.

[13] S. Khodakarami, H. Zhao, K.F. Rabbi, N. Miljkovic, Scalable Corrosion-Resistant Coatings for Thermal Applications, ACS Applied Materials & Interfaces, 13 (2021) 4519-4534.

[14] Y. Fan, C. Li, Z. Chen, H. Chen, Study on fabrication of the superhydrophobic sol–gel films based on copper wafer and its anti-corrosive properties, Applied Surface Science, 258 (2012) 6531-6536.

[15] A.V. Rao, S.S. Latthe, S.A. Mahadik, C. Kappenstein, Mechanically stable and corrosion resistant superhydrophobic sol–gel coatings on copper substrate, Applied Surface Science, 257 (2011) 5772-5776.

[16] G. Jiang, L. Luo, L. Tan, J. Wang, S. Zhang, F. Zhang, J. Jin, Microsphere-Fiber Interpenetrated Superhydrophobic PVDF Microporous Membranes with Improved Waterproof and Breathable Performance, ACS applied materials interfaces, 10 (2018) 28210-28218.

[17] K.A. Emelyanenko, N.A. Sanzharovsky, E.V. Chulkova, A.A. Ganne, A.M. Emelyanenko, L.B. Boinovich, Superhydrophobic corrosion resistant coatings for copper via IR nanosecond laser processing, Materials Research Express, 5 (2018) 115001.

[18] Y. Wan, M. Chen, W. Liu, X. Shen, Y. Min, Q. Xu, The research on preparation of superhydrophobic surfaces of pure copper by hydrothermal method and its corrosion resistance, Electrochimica Acta, 270 (2018) 310-318.

[19] B. Zhang, W. Xu, Q. Zhu, Y. Sun, Y. Li, Mechanically robust superhydrophobic porous anodized AA5083 for marine corrosion protection, Corrosion Science, 158 (2019) 108083.

[20] N. Lin, L. Zhang, J. Zou, Q. Liu, S. Yuan, L. Zhao, Y. Yu, Z. Liu, Q. Zeng, X. Liu, A combined surface treatment of surface texturing-double glow plasma surface titanizing on AISI 316 stainless steel to combat surface damage: Comparative appraisals of corrosion resistance and wear resistance, Applied Surface Science, 493 (2019) 747-765.

[21] C. Scheuer, F. Possoli, P. Borges, R. Cardoso, S. Brunatto, AISI 420 martensitic stainless steel corrosion resistance enhancement by low-temperature plasma carburizing, Electrochimica Acta, 317 (2019) 70-82.

[22] E. Berretti, N. Calisi, A. Capaccioli, L. Capozzoli, A. Hamouda, A. Giaccherini, W. Giurlani, A. Ienco, S. Martinuzzi, M. Innocenti, Electrodeposited white bronzes on brass: Corrosion in 3.5% sodium chloride solution, Corrosion Science, 175 (2020) 108898.

[23] R. Tang, G.R. Joshi, H. Zhao, S.P. Venkateswaran, P.J. Withers, P. Xiao, The influence of electrodeposited Ni-Co alloy coating microstructure on CO2 corrosion resistance on X65 steel, Corrosion Science, 167 (2020) 108485.

[24] C.-X. Wang, X.-F. Zhang, A non-particle and fluorine-free superhydrophobic surface based on one-step electrodeposition of dodecyltrimethoxysilane on mild steel for corrosion protection, Corrosion Science, 163 (2020) 108284.

[25] J. Ou, W. Hu, M. Xue, F. Wang, W. Li, Superhydrophobic surfaces on light alloy substrates fabricated by a versatile process and their corrosion protection, ACS applied materials & interfaces, 5 (2013) 3101-3107.

[26] J.-P. Lee, S. Choi, S. Park, Extremely superhydrophobic surfaces with micro-and nanostructures fabricated by copper catalytic etching, Langmuir, 27 (2010) 809-814.

[27] B. Qian, Z. Shen, Fabrication of superhydrophobic surfaces by dislocation-selective chemical etching on aluminum, copper, and zinc substrates, Langmuir, 21 (2005) 9007-9009.

[28] T. Darmanin, E.T. de Givenchy, S. Amigoni, F. Guittard, Superhydrophobic surfaces by electrochemical processes, Advanced materials, 25 (2013) 1378-1394.

[29] G. He, S. Lu, W. Xu, S. Szunerits, R. Boukherroub, H. Zhang, Controllable growth of durable superhydrophobic coatings on a copper substrate via electrodeposition, Physical Chemistry Chemical Physics, 17 (2015) 10871-10880.

[30] F. Su, K. Yao, C. Liu, P. Huang, Rapid fabrication of corrosion resistant and superhydrophobic cobalt coating by a one-step electrodeposition, Journal of The Electrochemical Society, 160 (2013) D593-D599.

[31] F. Su, K. Yao, Facile fabrication of superhydrophobic surface with excellent mechanical abrasion and corrosion resistance on copper substrate by a novel method, ACS applied materials interfaces, 6 (2014) 8762-8770.

[32] A. Haghdoost, R. Pitchumani, Fabricating superhydrophobic surfaces via a two-step electrodeposition technique, Langmuir, 30 (2013) 4183-4191.

[33] J. Liu, X. Fang, C. Zhu, X. Xing, G. Cui, Z. Li, Fabrication of superhydrophobic coatings for corrosion protection by electrodeposition: A comprehensive review, Colloids and Surfaces A: Physicochemical and Engineering Aspects, 607 (2020) 125498.

[34] E. Vazirinasab, R. Jafari, G. Momen, Application of superhydrophobic coatings as a corrosion barrier: A review, Surface and Coatings Technology, 341 (2018) 40-56.

[35] Y. Liu, S. Li, J. Zhang, Y. Wang, Z. Han, L. Ren, Fabrication of biomimetic superhydrophobic surface with controlled adhesion by electrodeposition, Chemical Engineering Journal, 248 (2014) 440-447.

[36] L. Liu, R. Chen, W. Liu, Y. Zhang, X. Shi, Q. Pan, Fabrication of superhydrophobic copper sulfide film for corrosion protection of copper, Surface Coatings Technology, 272 (2015) 221-228.

[37] P. Wang, R. Qiu, D. Zhang, Z. Lin, B. Hou, Fabricated super-hydrophobic film with potentiostatic electrolysis method on copper for corrosion protection, Electrochimica Acta, 56 (2010) 517-522.

[38] P. Wang, D. Zhang, R. Qiu, J. Wu, Super-hydrophobic metal-complex film fabricated electrochemically on copper as a barrier to corrosive medium, Corrosion Science, 83 (2014) 317-326.

[39] Y. Liu, S. Li, J. Zhang, J. Liu, Z. Han, L. Ren, Corrosion inhibition of biomimetic super-hydrophobic electrodeposition coatings on copper substrate, Corrosion Science, 94 (2015) 190-196.

[40] A. International, Standard Practice for Conventions Applicable to Electrochemical Measurements in Corrosion Testing, in: ASTM G3-14(2019), West Conshohocken, PA, 2019.

[41] N.T. Kirkland, N. Birbilis, M. Staiger, Assessing the corrosion of biodegradable magnesium implants: a critical review of current methodologies and their limitations, Acta biomaterialia, 8 (2012) 925-936.

[42] M.C. Biesinger, Advanced analysis of copper X-ray photoelectron spectra, Surface and Interface Analysis, 49 (2017) 1325-1334.

[43] M. Stern, A.L. Geary, Electrochemical polarization I. A theoretical analysis of the shape of polarization curves, Journal of the electrochemical society, 104 (1957) 56-63.

[44] F. Su, K. Yao, C. Liu, P. Huang, Rapid fabrication of corrosion resistant and superhydrophobic cobalt coating by a one-step electrodeposition, Journal of the Electrochemical Society, 160 (2013) D593.

[45] N. Xu, D.K. Sarkar, X.G. Chen, H. Zhang, W. Tong, Superhydrophobic copper stearate/copper oxide thin films by a simple one-step electrochemical process and their corrosion resistance properties, RSC advances, 6 (2016) 35466-35478.

[46] S. Cruz-Manzo, Kramers-Kronig (K-K) Analysis in ZView Software for Evaluation of EIS Measurements in Polymer Electrolyte Fuel Cells, https://dx.doi.org/10.13140/RG.2.1.1094.0887/1 (Accessed February 2021).

[47] D.Q. Zhang, P.-H. Liu, L.X. Gao, H.G. Joo, K.Y. Lee, Photosensitive self-assembled membrane of cysteine against copper corrosion, Materials Letters, 65 (2011) 1636-1638.

[48] F. Growcock, R. Jasinski, Time-Resolved Impedance Spectroscopy of Mild Steel in Concentrated Hydrochloric Acid, Journal of the Electrochemical Society, 136 (1989) 2310-2314.

[49] B. Hirschorn, M.E. Orazem, B. Tribollet, V. Vivier, I. Frateur, M. Musiani, Determination of effective capacitance and film thickness from constant-phase-element parameters, Electrochimica Acta, 55 (2010) 6218-6227.

[50] J.O.M. Bockris, A.K. Reddy, Modern electrochemistry 2B: electrodics in chemistry, engineering, biology and environmental science, Springer Science & Business Media, 2000.

[51] L.B. Boinovich, A.M. Emelyanenko, A.D. Modestov, A.G. Domantovsky, K.A. Emelyanenko, Not simply repel water: the diversified nature of corrosion protection by superhydrophobic coatings, Mendeleev Communications, 27 (2017) 254-256.

[52] L. Boinovich, A. Emelyanenko, A. Modestov, A. Domantovsky, A. Shiryaev, K. Emelyanenko, O. Dvoretskaya, A. Ganne, Corrosion behavior of superhydrophobic aluminum alloy in concentrated potassium halide solutions: When the specific anion effect is manifested, Corrosion Science, 112 (2016) 517-527.

[53] C. Tian, Y. Shen, Structure and charging of hydrophobic material/water interfaces studied by phase-sensitive sum-frequency vibrational spectroscopy, Proceedings of the National Academy of Sciences, 106 (2009) 15148-15153.

[54] P. Creux, J. Lachaise, A. Graciaa, J.K. Beattie, A.M. Djerdjev, Strong specific hydroxide ion binding at the pristine oil/water and air/water interfaces, The Journal of Physical Chemistry B, 113 (2009) 14146-14150.

[55] R. Zimmermann, U. Freudenberg, R. Schweiß, D. Küttner, C. Werner, Hydroxide and hydronium ion adsorption—A survey, Current Opinion in Colloid Interface Science, 15 (2010) 196-202.

[56] K. Quast, The use of zeta potential to investigate the pKa of saturated fatty acids, Advanced Powder Technology, 27 (2016) 207-214.

[57] J.R. Kanicky, D.O. Shah, Effect of degree, type, and position of unsaturation on the pKa of long-chain fatty acids, Journal of colloid interface science, 256 (2002) 201-207.

[58] A.J. Bard, L.R. Faulkner, J. Leddy, C.G. Zoski, Electrochemical methods: fundamentals and applications, wiley New York, 1980.

TABLES

Table 2.1. Corrosion parameters from the potentiodynamic polarization tests in solutions of different pH values at 23°C

Samples	3.5% NaCl (pH ≈ 7)					pH = 1					pH = 14				
	β_{an}	β_{cat}	j_{corr}	E_{corr}	η	β_{an}	β_{cat}	j_{corr}	E_{corr}	η	β_{an}	β_{cat}	j_{corr}	E_{corr}	η
Bare Cu	66.38	107.05	6.55	-0.229	–	71.31	214.98	30.4	-0.008	–	48.94	276.92	350	-0.245	–
t_f = 1 h	47.15	153.03	1.97	-0.154	69.99	31.39	85.312	12.9	0.030	54.04	46.09	266.46	444	-0.255	26.14
t_f = 2 h	56.89	135.33	1.02	-0.191	84.50	38.41	715.81	3.60	0.010	79.67	44.26	298.05	304	-0.258	34.74
t_f = 4 h	60.88	127.53	0.79	-0.198	88.00	43.04	275.00	1.94	0.002	84.75	48.89	260.46	116	-0.246	71.30
t_f = 8 h	69.38	226.68	0.56	-0.211	91.41	16.83	20.671	1.13	0.032	99.63	50.504	251.27	77.7	-0.259	90.60
t_f = 24 h	67.85	162.77	0.16	-0.213	97.50	38.68	550.00	0.05	0.025	99.12	46.90	277.82	7.59	-0.260	99.46
t_f = 72 h	73.7	157.07	0.02	-0.219	99.78	45.79	371.72	0.006	0.003	99.97	33.05	155.61	1.34	-0.253	99.99

Units: β_{an} and β_{ca} [mV/dec.]; j_{corr} [μA/cm^2]; E_{corr} vs. Ag/AgCl [V]; η [%]

Table 2.2. Equivalent circuit model parameters for corrosion tests in a 3.5% NaCl solution at 23°C

Samples	R_s	CPE_f		R_f	CPE_{dl}		R_{ct}
		Q_f	n_f		Q_{dl}	n_{dl}	
Bare Cu	2.4	14.36	0.938	0.02	167.07	0.461	2.86
t_f = 1 h	5.6	1.04	0.852	0.90	23.70	0.566	13.61
t_f = 2 h	10.6	4.21	0.806	0.98	9.59	0.302	21.53
t_f = 4 h	10.6	1.62	0.778	1.07	13.30	0.507	60.48
t_f = 8 h	10.6	0.24	0.893	1.10	3.75	0.558	58.14
t_f = 24 h	10.6	0.11	0.897	1.42	2.42	0.518	244.09
t_f = 72 h	10.6	0.02	0.975	3.62	2.75	0.439	1502.60

Units: R_s [$\Omega \cdot cm^2$]; R_f and R_{ct} [$k\Omega \cdot cm^2$]; Q [$\mu\Omega^{-1}s^n cm^{-2}$]; n [dimensionless]

Table 2.3. Equivalent circuit model parameters for corrosion tests in solutions of pH = 1 and pH = 14 values at 23°C

Samples	pH = 1							pH = 14						
	R_s	CPE_f		R_f	CPE_{dl}		R_{ct}	R_s	CPE_f		R_f	CPE_{dl}		R_{ct}
		Q_f	n_f		Q_{dl}	n_{dl}			Q_f	n_f		Q_{dl}	n_{dl}	
Bare Cu	3.10	42.75	0.844	0.9	711.81	0.55	0.4	1.08	678.54	0.510	0.02	3211.10	0.626	0.03
t_f = 1 h	3.13	87.49	0.689	0.80	6032.30	0.442	2.8	1.10	1850.00	0.522	0.01	5118.90	0.651	0.04
t_f = 2 h	3.13	13.88	0.781	5.94	854.64	0.368	14.0	1.16	148.39	0.689	0.01	3870.10	0.529	0.08
t_f = 4 h	3.13	5.47	0.638	4.91	456.97	0.397	61.1	1.10	238.54	0.491	0.01	786.620	0.661	0.24
t_f = 8 h	3.13	0.27	0.770	2.50	4.43	0.493	69.5	1.57	20.38	0.688	0.11	515.93	0.534	0.57
t_f = 24 h	3.13	0.02	0.833	55.86	0.48	0.562	615.0	1.57	1.38	0.677	2.09	23.04	0.587	56.9
t_f = 72 h	3.13	0.01	0.951	540.00	0.40	0.587	1930.0	1.57	0.006	0.867	24.1	1.37	0.453	135.0

Units: R_s [$\Omega \cdot cm^2$]; R_f and R_{ct} [$k\Omega \cdot cm^2$]; Q [$\mu\Omega^{-1}s^n cm^{-2}$]; n [dimensionless]

Table 2.4. Contact angle and roll-off angle of different various pH and saline solution on superhydrophobic copper, $t_f = 72h$ at $23^{\circ}\mathrm{C}$

Acidity	Contact angle	roll-off angle	Basicity	Contact angle	roll-off angle	Salinity	Contact angle	roll-off angle
$pH = 1$	158.6±1.2	7.0±3.8	$pH = 8$	160.3±1.1	4.3±1.8	$1\ M$	160.8±1.5	6.4±3.5
$pH = 2$	159.5±1.9	3.2±1.6	$pH = 9$	160.5±2.3	3.0±0.9	$1\ M$	158.9±3.9	7.4±3.9
$pH = 3$	161.6±1.3	3.2±0.8	$pH = 10$	159.7±1.9	4.0±1.3	$3\ M$	158.2±1.7	4.8±2.3
$pH = 4$	160.7±1.8	3.0±1.1	$pH = 11$	160.1±1.8	4.2±1.9	$4\ M$	161.4±3.9	5.7±4.8
$pH = 5$	160.8±0.9	3.0±1.0	$pH = 12$	160.9±2.7	6.2±1.5	$5\ M$	161.3±2.6	4.5±3.9
$pH = 6$	161.4±1.6	2.4±0.5	$pH = 13$	160.1±1.5	15.8±3.5			
$pH = 7$	159.6±1.3	3.3±1.6	$pH = 14$	153.4±3.2	22.0±4.7			

Units: Contact angle [degree]; Sliding angle: [degree]

Chapter 3. Bioinspired Nonwetting Surfaces for Corrosion Inhibition over a Range of Temperature and Corrosivity

The work reported in this chapter is the basis for the following journal publication:

S.M.A. Mousavi and R. Pitchumani. "Bioinspired Nonwetting Surfaces for Corrosion Inhibition over a Range of Temperature and Corrosivity." *Journal of Colloid and Interface Science*, **607**, 323-333, 2022.

3.1. ABSTRACT

Applications of superhydrophobic (SHS) and lubricant infused surfaces (LIS) involve exposure to corrosive environments from the acidic to the basic, at a range of temperatures, that are not fully characterized. We present for the first time a multifactorial study of the effects of surface fabrication method, surface modification, surface functionalization time, temperature and pH of the immersion medium on the corrosion performance of nonwetting copper surfaces. Bioinspired SHS and LIS fabricated using facile methods of etching and electrodeposition are systematically assessed using potentiodynamic polarization measurements for their corrosion resistance in saline solution (pH ≈ 7) over a temperature range 23–85°C. SHS and LIS are shown to exhibit diminished corrosion rate, by up to two orders of magnitude, compared to bare copper surface. An Arrhenius model is developed for the first time, describing the temperature-dependent corrosion rate of SHS and LIS. Electrochemical impedance spectroscopy is used to show that corrosion resistance of LIS is larger by three orders of magnitude in extremely acidic (pH = 1) and by an order magnitude in extremely alkaline (pH = 14) media compared to bare copper surface. Etched LIS are generally more resistant to corrosion compared to SHS at all temperatures with excellent microstructural durability.

KEYWORDS: superhydrophobicity; lubricant infused surface; corrosion; high temperature; acidic and basic solution.

3.2. INTRODUCTION

Metallic surfaces used in diverse applications are often exposed to severely corrosive fluids in their operating environment at different temperatures. For example, copper tubes that are

commonly used in condensers and evaporators of refrigeration or air condition systems are frequently corroded by organic acids [1]. In power plants, online chemical cleaning of condenser tubes without plant shutdown is achieved using various acids [2,3]. Alkaline agents are typically used as additives to working heat transfer fluids to prevent or remove contamination of metal surfaces, as per ASTM protocols [4]. Chemical agents used for biological fouling mitigation are also of various acids and alkalis [5]. Design of surfaces that can endure a wide range of corrosivity over a range of temperature is, therefore, of much practical interest.

In the last decade, bioinspired water repellent superhydrophobic and lubricant infused surfaces have attracted significant attention for corrosion-mitigation in these applications, with various efforts focused on the fabrication of such surfaces and their wettability characterization [6,7]. The state of a liquid droplet on a rough surface is classified as either a wetting Wenzel [8] state or a non-wetting Cassie-Baxter [9] state. The latter provides a trapped layer of air between the corrosive liquid and the surface which is believed to be the main reason for the anti-corrosion property of SHS [10–12]. While the lotus leaf from nature has been the inspiration for superhydrophobic surfaces, another biological surface from nature, the *Nepenthes* pitcher-plant [13], has inspired the development of lubricant infused surfaces that incorporate a liquid medium in the inter-asperity valleys of the surface [14]. The infused liquid forms a protective layer between the base surface and the corrosive surrounding, which along the slipperiness of the surface is the basis for the corrosion deterrence of LIS.

Both SHS and LIS have been studied for their corrosion inhibition behavior. Among the corrosion studies involving LIS, Wang et al. designed liquid-infused aluminum to mitigate the adherence of sulfate-reducing bacteria in static seawater [15]. Shi et al. dealloyed CuZn in $CuSO_4$ bath, later added dodecanethiol by a chemical vapor deposition process, and lastly infused the surface with perfluorinated lubricant (PFL, Nascent FX 6200) for corrosion study in seawater with $pH = 8$ and 3% salinity. They reported lower corrosion current density by up to two orders of magnitude compared to the bare CuZn at room temperature [16]. Song et al. used an electrochemical anodizing method to texture an Al substrate with ordered pores of several tens of nanometers, and then changed the surface to lubricant infused surface by subsequent immersion in methyl silicone oil, fluoroalkyl silane, and finally Krytox104 oil and showed excellent anti-corrosion property in 3.5% saline solution at low temperature [17]. Xiang et al. [18] coated mild

steel with Zn-Ni via electroplating at 4 $A \cdot dm^{-2}$ at 35 °C for 20 min. After the coating, the samples were immersed in fluoroalkyl silane solution and further lubricated with Krytox100 oil. Subsequently, the corrosion behavior was studied in 3.5 wt% NaCl solution ($pH = 5.9$) at room temperature. The mild steel LIS was reported to show about three orders of magnitude decrease in corrosion current compared to a bare iron. Qiu et. al. grown micro/nanoscale copper via electrodeposition for 10 minutes at -1000 mV on Cu/Al and Al/Mg alloys, to use it as a catalyzer for growing carbon fiber. The textured substrates were placed in a tube furnace at 350°C in acetylene gas flow to grow hydrophobic carbon fibers and further infused with lubricant. The liquid-infused surface showed higher corrosion impedance at 3.5% NaCl solution at room temperature compared to hydrophobic surface without liquid infusion [19]. Similar studies have been reported on SHS, as reviewed by Mousavi and Pitchumani [11], which is not repeated here.

Fabrication of SHS and LIS start with the first step of texturing of the surface, followed by functionalization of the surface with a low surface energy coating. The creation of LIS requires the additional step of infiltrating the porous, functionalized textures with a lubricant. It is clear, therefore, that the performance of SHS and LIS is directly related to the texturing method, which can be achieved in a number of ways, including templating, sol-gel method [20,21] , electrospinning [22], laser etching [23], hydrothermal synthesize [24], anodization, plasma techniques [25], and electrodeposition [26,27]. SHS and LIS have been studied for three major applications such as anti-microbial and mineral fouling [28,29], anti-icing [27,30], and anti-corrosion [31–34]. Although each study of corrosion of SHS or LIS in the literature has considered a specific method, the effect of different texturing methods on the resulting corrosion inhibition is not examined. Moreover, a comparative study of SHS and LIS produced from the same texturing method is also not reported. Furthermore, the studies on LIS discussed above and those on SHS [35–37] are focused on a single temperature and a single corrosive medium.

It is evident from the foregoing discussion that a systematic study on the multiparametric effect of texturing method, surface modification (SHS or LIS), temperature and the corrosive environment is presently lacking, which forms the motivation for the present work. In this study, copper was selected as the model metal substrate for fabrication of SHS and LIS that mimic the nonwetting surfaces found in nature, and studies on their corrosion behavior at various conditions. Two methods of surface texturing—electrodeposition (an additive process) and etching (a material

removal process)—which both are scalable and facile, are juxtaposed for the first time to bring further insight into the effect of fabrication method on corrosion performance of SHS and LIS. Systematic corrosion studies are conducted using potentiodynamic polarization to quantify the corrosion inhibition of SHS and LIS over a range of temperatures above room temperature from which a relationship between corrosion rate and temperature is derived, for the first time, for SHS and LIS on copper. At the low temperature, electrodeposited SHS and etched SHS and LIS exhibited a 50-70 fold reduction in corrosion rate while electrodeposited LIS reduced corrosion rate by two orders of magnitude. At the higher temperature, SHS reduced corrosion by a factor of 2–3, whereas LIS was characterized by corrosion rate that was an order of magnitude lower than the bare copper surface. Microstructural evaluation of LIS before and after corrosion testing is used to demonstrate the durability of the surface to corrosion. Finally, the performance of LIS in harsh acidic ($pH = 1$) and basic ($pH = 14$) environments is examined through electrochemical impedance spectroscopy measurements, for the generalized applicability of the surfaces developed in this study.

3.3. EXPERIMENTAL METHODS

3.3.1. **Materials and reagents used in experimental studies**

Hydrochloric acid (HCl), analytical-grade copper sulfate ($CuSO_4$, 99+%), sulfuric acid (H_2SO_4), acetone (99.5+%), methanol (99.8+%), and stearic acid ($CH_3(CH_2)_{16}CO_2H$, 97%) were purchased from Fisher Scientific (Pittsburgh, PA, USA) and used as received without any further purification. Hydrogen peroxide solution (H_2O_2) was purchased from Sigma-Aldrich. Deionized water with a resistivity of 14MΩ.cm was purchased from CQ Concepts (Illinois, IL, USA) for the preparation of aqueous solutions. Silicone oil, Dowsil500™, was purchased from DuPont (Wilmington, Delaware, USA). Plain multipurpose copper sheet was purchased from McMaster, USA.

3.3.2. **Fabrication of superhydrophobic surfaces (SHS)**

For investigating the effects of texturing on the corrosion of the nonwetting surfaces, copper surfaces were textured using two methods: electrodeposition, an *additive* method, and etching, a material *removal* method. The as-received copper sheets were cut into rectangular

coupons and degreased in a sonication bath of methanol, acetone, and DI-water sequentially, for ten minutes each.

In the electrodeposition method, multiscale asperities were grown on top of the surface using a three-electrode electrochemical setup [11]. The electrodeposition was conducted in an AUTOLAB PGSTAT128N electrochemical station (ECO Chemie, Utrecht, The Netherlands) in which the degreased copper coupons were used as the working electrode, a platinum mesh was used as the counter electrode, and a copper sheet served as a reference electrode. De-aerated aqueous solution of 1M $CuSO_4$ and 0.5M H_2SO_4 was used as the electrolyte. The electrodeposition process was started by applying -1.1 V potential to the working electrode for 5 minutes and finished by a second deposition at 0.15 V for 10 seconds. The second deposition is done to further stabilize the first coating onto the surface. The electrodeposition time of 5 minutes was chosen so as to yield an approximately 30-micrometer deposition thickness (h), estimated using the following relationship: $h = QM/nF\rho A$, where F is the Faraday constant, A is the surface area of the deposition, ρ is the density of the deposited copper, Q is the charge transferred in coulomb throughout the deposition ($Q = i.dt$), M is the molar weight of copper, and n is the number of transferred electrons in the copper reduction reaction, $Cu^{2+} + 2e^- \rightarrow Cu$. In the chemical etching method, roughness features was carved into the surface by submerging the degreased copper coupons in an etchant aqueous solution containing 0.02 M hydrochloric acid and 0.05 M hydrogen peroxide for 20 minutes.

The coupons fabricated via both the electrodeposition and the etching methods were rinsed with a copious amount of DI-Water and dried overnight. Finally, the textured surfaces were turned into superhydrophobic surfaces (SHS) by further lowering the surface energy with chemisorption of stearic acid, an environmentally benign fatty acid, onto the surface. This functionalization was achieved by immersion of the textured surfaces in a solution of 0.02 M stearic acid in methanol at ambient conditions for time (t_f) ranging from 1 h to 72 h, for a systematic study of the influence of functionalization time on the corrosion behavior.

3.3.3. **Fabrication of lubricant infused surfaces (LIS)**

The as-fabricated SHS described in the foregoing subsection were infused with lubricant oil and tuned to liquid-infused surfaces. To do so, copious Dowsil™ silicone oil, 500 cSt viscosity, was dripped onto the SHS. As the final step, the lubricant infused surfaces were hanged vertically

for at least twenty minutes to drain any excess oil and also let the lubricant wick into the interasperity spaces.

3.3.4. **Morphology and wettability characterization**

Surface morphology was revealed via a field-emission scanning electron microscope (SEM) (JEOL 2100, Japan), operating at an acceleration voltage of 15 kV. The optical image of liquid-infused surfaces was obtained via Nikon Eclipse LV100ND Microscope (Nikon Instruments Inc.) with an epifluorescence filter. The intrinsic wettability of water on the surfaces was characterized using a goniometer (ramé-hart model 590, NJ USA), in which 10 µl sessile DI-water droplet was used at five different positions on each sample for contact angle measurements. The sliding angle was measured via the tilting cradle method by the same apparatus with 25 µl DI-water. The sliding angle for a droplet on SHS was measured when the droplet rolls of the surface. The sliding angle for a droplet on LIS was recorded when both the rear and front contact line of the droplet begins to slide. Laser and white light scanning confocal microscope (Keyence model VK-X, Osaka-Japan) was used for 3D reconstruction of the surface profile and subsequent roughness analysis.

3.3.5. **Characterization of corrosion inhibition**

Electrochemical tests were carried out to measure and characterize the corrosion inhibition of the samples via a three-electrode setup. Ag/AgCl (NaCl saturated) served as a reference electrode with less than 3 mm distance from the working electrode (sample surface) to minimize the solution resistance. Platinum mesh was used as a counter electrode, placed at an equal distance from the other two electrodes. Linear polarization (LP), potentiodynamic polarization (PDP), and electrochemical impedance spectroscopy (EIS) data were obtained with a potentiostat device Solarton Inc. (model 1240 PA, USA) equipped with a frequency response analyzer. Linear polarization tests were recorded at a scan range of −20 mV to +20 mV, and PDP tests were recorded at a scan range of −300 mV to +300 mV with respect to open circuit potential, at the scan rates of 1/6 V/h and 1 mV/s, respectively, as suggested by ASTM G3-14 [38]. Impedance spectra were registered in a range of 100 kHz with sinusoidal signals of 10 mV amplitude with respect to the open circuit potential.

3.4. RESULTS AND DISCUSSION

In this section, the study's findings are summarized and discussed in terms of the morphology and wettability of the fabricated SHS and LIS as well as the corrosion inhibition characteristics of SHS and LIS relative to bare unmodified surface at various temperatures and various pH solutions.

3.4.1. **Morphology and wettability**

Surface morphology of the textured electrodeposited and etched copper surfaces are shown in the scanning electron microcroscopic (SEM) images in Figure 3.1(a) and (b), respectively. The SEM image of the electrodeposited surface (Figure 3.1(a)) showed cauliflower-shaped multiscale asperities, while the etched copper surface, Figure 3.1(b), exhibited roughness pattern in the form of random grooves. Two main differences were noted between the two textures: first, the scale of the asperities ranged up to ~40 microns on the electrodeposited surface and up to ~20 microns on the etched surface; second, multiscale asperities formed on the electrodeposited surface were more or less isotropic, while roughness features grooved into the surface with a preferential direction on the etched surfaces. The two methods served to study the effects of additive and removal approaches on the resulting corrosion performance [39]. Surface roughness and surface energy are the two factors that play a major role in converting a surface to a superhydrophobic surface [12]. The insets in Figure 3.1(a)-(b) illustrate the wettability characteristics of the electrodeposited and etched surfaces after functionalization in stearic acid for 1 h that served to reduce the surface energy. Despite the differences in the roughness textures, both electrodeposited and etched coupons sustained a water contact angle (CA) above 155° and a very low contact angle hysteresis (CAH) below 5° which meet the criteria for superhydrophobicity (CA > 150° and CAH < 10°).

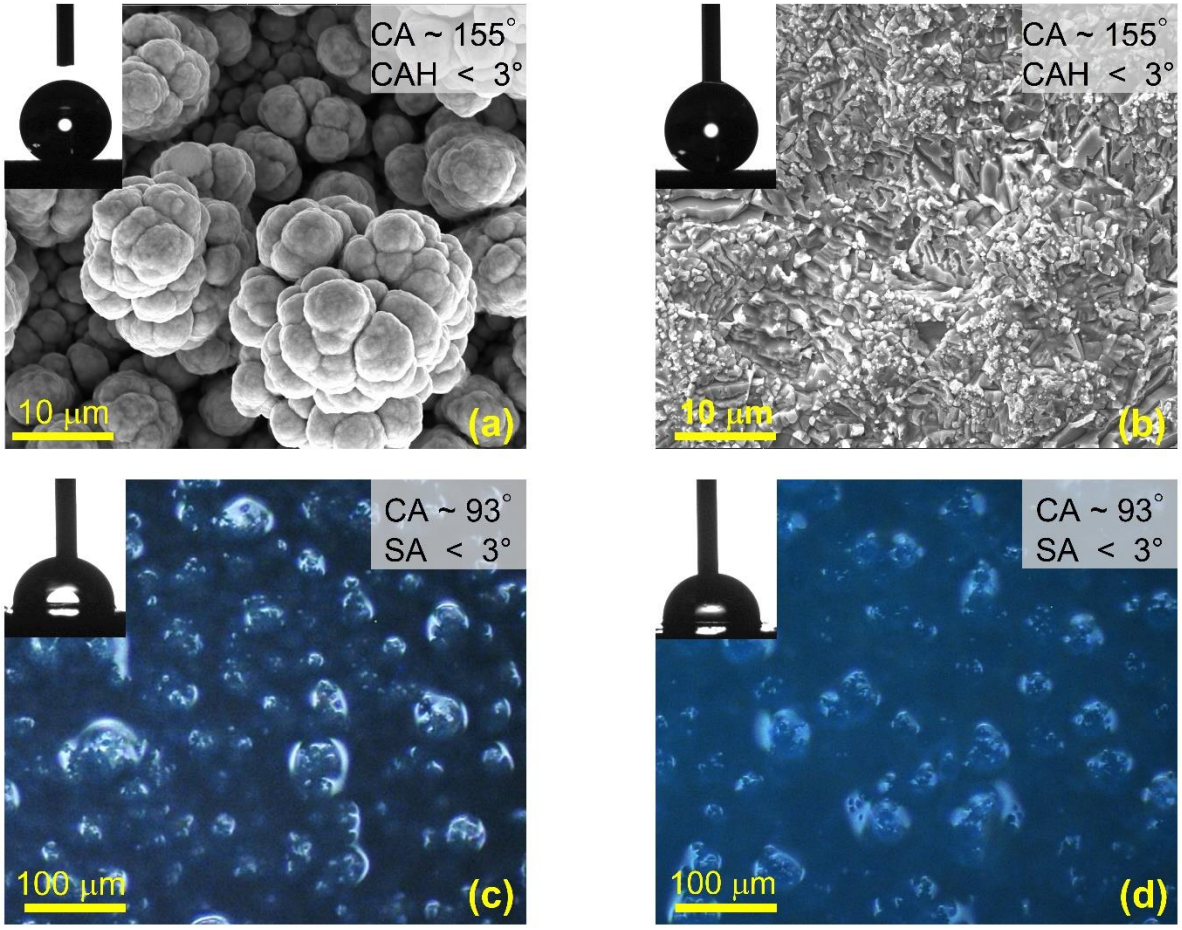

Figure 3.1. SEM images of textured copper surfaces fabricated via (a) electrodeposition and (b) chemical etching. Optical microscopic images of (c) electrodeposited and (d) etched LIS. Measured values of apparent contact angle (CA), contact angle hysteresis (CAH) and sliding angle (SA) are shown in insets.

Figure 3.1(c) and (d) are optical microscopic images taken with an epifluorescence filter on LIS samples. Liquid-infused electrodeposited copper is shown in Figure 3.1(c) where the multiscale asperities are inundated with the infused silicone oil; similarly, the infused oil is seen to cover the chemically etched LIS in Figure 3.1(d). For LIS, sliding angle was used as a secondary wettability metric instead of contact angle hysteresis and are shown as insets in the corresponding figures. Figure 3.1(c) and (d) shows that both electrodeposited and etched LIS feature apparent contact angle of ~93° with a sliding angle of 3±0.5°. For both texturing methods, the measured wettability of SHS and LIS were similar, irrespective of the functionalization time, t_f, from 1 h to 72 h.

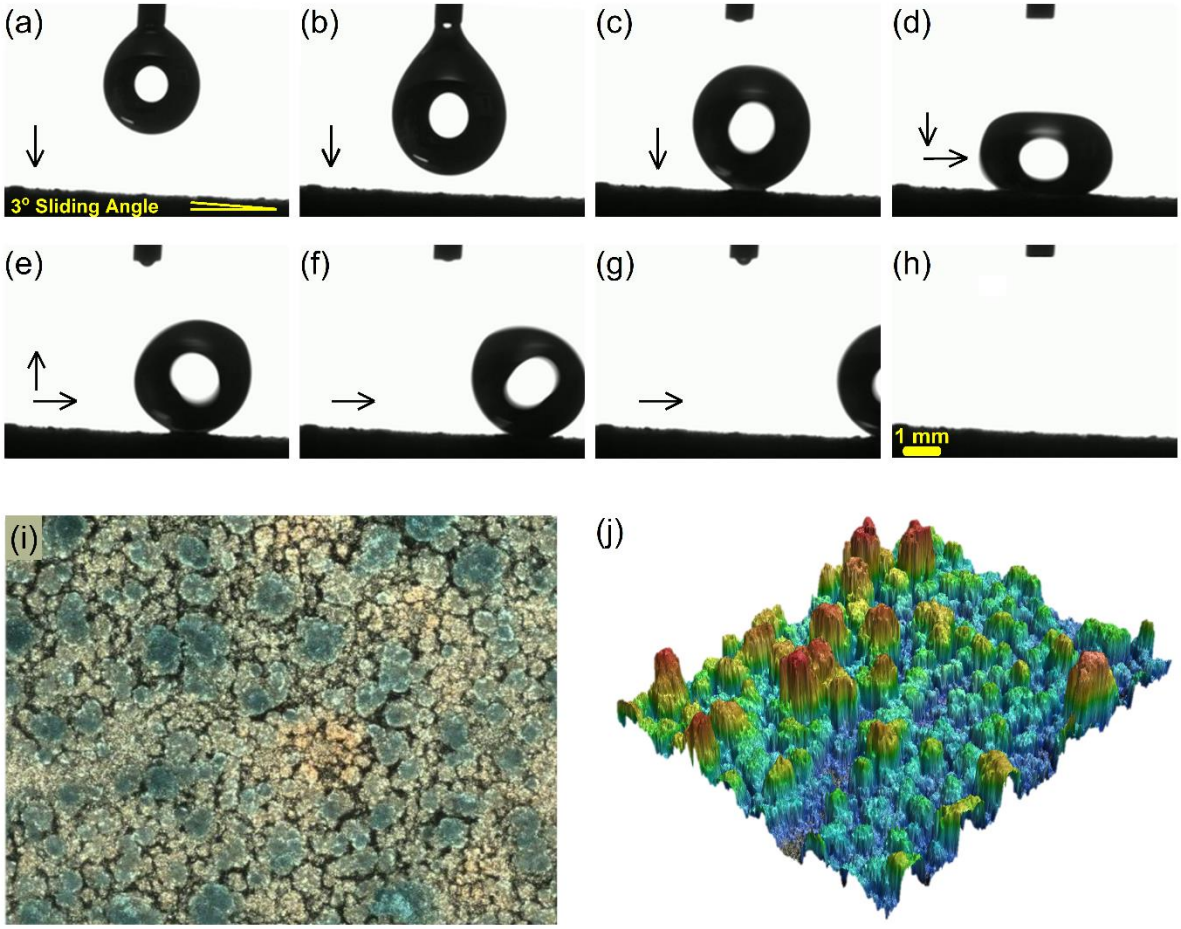

Figure 3.2. Dynamic anti-wetting property of as-fabricated superhydrophobic electrodeposited surface: (a-h) Time-lapsed images at 50 ms intervals of 25 µl DI-water droplet with a base tilting angle of 3° showing strong superhydrophobic nature, and (i) white light scanning and (j) 3D laser scanning confocal microscopic images. The height of the highest asperity is ~40 µm.

Dynamic wettability test of electrodeposited superhydrophobic copper surface is shown through successive snapshots of a 25 µl DI-water droplet rolling off the surface in Figure 3.2(a)-(h) (see Video S1 in the supporting information), where the time interval between two successive snapshots is 50 ms. The droplet rolled off the superhydrophobic surface at a nearly horizontal orientation with a roll off angle of 3°, demonstrating excellent water repellency. Figure 3.2(i) represents the white light optical microscopic image of the electrodeposited SHS sample, and Figure 3.2(j) shows the corresponding 3D profile of the same surface by confocal laser scan, where the peaks stand at about 40 µm height. The peak-to-valley height for the etched surface, in comparison, is at about 20 µm.

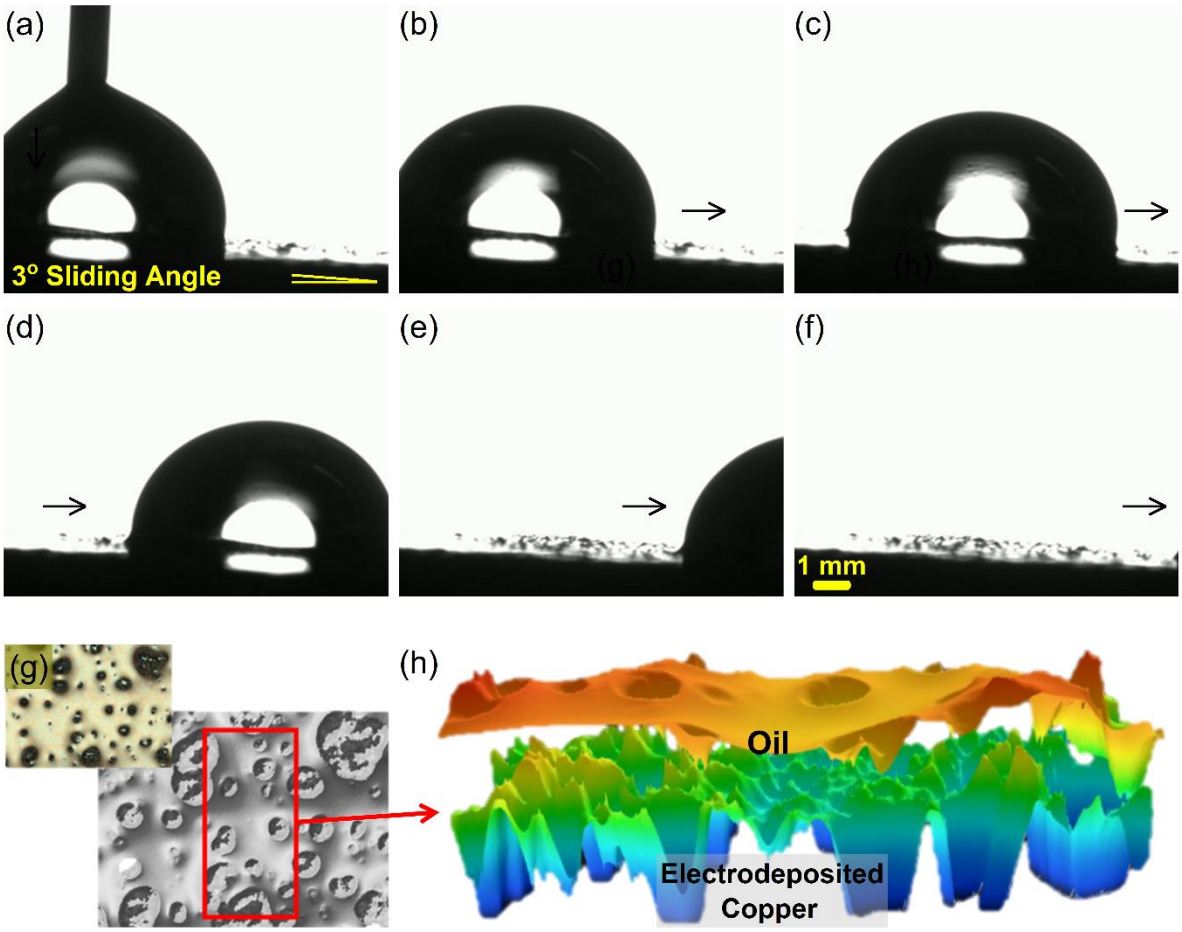

Figure 3.3. Dynamic anti-wetting property of as-fabricated lubricant infused electrodeposited copper surface: (a-f) Time-lapsed images at 6 s intervals of 25 µl DI-water droplet with a base tilting angle of 3° showing strong slipperiness of the surface on almost horizontal surface, and (g) white light scanning confocal microscopic image of the electrodeposited lubricant infused copper surface, and (h) exploded 3D laser scanning confocal microscopic image of the electrodeposited copper substrate and the infused lubricant. The average oil film thickness is measured as about 22 µm.

Figure 3.3(a)-(f) (see Video S2 in the supporting information) illustrates successive snapshots taken at 6 s interval of 25 µl DI-water droplet sliding off the electrodeposited LIS at the same stage angle, 3°, as in Figure 3.2. Even at this extremely low angle the water droplets slide off the LIS easily, demonstrating excellent slipperiness and water repellent property of the surface. The sliding angle is much less than the value of 10° reported in the literature [15]. Figure 3.3(g)

shows an optical and laser confocal microscopic image of electrodeposited slippery liquid-infused surface, where the lubricant filled regions between asperity peaks are evident. Figure 3.3(h) shows for the very first time an exploded view of the lubricant infused surface, where the 3D profile of the infused oil layer and the surface roughness underneath it are evident. The average lubricant film thickness was measured as 22.19 μm.

3.4.2. **Corrosion properties of SHS and LIS**

A series of parametric experiments was performed to examine the effect of temperature, T_i, along with the effect of functionalization time, t_f, for electrodeposited and etched SHS and LIS immersed in 3.5% NaCl solution ($pH \approx 7$). The functionalization time in the fabrication process of the electrodeposited and the etched SHS was varied from $t_f = 1$ h to $t_f = 72$ h. Further, the corrosion parameters were measured for each case at room temperature, $T_i = 23°C$, and an elevated temperature, $T_i = 70°C$. Bare copper sample was also tested as the reference for comparison at each temperature.

The electrochemical corrosion of metallic surfaces involves reduction and oxidation reactions and the rate of metal corrosion is determined by the reaction activities that are reflected in PDP tests. High polarization current densities at a certain polarization potential suggest high electrochemical reaction activity and, correspondingly, higher corrosion rate. Figure 3.4(a) shows a selection of PDP data recorded in 3.5% NaCl solution for bare copper, electrodeposited SHS, and electrodeposited LIS at $t_f = 72$ h and the two different temperature values. The Tafel asymptotes are illustrated for the case of bare copper in Figure 3.4(a), where the slope of the linear part of the cathodic and anodic regions are β_c and β_a, in mV/decade, respectively. The intersection of the asymptotes is used to determine the corrosion current, j_{corr} ($\mu A \cdot cm^{-2}$), and corrosion potential, E_{corr} (V). It is seen in Figure 3.4(a) that the electrodeposited SHS copper, at room temperature, has ~2 orders of magnitudes lower polarization current compared to the bare copper sample. At higher temperature the available energy for the redox reactions increases and along with it, the corrosion current. This trend is reflected in the about one order of magnitude increase in polarization current for bare copper at 70°C compared to 23°C. In comparison, the PDP curve of the electrodeposited LIS copper surface at 70°C is seen to be ~2 orders of magnitude below that

of bare copper at the same temperature, demonstrating a significant corrosion inhibition characteristic of the LIS.

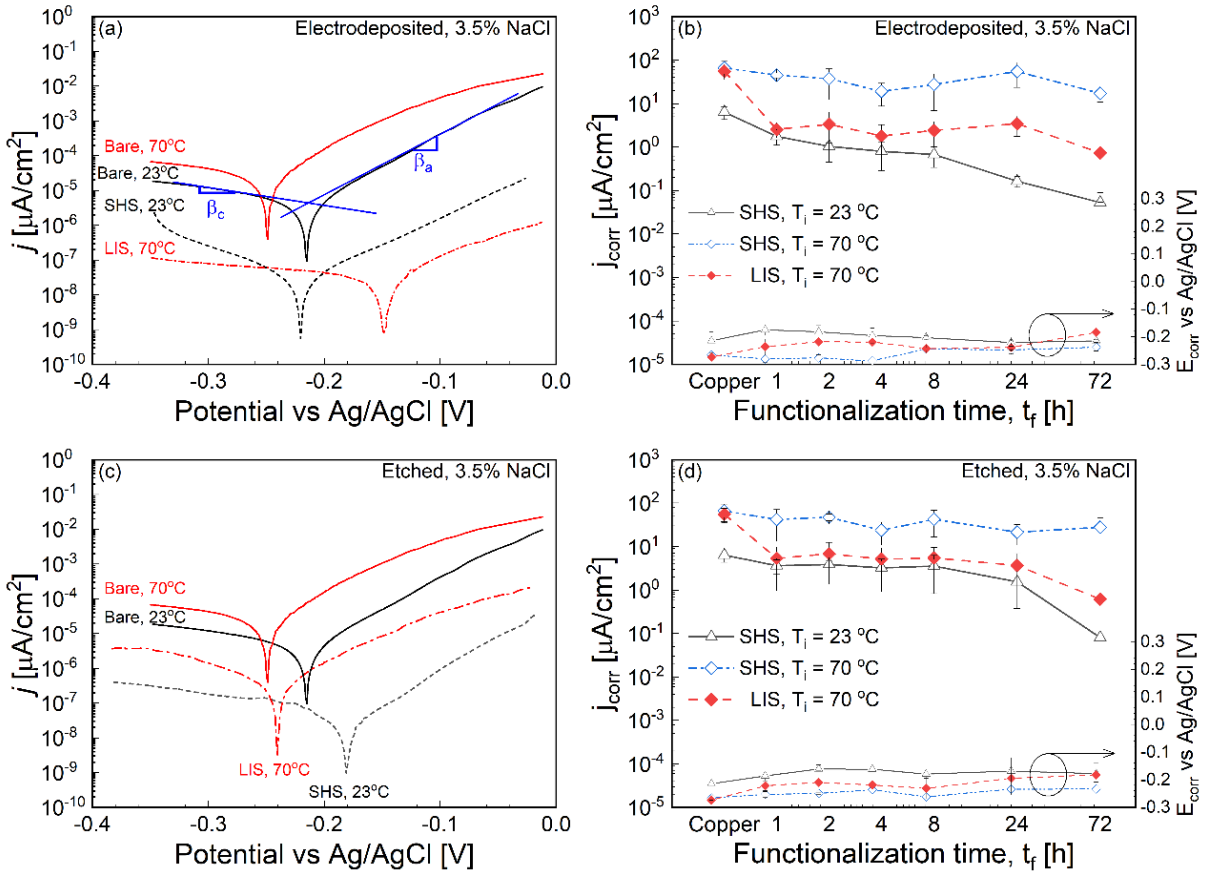

Figure 3.4. Electrochemical corrosion measurements on superhydrophobic and lubricant-infused copper surfaces in 3.5% NaCl aqueous solution: (a) PDP curves for bare and electrodeposited SHS and LIS at 23°C and 70°C; (b) variation of corrosion current density, j_{corr}, and corrosion voltage, E_{corr}, with functionalization time, t_f, for electrodeposited SHS and LIS at 23°C and 70°C; (c) PDP curve for bare and etched SHS and LIS at 23°C and 70°C; (d) variation of corrosion current density, j_{corr}, and corrosion voltage, E_{corr}, with functionalization time, t_f, for etched SHS and LIS at 23°C and 70°C.

Potentiodynamic polarization curves were obtained for electrodeposited SHS immersed in saline solution at 23°C and 70°C and compared to those for electrodeposited LIS at 70°C. The functionalization time in the fabrication of SHS and LIS was varied systematically from $t_f = 1$ h to 72 h. For reference, PDP measurements were also made on bare copper are also presented. The slopes of the Tafel asymptotes, β_c and β_a, along with the j_{corr} and E_{corr} values from all these

studies are summarized in Table 3.1. For ease of visualization of the trends, the variation of the corrosion current density and corrosion potential with functionalization time for electrodeposited SHS at 23°C and 70°C and electrodeposited LIS at 70°C is plotted in Figure 3.4(b). At room temperature, Figure 3.4(b) shows that the corrosion current for the 1 h functionalized electrodeposited SHS is reduced from the value for bare copper and decreases monotonically by over two decades with increasing functionalization time. However, at the higher temperature, 70°C, the corrosion current is seen to decrease only slightly for electrodeposited SHS compared to the bare copper sample at this temperature. On the other hand, at 70°C, electrodeposited LIS with 1 h functionalization shows sharp decrease in the corrosion current by over one order of magnitude relative to bare copper. The corrosion current remains nearly the same with further increase in the functionalization time and demonstrates a further decrease between 24 h and 72 h functionalization time, for an overall reduction in the corrosion current density by over two orders of magnitude compared to the control copper sample at the same temperature. Figure 3.4(b) further shows that the corrosion potential increases toward nobility for SHS and LIS relative to the bare copper surface. For example, at 70°C, a net change of about +25 mV and +80 mV are observed for the 72 h functionalized, electrodeposited SHS and LIS with respect to the bare copper surface, respectively.

The PDP curves of 72 h functionalized, etched SHS at 23°C and etched LIS at 70°C are presented in Figure 3.4(c), along with the data for bare copper at the two temperatures, for reference. Two orders of magnitude reduction in polarization current is seen for SHS and LIS compared to the bare control sample at the respective temperatures. The effect of functionalization time, t_f, on the Tafel slopes, β_a and β_c, corrosion current density (j_{corr}) and corrosion potential (E_{corr}) derived from PDP measurements on etched SHS, etched LIS and bare copper at T_i = 23°C and 70°C is summarized in Table 3.2. The variation of j_{corr} and E_{corr} with functionalization time, t_f, is depicted in Figure 3.4(d) for etched SHS at 23°C and 70°C and etched LIS at 70°C, in comparison to the corresponding parameters of bare copper surface. As with electrodeposited SHS, the etched SHS samples also exhibit a significant decrease in j_{corr} at 23°C with increase in functionalization time, relative to the bare copper control sample. Insignificant change in corrosion current was observed for the etched SHS at 70°C whereas the etched LIS sample shows two orders of magnitude reduction in corrosion current, similar to that for etched SHS at room temperature. The corrosion potential, E_{corr}, is seen to increase slightly from that of the control samples toward

nobility in Figure 3.4(d), mirroring the trend and the magnitude of increase in E_{corr} in Figure 3.4(b) for the electrodeposited nonwetting surfaces.

The reduction in the corrosion current density and the increase in the corrosion voltage together point to the enhanced corrosion resistance of the etched and electrodeposited SHS and LIS at both temperatures considered in Figure 3.4. The significantly reduced corrosion current density, by about two decades, translates to low corrosion rates, which is attributed mainly to the nonwetting nature of the surfaces. For SHS, a protective air cushion between the surface and the corrosive solution prevents the halide oxidative species from reaching the substrate surface [11], whereas for LIS the infused lubricant forms the added protective layer for further corrosion inhibition, as evident from the comparison of the SHS and LIS lines at 70°C in Figure 3.4(b) and (d).

The efficiency of SHS and LIS in mitigating corrosion relative to bare copper control sample in the same corrosion condition is obtained as follow: $\eta = 1 - \frac{j_{corr}}{j^0_{corr}} \times 100\%$, where j^0_{corr} and j_{corr} are the corrosion current density of the bare copper surface and the nonwetting surface, respectively. Based on the corrosion density values obtained from the PDP measurements, Table 3.1 and 2 also present the corrosion efficiency for the different surfaces in terms of the functionalization time and immersion temperature. It is seen from Table 3.1 and 2 that electrodeposited as well as etched SHS with functionalization time $t_f > 24$ h offer over 90% corrosion efficiency at 23°C and LIS has an efficiency over 90% uniformly for all functionalization times studied, regardless of texturing. Highest corrosion efficiency of 99% was obtained with 72 h functionalization for SHS at 23°C and LIS at 70°C. Electrodeposited and etched SHS demonstrate least corrosion efficiency.

3.4.3. **Effect of temperature on SHS and LIS**

The corrosion tests discussed so far illustrated the performance of SHS and LIS fabricated via electrodeposition or etching at two specific temperatures, 23°C and 70°C. It is of further interest to examine the corrosion inhibition characteristics of the surfaces over a range of temperatures. To this end, corrosion tests were conducted on SHS and LIS immersed in 3.5% NaCl solution, where the corrosion rate was measured using the PDP method. The surfaces were fabricated by electrodeposition or etching and functionalized for 72 h, based on the low corrosion current seen in Figure 3.4 for this functionalization duration. The corrosion tests of

electrodeposited or etched SHS and LIS as well as bare copper were conducted in 3.5% NaCl solution at temperature values of 23°C, 35°C, 50°C, 70°C, and 85°C.

From the corrosion current density, j_{corr}, deduced from the PDP curves, the corrosion rate CR, in mm/y (denoted as mmPY), was calculated as $\mathrm{CR} = 3276.6 j_{corr} E_w/\rho$ where ρ is the metal density and E_w is equivalent weight defined as $\frac{A_w}{nF}$, in which F is the Faraday constant and n is the number of electrons transferred per metal atom of atomic weight, A_w, as per the anodic corrosion reaction: $M \rightarrow M^{n+} + n \cdot e^-$. Figure 3.5 presents the corrosion rate as a function of temperature for SHS and LIS fabricated by electrodeposition (Figure 3.5(a)) and etching (Figure 3.5(b)). Also included in the plots are the corrosion rate values for bare copper at the smallest temperature (23°C) and the largest temperature (85°C) studied. At 23°C, both SHS and LIS show similar, about two orders of magnitude reduced, corrosion rate compared to bare copper at the same temperature, regardless of the texturing method. With increasing temperature, more energy is available for the species to overcome the activation energy barrier in the corrosion redox reactions and the corrosion rate expectedly increases with temperature in Figure 3.5(a) and (b). While the corrosion rate for SHS increases and approaches that of bare copper at 85°C, the corrosion rate for LIS is seen to be at least an order of magnitude less in comparison. For example, it is seen in Figure 3.5(b) that at 85°C, the average corrosion rate for etched SHS is about 0.310 mmPY whereas, the corrosion rate for etched LIS is 0.022 mmPY. Nevertheless, the corrosion rate of etched SHS is about only half that of bare copper, 0.631 mmPY, at the same temperature. The observed trends are consistent for both electrodeposited (Figure 3.5(a)) and etched (Figure 3.5(b)) non-wetting surfaces.

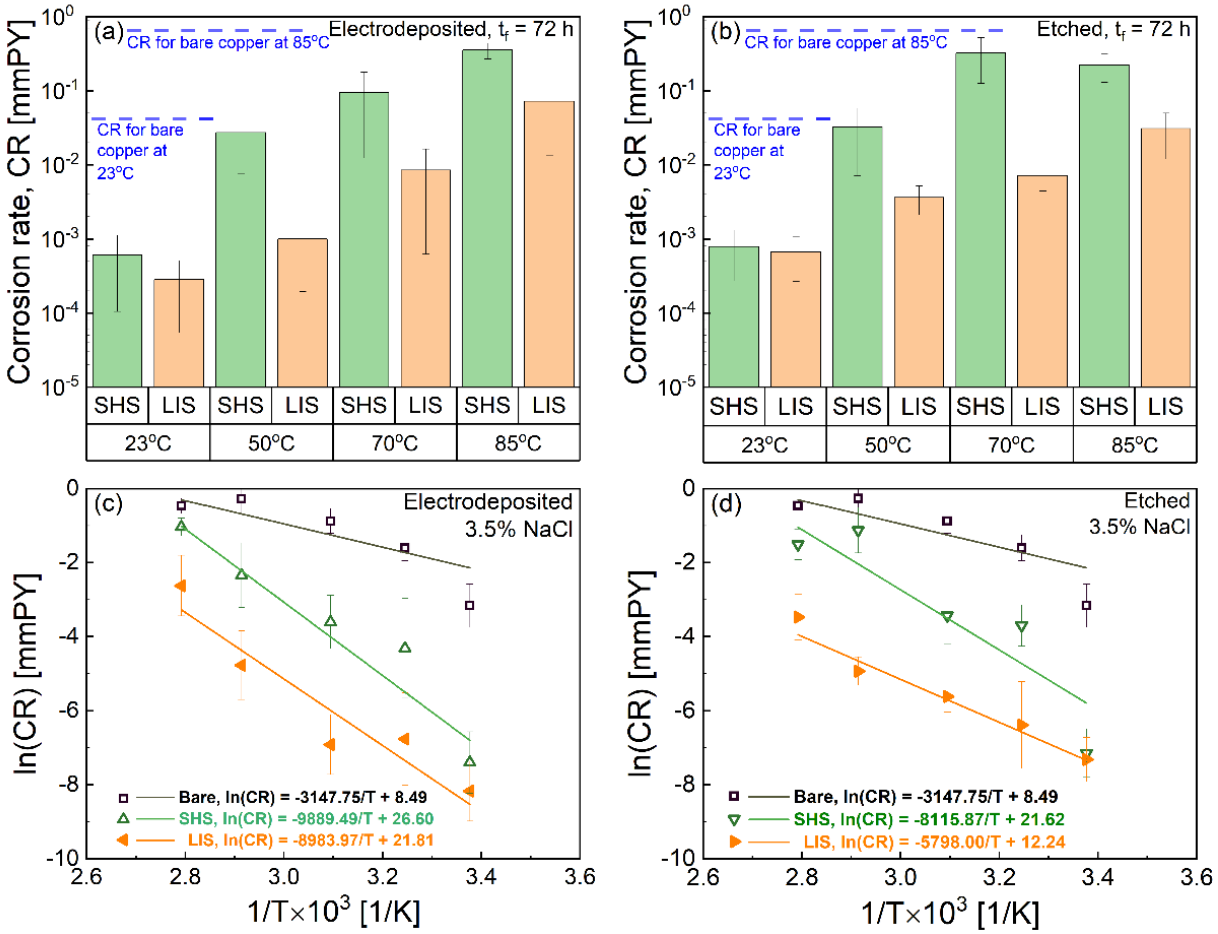

Figure 3.5. Variation of corrosion rate with temperature for (a) electrodeposited and (b) etched copper SHS and LIS with t_f = 72 h immersed in 3.5% NaCl aqueous solution. Arrhenius plot of the natural logarithm of the corrosion rate with reciprocal of absolute temperature for (c) electrodeposited and (d) etched SHS and LIS.

Overall, Figure 3.5(a) and (b) points to the excellent corrosion resistance of non-wetting surfaces over the entire range of temperature studied. In particular, the lubricant infused surfaces demonstrate excellent corrosion stability that leads to distinctly lower corrosion rate compared to bare copper. The increase in corrosion rate with temperature suggests an Arrhenius relationship that is explored in Figure 3.5(c) and (d), where the calculated corrosion rate is plotted against the inverse of the absolute temperature (in Kelvin) on a semi-log plot, for electrodeposited and etched non-wetting surfaces in comparison to the bare surface. The linear variation of the data in the plots confirms the Arrhenius relationship between the corrosion rate and the temperate of the form CR =

$\beta\, e^{-\alpha/T}$. The activation energy, α, is obtained as the slope of a linear fit in the semi-log plot and the pre-exponential factor, β, is the intercept on the ordinate. The least-squares linear regression fits through the experimentally derived corrosion rate data are presented for bare, SHS and LIS surfaces fabricated by electrodeposition (Figure 3.5(c)) and etching (Figure 3.5(d)).

The corresponding analytical correlations are also included in the plots from which the activation energy and pre-exponential factors may be compared for the different surfaces and texturing methods. A larger value of the activation energy signifies a greater barrier to corrosion and a reduced sensitivity of the corrosion rate to temperature. It is evident from Figure 3.5(c) and (d) that SHS and LIS have significantly larger activation energy compared to bare copper, corresponding to the excellent corrosion inhibition by the non-wetting surfaces. Further, the ratio of activation energy for LIS to that for SHS is 0.91 for electrodeposited surfaces (Figure 3.5(c)) and 0.71 for etched surfaces (Figure 3.5(d)), both below unity, signifying the greater temperature insensitivity of corrosion rate for LIS compared to SHS for both texturing methods. Furthermore, the ratio of the activation energy for etched LIS to that for electrodeposited LIS is 0.65, which points to the greater corrosion stability of etched LIS with temperature compared to electrodeposited LIS. The difference in the ratios is attributed to the difference in the texturing methods, whereby the average roughness and peak-to-valley height are greater for the electrodeposited surfaces. As a result, electrodeposited surfaces, which have multiscale asperities that are deposited on top of the base substrate, might have bare asperities protruding over the infused oil level. In contrast, the asperities are grooved into the base substrate through the etching process which lowers the chance of protruded asperities over the infused lubricant. It is worth noting that, irrespective of the texturing method, etched or electrodeposition, the LIS surfaces have at least one order of magnitude less corrosion rate at any tested temperature compared to the corrosion rate of bare control sample at the corresponding temperature. The Arrhenius correlation between the corrosion rate and temperature serves to predict corrosion rate of the electrodeposited or etched non-wetting surfaces in a saline environment, over a temperature range of 23°C to 85°C.

Optical images of the LIS surfaces before and after the corrosion test at temperatures of 50°C, 70°C, 85°C are shown for comparison in Figure 3.6 and 7, for electrodeposited LIS and etched LIS, respectively. The images of LIS after the corrosion test at 50°C and 70°C, Figure 3.6(d, e) and Figure 3.7(d, e), do not show significant change relative to the corresponding images of the

surfaces before the corrosion test, Figure 3.6(a, b) and Figure 3.7(a, b). However, comparing the electrodeposited LIS image after corrosion test at 85°C, Figure 3.6(f), to the surface before the test, Figure 3.6(c), shows signs of surface degradation, evident in the discoloration of the protruding asperities encircled in Figure 3.6(c) and (f). At the same temperature, relatively less degradation was observed for the etched LIS after corrosion test, cf. Figure 3.7(c) and (f), owing to the smaller peak-to-valley asperity height for the etched LIS. The observation in Figure 3.6 and 7 matches the difference in the average corrosion rate of the electrodeposited LIS compared to the etched LIS at 85°C discussed in Figure 3.5.

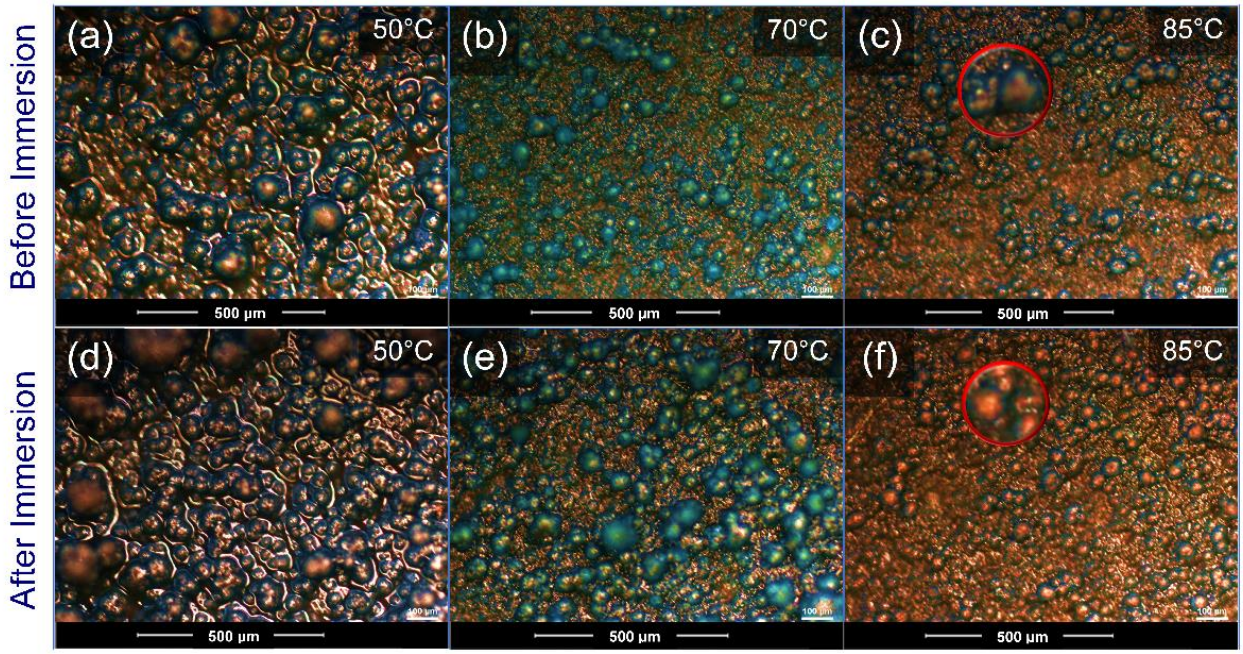

Figure 3.6. Optical microscope image of electrodeposited LIS surfaces functionalized for 72 h, (a-c) before and (d-f) after PDP electrochemical corrosion test in 3.5% NaCl aqueous solution at temperatures of 50°C, 70°C and 85°C.

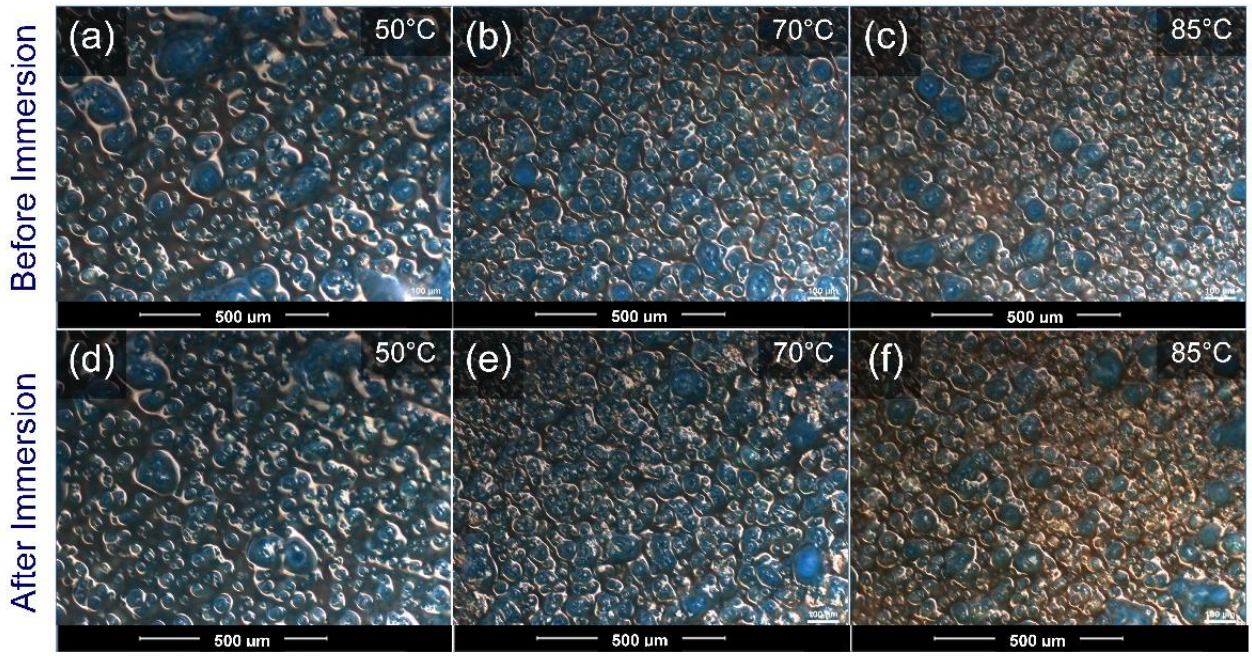

Figure 3.7. Optical microscope image of etched LIS surfaces functionalized for 72 h, (a-c) before and (d-f) after PDP electrochemical corrosion test in 3.5% NaCl aqueous solution at temperatures of 50°C, 70°C and 85°C.

3.4.4. **Chemical stability in harsh acidic and basic environments**

The results discussed so far demonstrate the excellent corrosion inhibition performance of LIS in 3.5% NaCl ($pH \approx 7$) solution. It is also of interest to examine the corrosion resistance of the surfaces to extremely acidic and extremely basic environments, as may be encountered in applications. To this end, electrochemical impedance spectroscopy (EIS) was used to measure the corrosion impedance of etched LIS ($t_f = 72\ h$) and bare copper control samples immersed in solutions of $pH = 1$ and $pH = 14$, at 23°C. The solutions with extreme acidity (pH = 1) and extreme alkalinity (pH = 14) were prepared by hydrolysis of sulfuric acid and sodium hydroxide in de-ionized water, respectively.

Figure 3.8 compares the Bode plots of the measured EIS impedance data of the etched LIS (filled markers) with that of bare copper (open markers) at $pH = 1$ (red markers) and $pH = 14$ (blue markers). It is seen that the Bode plots shift toward a higher impedance modulus over the entire scanned frequency range for LIS compared to bare copper for both $pH = 1$ and $pH = 14$ solutions. The impedance modulus value in the low-frequency region of the Bode diagram has

been suggested as a possible predictor of corrosion inhibition characteristic [29]. The impedance magnitude at a frequency of 0.1 Hz, for the LIS, is seen to be about an order of magnitude larger than the corresponding value for the bare copper sample for immersion in harshly basic solution of $pH = 14$. Similarly, excellent corrosion behavior is recorded for LIS with an impedance value of $10^6\ \Omega.\text{cm}^2$, three orders of magnitude larger than the impedance value of $10^3\Omega.\text{cm}^2$ for bare copper, for immersion in $pH = 1$ solution.

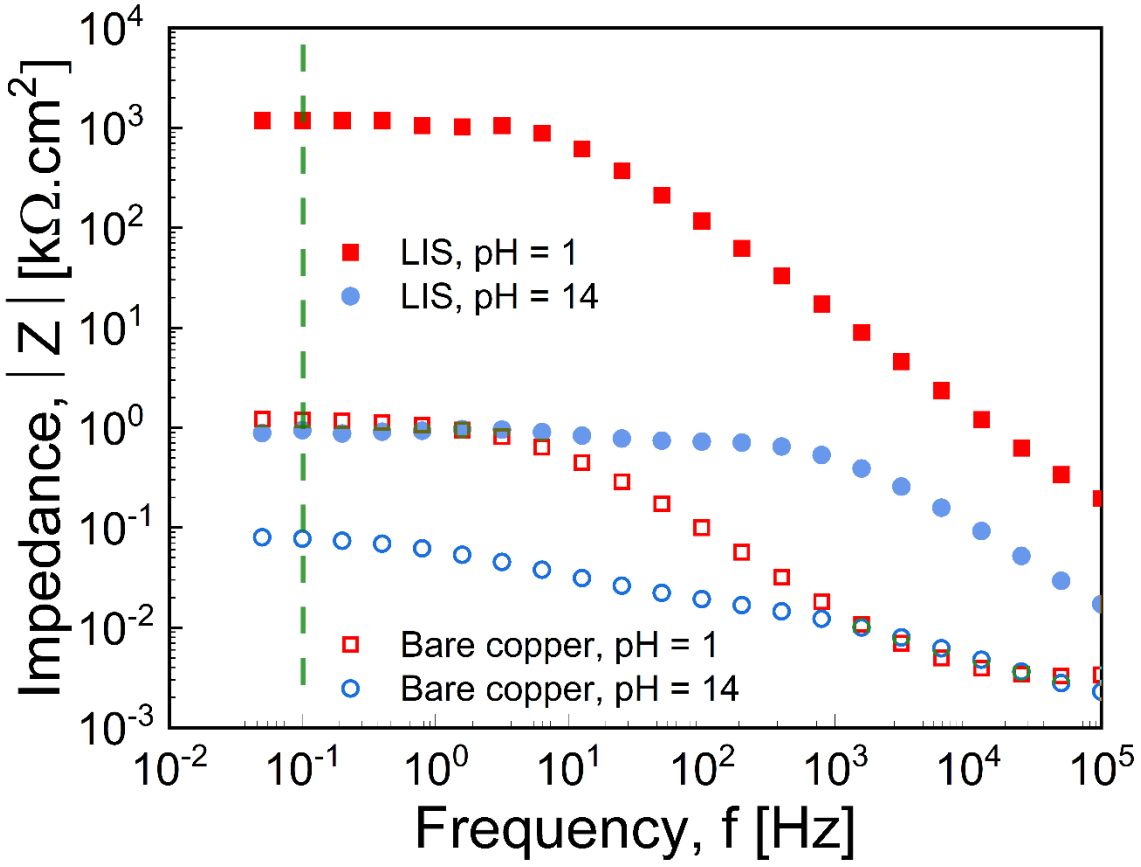

Figure 3.8. Bode plot for etched LIS functionalized for 72 h and bare copper surface immersed in harshly acidic, pH=1, and harshly basic, pH=14, aqueous solutions at room temperature.

Additionally, based on the discussed anti-corrosion mechanism for SHS, which is mainly due to its heterogeneous wetting characteristic, wetting properties of SHS in varying corrosive environments were studied by placing droplets of $pH = 1$ and $pH = 14$ solutions on the surfaces, in addition to measurements in $pH \approx 7$ (3.5% NaCl) solution discussed in Figure 3.1. For droplets of all pH values, CA > 150 degrees was recorded on SHS. Droplets of $pH = 1$ and $pH \approx 7$ had

sliding angle below 10 degrees while the sliding angle was recorded to be below 23 degrees for $pH = 14$, pointing to the excellent corrosion resistance of SHS in solutions with a range of corrosivity from $pH = 1–14$.

The focus of this article is on the effects of surface fabrication method, surface modification, surface functionalization time, temperature and pH of the immersion medium on the corrosion performance of nonwetting superhydrophobic and lubricant-infused copper surfaces. Chemical and mechanical durability of the fabricated surfaces under simulated use environments is also an important aspect in the design of the surfaces for applications. To this end, extensive corrosion durability characterizations of SHS subjected to falling sand testing and SHS and LIS subjected to mechanical scratch testing and high-pressure water jet impingement are reported in separate studies [40,41], which the interested reader is referred to.

3.5. CONCLUSIONS

The effects of fabrication methods, functionalization time, temperature and range of corrosivity on the corrosion behavior of SHS and LIS were presented in this study. Two facile methods for the fabrication—*additive* (electrodeposition) and *removal* (etching) processes—were considered, which yielded different texturing levels. Functionalization was achieved using an environmentally benign stearic acid, and the functionalization time was varied from 0–72 h, to obtain SHS. LIS was fabricated by infusing the functionalized SHS with silicone oil. Corrosion tests were conducted using PDP in 3.5% NaCl for temperatures from 23°C to 85°C. Corrosion in extremely acidic and extremely basic solutions were also studied using EIS.

The study yielded the following significant findings: SHS, regardless of fabrication method, demonstrated water contact angle of over 155° and contact angle hysteresis below 5°, while LIS was characterized by an extremely low sliding angle of 3°, much smaller than the typical values of 10° reported in prior studies. The corrosion rate for SHS and LIS at all functionalization time was at least one order of magnitude lower than that for bare copper surface, with 72 h functionalization time yielding about two orders of reduced corrosion rate for LIS compared to the bare surface. Electrodeposited as well as etched SHS and LIS were shown to reduce corrosion rate over the temperature range 23°C to 85°C, by at least a factor of two for SHS and by over an order of magnitude for LIS. An Arrhenius relationship was derived for the temperature-dependent corrosion rate. The activation energy for SHS and LIS were shown to be higher by a factor of two

and three, respectively, for LIS and SHS compared to the bare copper surface, reflecting an increased barrier to corrosion and the reduced corrosion rate for SHS and LIS. Furthermore, comparison of the activation energy for LIS and SHS showed that etched LIS has greater corrosion stability with temperature compared to electrodeposited LIS, reflecting the effect of fabrication on the corrosion performance. Optical images of LIS after corrosion showed no deterioration at the lower temperatures, and a slight deterioration of the electrodeposited LIS at 85 °C due to the taller asperities on the surface compared to etched LIS. Etched LIS was shown to have excellent corrosion resistance and SHS was shown to preserve superhydrophobicity and low contact angle at the extremes of corrosivity, $pH = 1$ and 14.

Overall, the study presented, for the first time, the interactive effects of fabrication, functionalization, temperature and corrosivity on the corrosion inhibition characteristics of SHS and LIS. The Arrhenius model developed in the study may be used for predicting the temperature-dependent corrosion rate of the surfaces in practice.

ACKNOWLEDGMENT AND DISCLAIMER

The material reported in this publication is based upon work supported by the U.S. Department of Energy under Award Number DE-FE0031556. This publication was prepared as an account of work sponsored by an agency of the United States Government. Neither the United States Government nor any agency thereof, nor any of their employees, makes any warranty, express or implied, or assumes any legal liability or responsibility for the accuracy, completeness, or usefulness of any information, apparatus, product, or process disclosed, or represents that its use would not infringe on privately owned rights. Reference herein to any specific commercial product, process, or service by trade name, trademark, manufacturer, or otherwise does not necessarily constitute or imply its endorsement, recommendation, or favoring by the United States Government or any agency thereof. The views and opinions of the authors expressed herein do not necessarily state or reflect those of the United States Government or any agency thereof.

DATA AVAILABILITY

The raw data required to reproduce these findings are already included in the presented figures. The processed data required to reproduce these findings are included in the presented figures.

REFERENCES

[1] X. Liu, H. Li, X. Zhao, Y. Chen, S. Wang, Comparison of the corrosion behavior of copper tubes in formic acid and acetic acid environment, Mater. Corros. (2021). https://doi.org/10.1002/MACO.202112568.

[2] A. V. Kirilina, S.Y. Suslov, V. V. Kozlovskii, A.B. Larin, Water Chemistry Development for a Thermal Power Plant Circulating Cooling System Using the VTIAMIN EKO-1 Chemical Agent, Therm. Eng. 2019 6610. 66 (2019) 750–759. https://doi.org/10.1134/S0040601519100021.

[3] L. Yao, H. Fengyuan, W. Fei, L. Chengming, Application of on Line Chemical Cleaning for Stainless Steel Tube Condenser in a Power Plant, IOP Conf. Ser. Earth Environ. Sci. 791 (2021) 012106. https://doi.org/10.1088/1755-1315/791/1/012106.

[4] ASTM A380 / A380M-17, Standard Practice for Cleaning, Descaling, and Passivation of Stainless Steel Parts, Equipment, and Systems, ASTM Int. (2017). https://doi.org/10.1520/A0380_A0380M-17.

[5] K. P.S, R. Kumar, V.V. N, Comparative study of mechanical and chemical methods for surface cleaning of a marine shell-and-tube heat exchanger, Heat Transf. Res. 47 (2018) 520–530. https://doi.org/10.1002/HTJ.21316.

[6] E. Vazirinasab, R. Jafari, G. Momen, Application of superhydrophobic coatings as a corrosion barrier: A review, Surf. Coatings Technol. 341 (2018) 40–56. https://doi.org/10.1016/j.surfcoat.2017.11.053.

[7] D.J. Preston, Y. Song, Z. Lu, D.S. Antao, E.N. Wang, Design of Lubricant Infused Surfaces, ACS Appl. Mater. Interfaces. 9 (2017) 42383–42392. https://doi.org/10.1021/acsami.7b14311.

[8] R.N. Wenzel, Resistance of solid surfaces to wetting by water, Ind. Eng. Chem. 28 (1936) 988–994. https://doi.org/10.1021/ie50320a024.

[9] A.B.D. Cassie, S. Baxter, Wettability of porous surfaces, Trans. Faraday Soc. 40 (1944) 546–551.

[10] L.B. Boinovich, A.M. Emelyanenko, A.D. Modestov, A.G. Domantovsky, K.A. Emelyanenko, Synergistic Effect of Superhydrophobicity and Oxidized Layers on Corrosion Resistance of Aluminum Alloy Surface Textured by Nanosecond Laser

Treatment, ACS Appl. Mater. Interfaces. 7 (2015) 19500–19508. https://doi.org/10.1021/acsami.5b06217.

[11] S.M.A. Mousavi, R. Pitchumani, A Study of Corrosion on Electrodeposited Superhydrophobic Copper Surfaces, Corros. Sci. 186 (2021) 109420. https://doi.org/10.1016/j.corsci.2021.109420.

[12] Y. Jiang, C.H. Choi, Droplet Retention on Superhydrophobic Surfaces: A Critical Review, Adv. Mater. Interfaces. 8 (2021) 2001205. https://doi.org/10.1002/admi.202001205.

[13] T. Eisner, D.J. Aneshansley, Defense by foot adhesion in a beetle (Hemisphaerota cyanea)., Proc. Natl. Acad. Sci. U. S. A. 97 (2000) 6568–73. https://doi.org/10.1073/pnas.97.12.6568.

[14] T.S. Wong, S.H. Kang, S.K.Y. Tang, E.J. Smythe, B.D. Hatton, A. Grinthal, J. Aizenberg, Bioinspired self-repairing slippery surfaces with pressure-stable omniphobicity, Nature. 477 (2011) 443–447. https://doi.org/10.1038/nature10447.

[15] P. Wang, D. Zhang, Z. Lu, Slippery liquid-infused porous surface bio-inspired by pitcher plant for marine anti-biofouling application, Colloids Surfaces B Biointerfaces. 136 (2015) 240–247. https://doi.org/10.1016/j.colsurfb.2015.09.019.

[16] Z. Shi, Y. Xiao, R. Qiu, S. Niu, P. Wang, A facile and mild route for fabricating slippery liquid-infused porous surface (SLIPS) on CuZn with corrosion resistance and self-healing properties, Surf. Coatings Technol. 330 (2017) 102–112. https://doi.org/10.1016/j.surfcoat.2017.09.053.

[17] T. Song, Q. Liu, J. Liu, W. Yang, R. Chen, X. Jing, K. Takahashi, J. Wang, Fabrication of super slippery sheet-layered and porous anodic aluminium oxide surfaces and its anticorrosion property, Appl. Surf. Sci. 355 (2015) 495–501. https://doi.org/10.1016/j.apsusc.2015.07.140.

[18] T. Xiang, M. Zhang, H.R. Sadig, Z. Li, M. Zhang, C. Dong, L. Yang, W. Chan, C. Li, Slippery liquid-infused porous surface for corrosion protection with self-healing property, Chem. Eng. J. 345 (2018) 147–155. https://doi.org/10.1016/j.cej.2018.03.137.

[19] R. Qiu, Q. Zhang, P. Wang, L. Jiang, J. Hou, W. Guo, H. Zhang, Fabrication of slippery liquid-infused porous surface based on carbon fiber with enhanced corrosion inhibition property, Colloids Surfaces A Physicochem. Eng. Asp. 453 (2014) 132–141. https://doi.org/10.1016/j.colsurfa.2014.04.035.

[20] X.X. Zhang, S. Cai, D. You, L.H. Yan, H.B. Lv, X.D. Yuan, B. Jiang, Template-free sol-gel preparation of superhydrophobic ORMOSIL films for double-wavelength broadband antireflective coatings, Adv. Funct. Mater. 23 (2013) 4361–4365. https://doi.org/10.1002/adfm.201203059.

[21] S. Khodakarami, H. Zhao, K.F. Rabbi, N. Miljkovic, Scalable corrosion-resistant coatings for thermal applications, ACS Appl. Mater. Interfaces. 13 (2021) 4519–4534. https://doi.org/10.1021/acsami.0c19683.

[22] S. Lee, B. Kim, S.H. Kim, E. Kim, J.H. Jang, Superhydrophobic, Reversibly Elastic, Moldable, and Electrospun (SupREME) Fibers with Multimodal Functions: From Oil Absorbents to Local Drug Delivery Adjuvants, Adv. Funct. Mater. 27 (2017) 1702310. https://doi.org/10.1002/adfm.201702310.

[23] K.A. Emelyanenko, N.A. Sanzharovsky, E. V. Chulkova, A.A. Ganne, A.M. Emelyanenko, L.B. Boinovich, Superhydrophobic corrosion resistant coatings for copper via IR nanosecond laser processing, Mater. Res. Express. 5 (2018) 115001. https://doi.org/10.1088/2053-1591/aadc16.

[24] Y. Wan, M. Chen, W. Liu, X.X. Shen, Y. Min, Q. Xu, The research on preparation of superhydrophobic surfaces of pure copper by hydrothermal method and its corrosion resistance, Electrochim. Acta. 270 (2018) 310–318. https://doi.org/10.1016/j.electacta.2018.03.060.

[25] P. Dimitrakellis, K. Ellinas, G.D. Kaprou, D.C. Mastellos, A. Tserepi, E. Gogolides, Bactericidal Action of Smooth and Plasma Micro-Nanotextured Polymeric Surfaces with Varying Wettability, Enhanced by Incorporation of a Biocidal Agent, Macromol. Mater. Eng. 306 (2021) 2000694. https://doi.org/10.1002/mame.202000694.

[26] Z. He, Y. Zeng, M. Zhou, Y. Min, X. Shen, Q. Xu, Superhydrophobic Films with Enhanced Corrosion Resistance and Self-Cleaning Performance on an Al Alloy, Langmuir. 37 (2021) 524–541. https://doi.org/10.1021/acs.langmuir.0c03222.

[27] J. Liu, X. Fang, C. Zhu, X. Xing, G. Cui, Z. Li, Fabrication of superhydrophobic coatings for corrosion protection by electrodeposition: A comprehensive review, Colloids Surfaces A Physicochem. Eng. Asp. 607 (2020) 125498. https://doi.org/10.1016/j.colsurfa.2020.125498.

[28] N. Lavielle, D. Asker, B.D. Hatton, Lubrication dynamics of swollen silicones to limit long term fouling and microbial biofilms, Soft Matter. 17 (2021) 936–946. https://doi.org/10.1039/d0sm01039a.

[29] S.S. Latthe, R.S. Sutar, A.K. Bhosale, S. Nagappan, C.S. Ha, K.K. Sadasivuni, S. Liu, R. Xing, Recent developments in air-trapped superhydrophobic and liquid-infused slippery surfaces for anti-icing application, Prog. Org. Coatings. 137 (2019) 105373. https://doi.org/10.1016/j.porgcoat.2019.105373.

[30] C. Liu, Y. Li, C. Lu, Y. Liu, S. Feng, Y. Liu, Robust Slippery Liquid-Infused Porous Network Surfaces for Enhanced Anti-icing/Deicing Performance, ACS Appl. Mater. & Interfaces. 12 (2020) 25471–25477. https://doi.org/10.1021/acsami.0c05954.

[31] Z. He, Y. Zeng, M. Zhou, Y. Min, X. Shen, Q. Xu, Superhydrophobic Films with Enhanced Corrosion Resistance and Self-Cleaning Performance on an Al Alloy, Langmuir. 37 (2020) 524–541. https://doi.org/10.1021/acs.langmuir.0c03222.

[32] R. Deng, T. Shen, H. Chen, J. Lu, H.C. Yang, W. Li, Slippery liquid-infused porous surfaces (SLIPSs): A perfect solution to both marine fouling and corrosion?, J. Mater. Chem. A. 8 (2020) 7536–7547. https://doi.org/10.1039/d0ta02000a.

[33] P. Yu, Z. Lian, J. Xu, H. Yu, Slippery liquid infused porous surfaces with corrosion resistance potential on aluminum alloy, RSC Adv. 11 (2020) 847–855. https://doi.org/10.1039/d0ra08674f.

[34] F. Guo, S. Duan, D. Wu, K. Matsuda, T. Wang, Y. Zou, Facile etching fabrication of superhydrophobic 7055 aluminum alloy surface towards chloride environment anticorrosion, Corros. Sci. 182 (2021) 109262. https://doi.org/10.1016/j.corsci.2021.109262.

[35] J. Lee, S. Shin, Y. Jiang, C. Jeong, H.A. Stone, C.H. Choi, Oil-Impregnated Nanoporous Oxide Layer for Corrosion Protection with Self-Healing, Adv. Funct. Mater. 27 (2017) 1606040. https://doi.org/10.1002/adfm.201606040.

[36] D. Zang, R. Zhu, W. Zhang, X. Yu, L. Lin, X. Guo, M. Liu, L. Jiang, Corrosion-Resistant Superhydrophobic Coatings on Mg Alloy Surfaces Inspired by Lotus Seedpod, Adv. Funct. Mater. 27 (2017) 1605446. https://doi.org/10.1002/adfm.201605446.

[37] Z. Dai, G. Chen, S. Ding, J. Lin, S. Li, Y. Xu, B. Zhou, Facile Formation of Hierarchical Textures for Flexible, Translucent, and Durable Superhydrophobic Film, Adv. Funct. Mater. 31 (2021) 2008574. https://doi.org/10.1002/adfm.202008574.

[38] ASTM International, Standard Practice for Conventions Applicable to Electrochemical Measurements in Corrosion Testing, (2019) ASTM G3-14.

[39] C. Howell, A. Grinthal, S. Sunny, M. Aizenberg, J. Aizenberg, Designing Liquid-Infused Surfaces for Medical Applications: A Review, Adv. Mater. 30 (2018) 1802724. https://doi.org/10.1002/adma.201802724.

[40] R. Jain, R. Pitchumani, Facile Fabrication of Durable Copper-Based Superhydrophobic Surfaces via Electrodeposition, Langmuir. 34 (2017) 3159–3169. https://doi.org/10.1021/ACS.LANGMUIR.7B02227.

[41] S.M.A. Mousavi and R. Pitchumani, Mechanical and Chemical Durability of Non-wetting Superhydrophobic and Lubricant-Infused Surfaces, Chem. Eng. J. In Review (2021).

TABLES

Table 3.1. Corrosion parameters of electrodeposited SHS and LIS from PDP tests in 3.5% NaCl (pH ≈ 7) at 23°C and 70°C.

Samples	Electrodeposited SHS at 23°C					Electrodeposited SHS at 70°C					Electrodeposited LIS at 70°C				
	β_{an}	β_{cat}	j_{corr}	E_{corr}	η	β_{an}	β_{cat}	j_{corr}	E_{corr}	η	β_{an}	β_{cat}	j_{corr}	E_{corr}	η
Bare Cu	61.78	157.65	6.42	-0.21	–	77.161	380.44	66.02	-0.27	–	77.161	380.44	66.02	-0.27	–
t_f = 1 h	55.80	155.48	1.76	-0.18	72.55	158.67	203.53	45.04	-0.28	31.78	105.17	390.19	2.56	-0.24	96.12
t_f = 2 h	56.28	145.18	1.04	-0.18	83.76	85.84	193.49	37.54	-0.28	43.13	79.84	286.06	3.37	-0.22	94.90
t_f = 4 h	63.45	161.42	0.80	-0.20	87.56	182.37	186.12	19.07	-0.29	71.12	106.01	158.48	1.80	-0.22	97.27
t_f = 8 h	68.09	216.01	0.67	-0.20	89.51	119.13	181.77	27.66	-0.24	58.10	86.67	221.73	2.42	-0.24	96.33
t_f = 24 h	67.94	193.56	0.16	-0.22	97.44	143.65	212.91	55.22	-0.25	16.36	105.91	377.13	3.47	-0.24	94.75
t_f = 72 h	64.17	138.46	0.05	-0.22	99.18	96.53	224.68	17.21	-0.24	73.94	74.49	291.31	0.73	-0.18	98.89

Units: β_{an} and β_{cat} [mV/dec.]; j_{corr} [μA/cm^2]; E_{corr} vs. Ag/AgCl [V]; η [%]

Table 3.2. Corrosion parameters of etched SHS and LIS from PDP tests in 3.5% NaCl (pH ≈ 7) at 23°C and 70°C.

Samples	Etched SHS at 23°C					Etched SHS at 70°C					Etched LIS at 70°C				
	β_{an}	β_{cat}	j_{corr}	E_{corr}	η	β_{an}	β_{cat}	j_{corr}	E_{corr}	η	β_{an}	β_{cat}	j_{corr}	E_{corr}	η
Bare Cu	61.78	157.65	6.42	-0.21	–	77.161	380.44	66.02	-0.27	–	77.161	380.44	66.02	-0.27	–
t_f = 1 h	57.15	150.73	3.65	-0.19	43.15	80.63	195.75	42.22	-0.25	36.06	55.10	136.06	5.42	-0.22	91.80
t_f = 2 h	55.73	139.09	3.87	-0.16	39.72	85.88	192.45	47.58	-0.25	27.93	67.38	185.89	6.89	-0.21	89.56
t_f = 4 h	76.94	137.88	3.26	-0.16	49.22	88.97	175.83	23.88	-0.24	63.83	63.72	161.73	5.15	-0.15	92.20
t_f = 8 h	60.62	142.07	3.33	-0.18	48.13	151.95	229.38	42.61	-0.26	35.46	86.26	186.71	5.53	-0.23	91.63
t_f = 24 h	67.93	130.84	1.56	-0.17	75.70	107.19	181.45	21.44	-0.23	67.53	120.48	152.26	3.68	-0.19	94.43
t_f = 72 h	60.03	165.62	0.08	-0.18	98.75	96.36	157.22	28.07	-0.23	57.49	91.24	251.82	0.62	-0.18	99.06

Units: β_{an} and β_{cat} [mV/dec.]; j_{corr} [μA/cm^2]; E_{corr} vs. Ag/AgCl [V]; η [%]

Chapter 4. Mechanical and Chemical Durability of Non-wetting Superhydrophobic and Lubricant-Infused Surfaces

The work reported in this chapter is the basis for the following journal publication currently in re view:

S.M.A. Mousavi and R. Pitchumani. "Mechanical and Chemical Durability of Non-wetting Superhydrophobic and Lubricant-Infused Surfaces." In Review, (2021).

4.1. ABSTRACT

Fabrication of bioinspired non-wetting superhydrophobic surfaces (SHS) and lubricant-infused surfaces (LIS) has been studied extensively on a variety of materials. In contrast, durability of the surfaces exposed to harsh mechanical and chemical environments has been the subject of little attention. This study considers the mechanical and chemical durability of SHS and LIS copper surfaces fabricated via facile electrodeposition and chemical etching methods. The as-fabricated surfaces demonstrate excellent non-wetting characteristics with water contact angle of 160° and sliding angle below 5°. The surfaces are subject to mechanical wear through scratch test and water jet impingement at 15 psi and 20 psi as well as accelerated corrosion following the ASTM E407 standard. The performance of the electrodeposited and etched non-wetting surfaces is systematically assessed in terms of contact and sliding angles and corrosion rate in a simulated marine environment. All surfaces are shown to be robust to mechanical wear after scratch test, with excellent stability of contact and sliding angles, and up to two orders of magnitude reduced corrosion rate compared to bare copper surface. SHS retained steadfast non-wetting characteristics under high-pressure water jet tests compared to the other surfaces while LIS, regardless of texturing method, showed one to two orders of magnitude reduced corrosion rate compared to bare copper surface throughout water jet impingement and chemical durability tests. The study presents for the first time a systematic comparison of durability of SHS and LIS through a common set of fabrication and testing protocol and helps identify appropriate nonwetting surfaces and fabrication methods based on the use environment.

Keywords: superhydrophobicity; lubricant-infused surface; mechanical durability; chemical durability; corrosion; contact angle

4.2. 1. INTRODUCTION

Nature-inspired water repellency has been studied on various engineered materials for potential applications such a self-cleaning [1], anti-icing [2], anti-fouling [3–5], energy-efficient fluid transport [6–11], oil-water separation [12,13] and enhanced phase change heat transfer [14,15]. Superhydrophobic and lubricant-infused porous surfaces are two classes of non-wetting surfaces that are inspired by the adaptation of natural surfaces such as *lotus* leaves [16], *pond skater* legs [16], *butterfly* wings [17] and *Nepenthes* pitcher-plant [18]. Hierarchical micro/nanoscale surface patterns (texturing) treated with low-surface-energy materials (functionalization) are used to achieve water repellency effect on superhydrophobic surfaces (SHS). Impregnation of a lubricant in the micro/nanoscale texture of the surface provides the slipperiness and water repellency on lubricant-infused surfaces (LIS).

Water affinity to any surface is characterized by the water contact angle (CA) and roll-off angle. Generally, a hydrophobic surface is defined as a surface with $90^{o} < CA < 150^{o}$ while a surface with $CA > 150^{o}$ and roll-off angle $< 10^{o}$ is called a superhydrophobic surface (SHS). Apparent water contact angle on lubricant-infused surfaces (LIS) is typically in a range of 80–140° with a sliding angle $< 20^{o}$. A droplet on a rough hydrophobic/superhydrophobic surface is supported partially by the solid surface and mostly by the trapped air in the micro/nano hierarchical structure of the surface. This composite interface (the trinary contact phase between the liquid, surface, and the trapped air in the roughness features) facilitates the easy shedding of the droplet and is classified as heterogeneous wetting state or Cassie-Baxter state [19]. On the other hand, on a rough wettable surface, the droplet penetrates the micro/nano hierarchical structure of the surface and stays in the so-called homogeneous wetting state or Wenzel state [20]. Unlike hydrophobic/superhydrophobic surface that owes its self-cleaning/non-wetting effect due to partial detachment of the water droplet from the surface (the air pockets) [21], a lubricant-infused surface provides such property by low bonding energy between the droplet molecules and the infused liquid molecules on the surface, which facilitates the droplet slipping off the surface at a very low angle [22].

Fabrication of engineered SHS and LIS on different type of materials from composites [23] to wood [24] and metals [25] starts with surface texturing, that creates micro/nano structures, as the first step. Surface texturing can be accomplished by a variety of methods including templating,

sol-gel processing [26,27], different types of etching [28–30], electrochemical [31,32], coating [33] and others [34]. Among them, electrodeposition and chemical etching techniques provide a facile and, importantly, scalable method for fabricating metallic non-wetting surfaces. Despite numerous studies throughout the last decade on fabrication of excellent non-wetting surfaces, durability of the surfaces in application environments has been less understood. Existing reports on durability include tests such as tape peeling [35,36], sand abrasion [35,37,38], pencil hardness [38,39], bare finger contact [40,41] oscillating steel ring [40], solid particle impact [33,37,42], knife/blade [43,44], jet and droplet impact [45–47], and ultrasonic treatment [48,49], that are well summarized in review articles [50–52].

It is evident from the foregoing discussion that the studies focus on either SHS or LIS, fabricated by different techniques, each subject to different tests, that make a direct comparison of durability of the two nonwetting surface types difficult. Therefore, despite all the prior work in the literature there is a conspicuous lack of systematic durability studies, which is identified as a knowledge gap in the review articles [50–52]. Toward addressing the knowledge gap, the specific contributions of the present study are the following:

- SHS and LIS are fabricated by two facile methods: electrodeposition (an *additive* process) that produces deep aggressive multiscale texturing (asperity height of ~20 μm) and chemical etching (a material *removal* process) that produces relatively shallow texturing (asperity height of ~5 μm), followed by a common surface functionalization treatment. Use of the same fabrication methods for SHS and LIS allows for juxtaposition of durability characteristics of the two surfaces.
- Most applications of SHS and LIS are in environments of chemical stress (for example, corrosive cleaning solutions are commonly used to clean surfaces of bio or mineral foulants) or fluid impact or shear stress (such as surface condensation), and it is of interest to understand the durability of the surfaces in these conditions. It is common in the literature to study the mechanical durability of SHS via methods like falling sand particles, wear over sandpaper, tape peeling, or bare finger contact. However, these tests are not appropriate for LIS. Since the goal of the study is to compare the durability of SHS and LIS systematically, durability tests were selected to be applicable to both types of non-wetting surfaces. To this end, the fabricated SHS and LIS are subject to a common set of scratch, water impingement (ASTM D4049 [53]), and harsh corrosive chemical etching (ASTM E407 [54]) tests that provide, for the first time,

fundamental insight into the effects of fabrication and surface type on the mechanical and chemical durability of the two types of nonwetting surfaces.

The article is organized as follows: Section 2 describes the experimental methods of fabrication of copper SHS and LIS and their durability characterization. The results of scratch tests, water jet impingement tests and accelerated corrosion tests are presented and discussed in Section 3. The principal results of the study are summarized in Section 4.

4.3. EXPERIMENTAL METHODS

4.3.1. **Materials and reagents**

Plain multipurpose copper sheet was purchased from McMaster, USA. Sulfuric acid (H_2SO_4), hydrochloric acid (HCl), analytical-grade copper sulfate ($CuSO_4$, 99+%), acetone (99.5+%), methanol (99.8+%), iron(III) chloride (98%), and stearic acid ($CH_3(CH_2)_{16}CO_2H$, 97%) were purchased from Fisher Scientific (Pittsburgh, PA, USA) and used as-received without any further purification. Deionized water (14MΩ.cm resistance) was purchased from CQ Concept (Illinois, USA). Hydrogen peroxide solution (H_2O_2) was purchased from Sigma-Aldrich, and silicone oil, Dowsil™, was purchased from DuPont (Wilmington, Delaware, USA).

4.3.2. **Fabrication of SHS and LIS**

Surface texturing is the first step in the fabrication of SHS that was accomplished using two methods: chemical etching, a material *removal* method and electrodeposition, an *additive* method.

The as-received copper sheet was cut into coupons of 1×5 cm, and the coupons were washed in a sonication bath of methanol, acetone, and DI-water for ten minutes each, sequentially. In the material *removal* method, the roughness features were carved into the surface via chemical etching in an aqueous solution of 0.02 M hydrochloric acid and 0.05 M hydroperoxide. The cleaned and cut coupons were submerged in the etchant solution for 20 minutes.

In the additive method, multiscale asperities were grown on top of the copper surface by a three-electrode, two-step electrodeposition process [31] using an AUTOLAB PGSTAT128N electrochemical station (ECO Chemie, Utrecht, The Netherlands). A platinum mesh was used as the counter electrode and a copper sheet as the reference electrode. De-aerated aqueous solution

of 1M $CuSO_4$ and 0.5M H_2SO_4 was used as the electrolyte. The two-step electrodeposition process was initiated by applying –1.1 V for 5 minutes to the copper sample as the working electrode followed by a 10 second electrodeposition at –0.15 V as the second step. The second deposition served to further stabilize the first coating onto the surface. The electrodeposition time of 5 minutes was chosen as the first step to yield an approximately 30-micrometer deposition thickness, estimated as $QM/nF\rho A$, where F is the Faraday constant, A is the surface area of the deposition, ρ is the density of the deposited copper, Q is the charge transferred in coulomb throughout the deposition ($Q = i.\, dt$), M is the molar weight of copper, and n is the number of transferred electrons in the copper reduction reaction, $Cu^{2+} + 2^{e-} \rightarrow Cu$.

The coupons fabricated via both electrodeposition and etching methods were rinsed with copious amount of DI-water. In a following step, samples were stored in a vacuum oven at 110°C overnight to dry in order to enhance the surface with a monolayer of hydrophobic copper oxide in the form of Cu(I) as suggested in [55]. Furthermore, the textured surfaces were functionalized by immersion in 0.02 M stearic acid-methanol solution for 72 hours. The chemisorption of the stearic acid lowers the surface energy of the textured surfaces to become SHS.

LIS was fabricated by infusing the SHS with lubricant oil. Drops of Dowsil™ silicone oil with 500 cSt viscosity were placed onto the SHS and hanged vertically for twenty minutes to allow for the lubricant to wick into the interasperity spaces and also to drain any excess oil.

4.3.3. **Morphology and wettability characterization**

Surface morphology was revealed via a field-emission scanning electron microscope (SEM) (JEOL 2100, Japan), operating at an acceleration voltage of 15 kV. The optical image of surfaces was obtained via Nikon Eclipse LV100ND Microscope (Nikon Instruments Inc.) equipped with an epifluorescence filter. Surface wettability was characterized in terms of water contact and sliding angle on the surfaces and recorded by a goniometer (ramé-hart model 590, New Jersey, USA). For contact angle measurement, a 10 µl sessile DI-water droplet was placed at five different locations on each sample, from which the average contact angle and the error bars around it was determined. The sliding angle was measured via the tilting cradle method wherein the angle at which a 25 µl DI-water droplet rolls of a SHS was measured. The sliding angle for a droplet on LIS was recorded when both the rear and front contact lines of the droplet started to slide.

4.3.4. **Corrosion characterization**

Besides non-wetting water repellency properties, corrosion inhibition was used as a metric to evaluate the SHS and LIS throughout durability tests. Three-electrode electrochemical tests were carried out to characterize the corrosion inhibition of the samples. Ag/AgCl (NaCl saturated) served as a reference electrode with less than 3 mm distance from the sample surface (working electrode) to minimize the measured solution resistance. Platinum mesh placed equidistant to the two other electrodes was used as a counter electrode. Linear polarization (LP) and electrochemical impedance spectroscopy (EIS) data were recorded via a Solarton Inc. potentiostat device (model 1240 PA, USA). LP experiments were done at the scan range of –20 mV to +20 mV with respect to open circuit potential at a scan rate of 1/6 V/h as suggested by ASTM standard [56]. EIS was measured over a frequency range of 1 Hz to 0.1 MHz at 10 mV sinusoidal potential versus reference. The LP and EIS characterization methods were used as relatively non-destructive measurements due to the low potential range, about 12 to 24 times smaller than the overpotential used in a typical potentiodynamic polarization test (PDP). The non-destructive nature of the tests allowed for multiple measurements at various intervals throughout the durability tests.

The electrochemical impedance spectroscopy (EIS) was used to characterize the corrosion inhibition of the tested surfaces in terms of surface impedance |Z| at marine simulated environment (3.5% NaCl Solution). The value of impedance at low frequency region, $|Z_{5kHz}|$, was used for comparison purposes.

The voltage-current density data obtained from linear polarization scans were processed to derive corrosion potential (E_c), corrosion current density (j_c), corrosion resistance (R_c) and the corrosion rate (CR). The corrosion potential, E_c, is obtained as the intersection of the $j = 0\ A/cm^2$ line and the measured voltage-current density data. Corrosion resistance, R_c, was derived as the slope of a linear fit to the data at ±10 mV of the E_c. Furthermore, j_c was estimated based on Stearn-Geary [57]: $j_c = \frac{\beta_a \cdot \beta_c}{2.3 \cdot (\beta_a + \beta_c) \cdot R_c}$, where β_c and β_a are the slope of the linear part of the cathodic and anodic regions in a potentiodynamic polarization, PDP, test in mV/decade, respectively. In cases that the slopes (β_a and β_c) cannot be calculated from the polarization curve, such as the non-destructive LP test, 0.12V/decade (120mV/decade) value are commonly used [58]

in the Stern-Geary relationship. Thus, the corrosion current density is approximately calculated as: $j_c = \frac{0.026}{R_{corr}}$. The corrosion rate (CR) was calculated from the measured corrosion current, j_c, as $CR = \frac{3276.6 j_c E_w}{\rho}$ where ρ is the metal density and E_w is equivalent weight defined as $\frac{A_w}{nF}$, in which F is the Faraday constant and n is the number of electrons transferred per metal atom of atomic weight, A_w, as per the anodic corrosion reaction: $M \rightarrow M^{n+} + n \cdot e^-$.

4.4. RESULTS AND DISCUSSION

The durability of SHS and LIS are presented and discussed in this section, in terms of the morphology and wettability as well as the corrosion resistance before and at several times/cycles of the various mechanical and chemical durability tests. The mechanical durability tests consisted of (a) blade scratch test and (b) water impingent test based on ASTM D4049 [53], and the chemical durability test was based on the ASTM E407 harsh chemical etching accelerated corrosion test [54]. The mechanical tests and their results are discussed in Sections 3.1 and 3.2, while the chemical durability tests are presented in Section 3.3.

4.4.1. **Mechanical durability—Scratch test**

A series of experiments was performed to study the durability of as-fabricated SHS and LIS under blade scratch test. Surfaces were scratched using a 100-μm thick stainless steel razor blade, with sufficient pressure to penetrate through the chemisorbed functionalization agent, destroy the surface texture morphology and reveal the base layer. Each cycle of the scratch test consisted of progressively adding two perpendicular scratches on a square test surface area of 1 cm^2.

Figure 4.1 shows the results of the scratch durability tests on electrodeposited and etched SHS and LIS in terms of the wettability characteristics and corrosion characteristics expressed as Bode plots obtained from EIS, as function of the number scratches on the surfaces. The wetting characteristics of the surfaces were measured as water contact angle (CA) and sliding angle (SA) as shown for the electrodeposited (Figure 4.1a) and etched (Figure 4.1b) SHS and LIS. The inset images in Figure 4.1(a) and 1(b) depict photographs of water droplets on the electrodeposited and etched SHS and LIS prior to scratch testing, demonstrating the high degree of non-wetting

characteristics. Considering the standard deviations, the CA and SA of electrodeposited SHS in Figure 4.1(a) are seen to be above 150° and below 5°, respectively, even after 10 scratches per cm^2. For the electrodeposited LIS, the sliding angle increased slightly from 3° on the unscratched surface to an average of 5° after 10 scratches per cm^2.

Figure 4.1(b) shows that the CA for etched SHS is an average of about 160° for no scratch and remains above 150° for fewer than 8 scratches per cm^2 but decreases to about 140° (hydrophobic) for 10 scratches per cm^2; the SA increased steadily from an average of 3° (unscratched SHS) to an average of 18° for 10 scratches per cm^2. Like electrodeposited LIS, no significant change in the wettability characteristics was observed on etched LIS surfaces with increasing number of scratches, as seen in Figure 4.1(b): CA remained stable at around 90° and SA remained below 5° throughout. From Figure 4.1(a) and 1(b) it is evident that electrodeposited SHS, characterized by more aggressive texturing, is more robust to mechanical wear compared to etched SHS. On the other hand, the preservation of SA below 5°, regardless of the texturing method, points to the excellent self-healing[1] characteristics of both electrodeposited and etched LIS despite the severity of surface damage due to the multiple scratches.

[1] The term self-healing is used in the dissertation to mean the ability of lubricant to move around the surface cavities and act as a filler in the damaged area to restore part or whole of the anti-corrosion property and not to mean reverting the surface to what it was before damage. The term, self-healing, as used here, is also commonly adopted in the literature [24] and [43].

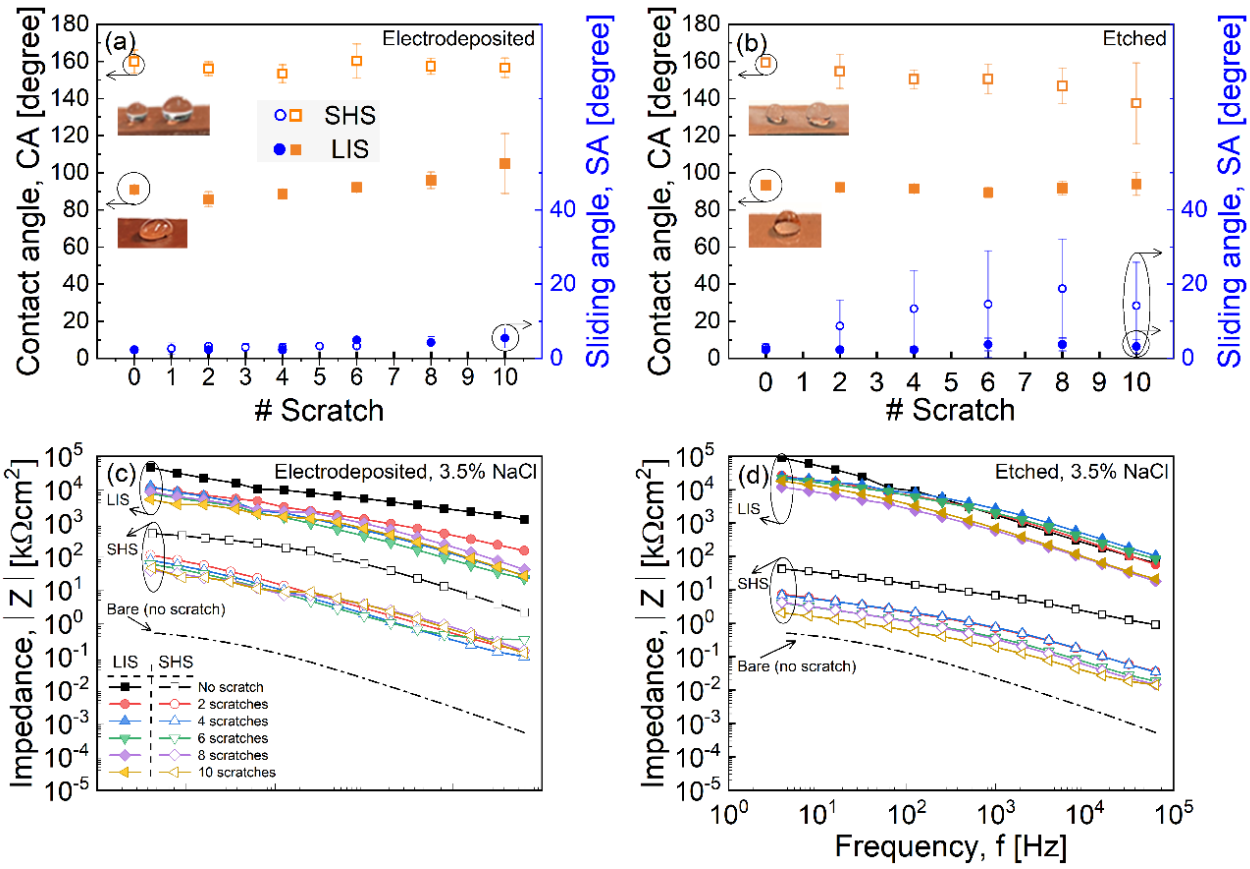

Figure 4.1. Wettability characteristics and (c,d) Bode plots from EIS for electrodeposited and etched SHS and LIS as function of the number of scratches. Photograph insets in (a,b) demonstrate the water contact angle on SHS and LIS.

The impedance modulus value in the low-frequency region of the Bode diagram obtained from EIS has been suggested as a possible predictor of corrosion inhibition characteristics [59]. Figure 4.1(c) shows the effect of number of scratches on the surface impedance of electrodeposited SHS and LIS in 3.5% NaCl corrosive solution. As the first scratches appeared on the surface, the impedance decreased by less than an order of magnitude for both electrodeposited SHS and LIS. After that, the increase in the number of scratches had relatively less effect on the recorded impedance where the characteristic low-frequency impedance values at 5 kHz stayed in a narrow range. On the other hand, as seen in Figure 4.1(d), etched SHS shows a monotonically decreasing surface impedance with the number of surface scratches, when immersed in brine corrosive solution. As shown in [31] the corrosion inhibition mechanism for SHS is predominantly due to the entrapped air pocket between the corrosive solution and the surface which works as a barrier

against corrosion. The steadfast superhydrophobic nature of SHS even after multiple scratches, seen in Figure 4.1(a), is reflected in the only minor change in the impedance of electrodeposited SHS in Figure 4.1(c), whereas the degradation of the non-wetting properties for etched SHS seen in Figure 4.1(b), from superhydrophobic to a hydrophobic, describes the observed decreasing trend of the recorded impedance in Figure 4.1(d). The self-healing non-wetting characteristics of both electrodeposited and etched LIS, seen in Figure 4.1(a) and 1(b), results in the relatively minor decrease in the measured impedance of LIS with increasing number of scratches in Figure 4.1(c) and 1(d).

The corrosion inhibition durability of electrodeposited and etched non-wetting surfaces was further evaluated through linear polarization tests after each cycle of scratches. Figure 4.2(a) presents corrosion rate (CR), calculated as explained in Section 4.2.4, as function of the number scratches for the different nonwetting surfaces. Figure 4.2(a) depicts an increase in CR from zero scratches to the first pair of scratches for all cases, following which both SHS and LIS showed no significant increase in CR, regardless of the texturing method. Furthermore, both electrodeposited and etched LIS outperformed SHS, exhibiting less than one order of magnitude increase in the CR with increasing number of scratches. Among the two texturing methods, etched LIS is seen to have the lowest corrosion rate that is durable for all number of scratches in the test. As a point of reference, throughout the course of the scratch durability test, the corrosion rate for all the nonwetting surfaces was recorded considerably lower than that of bare copper (~0.3 mmPY) shown by the dashed line in Figure 4.2(a), which points to the distinct, durable performance advantage of all the SHS and LIS fabricated using the facile methods presented in this study.

The difference in the performance of LIS and SHS is further illustrated in Figure 4.2(b-e) which displays the optical images of the samples after completion of 10 scratches in the scratch test. The images are taken with a fluorescent filter to visualize the liquid layer. Despite the depth of the scratches, which revealed the underlying copper surface in case of SHS, Figure 4.2(b) and (d), the hierarchical morphology coherency is preserved in the textured surfaces, which is essential for the stability of the non-wetting characteristics of the nonwetting surfaces. Etched SHS (Figure 4.2(d)) shows only minor flaking at the side of the scratch wall whereas electrodeposited SHS shows no sign of surface flaking. Figure 4.3(c) and 3(e) clearly show that the infused lubricant in LIS has wicked into the deep valleys created by the scratches. The infiltrated lubricant in the

micro/nano cavities served as a reservoir to provide self-healing characteristic to LIS, regardless of the facile fabrication method, electrodeposition or etching.

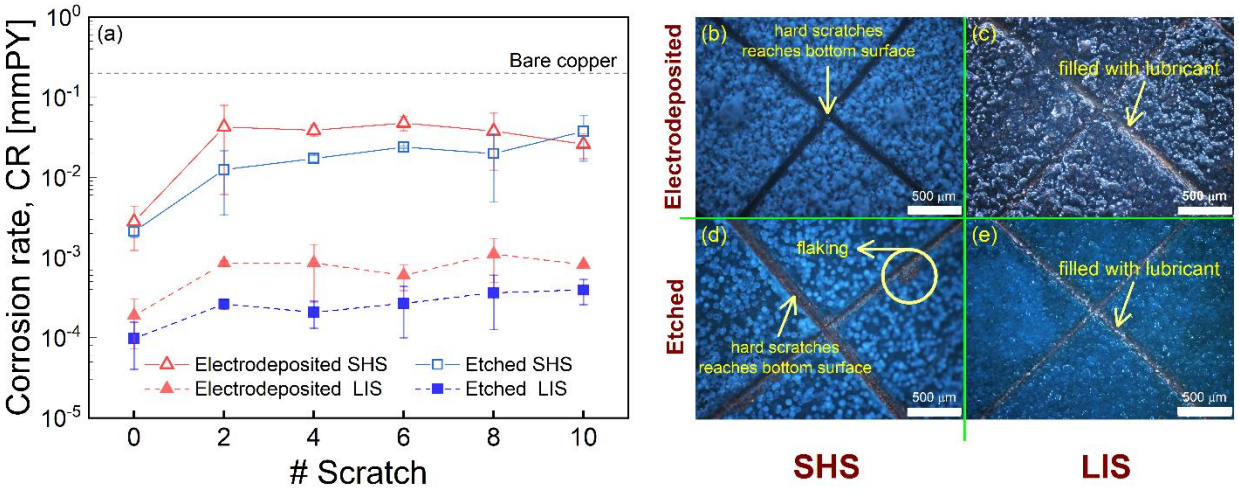

Figure 4.2. (a) Variation of corrosion rate (CR) in 3.5% NaCl aqueous solution at 23°C with the number of razor blade scratches per cm2 on electrodeposited and etched SHS and LIS; Optical images of scratches on (b) electrodeposited SHS, (c) electrodeposited LIS, (d) etched SHS, and (e) etched LIS. Scale bars are 500 µm.

4.4.2. **Mechanical durability—Water jet impingement test**

The results discussed so far demonstrate the excellent durability of the SHS and LIS subject to mechanical wear and damage through the scratch test. Durability of the surfaces under dynamic mechanical shear of water impingement was also studied. The surfaces were placed inclined at an angle of 45° with the horizontal and water jet was issued from a fixed height of 10 cm through a nozzle of diameter 5 mm at two different nozzle pressures of 15 psi and 20 psi. The impingement tests were repeated for 5 cycles of 10 s each, for a total of 50 seconds. The pressure and the impingement conditions were chosen to be harsher than typical application environments such as steam condensation or exposure to a thunderstorm. Considering a thunderstorm, for example, with 1 inch/h heavy rain [61] that equates to 7.06×10^{-6} $m^3/m^2/s$, using the relationship 1 mm of rain fall = 10^{-3} m^3 of water per square meter, and droplets with a maximum diameter of 5 mm (droplet volume = 6.545×10^{-8} m^3/droplet) reaching the ground with a terminal velocity of 9 m/s, the number density of droplets impinging on a surface is obtained as $\frac{7.06\times10^{-6}\ m^3/m^2\cdot s}{6.545\times10^{-8}\ m^3/droplet} = 107.8$ droplet/m^2/s. The kinetic energy density of the impinging water droplets in a thunderstorm with the droplet terminal velocity of 9 m/s is, therefore, $\frac{1}{2}(1000 \times 6.545 \times 10^{-8})(9)^2\ \frac{Joule}{droplet}$.

$107.8\ \frac{\text{droplet}}{\text{m}^2\cdot\text{s}} = 0.286\ \frac{\text{Joule}}{\text{m}^2\cdot\text{s}}$, where the density of water (ρ) is taken to be 1000 kg/m^3. In comparison, the kinetic energy density of the impinging jet of area, A_j, and impingement velocity, v_j, in the water jet impingement test is $\frac{1}{2}\left(\rho A_j v_j\right)v_j^2/A_j$. Relating the impingement jet velocity to the water jet pressure, p_j, using the Bernoulli equation as $v_j = \sqrt{\frac{2p_j}{\rho}}$, the impingement kinetic energy density in the tests evaluates to $1.487 \times 10^6\ \frac{\text{Joule}}{\text{m}^2\cdot\text{s}}$ and $2.290 \times 10^6\ \frac{\text{Joule}}{\text{m}^2\cdot\text{s}}$ for 15 psi and 20 psi impingement pressure, respectively. In other words, 10 s of water impingement at 15 psi and 20 psi mimic exposure to 1.65 years and 2.54 years of thunderstorm environment, respectively.

Figure 4.3 presents durability of the surfaces quantified in terms of the contact angle (CA), sliding angle (SA) and corrosion resistance (CR) as function of the number of water impingement cycles. Figure 4.3a) and 3(b) compare electrodeposited SHS and LIS with etched SHS and LIS for an impingement pressure of 15 psi. Regardless of texturing method, Figure 4.3(a) and 3(b) show that SHS samples demonstrated excellent robustness in CA that remained over 150° even after the fifth impingement cycle. The SA of electrodeposited SHS samples (Figure 4.3(a)) increased with time of impingement reaching 30° while the SA for etched SHS (Figure 4.3(b)) stayed below 10° throughout the test. This can be attributed to the larger variance in the heights of the asperity for the surface fabricated via electrodeposition method compared to the etched SHS. Figure 4.3(a) and 3(b) further show that both electrodeposited and etched LIS exhibited increase in CA with impingement cycles, suggesting removal of lubricant with water impingement and the surfaces approaching the behavior of the underlying SHS. The SA for electrodeposited LIS showed a stepwise increase to above 30° after the first cycle and no significant change thereafter, whereas the SA of etched LIS increased monotonically with impingement cycle. The higher porosity and macro pores grown on top of the surface of the electrodeposited LIS has provided a reservoir of the infused oil with a higher volume compared to the etched LIS and a higher lubricant-solid surface area which offered more surface tension for retention of the lubricant under shear stress. This hypothesizes the observed consistent sliding angle for the electrodeposited LIS after the first cyclein Figure 4.3(a,b).

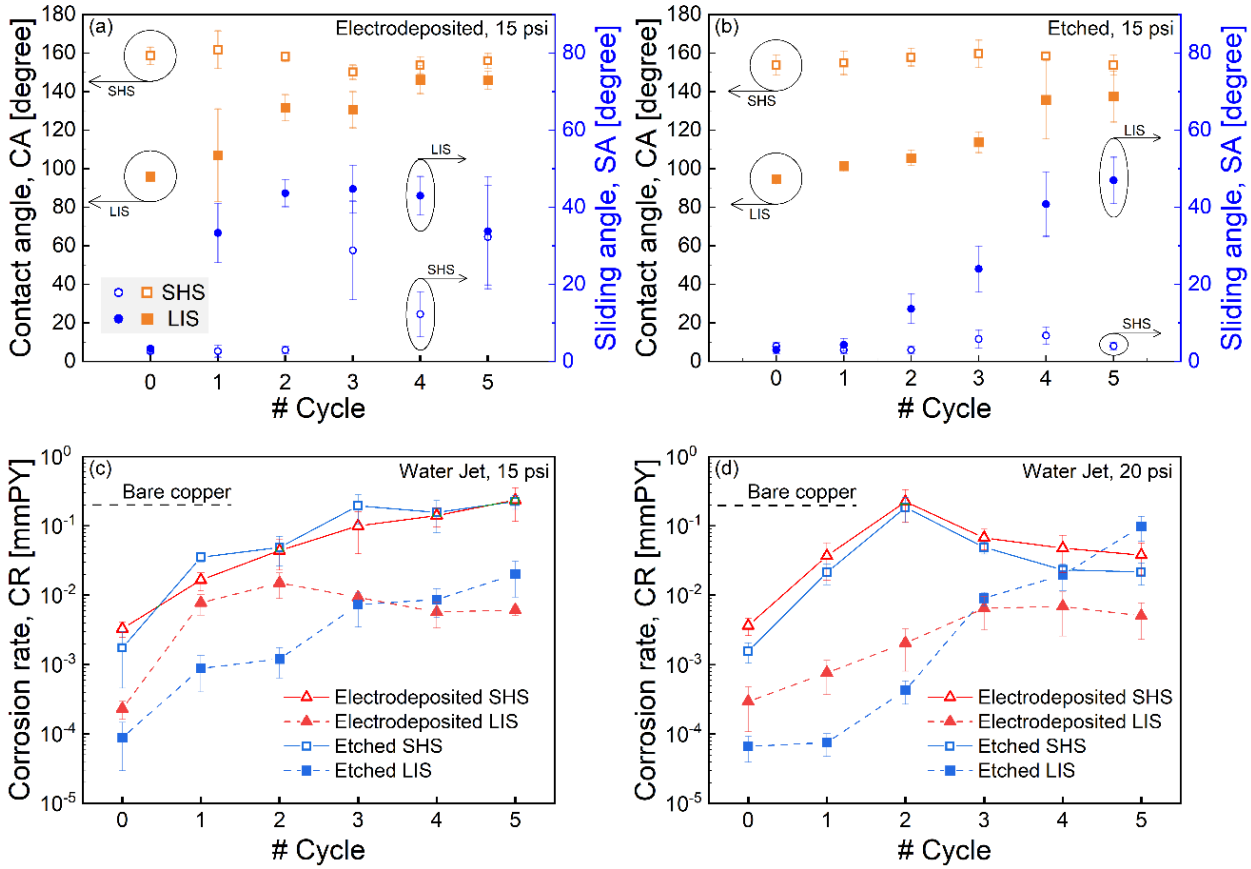

Figure 4.3. Variation of wettability of (a) electrodeposited and (b) etched SHS and LIS as function of water impingement cycles, at water pressure of 15 psi and 10 cm nozzle distance. Effect of water impingement cycles at (c) 15 psi and (d) 20 psi on corrosion rate (CR) of electrodeposited and etched SHS and LIS.

The corrosion rate (CR) of the surfaces in 3.5% NaCl solution was calculated after each cycle of water impingement using linear polarization measurements. Figure 4.3(c) and 3(d) present the variation of CR with water impingement cycle for nozzle pressure of 15 psi and 20 psi, respectively. Also shown for reference is the corrosion rate of bare copper sample (dashed lines) that is not subject to durability testing. The corrosion rate of SHS samples increased monotonically with water impingement cycle at 15 psi (Figure 4.3(c)), approaching that of bare copper after about 5 cycles. At the same pressure, CR of etched LIS also increased but remained at least a decade lower than that of bare copper throughout. The CR of electrodeposited LIS increased sharply after the first cycle and leveled off, maintaining its anti-corrosive behavior comparable to the etched LIS at the end of the five cycles. Similarly, the corrosion rate of all the surfaces increased with

number of cycles for water impingement at 20 psi (Figure 4.3(d)) at a somewhat larger rate compared to the 15 psi impingement tests. Both SHS lost the corrosion inhibition characteristic after 2 cycles, with their CR approaching that of bare copper. Electrodeposited LIS retained corrosion resistance of about 10^{-3} mmPY at 20 psi, while etched LIS degraded in CR to the levels of bare copper by the end of the five cycles of the test. Overall, the results of the water jet impingement test showed that LIS is more robust to SHS in terms of CR; in particular, electrodeposited LIS with a higher oil retention capacity in the multiscale porous structures of the deeper asperities is seen to be most durable throughout the water jet impingement tests.

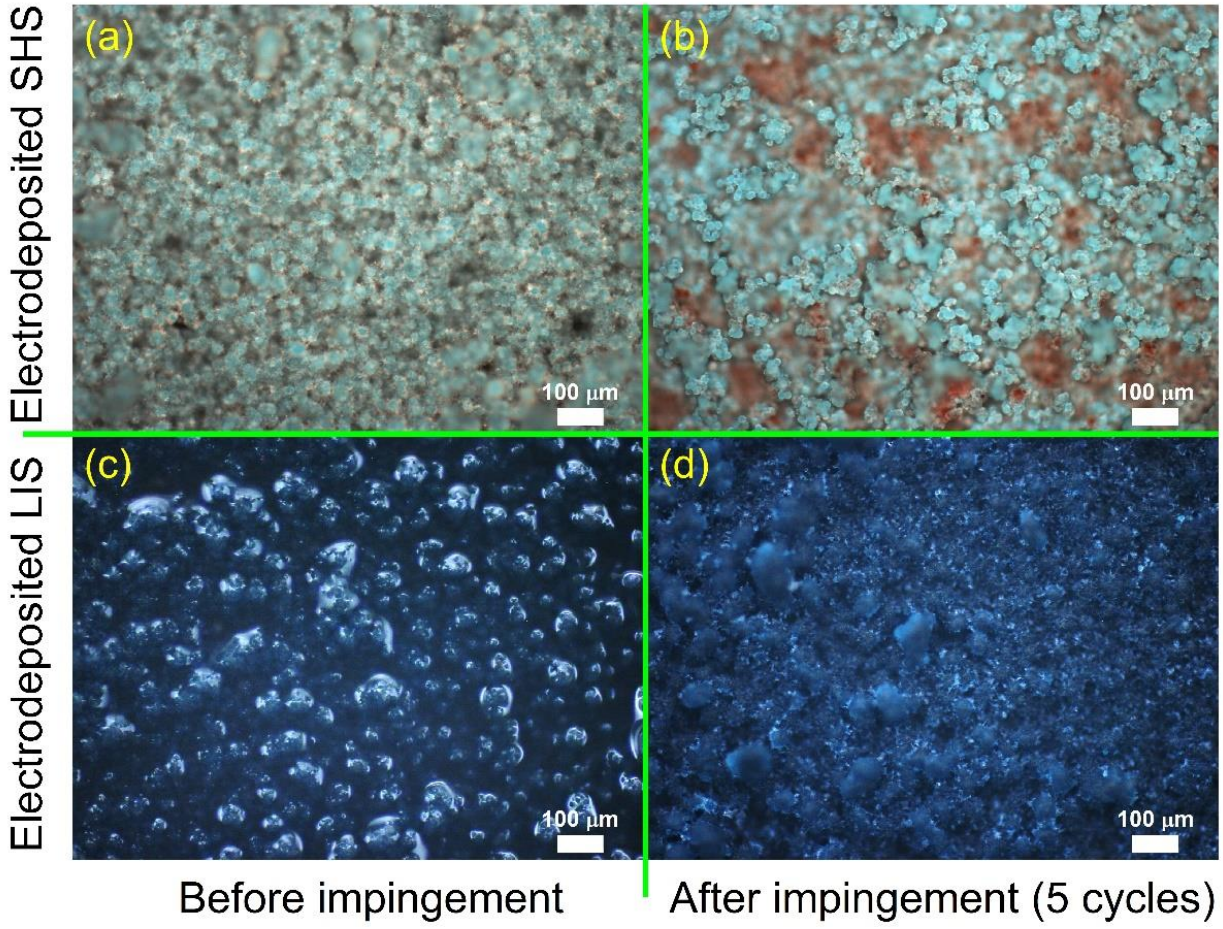

Figure 4.4. Optical images of electrodeposited SHS and LIS (a,c) before and (b,d) after 5 cycles of water jet impingement with a nozzle pressure of 15 psi.

The various surfaces were examined under an optical microscope before and after the 5 cycles of water jet impingement at 15 psi, as presented in Figure 4.4 and 5 for electrodeposited

and etched surfaces, respectively. A more severe damage is evident as the base copper-colored patches on the electrodeposited SHS after the test in Figure 4.4(b) relative to the original surface before the test, Figure 4.4(a). In comparison, etched SHS exhibited relatively less surface damage after the test (Figure 4.5(b)) and remained similar to the original surface (Figure 4.5(a)). The water impingement affected LIS surface morphology as well as the retention of the lubricant layer on the surface, as shown in Figure 4.4(c,d) and 5(c,d) for the electrodeposited LIS and etched LIS, respectively. Both electrodeposited and etched LIS show sign of partial lubricant depletion from the surfaces in the face of shear stress (Figure 4.4(d) and 5(d)) equal to 547 h (22 days) thunderstorm rain which was quantitatively characterized in terms of SA and CR in Figure 4.3. The CR of lubricant infused surfaces stayed one order of magnitude below bare copper CR despite the partial lubricant depletion and mechanical damages.

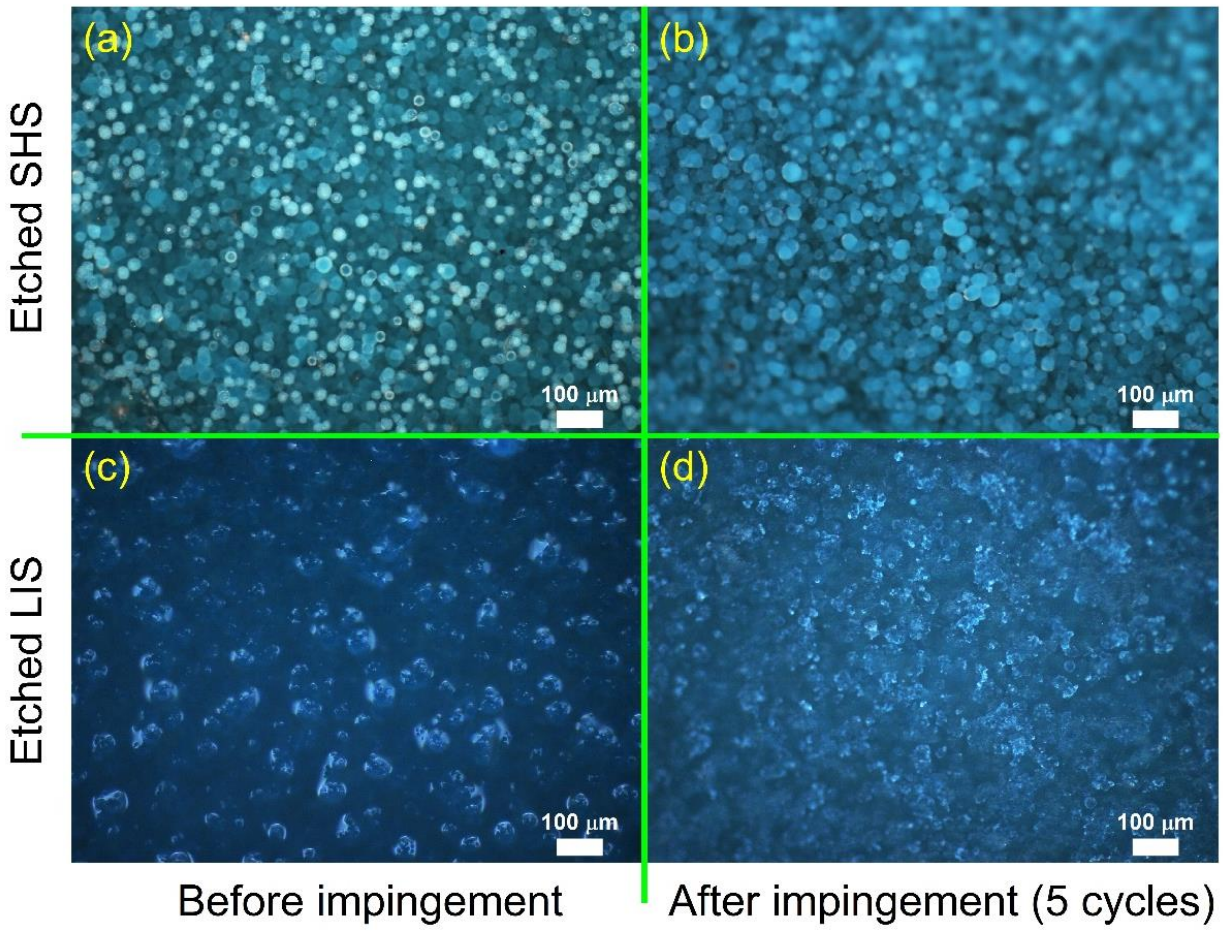

Figure 4.5. Optical images of etched SHS and LIS (a,c) before and (b,d) after 5 cycles of water jet impingement with a nozzle pressure of 15 psi.Chemical durability—Accelerated corrosion test.

Durability of the non-wetting surfaces under chemical stresses was studied using accelerated corrosion testing, following the ASTM E407 [54] standard for microetching. The experiment comprised immersion of the samples in a mixture of ferro chloride and hydrochloric acid as a strong corrosive solution in viscous glycerin to control the heat produced by the exothermic reactions. Unmodified bare copper coupons dissolve completely in this strong corrosive solution in less than 36 hours. The suggested time in the ASTM standard is only up to 60 seconds, but it was extended to 43,800 seconds (12 hours) in this study to deliberately examine the performance of the surfaces under harsher chemical stress environment (see Video S1 in the supporting information).

Wettability of the non-wetting surfaces was characterized at several time instants during the accelerated chemical durability test and the results of the measured CA and SA are shown in Figure 4.6(a) and 6(b) for electrodeposited and etched surfaces, respectively. Additionally, the corrosion rate of the surfaces in 3.5% NaCl aqueous solution was also measured at different times throughout the accelerated chemical durability test as shown in Figure 4.6(c). For both electrodeposited and etched SHS, CA decreased from 160° to an average of 130° at the end of the 12-hour accelerated chemical durability test. On the other hand, SA increased with immersion time, at a higher magnitude for etched SHS compared to electrodeposited SHS. This trend is well-matched with the relative lower CR of the electrodeposited SHS sample in each time step, as depicted in Figure 4.6(c).

The lubricant-infused surfaces maintained their CA throughout the testing, unlike SHS. Regardless of the texturing method, SA for the LIS only increased from ~3° before the test to ~10° up to 660 seconds into the accelerated chemical durability test and to ~30° at the end of the full duration of the experiments. In the case of LIS, the infused oil on top of the surfaces served as a protective barrier against penetration of the corrosive ions into the textured surfaces and maintained its non-wetting characteristic in terms of stable CA and relatively low SA, resulting in a lower CR compared to the bare copper surface and SHS. Regardless of the texturing method, the corrosion rate was more than 2.5 orders of magnitude lower for LIS after 10 minutes of the accelerated chemical durability test, compared to the bare copper sample. LIS showed superior corrosion inhibition even after the full course of the tests, with more than 1.8 orders of magnitude lower CR compared to the bare copper corrosion rate. Additionally, based on linear polarization

measurements on bare copper subject to long-term immersion in brine solution reported in the literature [31], 12 hours immersion time in the harshly corrosive solution in the chemical durability test translates to ~80 days of corrosion in a simulated marine solution of 3.5%NaCl. This suggests that both the electrodeposited and etched LIS are suitable surface modifications for corrosion inhibition in the short and long terms in application environment.

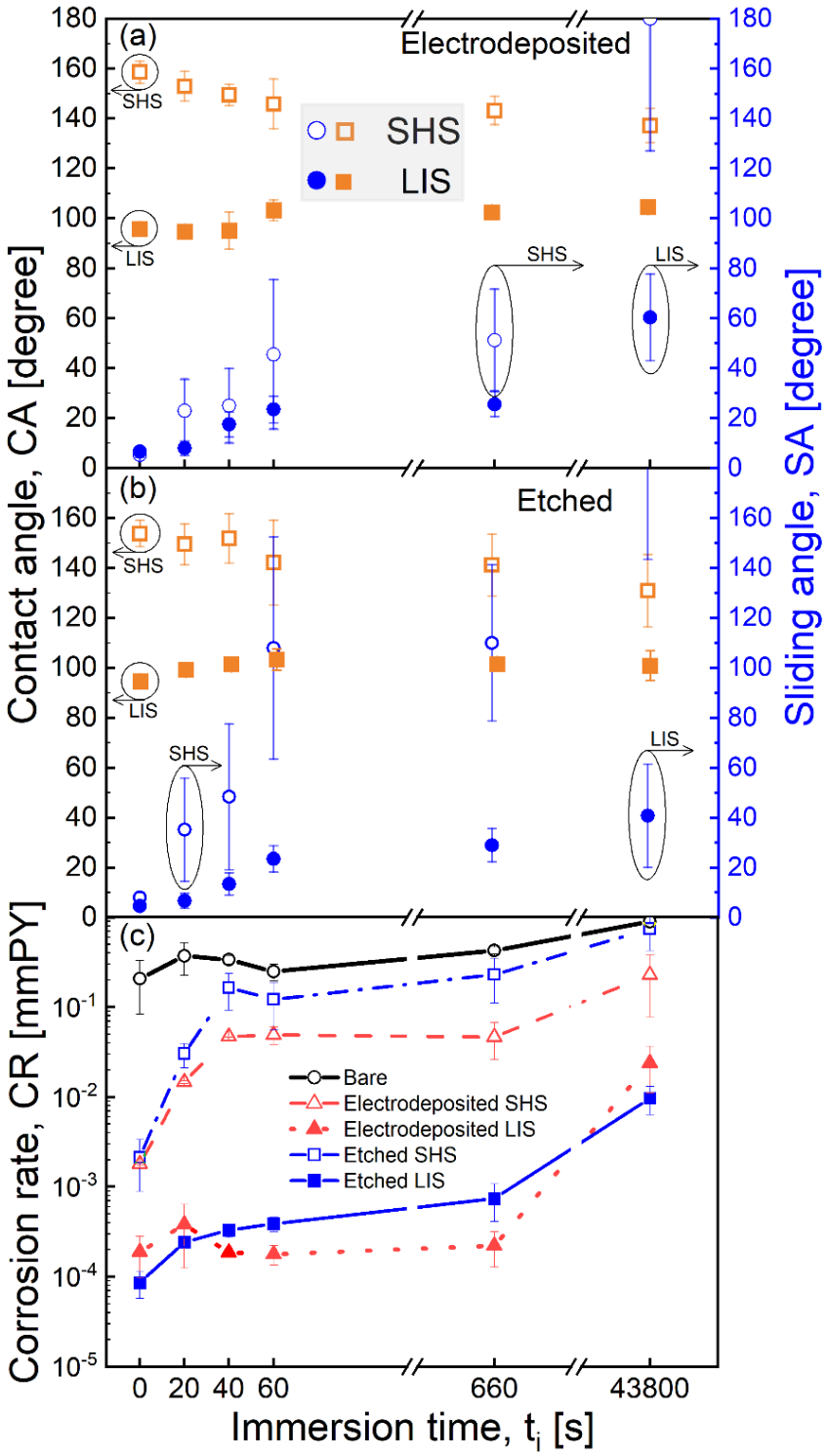

Figure 4.6. Variation of wettability of SHS and LIS fabricated via (a) electrodeposition and (b) etching during the accelerated corrosion test; (c) Variation of CR with immersion time for the nonwetting and the bare copper surfaces.

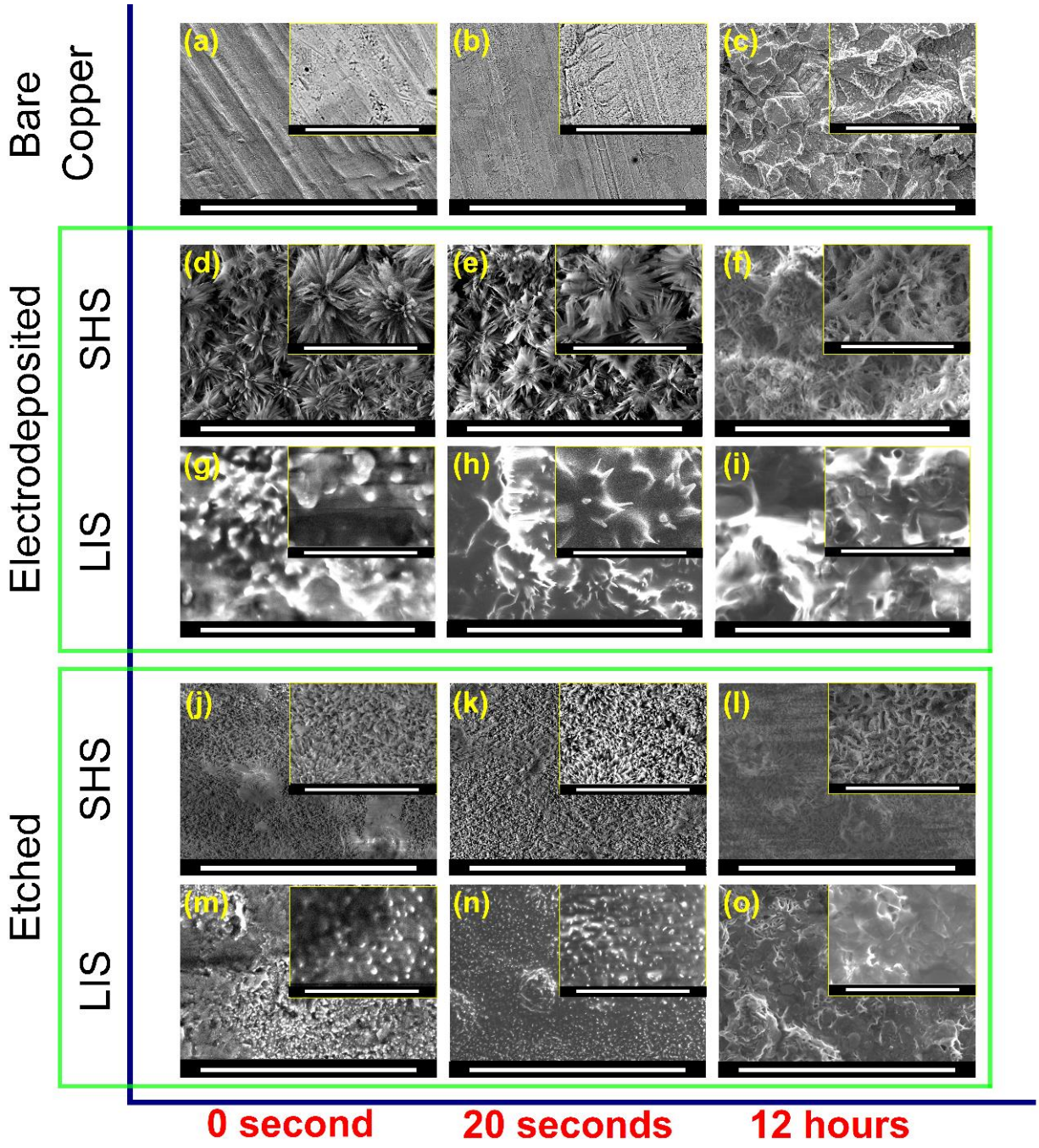

Figure 4.7. SEM image of surfaces before, during, and after accelerated corrosion test: (a-c) bare copper, (d-f) electrodeposited SHS, (g-i) electrodeposited LIS, (j-l) etched SHS, and (m-o) etched LIS. Images from oil infused surfaces (LIS) are blurry due to the limitation of imaging liquid in the microscope. Scale bars are 100 µm for (a-o) and 30 µm for the insets.

The change in morphology of the samples before and after accelerated chemical durability tests was investigated using environmental scanning electron microscopy (SEM). Figure 4.7(a-c)

shows how the smooth surface of the bare copper changed to a rough and etched surface in short immersion times as low as 20 seconds. For similar immersion time, SHS samples, Figure 4.7(d-e,j-k), were more durable in their morphology, but the needle-like asperities before the test, Figure 4.7d) and (j), lost their sharpness at the end of the accelerated chemical durability tests, Figure 7(f) and (l). This morphology change is reflected in the higher SA as discussed in Figure 4.6(a,b). The lubricant-infused samples exhibited similar morphology change at the end of the experiments, as seen by comparing Figure 4.7(h,n) with Figure 4.7(i,o), but with a lesser intensity. This resistance of LIS to morphological change throughout the accelerated chemical durability test correlates to the smaller values of CR and SA compared to SHS, as depicted and discussed in Figure 4.6.

4.5. CONCLUSIONS

In this study, superhydrophobic and slippery lubricant-infused surfaces fabricated by facile electrodeposition and chemical etching methods were evaluated through a unified set of mechanical and chemical durability tests. Mechanical durability tests included blade scratch tests, representative of dry mechanical wear in applications, and water jet impingement, mimicking water impact in applications such as steam condensation on surfaces or exposure of surfaces to hard rain. Chemical durability test was that of accelerated chemical corrosion, intended for use of the surfaces in corrosive environment such as marine applications. Durability was characterized in terms of contact angle and sliding angle, that represent the non-wetting properties, and corrosion resistance. The following are the major findings of this study:

(1) *Scratch Test* — LIS, regardless of the texturing method, demonstrated excellent durability with self-healing characteristics under dry mechanical wear, with sliding angle less than 5° throughout and low corrosion rate of 0.0003–0.0007 mmPY, three orders of magnitude lower than that of bare copper at the end of the test. Electrodeposited SHS with deep multiscale asperity features held durable non-wetting characteristics (CA ≈ 160° and SA ≈ 5°) compared to etched SHS and a corrosion rate of 0.025 mmPY, that is an order of magnitude smaller than that of bare copper, at the end of the test.

(2) *Water Jet Impingement Test* — Both electrodeposited and etched SHS exhibited durable contact angle of ~160° throughout the test, but etched SHS, in particular, maintained a low sliding angle of ~5° at the end of the test. The LIS samples experienced significant lubricant loss under the harsh water jet impingement test leading to increase in the contact angle toward

superhydrophobicity, characteristic of the base surface into which the lubricant was infused, and an undesirable increase in the sliding angle to more than 30°. In terms of corrosion resistance, however, both electrodeposited and etched LIS exhibited one to two orders of magnitude reduction in corrosion rate compared to bare copper at the end of the test.

(3) *Chemical Durability Test* — At the end of the chemical durability tests, LIS, regardless of texturing method, demonstrated superior anti-corrosion behavior with an average of two orders of magnitude lower corrosion rates compared to that for bare copper control sample at the end of the test. In the same environment, etched SHS degraded to the level of bare copper while the electrodeposited SHS maintained one order of magnitude less corrosion rate compared to that of the bare copper control sample throughout the chemical durability test.

The results of the study provide valuable insight, for the first time, into the interactive effects of fabrication method and surface type (SHS vs LIS) on the durability of the surfaces in dry, wet and chemically corrosive environments. The study helps identify appropriate nonwetting surfaces and fabrication methods based on the use environment.

ACKNOWLEDGMENT AND DISCLAIMER

The material reported in this publication is based upon work supported by the U.S. Department of Energy under Award Number DE-FE0031556. This publication was prepared as an account of work sponsored by an agency of the United States Government. Neither the United States Government nor any agency thereof, nor any of their employees, makes any warranty, express or implied, or assumes any legal liability or responsibility for the accuracy, completeness, or usefulness of any information, apparatus, product, or process disclosed, or represents that its use would not infringe privately owned rights. Reference herein to any specific commercial product, process, or service by trade name, trademark, manufacturer, or otherwise does not necessarily constitute or imply its endorsement, recommendation, or favoring by the United States Government or any agency thereof. The views and opinions of authors expressed herein do not necessarily state or reflect those of the United States Government or any agency thereof.

REFERENCES

[1] P. Ragesh, V. Anand Ganesh, S. V. Nair, A.S. Nair, A review on "self-cleaning and multifunctional materials," J. Mater. Chem. A. 2 (2014) 14773–14797. https://doi.org/10.1039/c4ta02542c.

[2] M.J. Kreder, J. Alvarenga, P. Kim, J. Aizenberg, Design of anti-icing surfaces: Smooth, textured or slippery?, Nat. Rev. Mater. 1 (2016) 1–15. https://doi.org/10.1038/natrevmats.2015.3.

[3] M. Cui, B. Wang, Z. Wang, Nature-Inspired Strategy for Anticorrosion, Adv. Eng. Mater. 21 (2019). https://doi.org/10.1002/adem.201801379.

[4] E. Vazirinasab, R. Jafari, G. Momen, Application of superhydrophobic coatings as a corrosion barrier: A review, Surf. Coatings Technol. 341 (2018) 40–56. https://doi.org/10.1016/j.surfcoat.2017.11.053.

[5] R. Deng, T. Shen, H. Chen, J. Lu, H.C. Yang, W. Li, Slippery liquid-infused porous surfaces (SLIPSs): A perfect solution to both marine fouling and corrosion?, J. Mater. Chem. A. 8 (2020) 7536–7547. https://doi.org/10.1039/d0ta02000a.

[6] S. Hatte, R. Pitchumani, Analytical model for drag reduction on liquid-infused structured non-wetting surfaces, Soft Matter. 17 (2021) 1388–1403. https://doi.org/10.1039/d0sm01272f.

[7] S. Hatte, R. Pitchumani, Fractal Model for Drag Reduction on Multiscale Nonwetting Rough Surfaces, Langmuir. 36 (2020) 14386–14402. https://doi.org/10.1021/ACS.LANGMUIR.0C02790.

[8] S. Hatte, R. Pitchumani, Analysis of Laminar Convective Heat Transfer Over Structured Non-Wetting Surfaces, Int. J. Heat Mass Transf. 167 (2021) 120810. https://doi.org/10.1016/J.IJHEATMASSTRANSFER.2020.120810.

[9] S. Hatte, R. Pitchumani, Analysis of convection heat transfer on multiscale rough superhydrophobic and liquid infused surfaces, Chem. Eng. J. 424 (2021) 130256. https://doi.org/10.1016/J.CEJ.2021.130256.

[10] K. Kant, R. Pitchumani, Laminar drag reduction in microchannels with liquid infused textured surfaces, Chem. Eng. Sci. 230 (2021) 116196. https://doi.org/10.1016/J.CES.2020.116196.

[11] C. Cottin-Bizonne, J.L. Barrat, L. Bocquet, E. Charlaix, Low-friction flows of liquid at nanopatterned interfaces, Nat. Mater. 2 (2003) 237–240. https://doi.org/10.1038/nmat857.

[12] S. Rasouli, N. Rezaei, H. Hamedi, S. Zendehboudi, X. Duan, Superhydrophobic and superoleophilic membranes for oil-water separation application: A comprehensive review, Mater. Des. 204 (2021) 109599. https://doi.org/10.1016/j.matdes.2021.109599.

[13] M.A. Gondal, M.S. Sadullah, T.F. Qahtan, M.A. Dastageer, U. Baig, G.H. McKinley, Fabrication and Wettability Study of WO3 Coated Photocatalytic Membrane for Oil-Water Separation: A Comparative Study with ZnO Coated Membrane, Sci. Rep. 7 (2017) 1–10. https://doi.org/10.1038/s41598-017-01959-y.

[14] R. Stoddard, K. Nithyanandam, R. Pitchumani, Steam condensation heat transfer on lubricant-infused surfaces, IScience. 24 (2021) 102336. https://doi.org/10.1016/j.isci.2021.102336.

[15] M. Edalatpour, L. Liu, A.M. Jacobi, K.F. Eid, A.D. Sommers, Managing water on heat transfer surfaces: A critical review of techniques to modify surface wettability for applications with condensation or evaporation, Appl. Energy. 222 (2018) 967–992. https://doi.org/10.1016/j.apenergy.2018.03.178.

[16] X. Feng, L. Jiang, Design and creation of superwetting/antiwetting surfaces, Adv. Mater. 18 (2006) 3063–3078. https://doi.org/10.1002/adma.200501961.

[17] Y. Zheng, X. Gao, L. Jiang, Directional adhesion of superhydrophobic butterfly wings, Soft Matter. 3 (2007) 178–182. https://doi.org/10.1039/b612667g.

[18] 2004_Bohn (pitcher lant)_ Insect aquaplaning Nepenthes pitcher, (n.d.).

[19] A.B.D. Cassie, S. Baxter, Wettability of porous surfaces, Trans. Faraday Soc. 40 (1944) 546–551.

[20] R.N. Wenzel, Resistance of solid surfaces to wetting by water, Ind. Eng. Chem. 28 (1936) 988–994. https://doi.org/10.1021/ie50320a024.

[21] D. Wang, Q. Sun, M.J. Hokkanen, C. Zhang, F.Y. Lin, Q. Liu, S.P. Zhu, T. Zhou, Q. Chang, B. He, Q. Zhou, L. Chen, Z. Wang, R.H.A. Ras, X. Deng, Design of robust superhydrophobic surfaces, Nature. 582 (2020) 55–59. https://doi.org/10.1038/s41586-020-2331-8.

[22] X. Chen, G. Wen, Z. Guo, What are the design principles, from the choice of lubricants and structures to the preparation method, for a stable slippery lubricant-infused porous surface?, Mater. Horizons. 7 (2020) 1697–1726. https://doi.org/10.1039/d0mh00088d.

[23] P. Wang, W. Wei, Z. Li, W. Duan, H. Han, Q. Xie, A superhydrophobic fluorinated PDMS composite as a wearable strain sensor with excellent mechanical robustness and liquid impalement resistance, J. Mater. Chem. A. 8 (2020) 3509–3516. https://doi.org/10.1039/c9ta13281c.

[24] K. Tu, X. Wang, L. Kong, H. Guan, Facile preparation of mechanically durable, self-healing and multifunctional superhydrophobic surfaces on solid wood, Mater. Des. 140 (2018) 30–36. https://doi.org/10.1016/j.matdes.2017.11.029.

[25] K. Liu, L. Jiang, Metallic surfaces with special wettability, Nanoscale. 3 (2011) 825–838. https://doi.org/10.1039/c0nr00642d.

[26] S. Khodakarami, H. Zhao, K.F. Rabbi, N. Miljkovic, Scalable corrosion-resistant coatings for thermal applications, ACS Appl. Mater. Interfaces. 13 (2021) 4519–4534. https://doi.org/10.1021/acsami.0c19683.

[27] X.X. Zhang, S. Cai, D. You, L.H. Yan, H.B. Lv, X.D. Yuan, B. Jiang, Template-free sol-gel preparation of superhydrophobic ORMOSIL films for double-wavelength broadband antireflective coatings, Adv. Funct. Mater. 23 (2013) 4361–4365. https://doi.org/10.1002/adfm.201203059.

[28] P. Dimitrakellis, K. Ellinas, G.D. Kaprou, D.C. Mastellos, A. Tserepi, E. Gogolides, Bactericidal Action of Smooth and Plasma Micro-Nanotextured Polymeric Surfaces with Varying Wettability, Enhanced by Incorporation of a Biocidal Agent, Macromol. Mater. Eng. 306 (2021) 2000694. https://doi.org/10.1002/mame.202000694.

[29] K.A. Emelyanenko, N.A. Sanzharovsky, E. V. Chulkova, A.A. Ganne, A.M. Emelyanenko, L.B. Boinovich, Superhydrophobic corrosion resistant coatings for copper via IR nanosecond laser processing, Mater. Res. Express. 5 (2018) 115001. https://doi.org/10.1088/2053-1591/aadc16.

[30] E. Yu, S.C. Kim, H.J. Lee, K.H. Oh, M.W. Moon, Extreme wettability of nanostructured glass fabricated by non-lithographic, anisotropic etching, Sci. Rep. 5 (2015) 1–6. https://doi.org/10.1038/srep09362.

[31] S.M.A. Mousavi, R. Pitchumani, A Study of Corrosion on Electrodeposited Superhydrophobic Copper Surfaces, Corros. Sci. 186 (2021) 109420. https://doi.org/10.1016/j.corsci.2021.109420.

[32] J. Liu, X. Fang, C. Zhu, X. Xing, G. Cui, Z. Li, Fabrication of superhydrophobic coatings for corrosion protection by electrodeposition: A comprehensive review, Colloids Surfaces A Physicochem. Eng. Asp. 607 (2020) 125498. https://doi.org/10.1016/j.colsurfa.2020.125498.

[33] Y. Zhang, D. Ge, S. Yang, Spray-coating of superhydrophobic aluminum alloys with enhanced mechanical robustness, J. Colloid Interface Sci. 423 (2014) 101–107. https://doi.org/10.1016/j.jcis.2014.02.024.

[34] Y. Wan, M. Chen, W. Liu, X.X. Shen, Y. Min, Q. Xu, The research on preparation of superhydrophobic surfaces of pure copper by hydrothermal method and its corrosion resistance, Electrochim. Acta. 270 (2018) 310–318. https://doi.org/10.1016/j.electacta.2018.03.060.

[35] L. Xu, D. Zhu, X. Lu, Q. Lu, Transparent, thermally and mechanically stable superhydrophobic coating prepared by an electrochemical template strategy, J. Mater. Chem. A. 3 (2015) 3801–3807. https://doi.org/10.1039/c4ta06944g.

[36] S. Barthwal, Y.S. Kim, S.H. Lim, Mechanically robust superamphiphobic aluminum surface with nanopore-embedded microtexture, Langmuir. 29 (2013) 11966–11974. https://doi.org/10.1021/la402600h.

[37] R. Jain, R. Pitchumani, Facile Fabrication of Durable Copper-Based Superhydrophobic Surfaces via Electrodeposition, Langmuir. 34 (2017) 3159–3169. https://doi.org/10.1021/ACS.LANGMUIR.7B02227.

[38] Z. Geng, J. He, An effective method to significantly enhance the robustness and adhesion-to-substrate of high transmittance superamphiphobic silica thin films, J. Mater. Chem. A. 2 (2014) 16601–16607. https://doi.org/10.1039/c4ta03533j.

[39] T. Simovich, A.H. Wu, R.N. Lamb, Energy efficient one-pot synthesis of durable superhydrophobic coating through nylon micro-rods, Appl. Surf. Sci. 295 (2014) 203–206. https://doi.org/10.1016/j.apsusc.2014.01.040.

[40] J. Groten, J. Rühe, Surfaces with combined microscale and nanoscale structures: A route to mechanically stable superhydrophobic surfaces?, Langmuir. 29 (2013) 3765–3772. https://doi.org/10.1021/la304641q.

[41] Z. Chu, S. Seeger, Robust superhydrophobic wood obtained by spraying silicone nanoparticles, RSC Adv. 5 (2015) 21999–22004. https://doi.org/10.1039/c4ra13794a.

[42] X. Tang, F. Yu, W. Guo, T. Wang, Q. Zhang, Q. Zhu, X. Zhang, M. Pei, A facile procedure to fabricate nano calcium carbonate-polymer-based superhydrophobic surfaces, New J. Chem. 38 (2014) 2245–2249. https://doi.org/10.1039/c3nj01592k.

[43] H. Wang, H. Zhou, A. Gestos, J. Fang, T. Lin, Robust, superamphiphobic fabric with multiple self-healing ability against both physical and chemical damages, ACS Appl. Mater. Interfaces. 5 (2013) 10221–10226. https://doi.org/10.1021/am4029679.

[44] H. Jin, X. Tian, O. Ikkala, R.H.A. Ras, Preservation of superhydrophobic and superoleophobic properties upon wear damage, ACS Appl. Mater. Interfaces. 5 (2013) 485–488. https://doi.org/10.1021/am302541f.

[45] A. Davis, Y.H. Yeong, A. Steele, E. Loth, I.S. Bayer, Nanocomposite coating superhydrophobicity recovery after prolonged high-impact simulated rain, RSC Adv. 4 (2014) 47222–47226. https://doi.org/10.1039/c4ra08622h.

[46] L. Xiong, L.L. Kendrick, H. Heusser, J.C. Webb, B.J. Sparks, J.T. Goetz, W. Guo, C.M. Stafford, M.D. Blanton, S. Nazarenko, D.L. Patton, Spray-deposition and photopolymerization of organic-inorganic thiol-ene resins for fabrication of superamphiphobic surfaces, ACS Appl. Mater. Interfaces. 6 (2014) 10763–10774. https://doi.org/10.1021/am502691g.

[47] W.H. Huang, C.S. Lin, Robust superhydrophobic transparent coatings fabricated by a low-temperature sol-gel process, Appl. Surf. Sci. 305 (2014) 702–709. https://doi.org/10.1016/j.apsusc.2014.03.179.

[48] H. Zou, S. Lin, Y. Tu, G. Liu, J. Hu, F. Li, L. Miao, G. Zhang, H. Luo, F. Liu, C. Hou, M. Hu, Simple approach towards fabrication of highly durable and robust superhydrophobic cotton fabric from functional diblock copolymer, J. Mater. Chem. A. 1 (2013) 11246–11260. https://doi.org/10.1039/c3ta12224g.

[49] L. Liu, F. Xu, L. Ma, Facile fabrication of a superhydrophobic Cu surface via a selective etching of high-energy facets, J. Phys. Chem. C. 116 (2012) 18722–18727. https://doi.org/10.1021/jp302794p.

[50] M. Villegas, Y. Zhang, N. Abu Jarad, L. Soleymani, T.F. Didar, Liquid-Infused Surfaces: A Review of Theory, Design, and Applications, ACS Nano. 13 (2019) 8517–8536. https://doi.org/10.1021/acsnano.9b04129.

[51] S.P. Dalawai, M.A. Saad Aly, S.S. Latthe, R. Xing, R.S. Sutar, S. Nagappan, C.S. Ha, K. Kumar Sadasivuni, S. Liu, Recent Advances in durability of superhydrophobic self-cleaning technology: A critical review, Prog. Org. Coatings. 138 (2020) 105381. https://doi.org/10.1016/j.porgcoat.2019.105381.

[52] A. Milionis, E. Loth, I.S. Bayer, Recent advances in the mechanical durability of superhydrophobic materials, Adv. Colloid Interface Sci. 229 (2016) 57–79. https://doi.org/10.1016/j.cis.2015.12.007.

[53] Standard Test Method for Determining the Resistance of Lubricating Grease to Water Spray, (2020) ASTM D4049-20.

[54] Standard Practice for Microetching Metals and Alloys, (2015) ASTM E407-07.

[55] R. Jagdheesh, M. Diaz, S. Marimuthu, J.L. Ocaña, Hybrid laser and vacuum process for rapid ultrahydrophobic Ti-6Al-4 V surface formation, Appl. Surf. Sci. 471 (2019) 759–766. https://doi.org/10.1016/j.apsusc.2018.12.047.

[56] ASTM International, Standard Practice for Conventions Applicable to Electrochemical Measurements in Corrosion Testing, (2019) ASTM G3-14.

[57] M. Stern, A.L. Geaby, Electrochemical Polarization, J. Electrochem. Soc. 104 (1957) 56. https://doi.org/10.1149/1.2428496.

[58] A.J. Bard, L.R. Faulkner, Fundamentals and applications, Electrochem. Methods. 2 (2001) 580–632.

[59] A.V. Rao, S.S. Latthe, S.A. Mahadik, C. Kappenstein, Mechanically stable and corrosion resistant superhydrophobic sol-gel coatings on copper substrate, Appl. Surf. Sci. 257 (2011) 5772–5776. https://doi.org/10.1016/j.apsusc.2011.01.099.

[60] M.A. Nearing, J.M. Bradford, R.D. Holtz, Measurement of Force vs. Time Relations for Waterdrop Impact, Soil Sci. Soc. Am. J. 50 (1986) 1532–1536. https://doi.org/10.2136/sssaj1986.03615995005000060030x.

Chapter 5. Long-term Corrosion Stability of Nonwetting Copper Surfaces

The work reported in this chapter is the basis for the following journal publication currently in re view:

S.M.A. Mousavi and R. Pitchumani. "Long-Term Corrosion Stability of Nonwetting Copper Surfaces," In Review (2021).

5.1. ABSTRACT

Superhydrophobic surfaces (SHS) and lubricant-infused surfaces (LIS) are two classes of materials that have drawn attention due to their advanced functional properties including corrosion inhibition. There is a conspicuous lack of corrosion study of SHS and LIS and their fabrication and material parameters in the environment of the applications, especially under flow conditions and higher temperatures and over long duration. Considering the knowledge gap, this work offers a comprehensive treatment in the rational design and systematic study of copper SHS and LIS. Two facile texturing processes, electrodeposition and etching, are presented as representative of additive and material removal methods of fabrication. For each of the fabrication routes, two different functionalization agents were selected along with two types of lubricant, one from the PFPE group and one from the PDMS group. For the first time, the long-term stability of the non-wetting surface was studied under both static and dynamic turbulent conditions. Additionally, the study spans a range of temperature from 23°C–90°C from which an Arrhenius model is developed for the corrosion rate of as-fabricated non-wetting surfaces. All in all, the study encompasses 234 tested surfaces and over 1,021 measurements, providing for the first time a comprehensive view of SHS and LIS by juxtaposing a full factorial combination of texturing method, functionalization agents, lubricants, and tests in various conditions, to elucidate the long-term performance characteristics of the advanced functional nonwetting surfaces and to provide valuable insight into their design for various applications.

Keywords: superhydrophobicity; lubricant infused surface; turbulent flow; long-term durability; corrosion; high temperature

5.2. INTRODUCTION

Surface wettability had a huge impact on our lives, from printing inks to the waxy coating used to protect cars. Throughout the years and for different purposes, the wetting, spreading, adhesion, and dewetting of a liquid on a solid have been optimized [1]. Some application includes adhesion of paint to surfaces, antifouling coatings for marine constructions [2,3], stain-resistant appliances [4–6], aviation sector anti-icing surfaces [7]. Also, self-cleaning metallic materials were widely explored for the reduction of biofouling [8,9], mineral scaling [10,11], and corrosion [12–14]. The vitality for looking into anti-fouling metallic surfaces naturally arises from their wide usage. For example, one of the hefty and costly problems for industries around the world is the direct and indirect cost of corrosion of metallic surfaces that costs equal to 3-5% of the global gross national products [15,16]. Metallic surfaces, including copper, are directly tied to our modern life for their omnipresence in condensers and evaporators of refrigerators or air conditioners, their key role in electricity generation in power plants heat exchangers, and their use in the marine industry. Therefore, corrosion inhibition of copper surfaces was the center of attention and was improved via various methods [12,17]. Adsorption of species, including corrosive ions, on a surface, can theoretically be prevented by reducing the wetted solid-electrolyte contact area and therefore mitigating different types of fouling including corrosion [18]. Pursuant to that and inspired by *lotus* leaf and *Nepenthes* pitcher-plant two classes of superhydrophobic surfaces (SHS) and lubricant-infused surfaces (LIS) have been adopted to mitigate fouling including corrosion. SHS with high contact angle above 150° and a low roll-off angle below 10° provides an air cushion between the electrolyte and surface, similarly, LIS with a slippery lubricated surface with a sliding angle below 10° provides protection against fouling. Wang et al. fabricated liquid-infused aluminum to ease the adherence of sulfate-reducing bacteria in a static seawater condition [15]. Song et al. texture Al substrate by electrochemical anodizing with ordered pores of several tens of nanometers, and further transformed it into a lubricant-infused surface by immersing the surface in methyl silicone oil, fluoroalkyl silane, and finally Krytox104 oil, which demonstrated excellent anti-corrosion properties in a 3.5% saline solution at low temperature [17]. Dealloying CuZn Shi et al. dealloyed CuZn in CuSO4 bath, later added dodecanethiol by a chemical vapor deposition process, and lastly infused the surface with perfluorinated lubricant for corrosion study in seawater 3% salinity. They reported lower corrosion current density by up to two orders of magnitude compared to the bare

CuZn at room temperature [16]. Xiang et al. coated mild steel with Zn-Ni via electroplating at 4 A·dm−2 at 35 °C for 20 min. After that, the samples were immersed in fluoroalkyl silane solution and then lubricated with Krytox100 oil. Later, the corrosion behavior was studied in 3.5 wt% NaCl solution at room temperature. The mild steel LIS was reported to show about three orders of magnitude decrease in corrosion current compared to a bare iron [18]. Qiu et. al. grown micro/nanoscale copper via electrodeposition for 10 minutes at -1000 mV on Cu/Al and Al/Mg alloys, to use it as a catalyzer for growing carbon fiber. To develop hydrophobic carbon fibers, the textured substrates were placed in a tube furnace at 350°C in an acetylene gas flow and further impregnated with lubricant. In a 3.5% NaCl solution at room temperature, the lubricant-infused surface had a higher corrosion impedance than the hydrophobic surface without liquid infusion [19].

In general, the fabrication of an SHS requires two steps: texturing and applying a functional group to the surface in order to reduce the surface energy. Besides, fabrication of a LIS requires three steps: texturing, functionalization, and lubricant impregnation. However, the first texturing step is not necessary for the fabrication of LIS, but it is almost accepted as a crucial requirement as it is known a textured surface considerably improves the LIS interface and promotes lubricant retention [19]. Several reviews have been dedicated to SHS and LIS fabrication as well as specific applications [19–21]. Various texturing method has been practiced including templating, sol-gel method [17,22] , electrospinning [23], laser etching [24], hydrothermal synthesize [25], anodization, plasma techniques [26], and electrodeposition [20,27]. In her review J. Aizenberg put the texturing methods into two categories *additive* and *removal* methods [28]. C. Neto reviewed LIS fabrication to have two main types of lubricants dominating the literature: perfluoropolyethers (PFPEs) and linear polydimethylsiloxane PDMS, also known as silicone oil or dimethicone [29].

Despite all the great effort reported in the literature, there is a conspicuous lack of study of SHS and LIS in an environment of the application, especially flow conditions and higher temperatures. In the light of the knowledge gap, and as mentioned in recent works [19,29,30], this article offers a very comprehensive approach in the rational design and a systematic study of both SHS and LIS. Two facile texturing processes are proposed to cover both additive and removal methods. Moreover, two different functionalization agents were selected along with two types of lubricant, one from PFPEs group and one from PDMS group. Through parametric tests, the effect of functionalization time on corrosion inhibition performance of the as-fabricated non-wetting

surfaces along bare copper control case was studied. There has been increasing attention to corrosion inhibition property of SHS and LIS in static or limited to laminar flow conditions [10,17,31,32], however, the environment of application is often turbulent, Herein, for the first time, the long-term stability of the non-wetting surface was studied at both static and dynamic turbulent conditions. The dynamic tests were done in a novel yet simple in-house built setup. This setup allows electrochemically measuring corrosion inhibition properties whereas the laminar flow test in literature often used weight method, which suffers from precision. SHS and LIS may experience weight change due to loss of material which is not necessarily the result of added/removed material from corrosion reactions. Additionally, for the first time, based on parametric tests an Arrhenius model is developed for the corrosion rate of the selected non-wetting surfaces on a range of temperature 23°C-90°C. All in all, this study not only offers facile methods of fabrication of advance functional surfaces, but also with 234 coupons and over 1,021 measurements provide for the first time a comprehensive view to the SHS and LIS by juxtaposing a rational selection over a gamut of texturing method, functionalization agents, lubricants, and tests in various conditions including stationary, dynamic and different temperatures. This is thought to provide a multifacet perspective to the emerging non-wetting surfaces and valuable insight into the advancement of such surfaces for various environments.

The article is organized as follows: the experimental methods of fabrication and characterization are described in the next section. The results of the study are presented and discussed in Section 3 and the principal conclusions are summarized in Section 4.

5.3. EXPERIMENTAL METHODS

5.3.1. **Materials and reagents**

Plain multipurpose 110 copper sheet was purchased from McMaster, USA. Sulfuric acid (H_2SO_4), hydrochloric acid (HCl), analytical-grade copper sulfate ($CuSO_4$, 99+%), acetone (C_3H_{6O}, 99.5+%), methanol (CH_3OH, 99.8+%), ethanol (C_2H_5OH, 99.8+%), n-Hexadecyl mercaptan ($C_{16}H_{34}S$, 90%), and stearic acid ($CH_3(CH_2)_{16}CO_2H$, 97%) were purchased from Fisher Scientific (Pittsburgh, PA, USA) and used as-received without any further purification. Hydrogen peroxide solution (H_2O_2, 3%) was purchased from Sigma-Aldrich (St. Louis, MO, USA).

Krytox™104 silicon lubricant was purchased from Miller-Stephenson Chemical Co. (Danbury, CT, USA), and Dowsil™510 Fluid was purchased from DuPont (Wilmington, Delaware, USA).

5.3.2. **Fabrication of SHS and LIS**

Surface texturing is the first step in the fabrication of non-wetting surfaces and was approached via two methods in this work: chemical etching, a material *removal* method, and electrodeposition, an *additive* method. The as-received copper sheet was cut into coupons of 1×3 cm, which then degreased in a sonication bath of methanol, acetone, and DI-water for ten minutes each, sequentially.

In the material removal method, the roughness features were carved into the surface via chemical *etching* in an aqueous solution of 0.02 M hydrochloric acid and 0.05 M hydroperoxide (6:25:19 v/v/v mixture of DI-Water:H_2O_2 (3%):HCl (12M)). The cleaned and cut coupons were submerged in the etchant solution for 20 minutes.

In the additive method, multiscale asperities were grown on top of the copper surface by a three-electrode, two-step *electrodeposition* process [12] using an AUTOLAB PGSTAT128N electrochemical station (ECO Chemie, Utrecht, The Netherlands). A platinum mesh was used as the counter electrode and a copper sheet as the reference electrode. De-aerated aqueous solution of 1M $CuSO_4$ and 0.5M H_2SO_4 was used as the electrolyte. The two-step electrodeposition process was initiated by applying –1.1 V for 5 minutes to the copper sample as the working electrode followed by 10-second electrodeposition at –0.15 V as the second step. The second deposition served to further stabilize the first coating onto the surface. The electrodeposition process involves the reduction of copper cations to solid copper deposited on the surface per $Cu^{2+} + 2e^- \rightarrow Cu$. Therefore, assuming a uniform coating, the deposition thickness, is estimated as $h = QM/nF\rho A$, where Q is the charge transferred in coulomb throughout the deposition ($Q = i.\,dt$), M is the molar weight of copper, n is the number of transferred electrons in the copper reduction reaction, F is the Faraday constant, A is the surface area of the deposition, ρ is the density of the deposited copper. Accordingly, 5 minutes of first stage electrodeposition was chosen to produce a coating with about 30 μm thickness.

Thereafter, the coupons fabricated via both electrodeposition and etching methods undergo the same processes. The textured coupons were rinsed with a copious amount of DI-water and

were stored in a vacuum oven at 110°C overnight to dry. It is to be noted that this step can be skipped and air drying is enough as well. Furthermore, the textured surfaces were functionalized by immersion in 0.02 mol/L either stearic acid-methanol solutions at room temperature or 0.02 mol/L mercaptan-ethanol solution at 60 °C. As part of a systematic study to investigate the influence of functionalizing time on corrosion behavior, the functionalizing period was varied from 1 hour to 24 hours. The chemisorption of the functionalization agent reduces the surface energy of the textured surfaces to become superhydrophobic surfaces (SHS).

Another class of non-wetting surfaces was fabricated by lubricant infusion process. The as-fabricated SHS has proper surface chemistry in order to host a lubricant that is immiscible with the foreign/attacking liquid, here brine solution. Therefore, lubricant-infused surfaces (LIS) were fabricated by infusing the SHS with selected lubricant oil. Drops of either Dowsil^{TM} Fluid (reported viscosity 500 cSt at 25°C) or Krytox104^{TM} (reported viscosity 177 at 20 °C [29] and 60 cSt at 40°C) were placed onto the SHS. As the last step, the coupons were hung vertically for at least 20 minutes to allow the lubricant to wick into the interasperity areas and to drain any surplus oil. The fabrication process is summarized in Figure 5.1(A) schematic.

5.3.3. **Morphology and wettability characterization**

A stylus profilometer (Dektak XT Bruker; Massachusetts, USA) with a 2 µm radius stylus tip working at 10 mg force with 0.1 µm scan resolution was utilized to evaluate the surface roughness. For 3D reconstruction of the surfaces, a white light scanning confocal microscope (Keyence model VK-X, Osaka, Japan) was employed. A field-emission scanning electron microscope, SEM, (LEO/Zeiss 1550, Germany) equipped with EDX (Oxford, UK) was used to highlight surface morphology and chemical composition working at 20 kV acceleration voltage. The optical picture of the surfaces was taken using a Nikon Eclipse LV100ND Microscope with an epifluorescence filter (Nikon Instruments Inc.). A goniometer (RAMÉ-hart model 590, New Jersey, USA) was used to measure surface wettability in terms of water contact and sliding angle on the surfaces. A 10 µl sessile DI-water droplet was placed at five different points on each sample to calculate the average contact angle (CA) and the error bars around it. The sliding angle (SA) was recorded via the tilting cradle method where the angle at which a 25 µl DI-water droplet rolls of an SHS is marked. The

SA for a droplet on LIS was recorded when both the rear and front contact lines of the droplet started to slide.

5.3.4. **Dynamic fouling test experimental design**

There has been increasing attention to the non-wetting surfaces and static or laminar flow condition experiments are used to characterize such surfaces. However, the flow conditions in the application environment are frequently turbulent. Therefore, here a simple yet novel dynamic condition test setup was designed and called drum setup hereafter. A cylindrical stationary tank with radius b and a co-centric inner rotating drum with radius a comprise the drum arrangement, Figure 5.1(B). An aluminum rod was manufactured to connect the drum to a controlled motor shaft. Aluminum was chosen for this purpose because it has a high modulus of elasticity to bear the high rotation rate stresses and a low weight to impose less undesired momentums. The coupons are mounted on the revolving drum's outside surface and immersed in a prepared marine simulated corrosive solution containing 3.5 % sodium chloride. As seen in Figure 5.1(B), the drum configuration mimics a rotating-Couette flow, and the Reynolds number is determined as in $Re_{\emptyset} = \frac{\rho.\Omega a.(b-a)}{\mu}$ where ρ is the fluid density, Ω_a is the rotational speed of the inner rotating drum, and μ is the fluid viscosity.

5.3.5. **Corrosion inhibition characterization**

To assess the corrosion inhibition of the samples, three-electrode (reference, counter, and working electrode) electrochemical tests were performed. As a reference electrode, Ag/AgCl (NaCl saturated) was placed less than 3 mm distance from the sample surface (working electrode) to minimize the solution resistance interference in the measurement. A counter electrode made of platinum mesh was put equidistant from the other two electrodes. A potentiostat device, Solarton Inc. (model 1240 PA, USA), was used to record potentiodynamic polarization (PDP) curves and linear polarization (LP) test data. After 40 minutes of immersion in corrosive solution, PDP curves were scanned from -300 mV to +300 mV with respect to open circuit potential. After 5 minutes of stabilization, LP tests were scanned in the range of -20 mV to +20 mV. Per ASTM G3-14 (2019) scan rates of 1 mV/s and 1/6 V/h were used for the PDP and LP test, respectively.

5.3.6. **Data reduction**

The PDP curve and the LP scan from corrosion tests were further reduced to corrosion rate and polarization resistance, respectively. A Tafel extrapolation approach was utilized to quantitatively determine the corrosion parameters from the measured PDP data. The PDP test data was plotted in a semi-log *j-v* form to obtain Tafel plot and further drive corrosion potential (E_{corr}), corrosion current density (j_{corr}), and corrosion rate (CR). The coordinate of the intersection of the asymptotes to the cathodic and anodic region of the Tafel plot is recorded as β_{cat} and β_{an}. After that CR in mm/year (mmPY) was calculated as $CR = \frac{3276.6 j_{corr} E_w}{\rho}$ where ρ is the metal density and E_w is equivalent weight defined as $\frac{A_w}{nF}$, in which A_w is atomic weight, F is the Faraday constant and n is the number of electrons transferred per metal atom, according to the anodic corrosion reaction: $M \rightarrow M^{n+} + n.e^-$.

The linear polarization potential-current density profile was used to calculate corrosion potential (E_{corr}) and polarization resistance (R_p). E_{corr} is obtained as the intersection of the $j = 0$ line and the scanned *v-j* profile. After that R_p, was recorded as the slope of a linear fit at ±10 mV around E_{corr} on the LP profile.

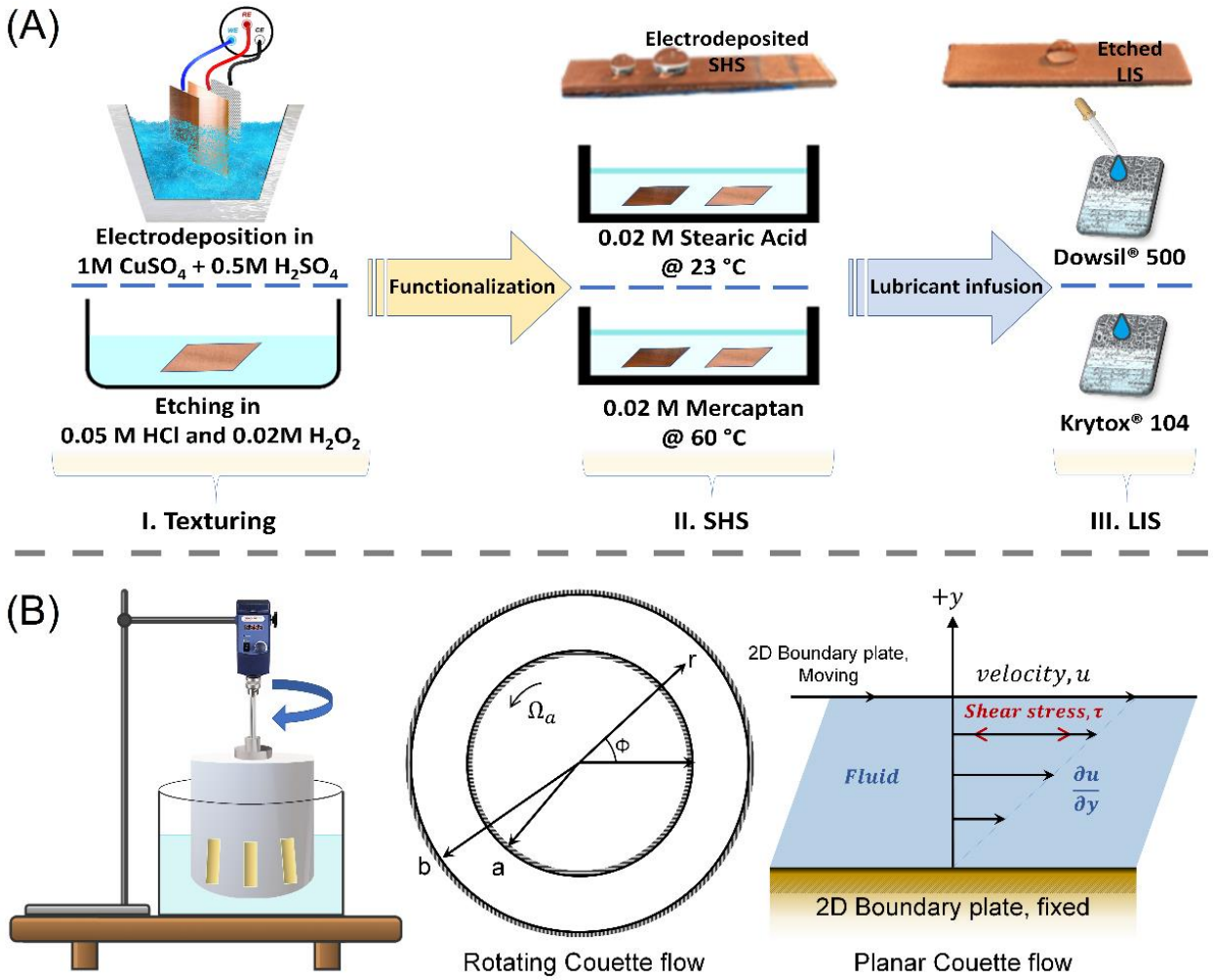

Figure 5.1. A) Schematic of three steps in fabrication of superhydrophobic surfaces (SHS) and lubricant infused surfaces (LIS). I) Texturing electrodeposition-additive and etching-removal methods. II) Functionalization in 0.02 M Stearic acid or Mercaptan solution. III) Lubricant infusion with Dowsil-PDMS or Krytox-PFPE. (B) Schematic of dynamic corrosion setup, rotating Couette flow, and planar Couette flow.

5.4. RESULTS AND DISCUSSION

In this section, the findings of the study are given where first the morphology and surface characterization of the as-fabricated SHS and LIS are discussed. After that, the result of a parametric study on the effect of functionalization time is presented. The section continues with discussions on the systematic static and dynamic corrosion study of the as-fabricated non-wetting surfaces along with bare copper control case. Additionally, the rejuvenation capability of the surfaces is explored. Furthermore, the corrosion inhibition characteristics of the superhydrophobic

and lubricant infused surfaces at various temperatures are put together and an Arrhenius relationship is offered for predictive and comparison purposes. This section ends with a summary of all the findings and conclusions.

5.4.1. **Morphology and wettability**

The SEM images in Figure 5.2 2 uncover the surface morphology of the electrodeposited copper surfaces. The electrodeposition process has added copper on the surface in form of micro and macro size features grown in a farmed fashion as shown in the lower magnification image of Figure 5.2(a). The higher magnification image of the unfunctionalized electrodeposited copper surface in Figure 5.2(d, g) reveals the features to be in form of cauliflowers where bigger dimensions and lower density flowers are grown atop smaller dimensions and higher density ones. After functionalization in Stearic acid solution for 1 hour, the chemisorbed fatty acid has covered first the top cauliflowers in form of cabbage-like features, Figure 5.2(b), and has covered the base smaller dimension flowers in form of a sheath, Figure 5.2(e, h). Contrary to the Stearic acid, functionalization with Mercaptan has not changed the surface morphology significantly as is illustrated in Figure 5.2(c, f, i).

The surface morphology of the etched surfaces before functionalization is depicted in Figure 5.3(a, d, g) at different magnifications and the random roughness that is introduced into the surface via the etching process is clearly shown. The effect of functionalization on the morphology was found to be similar for electrodeposited and etched surfaces. Functionalization of the etched surface in the stearic acid solution for 1 hour, Figure 5.3(b,e,h), has introduced a cabbage-like structure on the surface and 1 hour functionalization with Mercaptan solution, Figure 5.3(c,f,i) has not altered the surface morphology significantly, similar to the discussed electrodeposited cases.

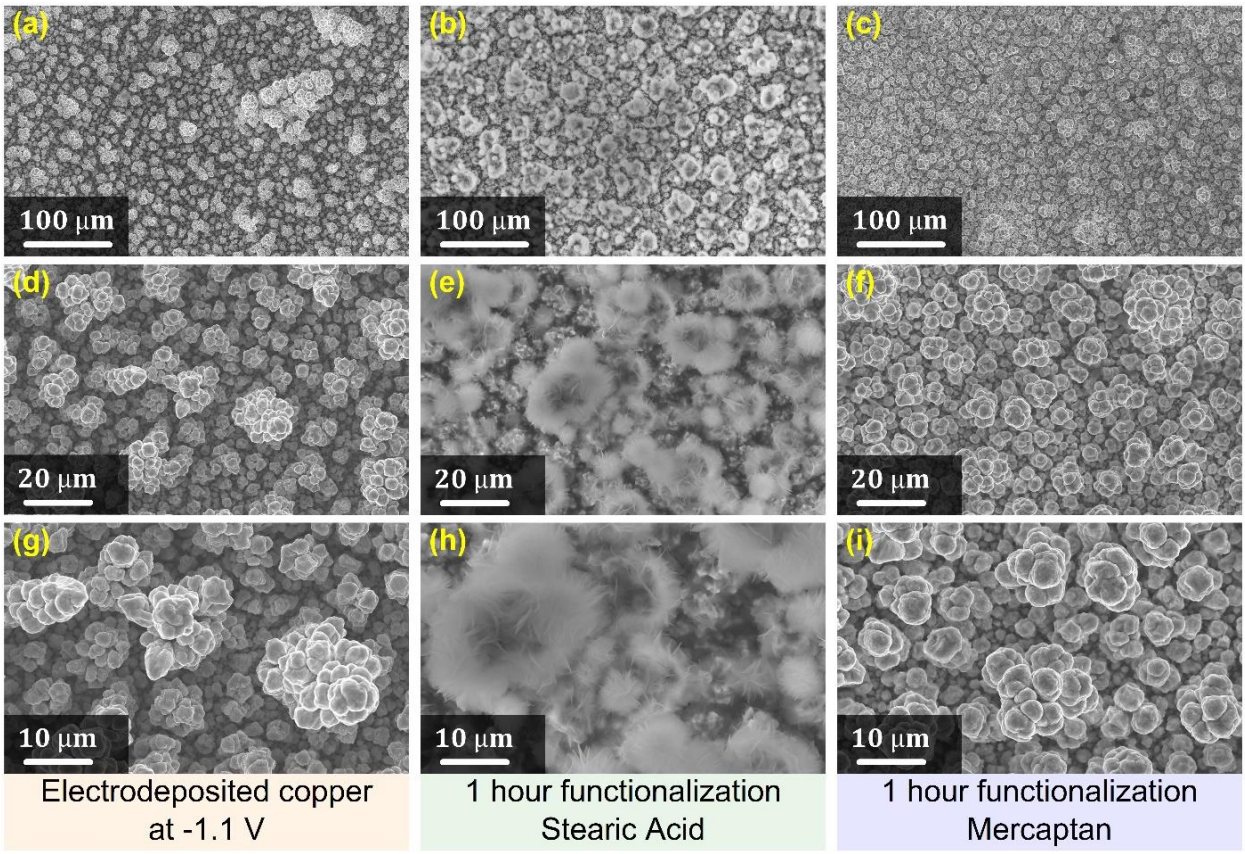

Figure 5.2. SEM image of: (a, d, g) electrodeposited copper on copper; (b, e, h) electrodeposited copper surface after 1 h immersion in 0.02M Stearic acid solution at room temperature; (c, f, i) electrodeposited copper surface after 1 h immersion in 0.02M Mercaptan solution at 60 °C.

Besides surface morphology, Figure 5.2 and 3 SEM images indicate the successful surface chemisorption of the stearic acid functionalization agent. However, unlike functionalization with stearic acid, 1 hour functionalization with Mercaptan solution has not shown visible surface alterations, therefore it is of interest to investigate other surface properties. This was investigated by measuring the surface energy of the surfaces in Figure 5.2 and 3. A two-liquid surface energy measurement method was utilized by using DI-Water (a polar molecule) and Diiodomethane (a non-polar molecule) and incorporating Fowkes theory [33] to calculate the polar (σ_p) and dispersive (σ_d) surface energies which both add up to the total surface energy, as summarized in Table 5.1. The bare copper coupon surface energy was measured to be ~40 mN/m. However, the etching process by itself has shown no effect on the total surface energy of the copper surface but

rather has increased the polar surface energy of the surface to about three folds, from ~2 mN/m to ~12 mN/m. The added cauliflower farm on the copper surface with electrodeposited process shows to have increased the total surface energy of the copper to ~50 mN/m. Diiodomethane a non-polar liquid completely wet this surface with 0 degree contact angle.

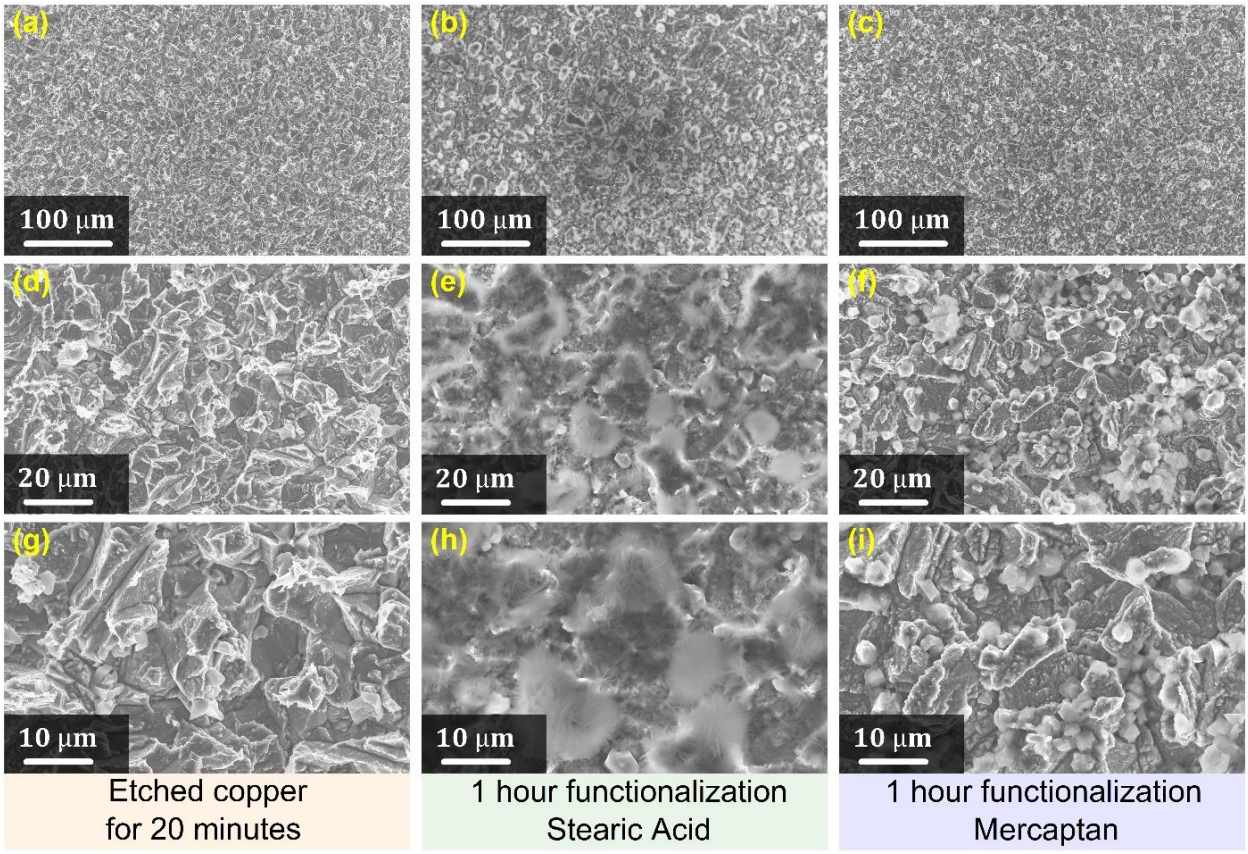

Figure 5.3. SEM image of: (a, d, g) etched copper on copper; (b, e, h) etched copper surface after 1 h immersion in 0.02M Stearic acid solution at room temperature; (c, f, i) etched copper surface after 1 h immersion in 0.02M Mercaptan solution at 60 °C.

After 1-hour functionalization the total surface energy was dropped to an average of ~11 mN/m for both cases of stearic acid and mercaptan regardless of the texturing method. This demonstrates that, despite the insignificant change in surface morphology after 1 hour of Mercaptan functionalization, a significant change in surface chemistry has occurred in the form of a more than 70% reduction in total surface energy (from 40 mN/m to 11 mN/m).

The 1 hour functionalized etched and electrodeposited surfaces that are integrated with low surface energy has also revealed non-wetting properties with an average water contact angle (CA) above 150° and low sliding angle (SA) below 10° as shown in Figure 5.4(a) which classifies these surfaces as superhydrophobic (SHS). Moreover, the added lubricant on the surfaces has tuned them to lubricant-infused surfaces (LIS) where their slipperiness is recorded with SA < 10°. The inset in Figure 5.4(a) shows a 25 µl droplet rolling of an electrodeposited superhydrophobic surface (SHS^D) and sliding of an electrodeposited surface that is functionalized with stearic acid and lubricated with Dowsil™ (LIS^D), at only 3° cradle tilt.

Table 5.1. Surface energy and its components calculated based on 2-liquid method.

	σ_p [mN/m]	σ_d [mN/m]	σ [mN/m]
Bare Copper	2.3 ± 0.6	36.6 ± 0.7	40.8 ± 0.9
Etched Copper	12.1 ± 0.6	28.4 ± 0.5	40.5 ± 0.9
Electrodeposited Copper	0.0 ± 0.3	50.8 ± 0.5	50.8 ± 0.8
Etched SHS (1h stearic acid)	3.3 ± 0.7	9.2 ± 1.8	12.5 ± 2.5
Electrodeposited SHS (1h stearic acid)	1.5 ± 0.6	8.2 ± 2.0	9.6 ± 2.6
Etched SHS (1h Mercaptan)	3.2 ± 0.7	9.2 ± 1.8	12.5 ± 2.5
Electrodeposited SHS (1h Mercaptan)	2.5 ± 0.6	7.8 ± 1.8	10.3 ± 2.4

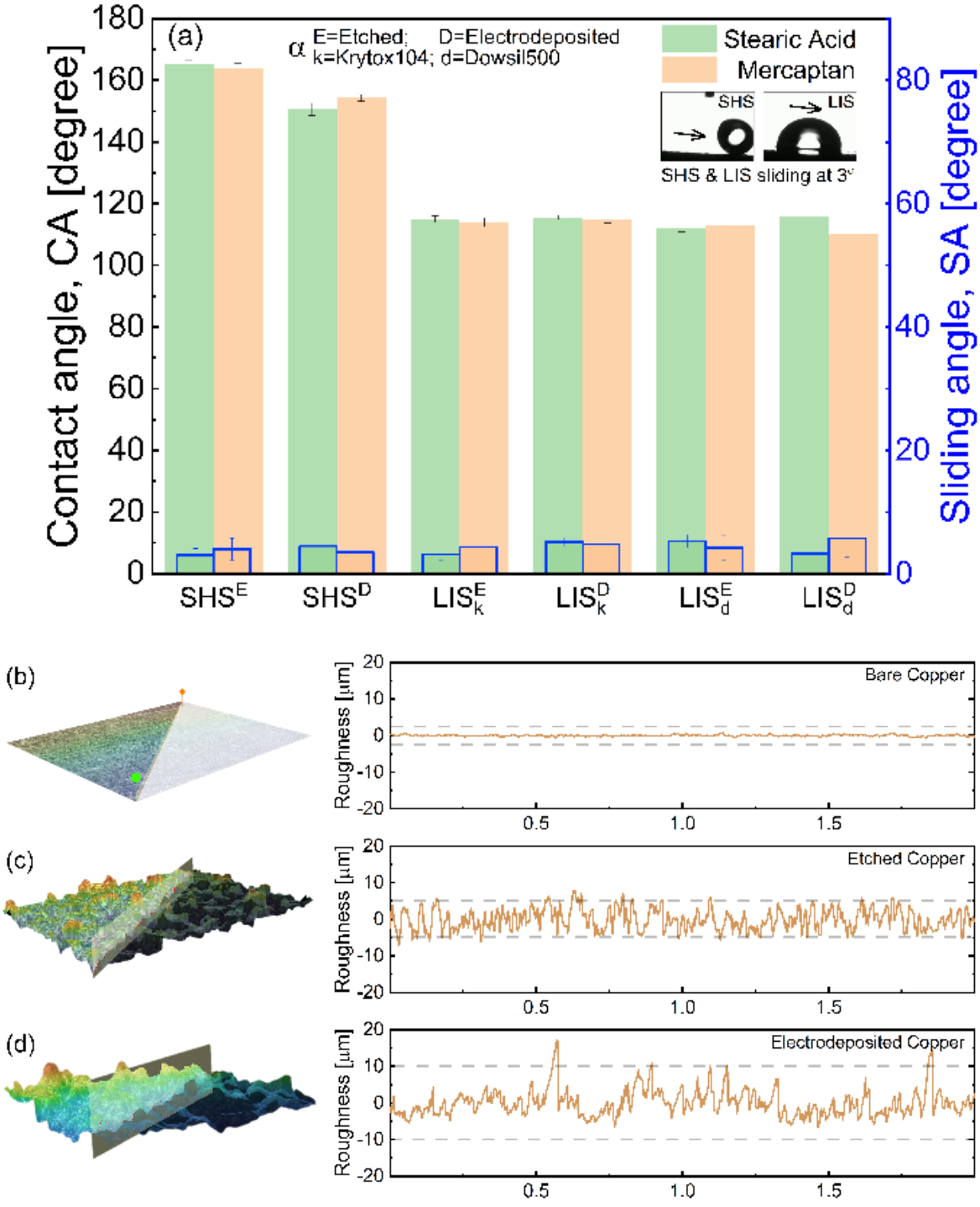

Figure 5.4. (a) Water contact angle and sliding angle on the fabricated copper superhydrophobic surfaces (SHS) and copper lubricant infused surfaces (LIS). Inset images shows a 25 μl droplet rolling of an electrodeposited superhydrophobic surface (SHSD) and sliding of an electrodeposited surface functionalized with stearic acid and lubricated with DowsilTM (LISD), at 3° cradle tilt. 3D reconstruction and roughness profile of (b) bare copper surface; (c) etched copper surface; (d) and electrodeposited copper surface

So far, the SEM images have provided a general view of the surface morphological structures and surface energy data while the wetting characterization has provided further insight into surface properties. It is also of interest to retrieve more information on the level of the surface topography, therefore, the bare and textured surfaces are scanned for roughness profilometry. Figure 5.4(b) depicts a 3D reconstruction of bare copper along with its roughness profile, demonstrating the smoothness of the surface with low height profiles smaller than 1 µm. Figure 5.4(c) shows that the removal etching texturing method has endowed the surface with a homogenous random profile with the Peak-to-valley height of ~12 µm. Contrary to that, the additive electrodeposition texturing method has provided at first look a relatively inhomogeneous random profile with a higher Peak-to-valley height of ~29 µm. The electrodeposited surface roughness profile can be divided into two levels: the base flower-farm and the grown cauliflowers protruded above the base (as shown in Figure 5.2(d)), In that perspective, Figure 5.4(d) shows a homogenous first level random base roughness within ±10 µm range and a more sporadic higher features in the range of ±20 µm for the second level. The measured surface roughness properties of the discussed surfaces, and along the functionalized surfaces, are summarized in Table 5.2. In general, for the case of etched textured surfaces, even after a long time of immersion in both of the functionalization agents (24 h), functionalization has relatively not changed the surface roughness. This is true for electrodeposited textured surfaces functionalized with Mercaptan, but the stearic acid has shown to rather increase the roughness for this surface. This is believed to be due to the second level roughness and the higher/protruded asperities for the case of electrodeposition, where is a favorite site for chemisorption and growth of the cabbagelike stearic acid features, therefore further increased the roughness with higher height asperities.

Table 5.2. Calculated surface roughness properties from profilometry scans.

	RMS roughness,[µm]	**Peak-to-valley height,[µm]**
Bare copper	0.15	0.69
Etched copper	2.92	12.84
Electrodeposited copper	3.72	29.82
Etched functionalized (24 h Stearic acid)	2.40	11.84
Electrodeposited functionalized (24 h Stearic acid)	6.90	49.12
Etched functionalized (24 h Mercaptan)	1.84	13.33
Electrodeposited functionalized (24 h Mercaptan)	4.08	28.06

5.4.2. **Effect of functionalization time on corrosion**

To find out the optimized functionalization time, t_f, and functionalization agent, sets of parametric tests were done on the corrosion inhibition behavior of superhydrophobic and lubricant infused etched copper surfaces immersed in chloride solution (3.5% NaCl). The texturing process was kept to the etching method integrated with a more homogenous surface roughness profile to keep the focus of the test on functionalization agent and functionalization time, along with lubricant type, and solution temperature. 72 coupons were tested and the full matrix of the test parameters is summarized in Table 5.3.

Table 5.3. Test parameter matrix for the study of the effect of functionalization time.

Parameter	**Value(s)**	**Level(s)**
Texturing method (Roughness)	Removal- *etching*	Fixed
Functionalization agent	Stearic Acid, Mercaptan	2
Lubricant	Dowsil™ Fluid (reported viscosity 500 cSt at 25°C), Krytox104™	2
Functionalization time	1 h, 2 h, 4 h, 6 h, 8 h, 24 h	6
Temperature	23 °C, 70 °C	2
Repetition*	Three coupons prepared for each test	3

* The total number of tested coupons for this parametric test was 72.

Figure 5.5 plots the calculated corrosion rates, CR, versus functionalization time, t_f, for etched SHS functionalized with stearic acid and mercaptan at two temperatures of 23 °C and 70 °C along with results for etched LIS at 70 °C. Although it is intuitively thought that LIS performs the same or better at 23 degrees Celsius when compared to 70 degrees Celsius, a separate parametric test was conducted to determine the influence of temperature, the findings of which are provided further in the article. Figure 5.5(a) depicts a decreasing trend in CR with increasing stearic acid functionalization time for etched SHS at room temperature, with an average value of CR of 0.037 mmPY for all t_f. Figure 5.5(a) also shows that at 70 °C the CR of stearic acid functionalized etched SHS, LIS (Krytox), and LIS (Dowsil) had more or less no change with functionalization time with calculated average CR of 0.408 mmPY, 0.394 mmPY, and 0.06 mmPY, respectively. Figure 5.5(b) displays CR of similar surfaces but functionalized with Mercaptan. For all the test conditions, increasing Mercaptan functionalization time had a decreasing effect on the CR. The etched SHS functionalized with Mercaptan showed an average CR value of 0.006 mmPY at room temperature. The mercaptan functionalized etched SHS, LIS (Krytox), and LIS (Dowsil) at 70 °C, regardless of the functionalization time, had an average CR of 0.024 mmPY, 0.017 mmPY, and 0.009 mmPY, respectively. The aggregated corrosion rate values are summarized in Table 5.S1.

Table 5.S1. Summary of corrosion rate showing effect of temperature and functionalization agent.

	CR [mmPY] @ 23 °C	**CR [mmPY] @ 70 °C**
Bare copper	0.0500	1.40000
Etched functionalized (24 h Stearic acid)	0.0365	0.40798
Etched functionalized (24 h Mercaptan)	0.0064	0.02352
E(STA)-LIS(krytox)		0.39392
E(Mer)-LIS(krytox)		0.01729
E(STA)-LIS (Dowsil)		0.05893
E(Mer) -LIS(Dowsil)		0.00869

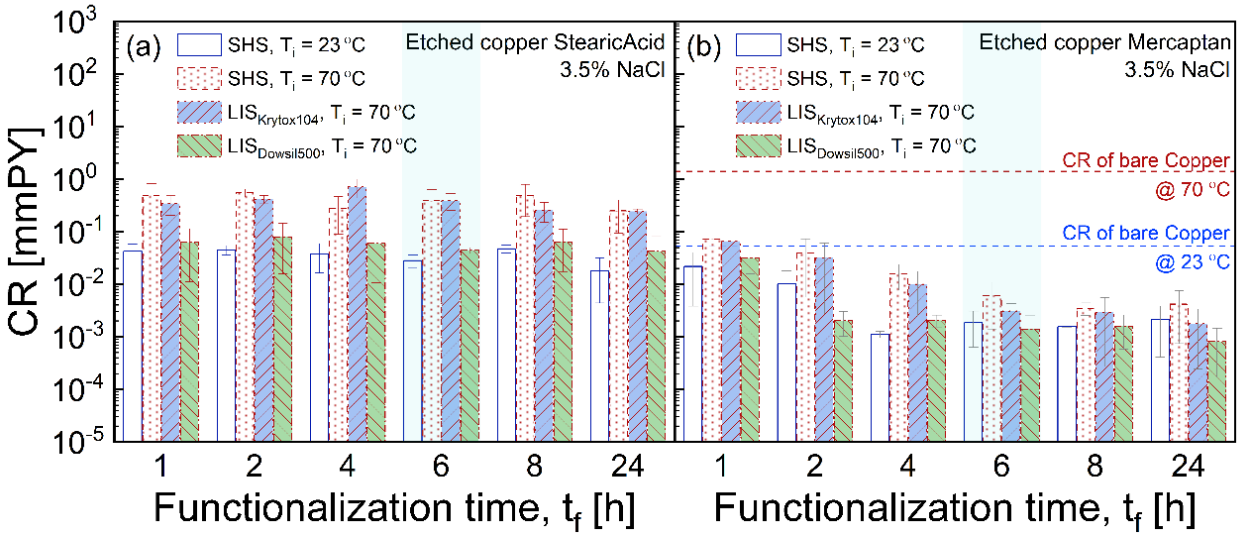

Figure 5.5. Corrosion rates, CR, versus functionalization time, t_f, for (a) etched SHS functionalized with stearic acid; and (b) mercaptan at two temperatures of 23 °C and 70 °C along with results for etched LIS at 70 °C.

In general, Figure 5.5 demonstrates that all the fabricated non-wetting surfaces are superior anti-corrosive surfaces, compared to the unmodified bare copper control case which has 0.05

mmPY and 1.4 mmPY CR at 23 °C and 70 °C, respectively. Mercaptan functionalized surfaces, SHS or LIS, excelled their counterpart stearic acid functionalized surfaces. Even the worst case among the fabricated non-wetting surfaces, $t_f = 1$ h, had shown an average CR at both the 23 °C and 70 °C, to be lower than the bare copper at its best case of 23 °C.

Based on the discussed parametric studies shown in Figure 5.5, both Stearic acid and Mercaptan functionalized samples was seen to have their best cases at functionalization time above 6 h. In order to explore the effect of texturing methods, 24 h functionalized electrodeposited SHS and LIS were fabricated and tested at similar experimental conditions. The results is juxtaposed in Figure 5.6 with the revisited etched case results. At room temperature, electrodeposited stearic acid and mercaptan functionalized SHS showed 1 order of magnitude better CR compared to their counterpart etched SHS. This was observed to be opposite for a similar surface at 70 °C, where electrodeposited did worth than etched however yet better than bare copper control case. This is attributed to the larger height asperities discussed in detail in the roughness analysis of section 3.1. While Stearic acid functionalized electrodeposited LIS has shown similar anti-corrosion characteristics to their etched counterparts, on the other hand, Mercaptan functionalized electrodeposited LIS outperformed similar etched LIS. This is attributed to the surface morphology of the electrodeposited surface which has a larger available volume for lubricant to wick in the interasperity spaces. All in all, the parametric studies in Figure 5.5 and 6 reveals Mercaptan functionalization agent and functionalization time above 6 h, as the optimum selection for fabrication of non-wetting surfaces to incorporate anti-corrosion properties at both low (23 °C) and high (70 °C) temperatures.

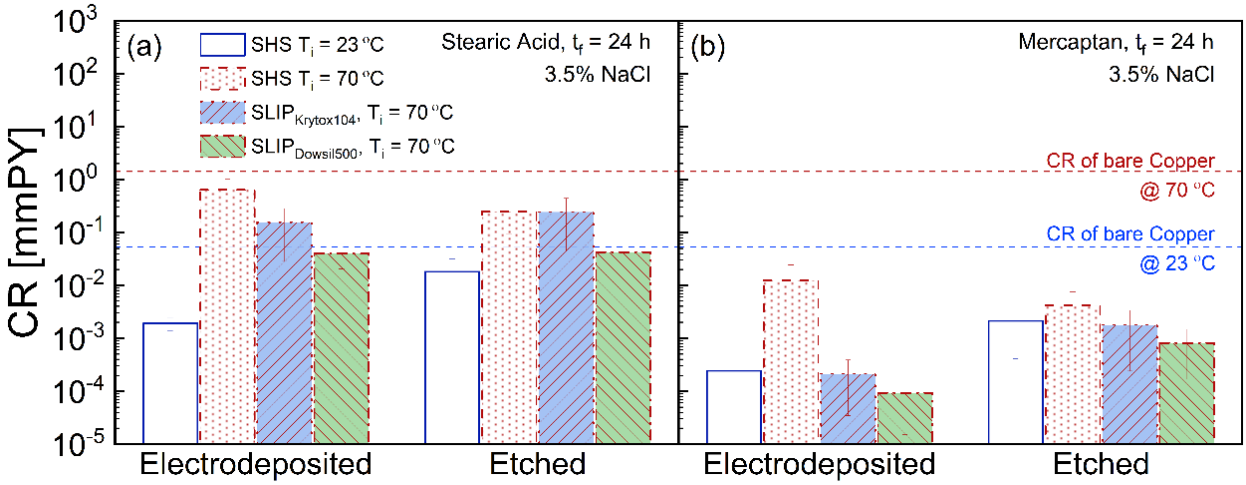

Figure 5.6. Corrosion rate (CR) for etched and electrodeposited SHS and LIS functionalized 24 h with (a): Stearic acid; and (b) Mercaptan.

5.4.3. **Long term static durability study**

To this end, the fabricated non-wetting surfaces have shown superior anti-corrosion performance after 40 minutes of stabilization in chloride solution. To explore the durability of the surfaces at longer immersion times a set of static immersion tests was performed. SHS and LIS was fabricated via the two texturing methods and functionalized for 24 h with Mercaptan, based on the result of section 3.2, and were immersed in 3.5% NaCl solution along with bare copper control case for up to 720 h. The coupons were removed from the solution at different time intervals and tested in fresh solution via a linear polarization (LP) test, a nondestructive corrosion test explained in section 2.5, and polarization/corrosion resistance was calculated. With three samples for each type of surface, 21 coupons were prepared and 252 corrosion tests were performed which the results are plotted in Figure 5.7 along with the optical images of the actual surfaces before and after the test.

The long term fouling tests were designed to cover a variety of test conditions as well as surfaces. The performed parametric tests are summarized in Table 5.4:

Table 5.4. Long term corrosion test experimental matrix

Parameter	Value(s)	Level(s)
Texturing method (Roughness)	Additive- *electrodeposition,* Removal- *etching*	2
Functionalization agent	Stearic Acid, Mercaptan	2
Lubricant	Dowsil^{TM} Fluid (reported viscosity 500 cSt at 25°C), Krytox104^{TM}	2
Functionalization time	1 h, 2 h, 4 h, 6 h, 8 h, 24 h	6
Repetition	Three coupons prepared for each test	3

Figure 5.7(a) shows the pristine smooth and clear bare copper surface before the tests. After 720 h static immersion in the chlorine solution, the surface is corroded and fully covered with patina as shown in Figure 5.7(e). The polarization resistance of bare copper has decreased from 7.6×10^3 Ω.cm^2 at 0.25 h immersion time to 1.9×10^3 Ω.cm^2 after 720 h static immersion. The bare copper has shown a slight increase in R_P between 24 h and 288 h which is due to the protective effect of the patina layer where that also began to degrade after 480 h. The optical microscopic images of the fabricated electrodeposited non-wetting surfaces, Figure 5.7(b-d), and etched non-wetting surfaces, Figure 5.7(f-h), after 720 h static immersion shows significantly less visible sign of corrosion in form of the green spot in comparison to the bare copper control case in Figure 5.7(e). Moreover, the inset illustrates images of the actual samples before and after long-term static immersion test which clearly shows the degree of surface discoloration due to corrosion in the following order: Bare copper > SHS > LIS(Dowsil) and LIS(Krytox). These qualitative observations very well match the quantitative results in Figure 5.7(i,j) where the polarization resistance of LIS are measured higher than SHS and both higher than the bare control case. Krytox and Dowsil lubricated electrodeposited LIS performed almost similarly throughout the static immersion test. For etched LIS both types of the lubricated surface have followed a similar trend, with Dowsil performing slightly better which is attributed to first the higher viscosity of Dwosil compared to Krytox and second to the less surface area of etched coupons and hence less capillary forces compared to electrodeposited surfaces.

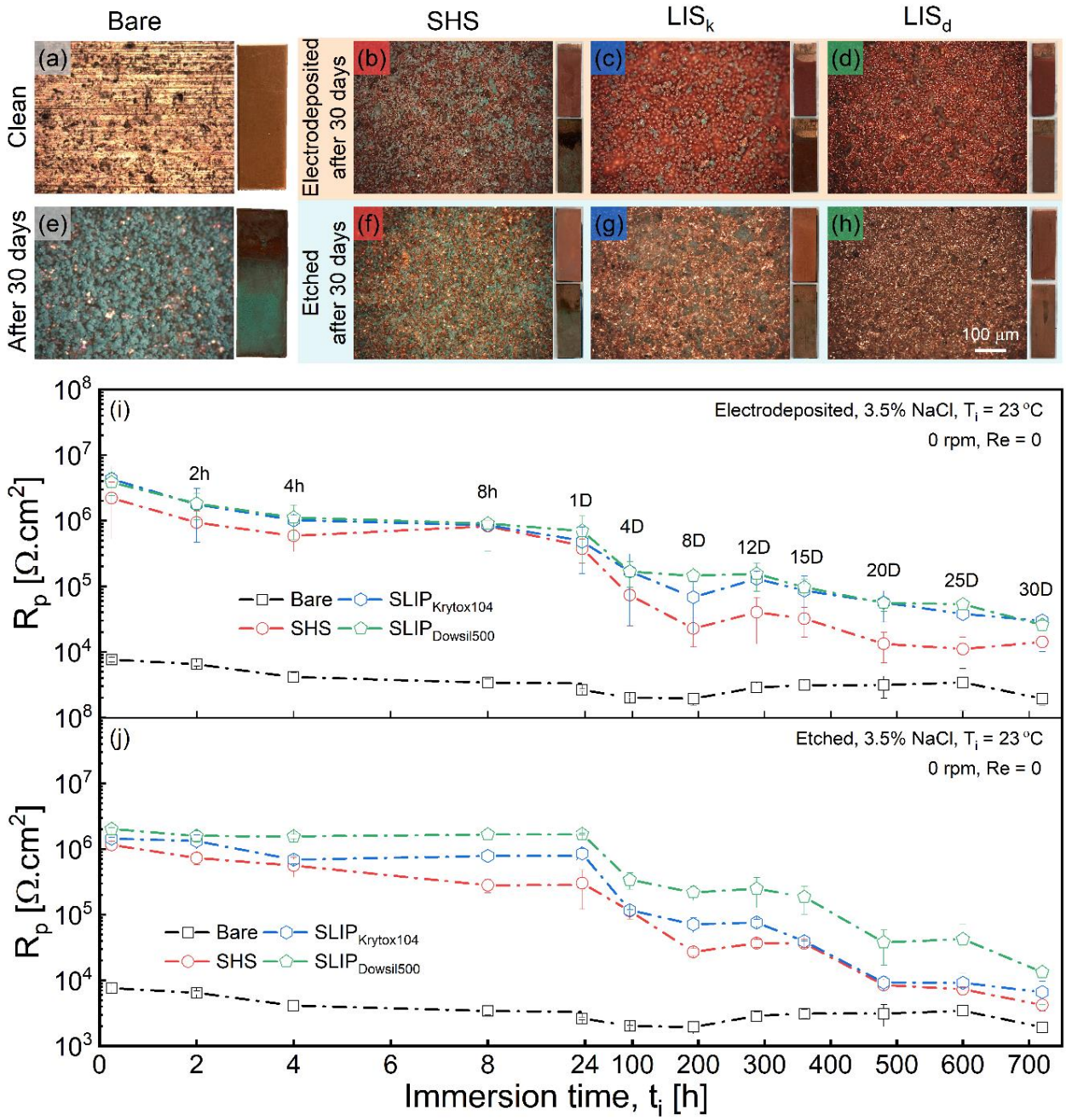

Figure 5.7. Optical image of (a): Clean bare copper; (b-h): bare copper and superhydrophobic and lubricant infused surfaces after 30 days of static immersion test in 3.5% NaCl solution at room temperature Inset shows actual 1×3 cm coupons before and after the long term static test. Polarization resistance, R_p, versus immersion time, t_i, (i): electrodeposited; and (j): etched SHS and LIS along bare copper control case immersed in 3.5% NaCl solution at room temperature.

5.4.4. **Long term dynamic durability study**

Flow conditions are common in many applications which have left quite unexplored for non-wetting surfaces. Therefore, a novel yet simple dynamic corrosion setup was designed to mimic the turbulent flow condition. The drum setup, detailed in section 2.4, was set to a rotation rate of 200 rpm corresponding to 49×10^3 Reynolds number. In a typical power plant with a 23 mm internal diameter condenser pipe and a working fluid speed of 1.8 m/s (2.5 m/s) the Reynolds number is 44×10^3 (62×10^3). Assuming 40,000 as Reynolds number threshold for a fully turbulent flow regime, the chosen dynamic condition is consistent with the turbulent application conditions and also provides insight on greater flow speed and/or larger pipe diameter conditions. A set of non-wetting SHS and LIS was fabricated via the two texturing methods and functionalized for 24 h with Mercaptan. The fabricated coupons along bare copper control samples were mounted on the outer surface of the rotating drum and were immersed in 3.5% NaCl solution for up to 720 h. Each type of surface was mounted on a separate setup to avoid unwanted interactions. Similar to static tests, three samples for each type of surface were prepared to add to a total of 21 coupons and 252 corrosion tests which the results are summarized in Figure 5.88 along with the optical images of the surfaces before, in middle, and after the long term dynamic experiments. It appears that polarization resistance of the LIS regardless of the type divides into a first stage, from beginning up to 96 h where the polarization resistance stayed relatively stable, and a second stage between 96 h to 720 h where the polarization resistance followed a decreasing trend. The first stage is extended up to 288 h for SHS cases. This can be attributed to the soft and solid nature of these two types of surfaces, LIS and SHS, respectively. Shear forces have pretty much affected the non-wetting surfaces instantaneously where a step-wise trend is observed between 0.25 h and 2h polarization resistance values. After that R_p stayed relatively constant up to the end of the first stage. The protective lubricant infused into the surfaces is naturally swept away by the shear forces in the turbulent condition and therefore the corrosion resistance has decreased. This can be followed in the optical microscopic images in Figure 5.8(C) (The insets images were taken with a fluorescent filter to better capture the transparent lubricant and other features). A significant morphological change is observed to the bare copper surface throughout the dynamic corrosion test. The clean smooth bare copper surface before the tests was covered with a patina layer by the middle of the test where at the end of the test salt crystal deposition has also been observed as

marked in Figure 5.8(C). The high turbulent condition of the test has impacted SHS in terms of slight erosion but no visible patina layer was observed. Among LIS, Dowsil infused surfaces has shown visible sign of available lubricant on the surface in the 15 days optical images, especially on electrodeposited LIS. The higher viscosity of the Dowsil oil and higher available surface area of the electrodeposited with which provides larger capillary forces to balance the opposite shear forces. Similar to SHS, the surface of LIS has shown no or significantly less sign of patina compared to the bare control case throughout the dynamic test.

Comparing the results from the static and dynamic corrosion test in Figure 5.7 and 8 suggest that flow condition has rather a corrosion mitigation effect, especially for the bare copper control sample. This can be explained by the removal shear force, which causes the corrosion species to be swept away from the surface, as well as the shorter available reaction time, particularly for flat surfaces. In the static condition, by the end of the 30 days, Dowsil infused LIS surfaces polarization resistance was measured larger or equal to Krytox infused LIS. Contrary, in the dynamic condition, at some point throughout the test the R_p value for Dowsil lubricated surfaces has dropped below Krytox lubricated surfaces. Figure 5.8 shows this has happened earlier for etched cases (after 8 days of immersion) than electrodeposited cases (after 20 days of immersion). This is hypothesized by putting in tandem the surface roughness characteristics of the surfaces and the viscosity of the lubricants. The higher the viscosity the harder is for a lubricant to infuse into smaller cavities. Looking at the profilometer scan of etched and electrodeposited surfaces in Figure 5.4(c) and 4(d), it can be seen by passing an imaginary line at zero height it crosses the profile in a way in which the space between asperities get smaller and peaks get denser compared to a similar horizontal line at the level of the highest asperities. This suggests that the high viscosity lubricant infuses the surface but cannot penetrate the small size interspaces at the base level of the surface but the same characteristics (higher viscosity) have endowed it a better protective property against corrosion. On the other hand, lower viscosity lubricant has a chance to wet the base level of the surface but cannot withstand the shear forces in the level that the higher viscosity lubricant does. By the end of the dynamic test, the strong shear force has swept the lubricant from the top level of the surfaces but balanced with the strong capillary forces at the base level where, if any lubricant available, would stay locked in. This is the point where Krytox lubricated surfaces begin to outperform the Dowsil case. As was observed, this switch in performance is sooner for etched case compared to

the electrodeposited textured LIS that is clearly explainable by the higher roughness of the latter which is capable of accommodating a larger volume of the lubricant at its top-level roughness. Thus, the surfaces that could have lubricant in their base level, the Krytox LIS, shall show better protection against corrosion compared to a surface that has been completely depleted from lubricant, Dowsil LIS. This hypothesizes the observed trends in R_p in Figure 5.7 and 8 by the end of the 30 days.

However, the corrosion resistance of the modified surfaces was recorded slightly better or similar to the control case at the end of the long-term dynamic corrosion test, the qualitative look of the actual coupon surfaces in Figure 5.9(a) shows significant discoloration of the bare copper (a sign of corrosion and patina layer) which is not observed for the modified surfaces. To quantify this, the elemental composition of the coupons was examined via Energy Dispersive X-Ray Analysis (EDX). The elemental analysis in Figure 5.9b) shows the presence of significantly higher Sodium and Chlorine compounds on the bare copper surface compared to all the other modified surfaces after 30 days of dynamic corrosion test. Moreover, the lower detected amount of copper for the bare copper surface after 30 days compared to the before the test asserts the presence of the thick patina layer which has worked as a relatively protective layer against corrosion for this surface as observed in R_p values of Figure 5.8.

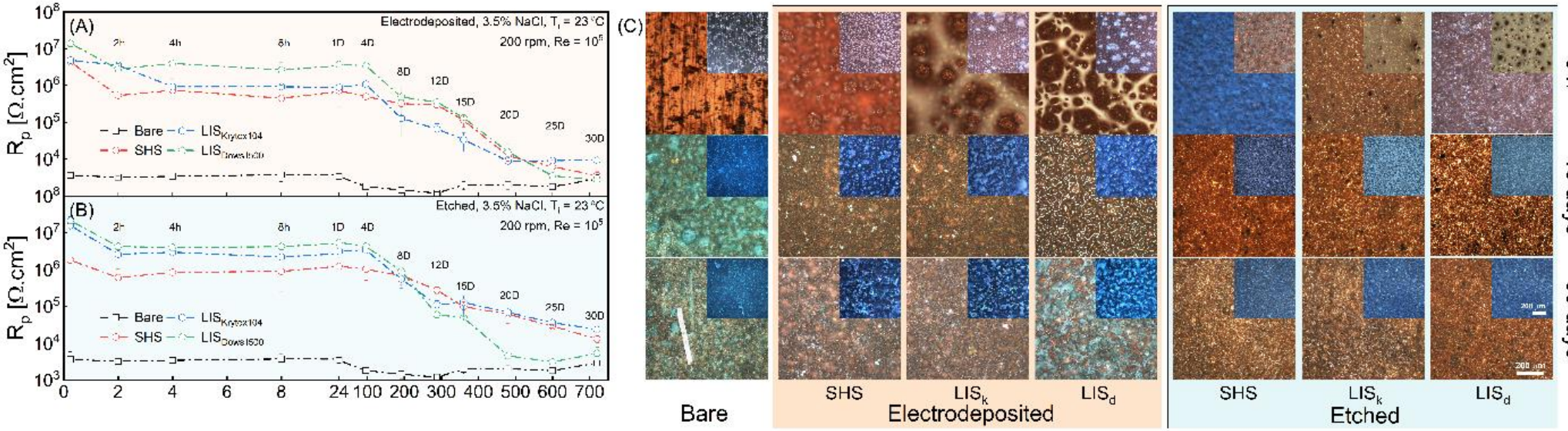

Figure 5.8. Polarization resistance, R_p, versus immersion time, t_i, (A): electrodeposited; and (B): etched SHS and LIS along bare copper control case immersed in 3.5% NaCl solution at room temperature at dynamic condition resembling turbulent flow with Reynolds number of about 105. (C): Optical microscopic images of surfaces before, in middle, and after dynamic corrosion test. Insets are images taken with fluorescent filter.

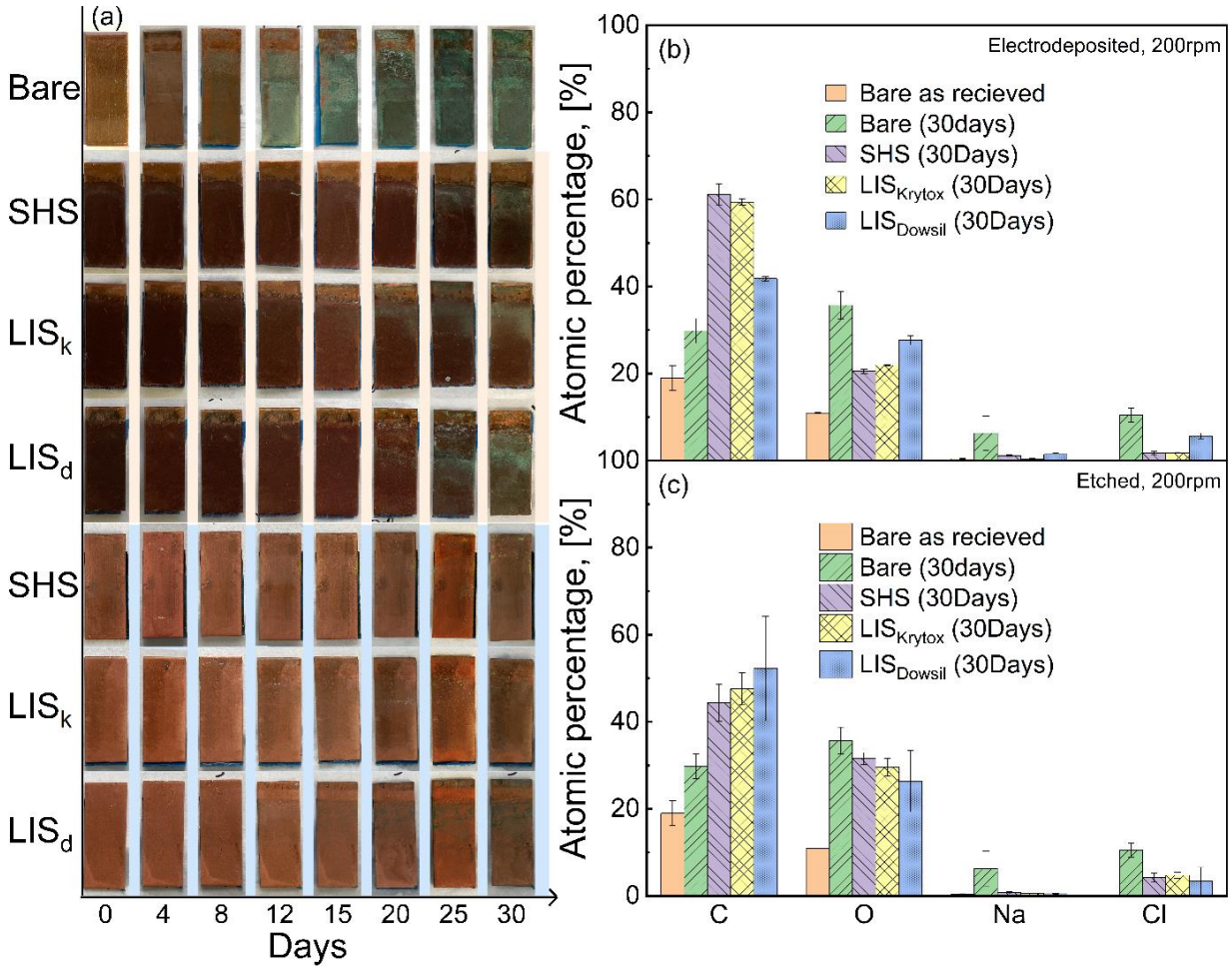

Figure 5.9. (a) Optical image of the actual 1×3 cm coupons versus time throughout the long term dynamic corrosion tests. Top 1 cm was used for handling purposes and the bottom 1 cm was used in corrosion measurements. EDX elemental composition analysis of (b): electrodeposited; and (c): etched copper SHS and LIS along bare control case after dynamic corrosion test at 105 Reynolds number and 3.5% NaCl solution.

5.4.5. **Rejuvenation**

So far, the corrosion inhibition properties of the fabricated non-wetting surfaces were examined at short term static condition, long term static condition, and long term harsh turbulent regime. It has also shown that even though the modified surfaces after long-term immersions have lost their superior corrosion inhibition to slightly better than bare copper, they still carry much less corrosive compounds and have preserved their rough textured. Therefore, the possibility of rejuvenation of the surfaces is explored by re-functionalizing and further lubricant infusion of the samples. Figure

5.10 shows that the electrodeposited and etched non-wetting surfaces had an average corrosion resistance of about 8 MΩ.cm^{2}and 2 MΩ.cm^2, respectively. After 720 h longterm corrosion dynamic test at 200 rpm (10^5 Reynolds number), the polarization resistance was decreased to about 0.004 MΩ.cm^2 and 0.017 MΩ.cm^2 for electrodeposited and etched non-wetting surfaces. After rejuvenation by immersion in Mercaptan solution the surfaces have revived and average polarization resistance of 5 MΩ.cm^2 and 2 MΩ.cm^2 was recorded for electrodeposited and etched based surfaces. After re-functionalization, the coupons which were lubricant infused before the dynamic corrosion test were re-infused with oil, and the average polarization resistance of 41 MΩ.cm^2 and 22 MΩ.cm^2 was measured for electrodeposited and etched based rejuvenated LIS, respectively. In general, the study shows successful rejuvenation of the surfaces and revived anti-corrosion properties of the modified copper surfaces. The process results are summarized in Table 5.S2.

Table 5.S2. Aggregation of data in Figure 5.10, rejuvenation study.

	Electrodeposited [MΩ.cm^2]	**Etched [MΩ.cm^2]**
0h	8.4	1.9
30 days	0.004	0.017
Rej. Func.	5.1	2.12
Rej. Func. Oil	41.5	22.5

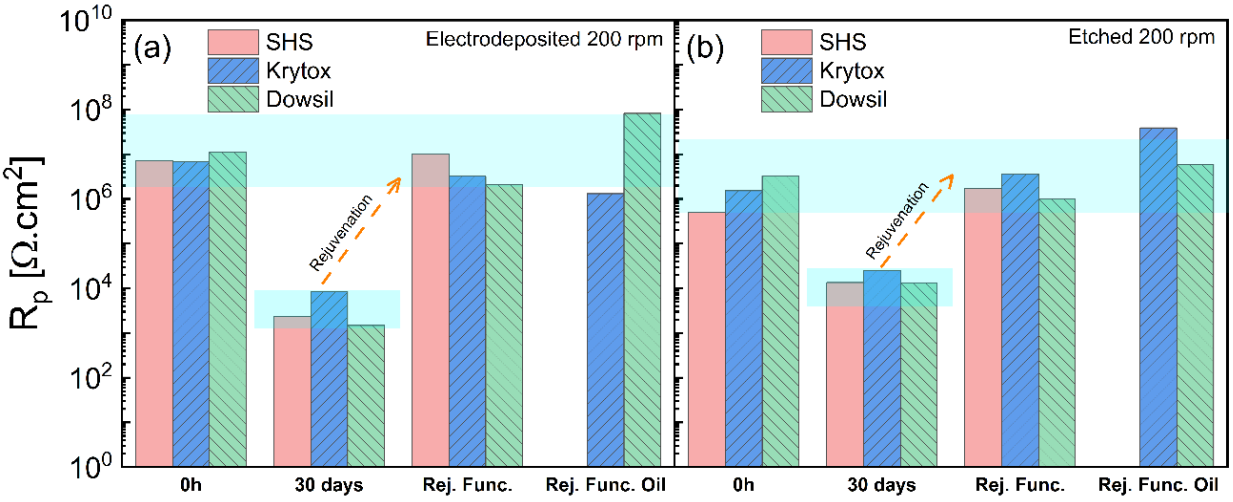

Figure 5.10. Polarization resistance, R_p, for non-wetting surfaces before, after dynamic corrosion test, after rejuvenation via functionalization process in Mercaptan solution, and after rejuvenation via functionalization and lubricant infusion (a): electrodeposited surfaces; (b) etched surfaces.

5.4.6. **Effect of temperature**

The fabricated non-wetting surfaces and unmodified control samples were studied at room temperature and one specific high temperature. It is of further interest to stress the surfaces to a range of temperatures. To this end, corrosion rates were recorded on selected SHS and LIS for immersion in 3.5% NaCl at temperature values of 23°C to 35°C, 50°C, 70°C, and 90°C. In order to avoid an excessive number of tests and focus on the effect of temperature, based on the functionalization study showed in Figure 5.5, the copper surface textured with etching method and functionalized for 6 h with Mercaptan was selected for SHS case and similar surface infused with Dowsil^{TM} lubricant was selected for LIS case. The experiments were done three times at each temperature for statistical significance. Figure 5.11(a) presents the variation of the corrosion rate with temperature for SHS and LIS etched copper surfaces. It is well known that the corrosion mechanisms are accelerated at higher temperatures due to higher available energy. to the species partaking in corrosion reaction. The average corrosion rate for bare copper at 23 °C increases from 0.05 mmPY, more than 1 order of magnitude or 28 folds, to 1.4 mmPY at 70 °C. A similar change for 6 hours mercaptan functionalized superhydrophobic etched copper surface is 1.9×10^{-3} mmPY to 6.2×10^{-3} mmPY, about three folds. This confirms the relative stability of the fabricated mercaptan superhydrophobic surfaces at different temperatures. Moreover, the increasing effect of

temperature on corrosion rate is suppressed for the lubricant-infused surfaces, Figure 5.11(a), and the LIS cases did not show a significant increase in corrosion rate with increasing temperature. Such low corrosion rates clearly indicate the effective anti-corrosive nature of the fabricated superhydrophobic and lubricant-infused surfaces and their stability over the range of studied temperatures.

Figure 5.11(b) presents the variation of the corrosion rate with the inverse of the absolute temperature (in Kelvin) on a semi-log plot. The linear nature of the variation in the semi-log plot suggests an Arrhenius relationship between the corrosion rate and the temperature, where the slope is the activation energy in the exponential term and the intercept on the ordinate is the pre-exponential factor. Equation (5.1 and Equation (5.2) are derived on the basis of least-square linear regression throughout the temperature dependent corrosion rate data of the mercaptan superhydrophobic and lubricant infused surface in 3.5% NaCl solution, respectively.

$$CR_{SHS} = 1.69 \times 10^{2}. \exp\left(-\frac{3424.90}{T}\right) \tag{5.1}$$

$$CR_{LIS} = 0.55 \times 10^{2}. \exp\left(-\frac{3503.94}{T}\right) \tag{5.2}$$

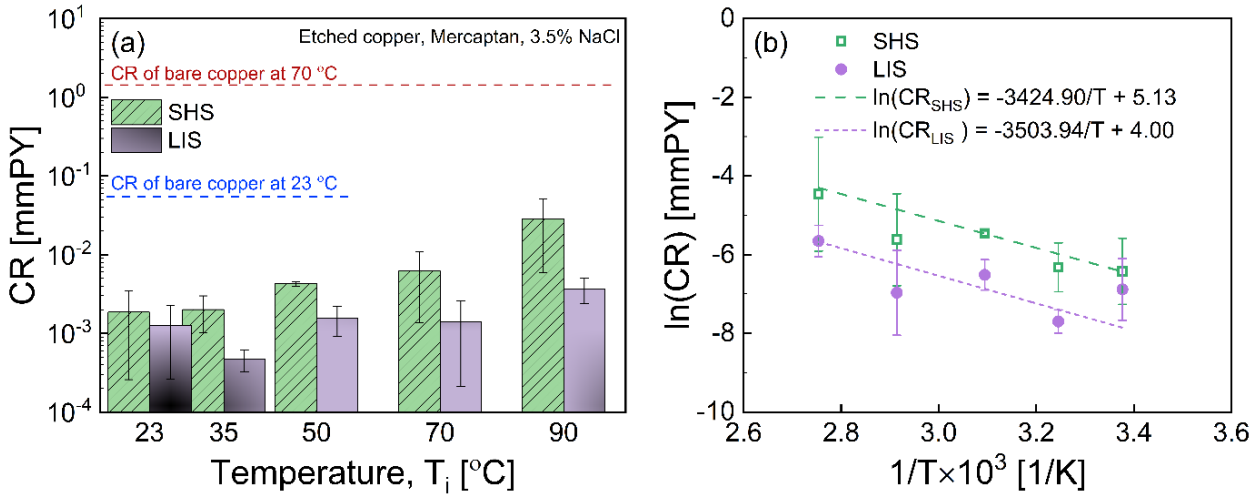

Figure 5.11. (a): Variation of corrosion rate, CR, with immersion temperature, T_i, in 3.56% NaCl aqueous solution for etched copper SHS and LIS. Surfaces were functionalized with Mercaptan and Dowsil. (b): Arrhenius plot of the natural logarithm of the corrosion rate with reciprocal of absolute temperature.

In previous studies, the Arrhenius relationship slope for stearic acid SHS was shown to be -9797.18 which is about 2.8 times larger in absolute value compared to the Arrhenius relationship slope of -3424.90 for mercaptan SHS. Likewise, the Arrhenius relationship slope for stearic acid and mercaptan LIS are shown to be -5798.00 and -3503.94, respectively. These all suggest higher sensitivity of stearic acid based SHS and LIS to temperature or in another world relative stability and robustness of Mercaptan based SHS and LIS over a range of temperatures. Moreover, the Arrhenius equation can be used as a predictive tool to examine corrosion rate of the superhydrophobic and lubricant-infused surfaces discussed in this article in a simulated marine environment at any temperature between 23 °C and 90 °C.

Collectively, this section presented evidence of the robustness of the offered non-wetting surfaces at different environments of application against corrosion namely dynamic and high temperature environments. While the focus of this article was on fabrication, functionalization optimization, and performance study of copper surfaces at static as well as dynamic flow condition, based on the discussion in this section, a dedicated study to the effect of surface roughness features and lubricant properties on the level of penetration and infusion is of further interest. This can be done via synthetic surfaces which adopt different roughness features fabricated via processes like sol-gel and templating and scrutinizing into the infusion process via methods like confocal microscopy techniques.

5.5. CONCLUSIONS

In this study, facile additive and removal methods were approached for texturing smooth copper surfaces. Two different functionalization agents were explored to endow superhydrophobicity to the surfaces. Two different lubricants were used to fabricate slippery surfaces. The fabricated modified surfaces were systematically studied for their corrosion inhibition performance in a range of functionalization time, immersion time in the corrosive solution, Reynolds number, and temperature. For that, over 234 coupons were prepared and over 1,021 measurements were performed which the major findings are as follow:

Texturing and functionalization— Both electrodeposition and etching method was shown to be facile approaches for introducing random roughness on a smooth surface. The

removal etching texturing method has endowed the surface with a homogenous random profile with the Peak-to-valley height of ~12 μm and the additive electrodeposition texturing method has provided roughness in two levels: dense base level and sparse top level, with a total higher Peak-to-valley height of ~29 μm. Surface features resembled cauliflower on the electrodeposited surface and random grooves into the etched surface. Between Stearic acid and Mercaptan functionalization agent, the former with chemisorbed grown cabbage-like structures on the surface showed to change the surface morphology more compared to the latter with almost no visible change to the structure. Both functionalization agents lowered the total surface energy of copper surface by at least 70%. with only 1 h functionalization. The functionalized textured surfaces showed superhydrophobic properties with a water contact angle above 150 °C and a sliding angle below 10 °C.

Surface modification and corrosion inhibition— The extent of the effect of varying functionalization time between 1 h and 24 h on corrosion rate showed 6 h and beyond to be effective functionalization time to record corrosion rates as low as in 10^{-4} order for non-wetting surfaces compared to bare control case in range of 10^{-2} at room temperature. Mercaptan functionalization agent corrosion inhibition properties excelled its stearic acid counterparts by one order of magnitude and above.

Static durability— At the end of the long term (720 h) static condition durability tests the results showed the following order for corrosion resistance values of the surfaces: Bare copper < SHS < LIS(Dowsil) and LIS(Krytox). The non-wetting SHS and LIS began with ~2.5 orders of magnitude larger polarization resistance and finished the test with 0.2-1.0 order of magnitude larger values compared to the bare control sample

Dynamic durability— At the end of the long term (720 h) dynamic corrosion durability test, turbulent Taylor-Couette flow condition characterized with 10^5 Reynolds number, the non-wetting surfaces showed either equal or higher (up to 1 order of magnitude) polarization resistance compared to the bare copper control surface. Despite close values, the elemental surface analysis showed the presence of sodium and chlorine elements in significant amounts higher on bare control cases compared to modified surfaces.

Surface Rejuvenation— Modified surfaces excellently responded to the rejuvenation process. Coupons experienced the harshest tests environments (dynamic

corrosion test for 720 h) regained their corrosion inhibition properties by 2 to 4 orders of magnitude increase in polarization resistance.

Temperature study— Mercaptan functionalization agent showed superior robustness at higher temperatures compared to stearic acid functionalization agent. Mercaptan functionalized SHS exhibited excellent corrosion inhibition over a range of temperatures. At 90 °C the SHS corrosion rate was half of the control sample CR at 23 °C and over 2 orders of magnitude lower than control sample CR at 90 °C. LIS showed stable corrosion inhibition properties over the tested temperature range of 23°C to 35°C, 50°C, 70°C, and 90°C. The difference between SHS and LIS corrosion rate was observed to increase with temperature starting at similar values at 23 °C to around 1 order of magnitude difference at 90 °C with lower CR for LIS.

For the first time, the result of this study shed light on the interactions between the various aspect of fabrication of non-wetting surfaces including texturing method, functionalization agent, and lubricant type, also on surfaces long term durability in various environments including static condition mimicking marine environment, and dynamic condition mimicking turbulent flow conditions. Moreover, corrosion inhibition over a wide range of temperatures was studied and an Arrhenius relationship was built. This study believes to pave the way for the selection of proper parameters for the fabrication of non-wetting surfaces for the application of interest.

ACKNOWLEDGMENT AND DISCLAIMER

The material reported in this publication is based upon work supported by the U.S. Department of Energy under Award Number DE-FE0031556. This publication was prepared as an account of work sponsored by an agency of the United States Government. Neither the United States Government nor any agency thereof, nor any of their employees, makes any warranty, express or implied, or assumes any legal liability or responsibility for the accuracy, completeness, or usefulness of any information, apparatus, product, or process disclosed, or represents that its use would not infringe privately owned rights. Reference herein to any specific commercial product, process, or service by trade name, trademark, manufacturer, or otherwise does not necessarily constitute or imply its endorsement, recommendation, or favoring by the United States

Government or any agency thereof. The views and opinions of authors expressed herein do not necessarily state or reflect those of the United States Government or any agency thereof.

REFERENCES

[1] K. Law, H. Zhao, Surface wetting: characterization, contact angle, and fundamentals, Springer, 2016.

[2] A. Ramanujam Padmavathi, P. Sriyutha Murthy, A. Das, T. Subba Rao, Enhanced antifouling property of polydimethylsiloxane-CuO nanocomposite in marine environment, Mater. Lett. 301 (2021) 130342. https://doi.org/10.1016/J.MATLET.2021.130342.

[3] Mengyue Liu, Shaonan Li, Hao Wang, Rijia Jiang, Xing Zhou, Research progress of environmentally friendly marine antifouling coatings, Polym. Chem. 12 (2021) 3702–3720. https://doi.org/10.1039/D1PY00512J.

[4] W. Guo, Z. Li, Z. Ma, Review of Non-Fluorinated Durable Water Repellent and Stain-Resistant Materials and Their Future development, J. Phys. Conf. Ser. 1904 (2021) 012010. https://doi.org/10.1088/1742-6596/1904/1/012010.

[5] J. Ou, F. Wang, W. Li, M. Yan, A. Amirfazli, Methyltrimethoxysilane as a multipurpose chemical for durable superhydrophobic cotton fabric, Prog. Org. Coatings. 146 (2020) 105700. https://doi.org/10.1016/J.PORGCOAT.2020.105700.

[6] M. Belhadjamor, M. El Mansori, … S.B.-S., undefined 2018, Anti-fingerprint properties of engineering surfaces: a review, Taylor Fr. 34 (2016) 85–120. https://doi.org/10.1080/02670844.2016.1258449.

[7] F. Piscitelli, F. Tescione, L. Mazzola, G. Bruno, M. Lavorgna, On a simplified method to produce hydrophobic coatings for aeronautical applications, Appl. Surf. Sci. 472 (2019) 71–81. https://doi.org/10.1016/J.APSUSC.2018.04.062.

[8] A.B. Tesler, P. Kim, S. Kolle, C. Howell, O. Ahanotu, J. Aizenberg, Extremely durable biofouling-resistant metallic surfaces based on electrodeposited nanoporous tungstite films on steel, Nat. Commun. 2015 61. 6 (2015) 1–10. https://doi.org/10.1038/ncomms9649.

[9] A.I. Ukolov, T.N. Popova, K.A. Viktorovich, The effect of the loss of superhydrophobic surface properties on biofouling and flow around shipbuilding's steel plates, Ocean Eng. 214 (2020) 107801. https://doi.org/10.1016/J.OCEANENG.2020.107801.

[10] A. Masoudi, P. Irajizad, N. Farokhnia, V. Kashyap, H. Ghasemi, Antiscaling Magnetic Slippery Surfaces, ACS Appl. Mater. Interfaces. 9 (2017) 21025–21033. https://doi.org/10.1021/ACSAMI.7B05564.

[11] Y. Zhu, H. Li, M. Zhu, H. Wang, Z. Li, Dynamic and active antiscaling via scale inhibitor pre-stored superhydrophobic coating, Chem. Eng. J. 403 (2021) 126467. https://doi.org/10.1016/J.CEJ.2020.126467.

[12] S.M.A. Mousavi, R. Pitchumani, A Study of Corrosion on Electrodeposited Superhydrophobic Copper Surfaces, Corros. Sci. 186 (2021) 109420. https://doi.org/10.1016/j.corsci.2021.109420.

[13] M. Cui, B. Wang, Z. Wang, Nature-Inspired Strategy for Anticorrosion, Adv. Eng. Mater. 21 (2019). https://doi.org/10.1002/adem.201801379.

[14] J. Xu, Q. Cai, Z. Lian, Z. Yu, W. Ren, H. Yu, Research Progress on Corrosion Resistance of Magnesium Alloys with Bio-inspired Water-repellent Properties: A Review, J. Bionic Eng. 2021 184. 18 (2021) 735–763. https://doi.org/10.1007/S42235-021-0064-5.

[15] B. Hou, X. Li, X. Ma, C. Du, D. Zhang, M. Zheng, W. Xu, D. Lu, F. Ma, The cost of corrosion in China, Npj Mater. Degrad. 2017 11. 1 (2017) 1–10. https://doi.org/10.1038/s41529-017-0005-2.

[16] J. Kruger, Cost of metallic corrosion, in: Uhlig's Corros. Handb., 2011: pp. 15–20.

[17] S. Khodakarami, H. Zhao, K.F. Rabbi, N. Miljkovic, Scalable corrosion-resistant coatings for thermal applications, ACS Appl. Mater. Interfaces. 13 (2021) 4519–4534. https://doi.org/10.1021/acsami.0c19683.

[18] S.S. Latthe, R.S. Sutar, A.K. Bhosale, S. Nagappan, C.S. Ha, K.K. Sadasivuni, S. Liu, R. Xing, Recent developments in air-trapped superhydrophobic and liquid-infused slippery surfaces for anti-icing application, Prog. Org. Coatings. 137 (2019) 105373. https://doi.org/10.1016/j.porgcoat.2019.105373.

[19] M. Villegas, Y. Zhang, N.A. Jarad, L. Soleymani, T.F. Didar, Liquid-Infused Surfaces: A Review of Theory, Design, and Applications, ACS Nano. 13 (2019) 8517–8536. https://doi.org/10.1021/ACSNANO.9B04129.

[20] J. Liu, X. Fang, C. Zhu, X. Xing, G. Cui, Z. Li, Fabrication of superhydrophobic coatings for corrosion protection by electrodeposition: A comprehensive review, Colloids Surfaces

A Physicochem. Eng. Asp. 607 (2020) 125498. https://doi.org/10.1016/j.colsurfa.2020.125498.

[21] L. Lin, P.S. Kollipara, Y. Zheng, Digital manufacturing of advanced materials: Challenges and perspective, Mater. Today. 28 (2019) 49–62. https://doi.org/10.1016/j.mattod.2019.05.022.

[22] X.X. Zhang, S. Cai, D. You, L.H. Yan, H.B. Lv, X.D. Yuan, B. Jiang, Template-free sol-gel preparation of superhydrophobic ORMOSIL films for double-wavelength broadband antireflective coatings, Adv. Funct. Mater. 23 (2013) 4361–4365. https://doi.org/10.1002/adfm.201203059.

[23] S. Lee, B. Kim, S.H. Kim, E. Kim, J.H. Jang, Superhydrophobic, Reversibly Elastic, Moldable, and Electrospun (SupREME) Fibers with Multimodal Functions: From Oil Absorbents to Local Drug Delivery Adjuvants, Adv. Funct. Mater. 27 (2017) 1702310. https://doi.org/10.1002/adfm.201702310.

[24] K.A. Emelyanenko, N.A. Sanzharovsky, E. V. Chulkova, A.A. Ganne, A.M. Emelyanenko, L.B. Boinovich, Superhydrophobic corrosion resistant coatings for copper via IR nanosecond laser processing, Mater. Res. Express. 5 (2018) 115001. https://doi.org/10.1088/2053-1591/aadc16.

[25] Y. Wan, M. Chen, W. Liu, X.X. Shen, Y. Min, Q. Xu, The research on preparation of superhydrophobic surfaces of pure copper by hydrothermal method and its corrosion resistance, Electrochim. Acta. 270 (2018) 310–318. https://doi.org/10.1016/j.electacta.2018.03.060.

[26] P. Dimitrakellis, K. Ellinas, G.D. Kaprou, D.C. Mastellos, A. Tserepi, E. Gogolides, Bactericidal Action of Smooth and Plasma Micro-Nanotextured Polymeric Surfaces with Varying Wettability, Enhanced by Incorporation of a Biocidal Agent, Macromol. Mater. Eng. 306 (2021) 2000694. https://doi.org/10.1002/mame.202000694.

[27] Z. He, Y. Zeng, M. Zhou, Y. Min, X. Shen, Q. Xu, Superhydrophobic Films with Enhanced Corrosion Resistance and Self-Cleaning Performance on an Al Alloy, Langmuir. 37 (2021) 524–541. https://doi.org/10.1021/acs.langmuir.0c03222.

[28] C. Howell, A. Grinthal, S. Sunny, M. Aizenberg, J. Aizenberg, Designing Liquid-Infused Surfaces for Medical Applications: A Review, Adv. Mater. 30 (2018) 1802724. https://doi.org/10.1002/adma.201802724.

[29] Sam Peppou-Chapman, J. Ki Hong, Anna Waterhouse, Chiara Neto, Life and death of liquid-infused surfaces: a review on the choice, analysis and fate of the infused liquid layer, Chem. Soc. Rev. 49 (2020) 3688–3715. https://doi.org/10.1039/D0CS00036A.

[30] Yun-Yun Quan, Zhong Chen, Yuekun Lai, Zu-Sheng Huang, Huaqiong Li, Recent advances in fabricating durable superhydrophobic surfaces: a review in the aspects of structures and materials, Mater. Chem. Front. 5 (2021) 1655–1682. https://doi.org/10.1039/D0QM00485E.

[31] J.S. Wexler, I. Jacobi, H.A. Stone, Shear-Driven Failure of Liquid-Infused Surfaces, Phys. Rev. Lett. 114 (2015) 168301. https://doi.org/10.1103/PhysRevLett.114.168301.

[32] J.S. Wexler, I. Jacobi, H.A. Stone, Shear-Driven Failure of Liquid-Infused Surfaces, Phys. Rev. Lett. 114 (2015) 168301. https://doi.org/10.1103/PhysRevLett.114.168301.

[33] F.M. Fowkes, Additivity of intermolecular forces at interfaces. I. Determination of the contribution to surface and interfacial tensions of dispersion forces in various liquids, J. Phys. Chem. 67 (1963) 2538–2541.

Chapter 6. A Study of Temperature-dependent Dynamic Fouling on Superhydrophobic and Slippery Nonwetting Copper Surfaces

The work reported in this chapter is the basis for the following journal publication currently in re view:

S.M.A. Mousavi, and R. Pitchumani. "A Study of Temperature-dependent Dynamic Fouling on Superhydrophobic and Slippery Nonwetting Copper Surfaces." In Review (2021).

6.1. ABSTRACT

Mineral fouling of heat transfer surfaces in contact with a flowing process fluid is a common cause of performance degradation in thermal and chemical engineering applications. Bioinspired, superhydrophobic and slippery liquid infused surfaces that offer nonwetting characteristics have been explored in recent years for fouling mitigation. However, most of the studies are in the context of biofouling or under static immersion at ambient temperature conditions that are not reflective of the dynamic flow environment in practice. This article presents, for the first time, a systematic study of dynamic fouling of superhydrophobic (SHS) and slippery lubricant-infused surfaces (LIS) over a range of flow and temperature conditions. Copper metallic surfaces were textured via electrodeposition or etching and further functionalized to achieve SHS and, additionally, infiltrated with a lubricant to fabricate LIS. The nonwetting surfaces were studied for their fouling behavior in a rotating Couette flow of a supersaturated calcium sulfate solution at different rotational speed and temperature. Fouling mineral mass accumulation on the different surfaces was measured as a function of time over a period of days using inductively coupled plasma mass spectroscopy and the fouled surfaces were investigated using scanning electron microscopy. Both SHS and LIS showed superior anti-scaling performance at all ranges of variables. An analytical Hill-Langmuir model is presented, for the first time, to describe the time evolution of scaling within 20% accuracy over the range of parameters studied. The study is the first to juxtapose two surface texturing methods, electrodeposition and etching, and two nonwetting surface types, SHS and LIS, subject to a common suite of experiments to elucidate fundamental understanding of mineral fouling on nonwetting surfaces.

KEYWORDS: multiscale texturing; superhydrophobicity; lubricant-infused surface; contact angle, anti-scaling; Hill-Langmuir model

6.2. INTRODUCTION

Fouling occurs on surfaces in two major ways: biological fouling and crystallization fouling; the latter—also called scaling—due to crystallization of salt ions onto a surface is the focus of this article. An excessive scaling of heat transfer surfaces by the soluble salts in a process fluid imposes performance degradation and maintenance cost. Phosphates, sulfates, and carbonates of calcium are among the salts that usually cause scaling, of which calcium sulfate is one of the most commonly reported in various industries such as seawater desalination[1], geothermal power plants working with brine[2], nanofiltration devices[3], heat exchangers[4], and condensers[5]. Consequently, there has been a lot of attention to understanding the underlying mechanism of mineral crystallization[6,7], in general, and calcium sulfate scaling, in particular[8–10].

Heterogeneous nucleation is a surface phenomenon that depends on several parameters including the saturation level of solution and surface properties like roughness and surface energy. Moreover, adhesion of the nucleated crystals to the surface is a function of surface properties as well as forces exerted from the solution to the crystal. Efforts for mitigating scaling fall into two general categories[11]. In one approach, the chemistry of the process/working fluid in contact with the metallic surface is modified in a way to deter the onset of nucleation, increase the solubility of the salt ions or dissolve the scaled salts by flowing harsh acidic fluids[12]. These methods, however, suffer from the adverse effect of the added chemicals on the fluid thermophysical properties, deterioration of the metallic surfaces themselves as well as environmental concerns of the additives[13]. The second approach of modifying surfaces to deter crystallization has attracted more attention from the scientific community in recent years[14–16]. Using this approach, studies have been reported on the scaling of calcium on different silicon surfaces with different surface energies, which suggest that lowering the surface energy on surfaces reduces scaling rate[17]. Moreover, there have been several studies on the effect of surface roughness and its effect on the extent of scaling[18–21]. Most of the literature suggests higher roughness to cause a higher scaling rate[22]; however, few studies show the reverse effect[23,24]. The contradictory observations in the literature may be attributed to the size of the surface roughness, although studies to isolate the effect of roughness are not available in the literature.

Among surface modification techniques, there has been an increasing number of studies on hydrophobic and superhydrophobic surfaces (SHS) against scaling, as well as slippery lubricant-infused surfaces (LIS) for their promising nonwetting properties. According to Jiang et al.[25], a superhydrophobic CuO nano-wire layer was formed on a Cu foil for use in the anti-scaling of $CaCO_2$. Anodization was used to create the CuO nanowire layer on the copper surface, which was the initial step. The water CA on the CuO nanowire increased dramatically after being coated with FAS-17, going from hydrophilic 4.5° to superhydrophobic 154° as a result of the decrease in surface energy. Furthermore, the scaling weight of attached $CaCO_3$ fell from 0.6322 to 0.1607 mg cm^{-2}. The test was done for 2 h at static condition in mixed solution of $CaCl_2$ and $NaHCO_3$ at 90 °C. Yu and colleagues[26] used a combination of electrodeposition and solution immersion to create a hierarchical CuO coating with nanoflake structures on a steel pipeline surface. The CuO coating became superhydrophobic after being modified with pentadecafluorooctanoic acid. They concluded the anti-scaling properties of the modified surfaces based on the shape of the deposited calcium crystals. The anti-scaling was investigated by immersing the steel sample in a 100 mL solution comprising 0.01 mol/L $CaCl_2$ and 0.01 mol/L $NaHCO_3$. The beaker was then placed in a water bath at 70°C for 6 h.

Qian et al.[27] developed a superhydrophobic polymer coating based on poly(phenylene sulfide)/polytetrafluoroethylene (PPS/PTFE) composites. The superhydrophobic coating was created by combining spraying coating with thermal solidification on steel as the substrate. The deposition rate of scaling on the superhydrophobic PPS/PTFE coating was 38.6% of that on the hydrophobic epoxy-silicone resin coating. The scaling experiment was done by static immersion in calcium containing solution at 60 °C. Charpentier et al.[28] used liquid-infused porous surfaces to investigate their potential to suppress $CaCO_3$ scale formation. They began by covering stainless steel substrates with microporous polypyrrole (PPy) coatings. Then, lubricant liquids with low surface energy, such as fluorinated lubricant (FC-70) and ionic liquid were infused to create liquid-repellent slippery surfaces. They discovered that PPy surfaces infused with ionic liquid had exceptional antifouling capabilities after 2 h immersion in static bulk jar of calcium carbonate at 50 °C when compared to untreated stainless steel.

Varanasi and colleagues[16] presented lubricant-impregnated nanostructured surfaces to obtain the requisite resistance to mineral scales. Using reactive ion etching, they first created a flat silicon surface with nanograss structures. To reduce its surface energy, they treated it with

octadecyltrichlorosilane (OTS). Silicone oil and DC704 have been impregnated further into the OTS-coated nanograss substrate, respectively. In a static test bath of $CaSO_4$ at 40 °C for 80 hours, the silicone oil-impregnated nanostructured silicon surface displayed antiscaling capabilities when compared to the uncoated smooth silicon surface. Similarly, LIS were made by infusing Krytox105 silicon oil into electropolymerized and silanized porous polyaniline, as described by Sousa et al.[29] In short, hierarchically rough polyaniline was electropolymerized onto stainless steel substrates and then further functionalized with low polarizability thiols (1H, 1H, 2H, 2H-perfluorodecanethiol, PFDT) to create superhydrophobic surfaces. LIS have a better preventive effectiveness against inorganic scales than nonlubricated surfaces. The tests were carried out for in static jar test at room temperature for 16 h.

It is evident from the foregoing discussion that while scaling on SHS and LIS under static conditions is well-studied, there is a conspicuous shortage of studies exploring the response of SHS and LIS to scaling under dynamic flow conditions that are encountered in several applications. Furthermore, there is nearly no theoretical model available for scaling that can be used for designing the surfaces for applications or for understanding the extent of scaling on a target surface.

The goal of the present study is to address the above knowledge gaps by considering scaling of calcium sulfate, the most common contributor to scaling in the industry, on copper, a widely used heat transfer surface in engineering systems. Copper metallic surfaces were textured and further functionalized to achieve SHS and, additionally, infiltrated with a lubricant to fabricate LIS. Surface texturing was achieved using electrodeposition, an additive method, or chemical etching, a material removal method. Systematic parametric experiments were conducted to explore, for the first time, the effects of dynamic flow conditions and temperature on scaling of SHS and LIS fabricated by the two methods. A Hill-Langmuir relationship is developed based on experimental data to model time evolution of scaling on nonwetting surfaces. The study juxtaposes, for the first time, two surface texturing methods, electrodeposition and etching, and two nonwetting surface types, SHS and LIS, subject to a common suite of experiments.

The article is organized as follows: In the next section, section 2, the experimental methods for fabrication of surfaces, dynamic fouling, and surface characterization are presented. Results of the full set of parametric tests on dynamic fouling and the kinetic model are described in section 3 on Results and Discussion. The principal findings of the study are summarized in section 4.

6.3. EXPERIMENTAL METHODS

6.3.1. **Materials and reagents**

Hydrochloric acid (HCl), analytical-grade copper sulfate ($CuSO_4$, 99+%), sulfuric acid (H_2SO_4), acetone (99.5+%), methanol (99.8+%), and stearic acid ($CH_3(CH_2)16CO_2H$, 97%) were purchased from Fisher Scientific (Pittsburgh, PA, USA) and used as received without any further purification. Hydrogen peroxide solution (H_2O_2) was purchased from Sigma-Aldrich (St. Louis, MO, USA), deionized water of resistivity 14MΩ.cm was purchased from CQ Concepts (Ringwood, IL, USA), silicone oil, Dowsil500™, was purchased from DuPont (Wilmington, Delaware, USA), and plain multipurpose copper sheet was purchased from McMaster (Elmhurst, ILUSA).

6.3.2. **Fabrication of nonwetting surfaces**

Fabrication of superhydrophobic (SHS) and lubricant-infused surfaces (LIS) was carried out by first texturing the surface, functionalizing the textured surface to create SHS, and additionally by infiltrating the porous textures with a lubricant liquid to create LIS. The as-received copper sheet was cut into coupons of 1×5 cm, and the coupons were degreased and cleaned by 5 minutes sonication in acetone, followed by 5 minutes sonication in ethanol, then rinsed with DI water and dried in a nitrogen stream. In the material *removal* method of texturing, the roughness features were carved into the surface via chemical etching in an aqueous solution of 0.02 M hydrochloric acid and 0.05 M hydrogen peroxide. The cleaned and cut coupons were submerged in the etchant solution for 20 minutes. In the *additive* method of texturing, multiscale asperities were grown on top of the copper surface by a three-electrode, two-step electrodeposition process[30],[31] using an AUTOLAB PGSTAT128N electrochemical station (ECO Chemie, Utrecht, The Netherlands). A platinum mesh was used as the counter electrode and Ag/AgCl served as the reference electrode. De-aerated aqueous solution of 1M $CuSO_4$ and 0.5M H_2SO_4 was used as the electrolyte. The two-step electrodeposition process was initiated by applying –1.1 V for 5 minutes to the copper sample as the working electrode followed by a 10 second electrodeposition at –0.15 V as the second step. The second deposition served to further stabilize the first coating onto the surface.

All the prepared textured surfaces were rinsed in DI-water bath and dried under vacuum at 110 °C overnight. As the next step, the textured surfaces were chemically functionalized via 24 h immersion in 0.02M stearic acid, which provided for reducing the surface energy through chemisorption of the long-chain fatty acids onto the surface. Stearic acid is chosen as an environmentally friendly chemical[32] compared to the other functionalization agents such as silane and perfluorinated compounds that are toxic[16,33,34]. The stearic-acid-functionalized surfaces exhibited a water contact angle over 150 degrees with low surface energy, forming superhydrophobic surfaces. LIS was fabricated by infusing the SHS with lubricant oil. Drops of Dowsil^{TM} silicone oil with 500 cSt viscosity were placed onto the SHS and hanged vertically for twenty minutes to allow for the lubricant to wick into the interasperity spaces and to drain any excess oil.

The SHS and LIS fabrication processes are versatile in their applicability to a variety of metallic materials of complex geometry and size. Copper was chosen as one of the ubiquitously used materials to perform dynamic scaling experiments.

6.3.3. **Dynamic fouling setup**

Dynamic fouling was studied using an annular Taylor-Couette flow[35] set up in which a rotating cylindrical drum of radius 10 cm was placed concentric inside an outer stationary cylindrical tank of radius 18 cm, as depicted in Figure 6.1. The rotation of the inner drum was driven by a motor with a vertical shaft, such that the rotational speed can be set to desired values. The annulus between the inner cylindrical drum and the outer cylindrical tank was filled with supersaturated $CaSO_4$ solution in water. The test coupons were mounted on the outer surface of the inner drum such that the they experienced a dynamic shear due to the rotational fluid flow in the annulus. The setup was placed on a hot plate so that the solution can be heated to a desired temperature, measured using a thermometer with a digital readout, immersed in the solution in the annulus. A feedback control loop was used to control the hot plate to achieve a set point temperature of the scaling solution. The open tank configuration follows that used in static scaling studies in the literature[17,36], and provided for maintaining solution supersaturation required for crystallization.

Dynamic fouling experiments were conducted on superhydrophobic and lubricant-infused copper surfaces fabricated by electrodeposition and etching, at three rotation rates of 100, 200 and

400 rpm, and at two different temperatures, 23 °C and 50 °C. In addition, for reference, dynamic fouling studies were also conducted on bare copper coupons at the three rotational speeds and the two temperature values. In each case, to understand the time evolution of scaling, coupons were removed at time durations of 12, 24, 48, 96 and 192 hours from the start of the experiment. Three replicates were analyzed at each parametric combination of surface type, rotation speed, temperature, and time duration for a total of 240 in the overall experimental matrix.

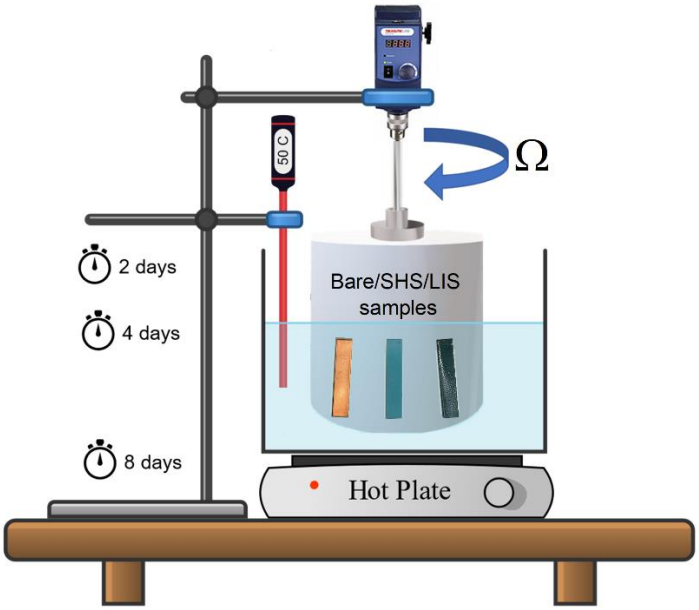

Figure 6.1. Schematic of the dynamic scaling setup depicting metallic coupons mounted on the outer surface of the inner rotating drum in a stationary cylindrical tank filled with $CaSO_4$ hemihydrate solution.

6.3.4. **Characterization**

Samples of the different surface types and fabrication methods were characterized for their surface morphology and wetting characteristics. Surface morphology was revealed via a field-emission scanning electron microscope (SEM) (JEOL 2100, Japan), operating at an acceleration voltage of 20 kV connected to an energy dispersive x-ray analyzer (OXFORD, UK). Optical image of lubricant infused surfaces was obtained via Nikon Eclipse LV100ND Microscope (Nikon Instruments Inc.) equipped with an epifluorescence filter. The apparent contact angle of the surfaces was characterized by a goniometer (ramé-hart model 590, NJ USA) via sessile droplet method and 10 µl DI-water and at least at five different positions on each sample. The sliding angle was measured via tilting plate method by the same apparatus with 25 µl DI-water.

Weight measurement of the samples before and after the fouling tests is a common way of quantifying the extent mineral deposits in static tests. In a dynamic test, however, since there might be loss of infused liquid, functionalization material, or the base material iteslf from the surface due to shear, erosion or corrosion, an alternative method was used. Following removal of a coupon from the dynamic fouling setup, the sample was dried for 24 hours at room pressure and temperature to remove any moisture. The dried coupon was immersed in 10 ml of 10% nitric acid (HNO_3) for 10 minutes to dissolve the scaled material into the solution. The solution was then diluted and prepared for measurement of calcium concentration using inductively coupled plasma mass spectroscopy (ICP-MS) (Thermo Electron X-Series, Waltham, MA, USA), which had an accuracy of 0.5 $\frac{\mu g}{L}$. The ICP-MS results on the scaling mass were divided by the sample planar surface area to obtain mass gain per unit surface area—termed *fouling density,* m_f''—for a quantitative characterization of fouling.

6.4. RESULTS AND DISCUSSION

The results of study are discussed in this section, organized as follows: surface morphology and wettability of the different surfaces are presented first in section 3.1, followed by the parametric effects of the rotation rate, temperature and surface type on the fouling of the surfaces in sections 3.2–3.4, respectively. A model based on the Hill-Langmuir relationship describing the time evolution of fouling on the different surfaces is presented in section 3.5.

6.4.1. **Surface wettability and morphology**

Surface wetting properties of the electrodeposited and etched SHS and LIS were measured in terms of deionized water contact angle (CA) and sliding angle (SA). As shown in Figure 2(a), the electrodeposited and etched copper surfaces after 24 h functionalization in stearic acid exhibit contact angle above 155° (orange markers) and very low roll-off angle below 5° (blue markers) which categorize them as superhydrophobic surfaces (SHS) in contrast to bare copper with contact angle of 82° ± 3.4°. Both the electrodeposited and etched lubricant-infused surfaces (LIS) revealed an apparent contact angle of ~92° (orange markers) and a water sliding angle below 5° (blue markers) that attest to the excellent slipperiness and self-cleaning characteristic of the surfaces.

The morphology of the copper surface textured by electrodeposition and functionalized with stearic acid is shown in the scanning electron microscope (SEM) image in Figure 6.2(b). The inset in the figure shows the surface prior to functionalization and reveals that the Cu^{2+} cations were deposited onto the surface in the form of Cu(s)[37] cauliflower-shaped features. The multiscale features covered the surface uniformly with micro and macro size cauliflower asperities exhibiting average diameter as small as 5 μm and as big as 30 μm. After functionalization with stearic acid, the cauliflower asperities were covered with the thin (nanometer thickness) leaflike chemisorbed functionalization agent in final form of dahlia-flowerlike structures as seen in the main image of Figure 6.2(b). Figure 6.2(c) shows the microstructure of an etched, functionalized copper surface. The inset micrograph in Figure 6.2(c) reveals random nano/micro-sized grooves on the as-etched surface before functionalization. The surface morphology of the functionalized etched copper in Figure 6.2(c) shows the surface to be carpeted with needle-like chemisorbed stearic acid to cover the surface with a needlelike carpet and sparse pom-pom ball structures in varying sizes up to about 20 μm in diameter. The higher surface area of the textured surfaces compared to the bare surface provides for chemisorption and growth of the stearic acid structure seen in Figure 6.2(b) and (c).

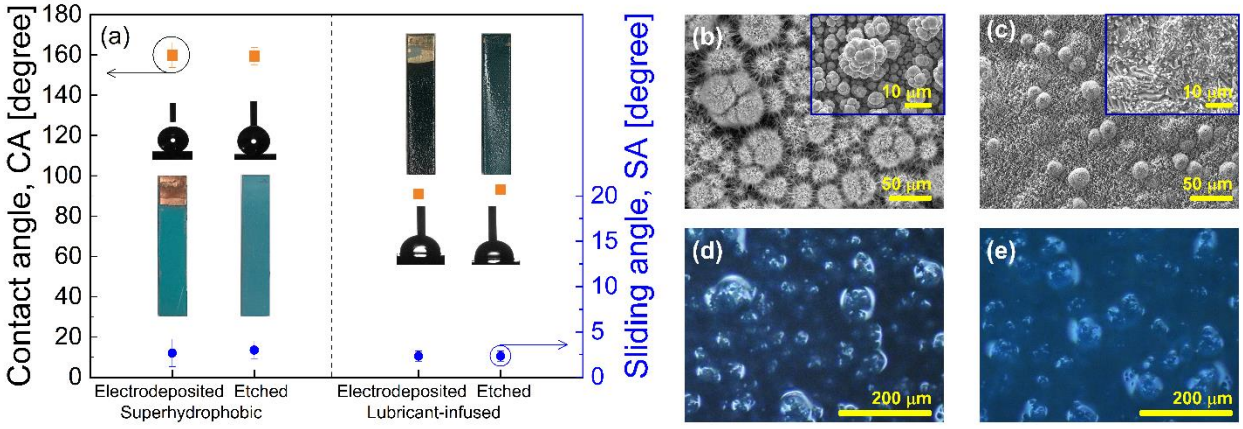

Figure 6.2. Nonwetting properties and morphology of textured and modified copper surfaces: (a) water contact angle and roll-off/sliding angle of SHS and LIS fabricated via electrodeposition and etching. Inset images are of 5 cm × 1 cm fabricated coupons; SEM images of (b) electrodeposited, functionalized SHS, inset showing unfunctionalized electrodeposited copper surface, and (c) etched, functionalized SHS, inset showing unfunctionalized etched copper surface; Optical images of (d) electrodeposited and (e) etched LIS.

Optical images of electrodeposited and etched LIS are shown in Figure 6.2(d) and (e), respectively. The underlying dahlia-flowerlike functionalized asperities of electrodeposited LIS appear prominent after the lubricant infusion compared to the pom ball-like structure of the etched LIS. This can be attributed to the differences between the size and sparsity of these structures on the two surfaces.

6.4.2. **Effect of rotation rate on dynamic fouling**

The effect of shear due to fluid flow on the extent of scaling on the nonwetting surfaces in comparison to the bare copper surface was studied through a suite of parametric tests that spanned three different rotational speeds and two temperatures. The Reynolds number corresponding to the rotational speeds of 100, 200, and 400 rpm are 49,000, 99,000, and 198,000, respectively, which correspond to the turbulent flow regime. As a point of reference, the Reynolds number for coolant water flow in a typical power plant condenser pipe of 23 mm internal diameter and flow speed of 1.8 m/s–2.5 m/s is in the range 44,000–62,000. The considered range of Reynolds number in the parametric studies elucidate the scaling dynamics for applications of the advanced functional surfaces to high flow rate and/or large pipe flows.

The time-evolution of fouling density (m_f'') for the as-received bare copper is shown in Figure 6.3(a) for different rotation rates at 23 °C . Regardless of the rotational speed, the measured mineral fouling mass density reached a steady state, called the asymptotic fouling mass density, $m_{f\infty}''$, at long duration in the experiments. Figure 6.3(a) further demonstrates a significant change in m_f'' and, in turn, $m_{f\infty}''$ with the rotational speed: the highest calcium deposition was recorded at 100 rpm as $m_{f\infty}''$ = 5 mg/cm^2, which decreased with increase in the rotational speed. Mineral deposition on the surface results from an equilibrium between the adhesion forces that draw the minerals to the surface and the shear forces due to the flow that tend to remove the mineral deposits from the surface. The observed decrease in $m_{f\infty}''$ with rotational speed correlates with the increased shear stress with increasing rotation rate (Reynolds number) that shifts the equilibrium towards lower fouling density.

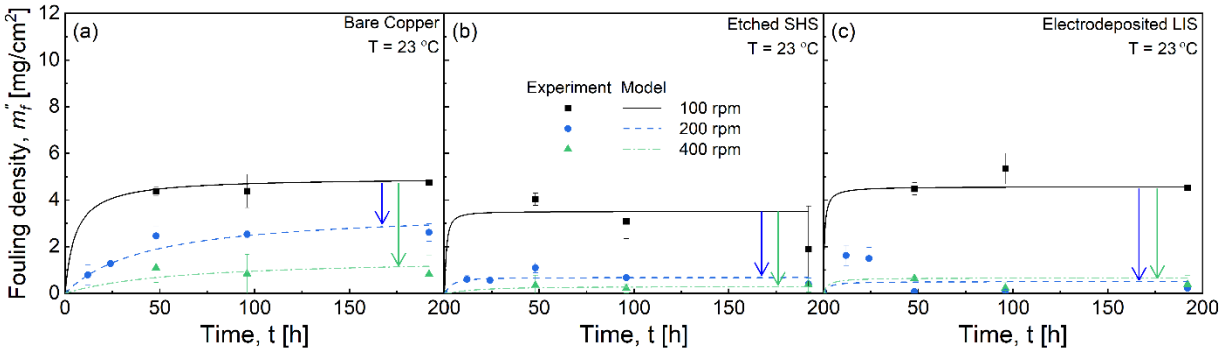

Figure 6.3. Effect of rotation rate on fouling density evolution with time for (a) bare copper, (b) etched SHS, and (c) electrodeposited LIS, at 23 °C.

Similar parametric tests were performed for SHS and LIS fabricated via electrodeposition and etching. For brevity, one set of results for etched SHS and electrodeposited LIS is illustrated from the full parametric test experimental matrix, in Figure 6.3(b) and 3(c), respectively. The physical trends with respect to time and rotation rate follow those for the bare surface. Of note is the reduction in the asymptotic fouling density for SHS and LIS compared to the bare surface, which is particularly significant at the higher rotational rates. The result points to the fact that for a given rotation speed, since the shear forces are identical across surface types, the nucleation of fouling and adhesion of minerals on the nonwetting SHS and LIS is significantly reduced compared to the bare surface, which leads to beneficial reduction in $m''_{f\infty}$. The lines through the experimental data markers in Figure 6.3 are obtained from the Hill-Langmuir model discussed later in this section.

6.4.3. **Effect of temperature on dynamic fouling**

Calcium sulfate in all its hydration forms, hemihydrate and dihydrate, exhibits an inverse solubility variation with temperature which, in turn, manifests in the differing fouling behavior with temperature. In practical applications, process fluids flow at different temperatures, and it is of interest to understand the effect of temperature on the extent of scaling. To this end, dynamic fouling studies were conducted at a low temperature of 23 °C, and a high temperature of 50 °C. The amount of calcium sulfate hemihydrate dissolved into DI water was chosen based on the solubility curve and to maintain the same supersaturation level at the two temperatures.

Figure 6.4(a) depicts the effect of temperature on the extent of scale mass gain on the as-received bare copper coupons versus time, for an intermediate rotational speed of 200 rpm. The fouling density is seen to be higher at 50 °C due to the higher rate of nucleation and the higher rate of crystallization growth. Based on heterogeneous nucleation theory[38], nucleation rate varies as the temperature to the power of 3 while crystal growth rate varies linearly with temperature, both contributing to the higher fouling density with increasing temperature. The aggressive fouling combined with the fact that the solubility of calcium sulfate hemihydrate at 50 °C is about 40% lower than that at 23 °C, the scaling is seen to reach an asymptotic value at the lower temperature, but not at the higher temperature, in the duration of the experiments.

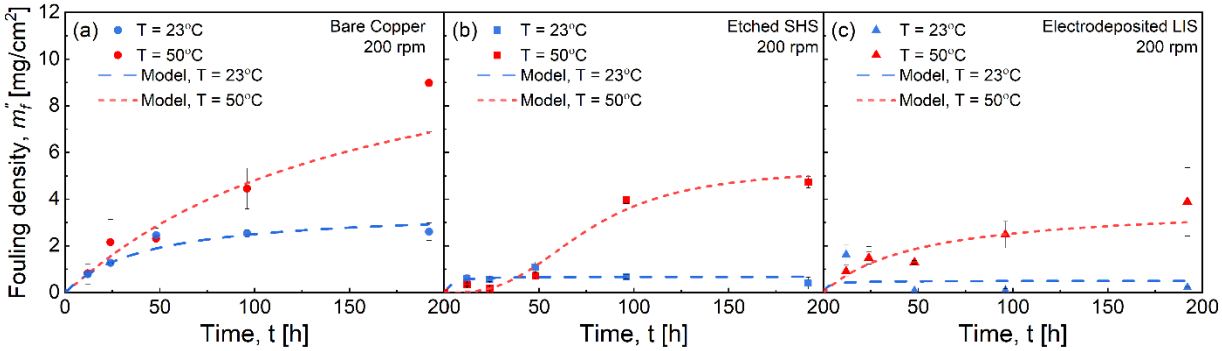

Figure 6.4. Effect of temperature on fouling density evolution with time for (a) bare copper, (b) etched SHS, and (c) electrodeposited LIS, at 200 rpm.

Figure 6.4(b) and 4(c) present the effect of temperature on the time-evolution of dynamic scaling for etched SHS and electrodeposited LIS, respectively, at a rotational speed of 200 rpm. Both plots show the enhanced scaling at the higher temperature, following the trend in Figure 6.4(a); however, at each temperature, the fouling density is lower for the nonwetting surfaces in comparison to the corresponding fouling density of the bare surface, due to the lower surface energy of SHS and LIS which weakens the adhesion and growth of the mineral deposits on the surface. The reduced strength of adhesion and driving force for deposition relative to the removal of the deposits by shear, also manifests in attaining the asymptotic fouling density at an earlier time for the nonwetting surfaces at 50 °C (Figure 6.4(b) and 4(c)), compared to the bare surface at the same temperature (Figure 6.4(a)). As in Figure 6.3, the lines through the experimental data markers in Figure 6.4(a)–(c) are obtained from the Hill-Langmuir model discussed later in this section. Overall, even though increase in temperature intensifies the rate of scale nucleation and

the rate of scale crystal growth, the nonwetting surfaces fabricated in this study are seen to inhibit scaling significantly. Moreover, SHS and LIS in the study also withstood the higher temperature condition of the tests without degradation.

6.4.4. **Effect of surface type on dynamic fouling**

While Figure 6.3 and 4 showed the effects of rotation rate and temperature considering selected nonwetting surfaces, it is instructive to examine the effects of fabrication and surface type on the resulting scaling of the surface under dynamic conditions. To this end, Figure 6.5 juxtaposes the different surfaces and fabrication methods with regard to the fouling density at three different times, for the case of 200 rpm at 23 °C. The results reveal that in comparison to bare copper all the nonwetting surfaces are characterized by significantly reduced fouling density. Among the nonwetting surfaces, LIS, regardless of fabrication method, is generally seen to inhibit fouling better than SHS owing to the infused liquid layer that presents less area for fouling deposits compared to the correspondingly fabricated SHS. Of the two fabrication methods, electrodeposition yields greater scaling mitigation compared to etching, owing the rougher multiscale asperity morphology and greater nonwettability of the surface. In the case of electrodeposited LIS, the deeper asperity structures allow for greater lubricant infusion and retention, increasing the resistance to scaling. With respect to the asymptotic fouling density (192 h), however, there is no distinct difference between the two fabrication methods or surface types. They all lead to over 75% reduction in fouling density compared to bare copper.

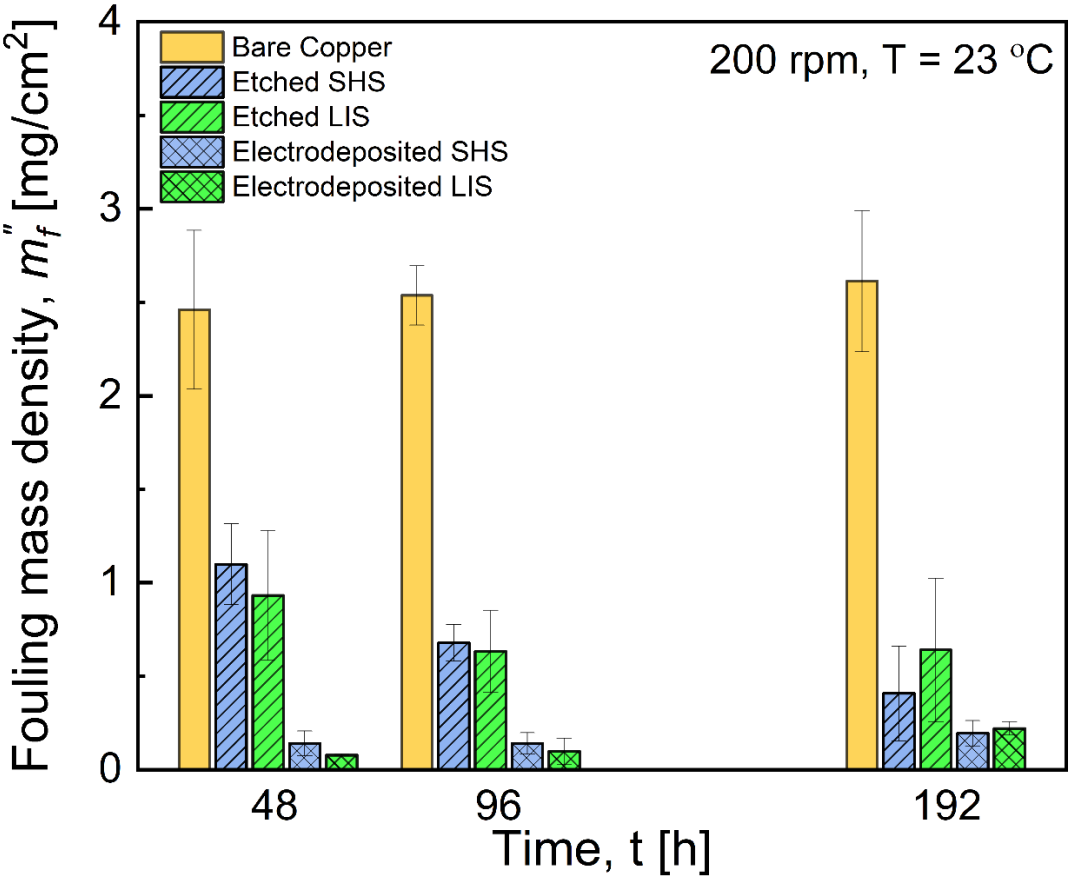

Figure 6.5. Variation of fouling density with time for the different surface types, at 200 rpm and 23 °C.

The effect of surface type on dynamic scaling was further investigated qualitatively via surface images after scaling for 48 h in the dynamic fouling experiments. Figure 6.6 shows SEM and optical images of bare, etched superhydrophobic and electrodeposited lubricant-infused copper surfaces after the dynamic scaling test at 200 rpm and 23 °C. The SEM image in Figure 6.6(a) shows extensive areas of scaling on the bare copper surface, while the SEM and optical images of SHS and LIS in Figure 6.6(b) and 6(c) reveal the sparsity of scaling deposits on the nonwetting surfaces. Quantitatively, over 60% of the surface area of the bare copper is covered with calcium sulfate deposits, while at the similar test condition the SEM image of etched superhydrophobic surface in Figure 6.6(b) shows ~4% surface area covered with foulant. In the optical image of the electrodeposited LIS, Figure 6.6(c), very small surface area (less than 4%) is seen to be covered with foulant. The extent of surface coverage is in agreement with the fouling density measurements from the ICP-MS reported in Figure 6.3–5.

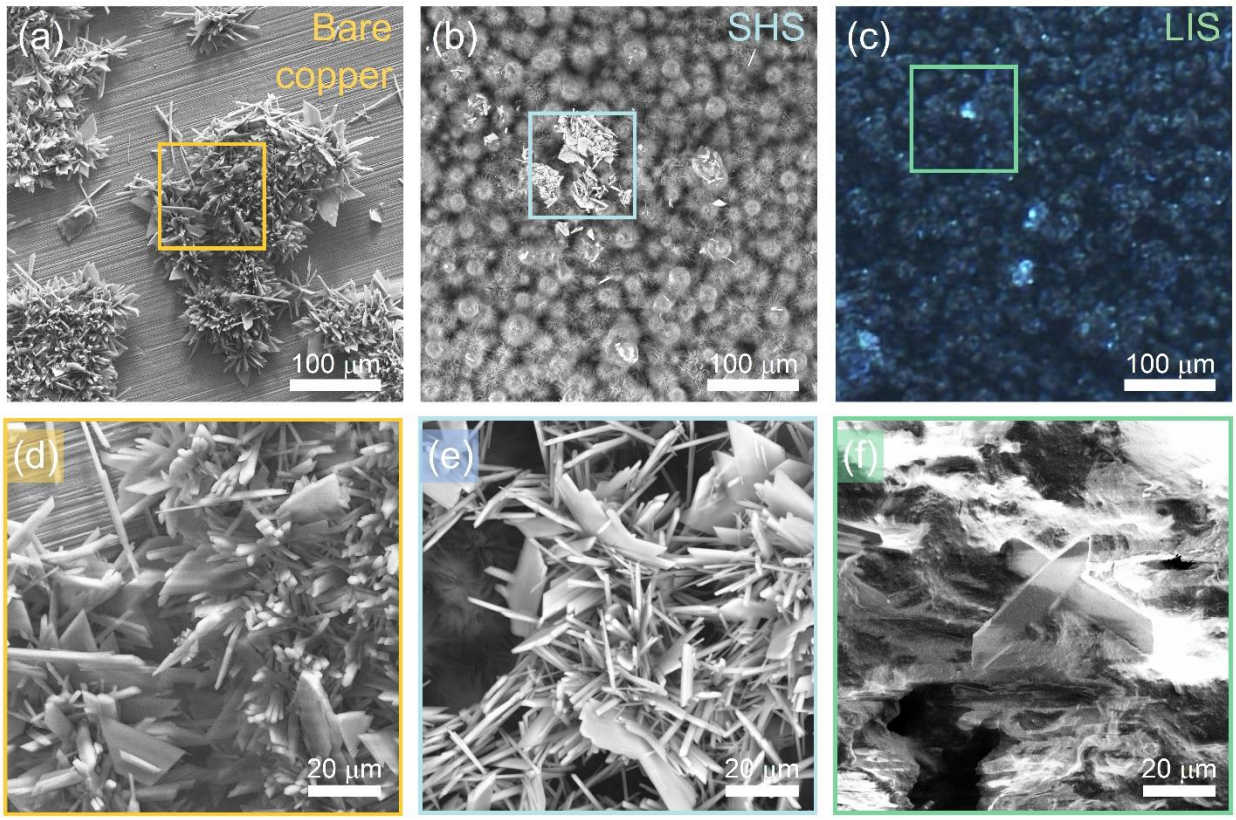

Figure 6.6. SEM and optical images of copper surfaces after 48 h dynamic scaling experiment at 200 rpm and 23 °C: SEM images of (a, d) bare copper, (b, e) etched superhydrophobic copper, (f) electrodeposited lubricant infused copper, and (c) optical image of electrodeposited lubricant infused copper surface taken with fluorescent filter.

The higher magnification SEM images in Figure 6.6(d-f) reveal more of the morphology and structure of calcium scaling on the bare, superhydrophobic and lubricant infused copper surfaces. The crystalline structure of the deposits is evident in all the micrographs that result from ion packing inside the crystal lattice such that attractive forces are maximized and repulsive forces are minimized[39]. Figure 6.6(d,e) show rhombohedral crystal units grown and accumulated on the stepped and kinked faces (S and K faces) forming two-dimensional leaf-like flakes on bare and superhydrophobic copper surfaces, along with accumulation on flat face (F face) to form needle-like gypsum crystal structure with rhombohedral and mostly hexagonal plane. The leaf-like flakes are consistent with the maple-leaf-like calcite crystals reported on CuO nanowire films in the literature[25]. The relatively scant calcium sulfate deposits on LIS in Figure 6.6(f) are seen to be

in form of the needlelike crystals. Overall, Figure 6.6 shows the anti-scaling effect of the nonwetting surfaces and supports the quantitative findings in Figure 6.3–5.

6.4.5. **Modeling**

Modeling of fouling on conventional surfaces has been studied in prior literature[40],[41], as reviewed in treatises such as Webb and Li[42]. In general, fouling models for conventional surfaces fall into one of four categories: linear, falling-rate, power law, and asymptotic or sigmoidal. The wide range of models reflects the large uncertainty inherent in the fouling process itself[43,44]. There is no prior modeling effort reported to describe scaling on nonwetting surfaces, and the present study seeks to contribute the first model describing scaling on SHS and LIS as well as smooth surfaces, in a generalized manner. To this end, we adopt a model that is a good representation of the experimental data, has a closed-form mathematical expression, and has a physical correlation to the phenomenon being modeled.

The measured experimental data on time evolution of fouling density in this study (Figure 6.3 and 4) show not only sigmoidal trends but also a power law variation. Such data can be well-described by the Hill-Langmuir equation[45,46] that is widely used in biochemistry for explaining different phenomena such as binding of ligands to macromolecules[47].

$$m_f'' = \frac{m_{f\infty}''}{1 + \left(\frac{k}{t}\right)^n} \quad (1)$$

where $m_{f\infty}''$ is the asymptotic fouling density introduced previously, n is the Hill exponent, and k is a time constant. The model is versatile in being able to represent both sigmoidal and power-law trends in data depending on the exponent, n.

The originality of this work is in using the Hill-Langmuir relationship for the first time in predicting foulant binding and growth on wetting and nonwetting surfaces. The model also bears clear physical significance of the parameters. The parameter n, mathematically, is a measure of ultrasensitivity of the relationship to time and, physically, is a measure of cooperativity in biochemistry. In this work, the cooperativity concept is related to the change in the affinity of the surface for fouling as the nucleation and binding progresses such that, $n > 1$ denotes positive cooperation, $n < 1$ signifies a negative cooperation, and $n = 1$ is interpreted as a completely

independent binding. The parameter k is the characteristic time for the half of the asymptotic maximum fouling mass, $m''_{f\infty}$, to deposit on the surface, and is physically significant in its importance in guiding system cleaning and maintenance.

As mentioned earlier, the asymptotic fouling density, $m''_{f\infty}$, represents an equilibrium between the effects of binding of the minerals on to the surface, measured in terms of a foulant material hardness, and the shear stress that tends to remove the deposits, and may be expressed as[41]:

$$\boldsymbol{m''_{f\infty} = \frac{K_D C_b p \psi}{\tau_a}} \quad (\mathbf{2})$$

where K_D is particle deposition coefficient (m/s), C_b is bulk ion concentration (kg/m^3), p is the sticking probability and a dimensionless parameter, ψ, is scaling bond strength (N.s/m^2), and τ_a is shear stress (N/m^2) at the rotating drum surface. The particle deposition coefficient, K_D, is assumed to be equal to the mass transfer coefficient K_m that is related to the Schmidt number of the scaling solution through the Chilton-Colburn analogy[48]. This assumption holds for typical thermal engineering systems where the particle deposition is controlled by Brownian motion[49,50]. The bulk ion concentration, C_b, is constant for fixed temperature and is set to the corresponding saturation level: 7 kg/m^3 for 23 ℃ and 5 kg/m^3 for 50 ℃. Surface properties, such as the nonwetting properties and surface energies, are reflected in the scaling bond strength of ψ, whereas the effect of the rotation rate reflects itself in the shear stress τ_a. Moreover, the surface properties affect the nucleation reaction activation energy, E, that with temperature, T, both affect the sticking probability as given by the empirical relationship of Watkinson and Epstein[51], $p = \frac{C'}{u^2}\exp\left(-\frac{E}{RT}\right)$, in which C' is constant, R is universal gas constant, and u is the flow velocity. Note that the probability of binding increases with temperature and decreases with increased flow velocity. The activation energy is higher for nonwetting surfaces having low surface energy[17], which reduces the probability of fouling deposition.

Equation (2) suggests that the asymptotic fouling density increases with parameters that improve adhesion and binding of foulants on the surface namely, surface wettability and temperature and decreases with increasing shear due to flow. Table 6.1 presents the values of $m''_{f\infty}$, k and n obtained from a least-squares regression fit of the Hill-Langmuir model, Equation (1), to the asymptotic fouling density measured in full suite of experiments covering the different surface

type, fabrication route, temperature and rotational speed. The following physical trends are elucidated by the parameter values in Table 6.1:

- The *asymptotic fouling density,* $m''_{f\infty}$, uniformly decreases with increasing rotation rate for all the surfaces, owing to the increased shear stress, τ_a, on the surface and is consistent with Equation (2), where the shear stress in the denominator has an inverse relationship with asymptotic fouling mass gain on the surface.

  Further, $m''_{f\infty}$ is lower for the nonwetting surfaces compared to the bare surface, reflecting the decrease in fouling bonding strength ψ which corresponds to decrease in surface energy of the nonwetting surfaces.

  Table 6.1 shows that the initial reduction in $m''_{f\infty}$ with rotational rate (from 100 rpm to 200 rpm) for the nonwetting surfaces is more dramatic compared to the bare copper surface, which is attributed to the lower adhesion strength of crystalized scale to the nonwetting surfaces. The almost zero slope between 200 rpm and 400 rpm for the nonwetting surfaces confirms that their anti-scaling effect is due to the lower surface energy rather than just the higher shear stress at the higher flow rate.

  The increase in $m''_{f\infty}$ with temperature in Table 6.1 is consistent with the increase in the sticking probability, p, through its Arrhenius relationship with temperature.

- The *parameter* k denotes the time for half population of possible nucleation sites, which increase with increase in rotation rate. An increase in rotation rate leads to a higher shear stress that, in turn, increases the removal rate and leads to a delayed foulant accumulation. Moreover, the value of k increases with increasing temperature, which reflects the fact that the asymptotic fouling density is higher at the higher temperatures, correspondingly necessitating a longer duration to achieve half the asymptotic value.

- The *parameter* n is about unity for bare copper at both room and higher temperature. The value of $n = 1$ corresponds to independent cooperativity which means that the affinity of the bare copper surface to fouling binding does not change with time. This is expected as the bare surface already carries surface defects suitable for nucleation and crystal growth. On the other hand, the SHS with low surface energy has a high activation energy and hence lower nucleation rate compared to the bare case. As the first nuclei grow on the SHS the roughness and the local surface energies increase, which then increases the affinity of the surface for further fouling binding. This physical significance is clearly observed in the $n > 1$ values recorded for SHS

in Table 6.1. The etched SHS has a higher affinity parameter than electrodeposited SHS, and furthermore, the affinity is greater at the higher temperature. The cooperativity coefficient n was recorded equal to 1 for LIS. Although LIS has low surface energy similar to SHS the dynamic nature of the infused lubricant causes wetting and cloaking of the deposited fouling, as imaged in Figure 6.6(c) and (f), which prevents change in the affinity of the LIS for fouling binding with time.

With the foregoing physical insights, the accuracy of the Hill-Langmuir model is investigated in Figure 6.7, which compares the fouling mass density predicted by the model (abscissa) with that obtained from the experimental measurements (ordinate) for all surfaces, fabrication methods, time, temperature and rotational speed studied, for a total of 60 points including the three rotation rates of 100 rpm, 200 rpm, and 400 rpm at 23 °C and 200 rpm at 50 °C, all for three times of 48 h, 96 h, 192 h. The different conditions of the experiments are denoted by the various markers as indicated in the plot. For the sake of clarity, experimental error bars around the mean values presented are omitted. The solid line diagonal to the plot frame denotes the line of exact agreement, while the dashed and the dash-dotted lines, respectively, represent the 10% and 20% error bars around the exact agreement. Overall, the Hill-Langmuir model with the associated parameters presented in Table 6.1 is seen to be effective in predicting the time-evolution of fouling over time: ~85% of all data lies within the 20% error bands, with most of the points lying outside the 20% error are very low fouling mass values below 1 mg.cm^{-2}. Considering the experimental measurement error bars, the proposed model has an accuracy of over 95% of data falling within the 20% error band. In comparison, the logistic regression model[43], when applied to the present data, was only 60% accurate with an 80% confidence interval[44]. Considering that crystallization is inherently a stochastic process in its nature, the model is exceptionally accurate in predicting the fouling on smooth as well as nonwetting surfaces fabricated by the two different approaches.

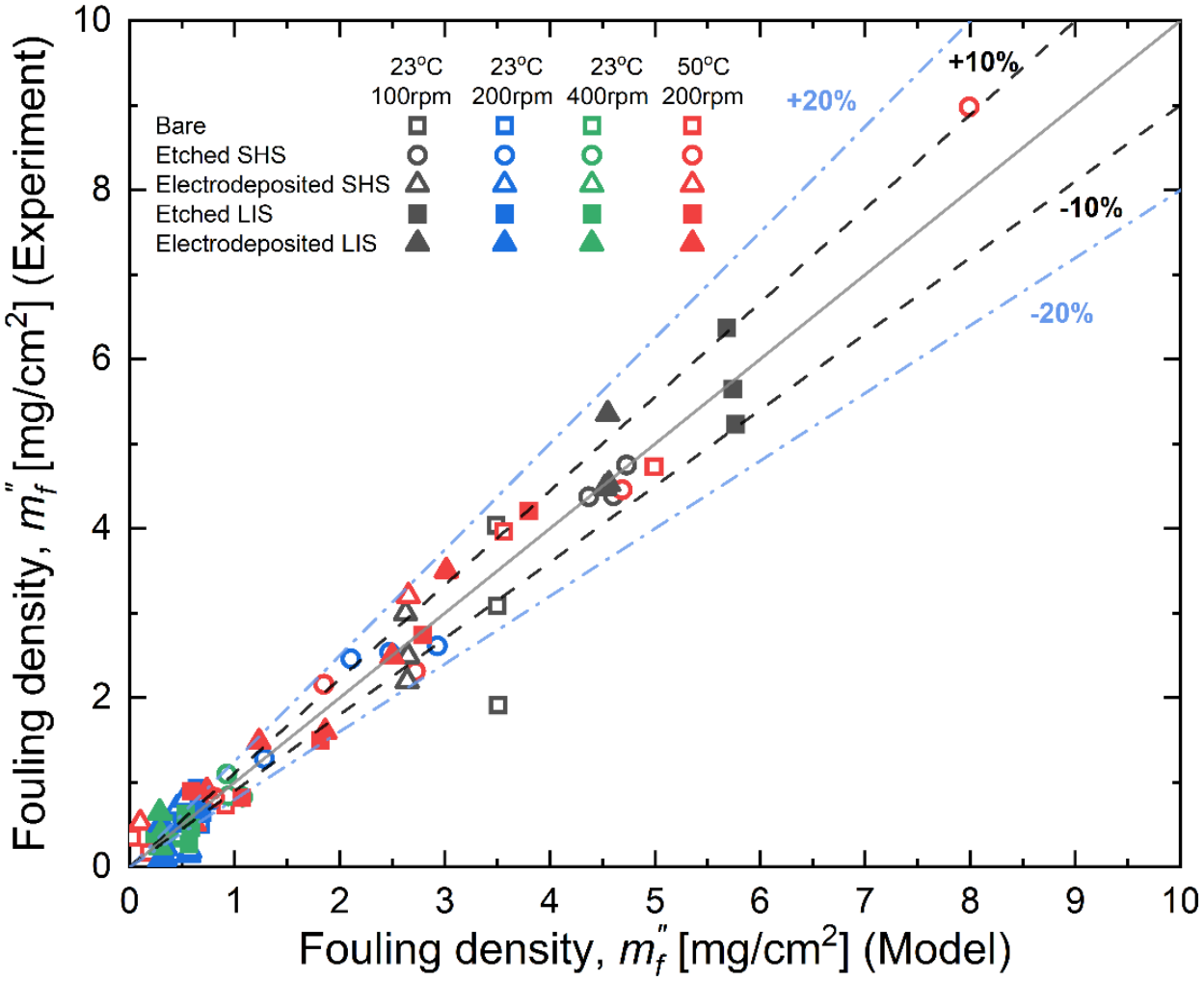

Figure 6.7. Comparison of the predictions of the Hill-Langmuir model with experimental measurements of fouling density for all the surfaces, rotational rate, and temperature studied, after 48 h, 92 h, and 192 h of immersion in calcium sulfate hemihydrate supersaturated solution.

It is seen throughout the results presented in this article that nonwetting surfaces fabricated by either method demonstrate significantly reduced fouling compared to bare copper surface in a wide range of dynamic conditions. The effectiveness of the presented method for fabrication of nonwetting surfaces on copper may be extended to other materials such as brass and aluminum. The scaling mitigation on these surfaces are also of much practical significance and will be explored in a future work.

6.5. CONCLUSIONS

The study presented the first systematic analysis of temperature-dependent dynamic fouling of calcium sulfate hemihydrate on superhydrophobic and lubricant-infused surfaces *vis-à-vis* bare surfaces using a Taylor-Couette flow setup. The effect of fabrication method on the performance of the resulting SHS and LIS was also assessed. Through systematic experiments, the time evolution of fouling mass per unit surface area was developed for a range of rotational speed and temperature. The study led to the following salient findings:

1. While bare copper exhibited a linear decrease in asymptotic fouling density with increasing *rotational speed*, the nonwetting surfaces exhibited a sharp initial decrease in fouling density followed by a relatively stable low fouling at the higher speeds.
2. Fouling increased with *temperature* due to the increase in the available energy in the system to overcome activation energy barrier and resulting increase in the fouling rate. However, SHS and LIS showed significantly reduced fouling compared to bare copper even at the high temperature at all times and in the asymptotic fouling density.
3. *Surface modification* had a significant effect on reducing deposited fouling compared to the unmodified bare copper surface. The superhydrophobicity of SHS and slipperiness of LIS showed similar anti-scaling effect compared to the bare copper control sample. While electrodeposited SHS and LIS showed less scaling mass deposited at early times compared to their etched counterparts, the asymptotic fouling showed no significant difference between the two types of fabrication. It was shown that the asymptotic fouling was lower on SHS and LIS by about 75% compared to bare copper surface.
4. A *Hill-Langmuir model* was developed based on the experimental studies for the first time for predicting foulant mass and its binding to both unmodified and modified nonwetting surfaces. The model was shown to capture the physics of the process and to be accurate in its predictions compared to the experimental measurements.

The study provides, for the first time, valuable insights into dynamic fouling process by juxtaposing different fabrication methods, different surface modifications, and various experimental environments.

ACKNOWLEDGMENT AND DISCLAIMER

The material reported in this publication is based upon work supported by the U.S. Department of Energy under Award Number DE-FE0031556. This publication was prepared as an account of work sponsored by an agency of the United States Government. Neither the United States Government nor any agency thereof, nor any of their employees, makes any warranty, express or implied, or assumes any legal liability or responsibility for the accuracy, completeness, or usefulness of any information, apparatus, product, or process disclosed, or represents that its use would not infringe privately owned rights. Reference herein to any specific commercial product, process, or service by trade name, trademark, manufacturer, or otherwise does not necessarily constitute or imply its endorsement, recommendation, or favoring by the United States Government or any agency thereof. The views and opinions of authors expressed herein do not necessarily state or reflect those of the United States Government or any agency thereof.

REFERENCES

[1] J. Zhao, M. Wang, H.M.S. Lababidi, H. Al-Adwani, K.K. Gleason, A review of heterogeneous nucleation of calcium carbonate and control strategies for scale formation in multi-stage flash (MSF) desalination plants, Desalination. 442 (2018) 75–88. https://doi.org/10.1016/J.DESAL.2018.05.008.

[2] J. Song, M. Liu, X. Sun, Model analysis and experimental study on scaling and corrosion tendencies of aerated geothermal water, Geothermics. 85 (2020) 101766. https://doi.org/10.1016/J.GEOTHERMICS.2019.101766.

[3] P.S. Goh, W.J. Lau, M.H.D. Othman, A.F. Ismail, Membrane fouling in desalination and its mitigation strategies, Desalination. 425 (2018) 130–155. https://doi.org/10.1016/J.DESAL.2017.10.018.

[4] F.L. Wang, Y.L. He, S.Z. Tang, Z.X. Tong, Parameter study on the fouling characteristics of the H-type finned tube heat exchangers, Int. J. Heat Mass Transf. 112 (2017) 367–378. https://doi.org/10.1016/J.IJHEATMASSTRANSFER.2017.04.107.

[5] M. Kamalipour, S.A.M. Dehghani, A. Naseri, S. Abbasi, Role of agitation and temperature on calcium sulfate crystallization in water injection process, J. Pet. Sci. Eng. 151 (2017) 362–372. https://doi.org/10.1016/J.PETROL.2016.12.039.

[6] T.H. Chong, R. Sheikholeslami, Thermodynamics and kinetics for mixed calcium carbonate and calcium sulfate precipitation, Chem. Eng. Sci. 56 (2001) 5391–5400. https://doi.org/10.1016/S0009-2509(01)00237-8.

[7] J.G. Lee, Y. Jang, L. Fortunato, S. Jeong, S. Lee, T.O. Leiknes, N. Ghaffour, An advanced online monitoring approach to study the scaling behavior in direct contact membrane distillation, J. Memb. Sci. 546 (2018) 50–60. https://doi.org/10.1016/J.MEMSCI.2017.10.009.

[8] S. Tang, Y. Ji, K. Ge, Crystallization Kinetics and Mechanisms of Calcium Sulfate Dihydrate: Experimental Investigation and Theoretical Analysis, Ind. Eng. Chem. Res. 59 (2020) 21676–21684. https://doi.org/10.1021/ACS.IECR.0C04220.

[9] K.S. Song, J. Lim, S. Yun, D. Kim, Y. Kim, Composite fouling characteristics of CaCO3 and CaSO4 in plate heat exchangers at various operating and geometric conditions, Int. J. Heat Mass Transf. 136 (2019) 555–562. https://doi.org/10.1016/J.IJHEATMASSTRANSFER.2019.03.032.

[10] F. Alimi, A. Gadri, Kinetics and morphology of formed gypsum, Desalination. 166 (2004) 427–434. https://doi.org/10.1016/J.DESAL.2004.06.097.

[11] M. Crabtree, D. Eslinger, P. Fletcher, M. Miller, Fighting scale: removal and prevention, Oilfield. (1999).

[12] J.G. Tanquero, E.-S.A. Abdel-Aal, R.S. Farinato, H. El-Shall, B.M. Moudgil, Inhibition of calcium sulphate hemihydrate crystallization under simulated conditions of phosphoric acid evaporation, Can. J. Chem. Eng. (2021). https://doi.org/10.1002/CJCE.24210.

[13] D. Hasson, H. Shemer, A. Sher, State of the Art of Friendly “Green” Scale Control Inhibitors: A Review Article, Ind. Eng. Chem. Res. 50 (2011) 7601–7607. https://doi.org/10.1021/IE200370V.

[14] H. Zettler, M. Wei, Q. Zhao, H.U. Zettler, Influence of surface properties and characteristics on fouling in plate heat exchangers, Heat Transf. Eng. 26 (2007) 3–17. https://doi.org/10.1080/01457630590897024.

[15] M. Forster, M. Bohnet, Modification of molecular interactions at the interface crystal/heat transfer surface to minimize heat exchanger fouling, Int. J. Therm. Sci. 39 (2000) 697–708. https://doi.org/10.1016/S1290-0729(00)00229-5.

[16] S.B. Subramanyam, G. Azimi, K.K. Varanasi, Designing Lubricant-Impregnated Textured

Surfaces to Resist Scale Formation, Adv. Mater. Interfaces. 1 (2014) 1300068. https://doi.org/10.1002/ADMI.201300068.

[17] G. Azimi, Y. Cui, A. Sabanska, K.K. Varanasi, Scale-resistant surfaces: Fundamental studies of the effect of surface energy on reducing scale formation, Appl. Surf. Sci. 313 (2014) 591–599. https://doi.org/10.1016/J.APSUSC.2014.06.028.

[18] D.E. Packham, Surface energy, surface topography and adhesion, Int. J. Adhes. Adhes. 23 (2003) 437–448. https://doi.org/10.1016/S0143-7496(03)00068-X.

[19] S. Keysar, R. Semiat, D. Hasson, J. Yahalom, Effect of Surface Roughness on the Morphology of Calcite Crystallizing on Mild Steel, J. Colloid Interface Sci. 162 (1994) 311–319. https://doi.org/10.1006/JCIS.1994.1044.

[20] H. Müller-Steinhagen, Q. Zhao, A. Helali-Zadeh, X.-G. Ren, The effect of surface properties on CaSO4 scale formation during convective heat transfer and subcooled flow boiling, Can. J. Chem. Eng. 78 (2000) 12–20. https://doi.org/10.1002/CJCE.5450780105.

[21] W.C. Cheong, P.H. Gaskell, A. Neville, Substrate effect on surface adhesion/crystallisation of calcium carbonate, J. Cryst. Growth. 363 (2013) 7–21. https://doi.org/10.1016/J.JCRYSGRO.2012.09.025.

[22] A. Herz, M.R. Malayeri, H. Müller-Steinhagen, Fouling of roughened stainless steel surfaces during convective heat transfer to aqueous solutions, Energy Convers. Manag. 49 (2008) 3381–3386. https://doi.org/10.1016/J.ENCONMAN.2007.09.034.

[23] T. Zhang, Y. Wang, F. Zhang, X. Chen, G. Hu, J. Meng, S. Wang, Bio-inspired superhydrophilic coatings with high anti-adhesion against mineral scales, NPG Asia Mater. 2018 103. 10 (2018) e471–e471. https://doi.org/10.1038/am.2017.224.

[24] F. Signorelli, M.F.B. Sousa, C.A. Bertran, Interfacial Phenomena on the Inorganic Scaling Prevention, (2019). https://doi.org/10.1021/acsomega.8b02878.

[25] W. Jiang, J. He, F. Xiao, S. Yuan, H. Lu, B. Liang, Preparation and Antiscaling Application of Superhydrophobic Anodized CuO Nanowire Surfaces, Ind. Eng. Chem. Res. 54 (2015) 6874–6883. https://doi.org/10.1021/ACS.IECR.5B00444.

[26] H. Li, S. Yu, X. Han, Y. Zhao, A stable hierarchical superhydrophobic coating on pipeline steel surface with self-cleaning, anticorrosion, and anti-scaling properties, Colloids Surfaces A Physicochem. Eng. Asp. 503 (2016) 43–52. https://doi.org/10.1016/J.COLSURFA.2016.05.029.

[27] H. Qian, Y. Zhu, H. Wang, H. Song, C. Wang, Z. Liu, H. Li, Preparation and Antiscaling Performance of Superhydrophobic Poly(phenylene sulfide)/Polytetrafluoroethylene Composite Coating, (2017). https://doi.org/10.1021/acs.iecr.7b03975.

[28] T.V.J. Charpentier, A. Neville, S. Baudin, M.J. Smith, M. Euvrard, A. Bell, C. Wang, R. Barker, Liquid infused porous surfaces for mineral fouling mitigation, J. Colloid Interface Sci. 444 (2015) 81–86. https://doi.org/10.1016/J.JCIS.2014.12.043.

[29] M.F.B. Sousa, G.F. Barbosa, F. Signorelli, C.A. Bertran, Anti-scaling properties of a SLIPS material prepared by silicon oil infusion in porous polyaniline obtained by electropolymerization, Surf. Coatings Technol. 325 (2017) 58–64. https://doi.org/10.1016/J.SURFCOAT.2017.06.038.

[30] S.M.A. Mousavi, R. Pitchumani, A Study of Corrosion on Electrodeposited Superhydrophobic Copper Surfaces, Corros. Sci. 186 (2021) 109420. https://doi.org/10.1016/j.corsci.2021.109420.

[31] S.M.A. Mousavi, R. Pitchumani, Bioinspired nonwetting surfaces for corrosion inhibition over a range of temperature and corrosivity, J. Colloid Interface Sci. 607 (2022) 323–333. https://doi.org/10.1016/J.JCIS.2021.08.064.

[32] I.S. Bayer, Superhydrophobic Coatings from Ecofriendly Materials and Processes: A Review, Adv. Mater. Interfaces. 7 (2020) 2000095. https://doi.org/10.1002/ADMI.202000095.

[33] Y. Wang, X. Zhou, M. Yin, J. Pu, N. Yuan, J. Ding, Superhydrophobic and Self-Healing Mg-Al Layered Double Hydroxide/Silane Composite Coatings on the Mg Alloy Surface with a Long-Term Anti-corrosion Lifetime, Langmuir. 37 (2021) 8129–8138. https://doi.org/10.1021/ACS.LANGMUIR.1C00678.

[34] M. Tenjimbayashi, R. Togasawa, K. Manabe, T. Matsubayashi, T. Moriya, M. Komine, S. Shiratori, Liquid-Infused Smooth Coating with Transparency, Super-Durability, and Extraordinary Hydrophobicity, Adv. Funct. Mater. 26 (2016) 6693–6702. https://doi.org/10.1002/ADFM.201602546.

[35] VIII. Stability of a viscous liquid contained between two rotating cylinders, Philos. Trans. R. Soc. London. Ser. A, Contain. Pap. a Math. or Phys. Character. 223 (1923) 289–343. https://doi.org/10.1098/RSTA.1923.0008.

[36] A. Masoudi, P. Irajizad, N. Farokhnia, V. Kashyap, H. Ghasemi, Antiscaling Magnetic

Slippery Surfaces, ACS Appl. Mater. Interfaces. 9 (2017) 21025–21033. https://doi.org/10.1021/ACSAMI.7B05564.

[37] A. Haghdoost, R. Pitchumani, Fabricating Superhydrophobic Surfaces via a Two-Step Electrodeposition Technique, (2013). https://doi.org/10.1021/la403509d.

[38] J. Mullin, Crystallization, 2001. https://books.google.com/books?hl=en&lr=&id=Et0EtojQmvsC&oi=fnd&pg=PP1&dq=Mullin,+John+William&ots=Vt8B4VSzvO&sig=kWyzHA5Ys0-EwMvbDe7aA6_zVn8 (accessed July 20, 2021).

[39] C. Yoder, Ionic compounds: applications of chemistry to mineralogy, 2006. https://books.google.com/books?hl=en&lr=&id=JsiDDwAAQBAJ&oi=fnd&pg=PA1&dq=Yoder,+Claude+H.+Ionic+compounds:+applications+of+chemistry+to+mineralogy.+John+Wiley+%26+Sons,+2006.,+ref&ots=a5R416AGCh&sig=vdBtz-QNL9KSd9ulCNIVnJ81fpg (accessed July 20, 2021).

[40] A.R. Konak, A new model for surface reaction-controlled growth of crystals from solution, Chem. Eng. Sci. 29 (1974) 1537–1543. https://doi.org/10.1016/0009-2509(74)87004-1.

[41] D.Q. Kern, R.E. Seaton, A theoretical analysis of thermal surface fouling, 4 (1959) 258–262.

[42] R.L. Webb, W. Li, Fouling in enhanced tubes using cooling tower water: Part I: long-term fouling data, Int. J. Heat Mass Transf. 43 (2000) 3567–3578. https://doi.org/10.1016/S0017-9310(99)00395-6.

[43] P.F. Verhulst, Notice sur la loi que la population suit dans son accroissement, Corresp. Mathématique Phys. 10: (1838) 113–126. https://ci.nii.ac.jp/naid/10015246307 (accessed July 20, 2021).

[44] E. Nebot, J.F. Casanueva, T. Casanueva, D. Sales, Model for fouling deposition on power plant steam condensers cooled with seawater: Effect of water velocity and tube material, Int. J. Heat Mass Transf. 50 (2007) 3351–3358. https://doi.org/10.1016/J.IJHEATMASSTRANSFER.2007.01.022.

[45] A. Hill, The possible effects of the aggregation of the molecules of haemoglobin on its dissociation curves, J. Physiol. (1910).

[46] I. Langmuir, The adsorption of gases on plane surfaces of glass, mica and platinum, J. Am. Chem. Soc. 40 (1918) 1361–1403. https://doi.org/10.1021/JA02242A004.

[47] R. Gesztelyi, J. Zsuga, A. Kemeny-Beke, B. Varga, B. Juhasz, A. Tosaki, The Hill equation and the origin of quantitative pharmacology, Arch. Hist. Exact Sci. 2012 664. 66 (2012) 427–438. https://doi.org/10.1007/S00407-012-0098-5.

[48] R. Bird, W. Stewart, E. Lightfoot, Transport Phenomena revised 2nd Edition, (2006). https://highlandsranchhistoricalsociety.org/sites/default/files/webform/speaker_request_files/pdf-transport-phenomena-revised-2nd-edition-r-byron-bird-warren-e-stewart-edwin-n-lightfoot-pdf-download-free-book-73159db.pdf (accessed September 17, 2021).

[49] W. Li, Modeling liquid-side particulate fouling in internal helical-rib tubes, Chem. Eng. Sci. 62 (2007) 4204–4213. https://doi.org/10.1016/J.CES.2007.04.052.

[50] R. Gao, C. Shen, X. Wang, Y. Yao, Experimental study on the sticking probability and deposit bond strength of fouling in enhanced tubes, Int. Commun. Heat Mass Transf. 103 (2019) 17–23. https://doi.org/10.1016/J.ICHEATMASSTRANSFER.2019.02.010.

[51] H. Müller-Steinhagen, M.R. Malayeri, A.P. Watkinson, Heat exchanger fouling: Mitigation and cleaning strategies, Heat Transf. Eng. 32 (2011) 189–196. https://doi.org/10.1080/01457632.2010.503108.

Table 6.1. Parameters of the Hill-Langmuir model for calcium sulfate scaling on bare, SHS and LIS copper surfaces

Surface	$m''_{f\infty}$ [mg. cm^{-2}]				k [h]				n			
	23 ℃			50 ℃	23 ℃			50 ℃	23 ℃			50 ℃
	100 rpm	200 rpm	400 rpm	200 rpm	100 rpm	200 rpm	400 rpm	200 rpm	100 rpm	200 rpm	400 rpm	200 rpm
Bare copper	4.86	3.59	1.53	11.99	5.4	43.1	60.0	146.4	1.00	1.00	1.00	1.05
Etched SHS	3.51	0.68	0.30	5.32	1.0	3.6	16.0	75.2	1.32	1.35	1.30	2.90
Electrodeposited SHS	2.66	0.58	0.52	6.50	1.1	4.3	18.4	220.0	1.20	1.24	1.23	2.72
Etched LIS	5.80	0.71	0.60	5.98	1.0	5.1	5.3	110.0	1.00	1.00	1.00	1.00
Electrodeposited LIS	4.58	0.35	0.30	3.80	0.5	2.3	2.3	50.0	1.00	1.00	1.00	1.00

Chapter 7. Dynamic Scaling of Nonwetting Brass and Aluminum Surfaces

The work reported in this chapter is the basis for the following journal publication currently in re view:

S.M.A. Mousavi, and R. Pitchumani. "Dynamic Scaling of Nonwetting Brass and Aluminum Surfaces." In Review (2021).

7.1. ABSTRACT

Crystallization fouling is fundamental to various surfaces of application, domestic and industrial. Surfaces modification has drawn attention as a preventive approach against scaling. In specific, enhanced non-wetting surfaces have been fabricated via physical and chemical modifications namely hydrophobic surfaces (HS), superhydrophobic surfaces (SHS), and lubricant-infused surfaces (LIS) for different applications including anti-scaling, and has been studied at static conditions. In contrast, there is very little information on the anti-scaling performance of such surfaces at dynamic conditions. This study considers a systematic comprehensive approach to anti-scaling based on nucleation theory. Metallic surfaces with different roughness, relatively rough and smooth, were chosen as the base material for dynamic scaling experiments. A facile etching method was employed for the fabrication of non-wetting enhanced HS and SHS and LIS on the metallic surfaces. Systematic dynamic scaling experiments on the five different types of surfaces were performed at three flow levels and two temperature levels. Finally, a comprehensive analysis was done on aggregated data to map the efficacy of different metallic surface modifications against scaling. We envision this rationale as an important step for the research and industrial community to pave the way toward robust and stable enhanced anti-scaling surfaces in the future.

Keywords: superhydrophobicity; lubricant infused surface; anti-fouling; calcium scaling; metallic surface; Reynolds number

7.2. INTRODUCTION

Fouling of surfaces of application, especially scaling of minerals present in the working fluids, has long been an unresolved major challenge [1]. This includes but is not limited to the power generation sector [2,3], heat-exchanger in chemical industries [4], water treatment (membrane desalination) [5–7], and food industry [8,9], naval transportation. For example, In the presence of scale accumulation on heat transfer surfaces, such as the inside of condenser tubes, the effectiveness of the heat transfer process decreases significantly. As a result, the increase in pressure drop and decrease in heat transfer rate ramp up the operation costs and incur additional maintenance and shorten the ultimate usable life of the facilities. Furthermore, scale accumulation contributes to further damages by a kind of corrosion known as "under-deposit corrosion" [10] which corrosion occurs when the metal is attacked aggressively beneath the scale layer, resulting in a crack or pit in the metal wall where the metal deteriorates considerably faster than ordinary corrosion elsewhere in the system, and it can go undetected. Once scale has bonded to the surfaces, it can be extremely difficult to remove, typically necessitating scraping through strong mechanical cleaning, or harsh chemical cleaning methods [11]. Neither of these scale-removal methods is favorable to the equipment life. Therefore, alternative preventive methods should be approached. This has been the focus of various studies and includes three general venues: water pretreatment methods [12–14]; scaling inhibitors [15–17]; and surface treatments [18–20]. The first two can be effective but imposes high relative costs and possible water and soil pollution. Besides they are limited in application, for instance, water pretreatment or using scale inhibitors are not applicable to shipyard surfaces. Surface treatment can be relatively low-cost and versatile and entails changing the morphology and chemistry [21] of the surface with the purpose of scale mitigation [22]. Heterogenous nucleation theory has been the basis of the efforts for surface modifications. The nucleation rate, J, based on this theory is [23]: $J = \mathrm{N_s} Z j exp\left(-\frac{-\Delta G^*}{\mathrm{K_B T}}\right)$, where N_s is the number of available nucleation sites, Z (Zeldovich factor) is the probability that a critical nuclei will develop into a stable crystal , k_B is the Boltzmann constant, T is the temperature, and $\Delta G^*$is critical nucleation energy barrier. The factors that are independent of working fluid are N_s (function of surface roughness), ΔG^* (function of surface energy of the substrate). Therefore, scaling can be mitigated by surface physical and chemical modification. Surface energy is a property which can be indirectly quantified through measuring wettability properties of a surface,

namely water contact angle (CA) and roll-of/sliding angle (SA). Lowering the surface energy of a substrates increases the CA and decreases SA. In general, surfaces having a CA less than 90 degrees are considered hydrophilic, surfaces with CA greater than 90 but less than 150° are said to be hydrophobic surface (HS) while surfaces with sustained CA greater than 150° and contact angle hysteresis or SA less than 10° are said to be superhydrophobic surfaces (SHS). Besides HS/SHS as non-wetting surfaces there is a class of lubricant-infused surfaces (LIS) which carries an apparent water contact angle in a range of 80–140° with a SA< 20°.

Hydrophobic and superhydrophobic surfaces have been studied in the last decades for many applications such as self-cleaning [24], anti-icing [25], including anti-scaling [26–29]. In recent years the emerging slippery lubricant-infused surfaces have drawn attention for similar applications [30–32] where there is a developing effort for anti-scaling studies utilizing LIS by surface modification of metallic and non-metallic surfaces [33–36]. It is evident from the foregoing discussion that the studies mostly focus on either SHS or LIS, or on selected materials. Besides, the anti-scaling properties have been looked only at static conditions. Therefore, despite all the prior work in the literature, there is a conspicuous lack of systematic studies on the anti-scaling of modified surfaces at dynamic conditions. Toward addressing the knowledge gap, a rational approach to the issue of scaling was adopted based on the science behind nucleation. In literature, the nucleation theory as discussed earlier has been approached for modification of surfaces against scaling studying only specific factors such as surface energy. Herein, for the first time, we have visited the nucleation theory from a comprehensive approach, by doing systematic studies on the controllable parameters including both surfaces related parameters and working fluid related parameters. the specific contributions of the present study are the following:

- Bare base substrates have been specifically selected to cover two levels of roughness, smooth and rough. In nucleation theory, roughness relates to the term N_s as the number of available nucleation sites. Moreover, many studies in literature had been done by modification of substrates like silicon wafers or metallic coated silicon wafer, the selected metallic substrates in this work (brass, and aluminum) are the ones ubiquitously used in many real-world applications. This makes the results from this study a valuable step toward understanding the applicability of non-wetting surfaces for anti-scaling purposes.
- The critical nucleation energy barrier term (ΔG^*) in nucleation theory, relates to surface energy and hence wettability. Water droplets pins to the selected bare metallic substrates (brass and

aluminum) with a low CA close to 90° that can categorize them as hydrophilic surfaces. Aluminum substrates were modified to achieve HS, while a facile surface modification approach was used to fabricate SHS from brass surfaces. Furthermore, slippery surfaces were fabricated by lubricant infusion to achieve low surface energy and atomically smooth surfaces which relates to both $\Delta G^*$and N_s in nucleation theory. With that, a wide range of wettability was considered: hydrophilic; hydrophobic, superhydrophobic, and slippery lubricant-infused. A detailed roughness and wettability analysis were performed.

- A dynamic scaling experiment was designed that yet benefits from the supersaturation condition that is commonly practiced in literature. A parametric study was performed on different dynamic conditions which reflect the terms N_s and Z in the nucleation theory.
- A systematic study was performed to cover the effect of temperature, relating to term T in nucleation theory.
- A comprehensive analysis was done by pooling large data to shed light on the level of efficacy of different metallic surface modifications for scale mitigation purposes. This is an important step for the research and industrial community as this analysis was performed on metallic surfaces that are ubiquitously used in a wide range of applications from shipyards, aviation, to power generation.

The following is a breakdown of the article's structure: Section 2 describes the experimental methods of fabrication of HS, SHS, and LIS and characterization methodologies. This section ends with experimental design methodology. After that, Section 3 begins with the surface morphology analysis and continues with parametric test results, and finishes with the comprehensive summary and analysis. The principal results of the study are concluded in Section 4.

7.3. EXPERIMENTAL METHODS

7.3.1. **Materials and reagents**

Multipurpose 110 Copper Sheet, 5052 Aluminum Sheet, and Brushed Weldable Marine-Grade 464 Brass Sheet was purchased from McMaster, USA. Nitric acid (HNO_3), sulfuric acid (H_2SO_4), hydrochloric acid (HCl), acetone (99.5+%), ethyl alcohol (99%) methanol (99.8+%), and stearic acid ($CH_3(CH_2)_{16}CO_2H$, 97%) were purchased from Fisher Scientific (Pittsburgh, PA, USA) and

used as received without any further purification. Deionized water (14MΩ.cm resistance) was purchased from CQ Concept (Illinois, USA). 3% Hydrogen peroxide solution (H_2O_2) was purchased from Sigma-Aldrich. Silicone oil, 500Dowsil™, was purchased from DuPont (Wilmington, Delaware, USA). Calcium sulfate hemihydrate ($CaSO_4.0.5H_2O_2$) was purchased from Alfa Aesar (Ward Hill, Massachusetts, USA).

7.3.2. **Surface texturing and surface modification**

Fabrication of non-wetting surfaces requires first texturing the substrate. For this, a facile chemical etching process was adapted. The as-received brass and aluminum sheet was cut into coupons of 1×5 cm. Methanol, acetone, and DI-water sonication baths for 10 minutes each were used to degrease the parts. After that, chemical etching was done by 20 minutes immersion of brass coupons in 1:1:6 v/v/v mixture of DI-Water:H_2O_2 (3%):HNO_3 (7M) and aluminum coupons in 3:4:1 v/v/v mixture of DI-Water:H_2O_2 (3%):HCl (12M). The etched coupons were then immersed in DI-water and the etched surfaces were soft brushed to remove any loose possible residues from the process and then dried overnight.

Next, the textured brass and aluminum surface energy were reduced via surface functionalization by immersion of the coupons in 0.02 M stearic acid-methanol solution for 24 hours. After the functionalization step, the brass coupons exhibited wetting properties corresponding to superhydrophobic surfaces (SHS) and aluminum coupons exhibited wetting properties corresponding to hydrophobic surfaces (HS).

The principal for fabrication of lubricant infused surfaces entails proper surface chemistry which that achieve a lubricant layer immiscible with the contact liquid of choice, here scaling solution. The functionalized SHS/HS brass and aluminum surfaces adopt such criteria; therefore the LIS was fabricated by infusing functionalized coupons with lubricant oil. Drops of Dowsil™ silicone oil with 500 cSt viscosity were placed onto the surfaces and hanged vertically for twenty minutes to allow the lubricant to completely wet the interasperity spaces while any excess oil to drain.

7.3.3. **Morphology and wettability characterization**

A field-emission scanning electron microscope (SEM) (LEO/Zeiss 1550, Germany) was used to characterize surface morphology, operating at an acceleration voltage of 10 kV connected to an energy dispersive x-ray analyzer (Oxford INCA E2H, UK). A white light scanning confocal microscope (Keyence model VK-X, Osaka-Japan) was used for 3D reconstruction of the surfaces and optical imagery. A stylus profilometer was used to characterize the surface roughness (Dektak XT Bruker; Massachusetts, USA) equipped with a 2.5 µm stylus tip operating at 10 mg force and 0.1µm resolution. A goniometer (ramé-hart model 590; New Jersey, USA) was used for surface wettability characterization. Water contact angle (CA) was measured by sessile drop method where a 10 µl sessile DI-water droplet was placed at five different locations on each coupon and averaged. The sliding angle (SA) was measured via the tilting cradle method wherein the angle at which a 25 µl DI-water droplet rolls of an SHS/HS. For the case of LIS, when both the rear and front contact lines of the droplet started to slide, the sliding angle was recorded.

7.3.4. **Fouling characterization**

In static tests, one common method of quantifying the extent of scaling is to measure the weight of the samples before and after the tests. An alternative method was used in a dynamic test condition of this work where it was anticipated that there would be loss of infused material or loss of material from the surface as a result of erosion or corrosion.

The masking tape on the backs of the coupon was gently removed to avoid disturbance to the deposited fouling on the top surface of the coupon (possibly loose on SHS/HS/LIS). After that, each coupon was immersed in 10 ml of 10% Nitric Acid (HNO3) for 10 minutes to dissolve the deposited fouling into the solution. At the last step, the solution was diluted ten times to be prepared for mass spectroscopy. An inductively coupled plasma mass spectroscopy (ICP-MS) was used to measure the calcium concentrations. The measurements had a reporting limit of 0.5 $\mu g/L$. The calcium concentration from ICP-MS data was then converted to mass gain per unit surface area.

7.3.5. **Dynamic fouling test experimental design**

There has been increasing attention to the non-wetting surfaces and static scaling experiment in an open tank is commonly used to characterized such surfaces against mineral fouling. However,

the flow conditions in the application environment are frequently turbulent. Therefore, here a simple yet novel dynamic condition was designed called drum setup hereafter. The drum setup includes a cylindrical stationary tank with radius b, and a co-centric inner rotating drum with radius a, Figure 7.1. An aluminum rod was machined to couple the drum to a controllable motor shaft. Aluminum was used for this purpose as a material with a high module of elasticity to withstand the high rotation rate stresses and low weight to impose less unwanted momentums. The coupons mount on the outer surface of the rotating drum and are immersed in a prepared fouling solution. A hot plate controlled with an immersed temperature probe regulates the temperature of the solution. The drum setup is an open tank that assures the supersaturation states of the solution required for the onset of nucleation and crystal growth. The drum setup resembles a rotating-Couette flow as shown in Figure 7.1 and the Reynolds number is calculated as in Equation 7.1:

$$Re_{\emptyset} = \frac{\rho.\Omega a.(b-a)}{\mu} \qquad \text{Equation 7.1}$$

where ρ is the fluid density, μ is the fluid viscosity, and Ω_a is the rotational speed of the drum.

The dynamic fouling tests were designed to cover a variety of dynamic conditions as well as surfaces. The performed parametric tests are summarized in Table 7.1:

Table 7.1. Dynamic fouling test experiment conditions.

Parameter	**Value(s)**	**Level(s)**
Tank radius, a	10 cm	Fixed
Drum outer radius, b	18 cm	Fixed
Temperature	23 °C, 50 °C	2
Rotation rate (Reynolds Number)	100 rpm, 200 rpm, 400 rpm	3
Immersion time	48 h, 96 h,192 h	3
Wettability (surface modification)	Hydrophilic rough (Br) Hydrophilic smooth (Al) Hydrophobic (Aluminum-HS) Superhydrophobic (Brass-SHS)	5
Repetition	Three coupons prepared for each	3
Concentration	8 g/l @ 23 °C, 5 g/l @ 50 °C	Fixed

*Total number of tested coupons: 324

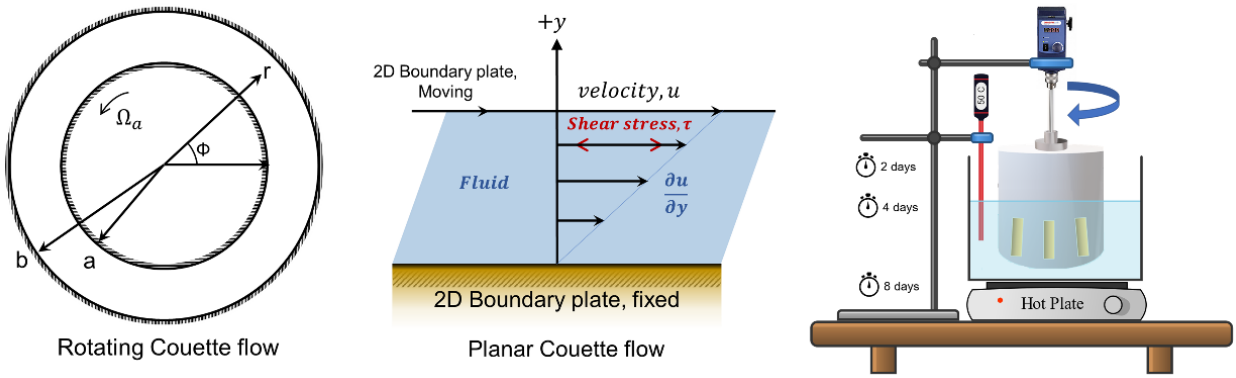

Figure 7.1. Left: Rotating-Couette flow where an internal cylinder with radius a rotates with angular velocity of Ω_a inside a filled cylindrical tank with inner diameter b. Middle: Planar-Couette flow between a stationary flat plate and a boundary plate moving with velocity u. Right: Schematic of the dynamic scaling drum setup. Three metallic coupons at the circumference of a rotating drum in a tank of Gypsum solution are depicted.

7.4. RESULTS AND DISCUSSION

The result of the dynamic scaling test is discussed in this section beginning with surface morphology and wettability. Furthermore, the parametric tests result on the effect of shear stress (rotation rate) are discussed. After that, the result of parametric test capturing the effect of temperature is presented. The discussion continues with the parametric tests on the effect of surface modification. Finally, the section ends with a summary of all the data in this article pooled with the result from literature.

7.4.1. **Surface morphology and wettability**

Surface morphology of the metallic surfaces was scrutinized via scanning electron imagery. Figure 7.2 and 3 display the SEM images of brass-based and aluminum-based coupon surfaces, respectively. As is shown in Figure 7.2(a-c) the bare brass inherits a level of roughness in form of parallel grooves/brushes. 20-minutes of etching has further textured the brass on top of the as-received grooves, Figure 7.2(e-g). However, the inherited grooves on the bare brass have been almost faded out on the etched brass surface, but the grooves are still distinguishable at lower magnification in Figure 7.2(e). The higher magnification SEM images of Figure 7.2(f,g) show that the etching process has successfully provided random roughness into the surface. The surface energy of the etched brass surfaces was reduced by functionalization with stearic acid where Figure

7.2(h-j) reveal the chemisorbed stearic acid onto the brass surface. Figure 7.2(h) shows a lower magnification SEM image where the functionalization agent is deposited onto the surface in form of a relatively low density/spars flower farm. The higher magnification images in Figure 7.2(i,j) further shows nano size leaflike structures beside Daliha-flower like structures in macro size diameters (10 μm) and nano size petals. The high contrasts of the SEM images of the functionalized surfaces are due to the charging effect happening owed to the nonconductive nature of organic material which further proves that the observed flower farm-like structure is the chemisorbed organic stearic acid.

The surface morphology of the aluminum-based tested coupons is shown in Figure 7.3. The footprint of rollers of the annealing machine in the fabrication process of the aluminum sheet is visible in Figure 7.3(a) in form of light surface shadings. The bare aluminum has a smooth surface with few and far between notches/defects, Figure 7.3(b, c). After 20 minutes of etching, the footprint of the annealing was completely faded away as illustrated in Figure 7.3(e), and has successfully textured the surface with random roughness. The high magnification imagery in Figure 7.3(f,g) exposed that the aluminum was etched in form of carved cubic cave-like structures. The size of the cubic caves varied from 1 μm to 10 μm in length/depth. The immersion of the textured aluminum surface in stearic acid solution left the cave-like structure with a layer of coating, Figure 7.3(h-j) in a way that the underlying cave-like texture stayed enact while the edges smoothened.

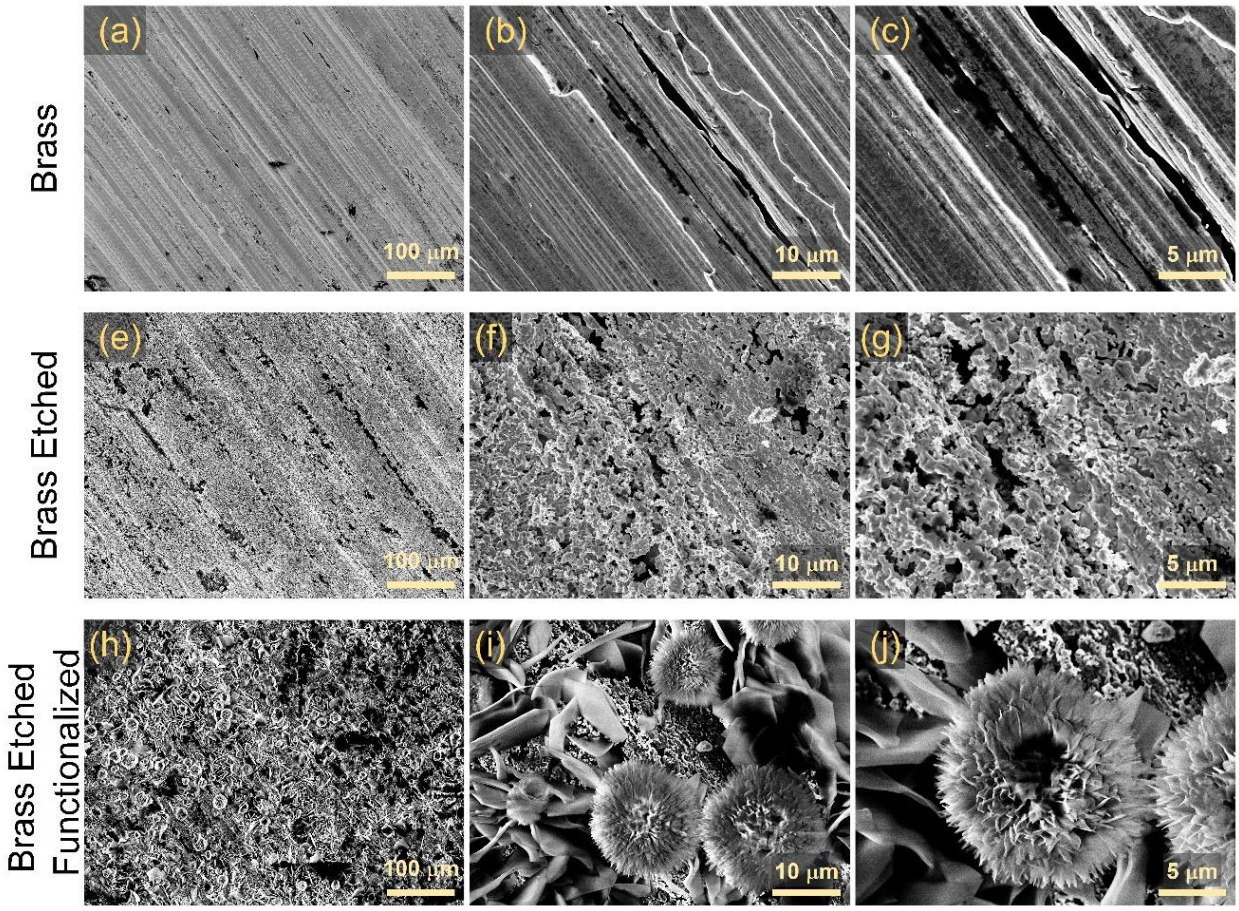

Figure 7.2. SEM images of brass-based surfaces. Displays surface morphology of (a, b, c) as received bare brass; (e, f, g) etched brass; (h, i, j) functionalize etched Brass.

Roughness profilometry of the surfaces was performed in order to further quantify the morphology of the surfaces besides the qualitative SEM images. The roughness profile of the as revived bare brass surface in Figure 7.4(a) indicates a 6.3 µm peak-to-valley height where after etching this value has increased (173%) to 17.2 µm as given away in Figure 7.4(b). Functionalization of the etched brass surfaces had a decreasing effect on the surface roughness. The 3D scanned image and the profilometer scan of the Functionalized etched brass in Figure 7.4(c) shows a 9.4 µm peak-to-valley height which is a 45% decrease (smoother) than the etched brass but yet 50% rougher than bare brass. The effect of functionalization is not only on the morphology but more on the chemical property of the surface which reflects itself on the wettability characteristics. For functionalized etched brass the water contact angle (CA) was

recorded ~155 degrees with a sliding angle (SA) (roll-off angle) of ~5 degrees which are characteristics of a superhydrophobic surface (SHS). Similar measurement for lubricant infused functionalized etched brass indicates a CA of ~96° and very low SA of ~4° which characterized the LIS brass surface with a great slipperiness. The optical images of the brass SHS and LIS are shown in Figure 7.4(c) and insets show a 10 µl sessile droplet on the surfaces and corresponding CA and SA values.

Table 7.2. Surface roughness and wettability properties.

	RMS roughnes, R_a [μm]	**Peak-to-valley height, R_t [μm]**	**CA**	**SA**
Bare Brass	1.5	6.3	102.0 ± 3.0	Pinning
Bare Aluminum	0.5	2.1	105.6 ± 6.6	Pinning
Etched Brass	3.0	17.2	-	-
Etched Aluminum	2.2	11.1	-	-
Functionalized Etched Brass	1.5	9.4	154.4 ± 4.6	5.3 ± 2.5
Functionalized Etched Aluminum	3.3	17.1	146.4 ± 4.0	55.0 ± 14.4
Lubricant infused Func. Etch. Br	-	-	96.0 ± 0.5	3.8 ± 1.0
Lubricant infused Func. Etch. Al	-	-	97.2 ± 42.2	3.7 ± 1.2

The roughness profile of the bare aluminum in Figure 7.4(d) with 2.1 µm peak-to-valley height asserts the relatively smooth surface observed in the SEM image of Figure 7.3(a). After etching, the roughness profile in Figure 7.4(e) shows a significant 430% increase in peak-to-valley height (11.1 µm). Moreover, for the functionalized etched aluminum the peak-to-valley height was recorded at 17.1 µm which is a further 54% increase compared to the etched aluminum, Figure 7.4(f). The functionalized etched aluminum surface has been characterized as a hydrophobic surface (HS) with CA of ~146° and SA of ~55°. The aluminum HS after lubricant infusion showed very high slipperiness with a CA of ~98° and a very low SA of ~4°. The optical image of aluminum HS and LIS are shown in Figure 7.4(f) with insets showing CA and SA values.

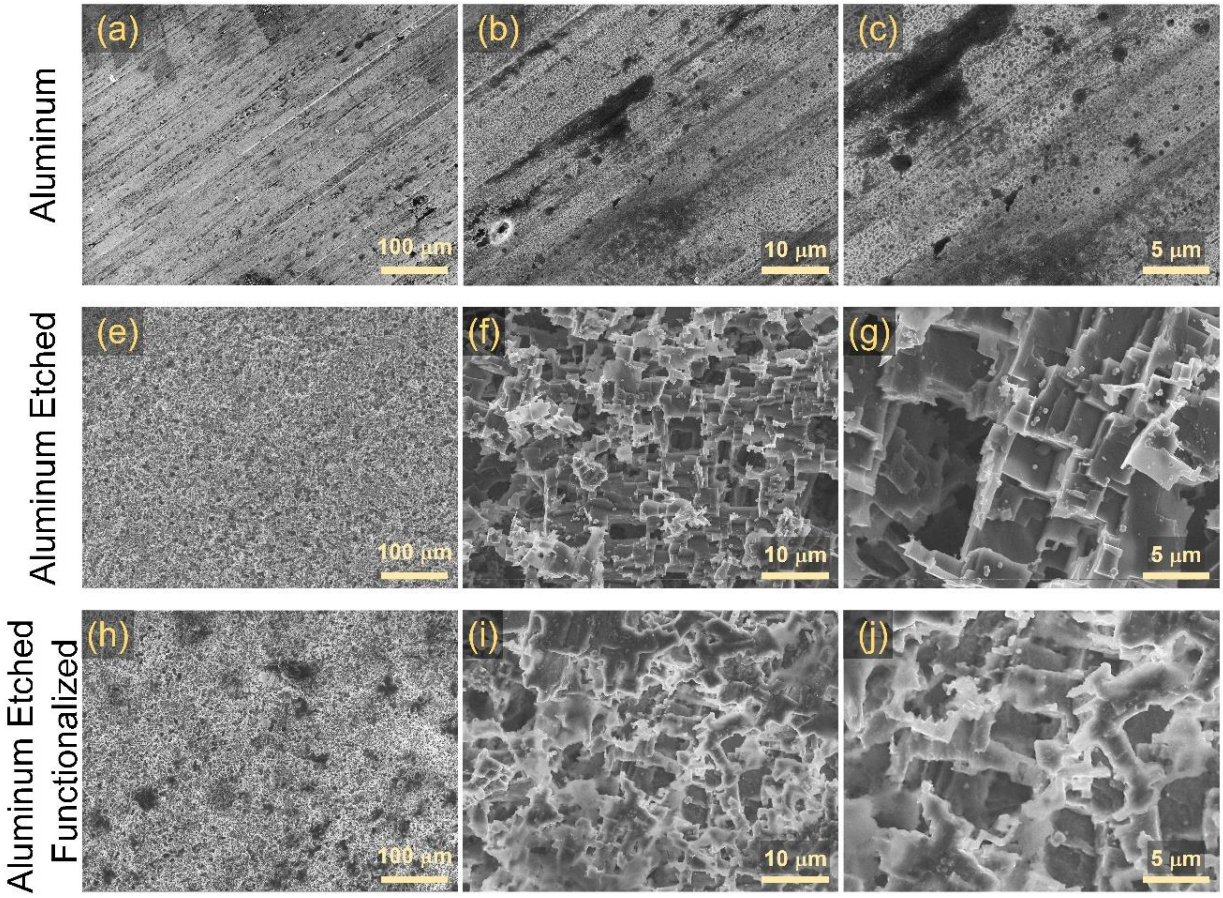

Figure 7.3. SEM images of aluminum-based surfaces. Exhibits surface morphology of (a, b, c) as received bare aluminum; (e, f, g) etched aluminum; (h, i, j) functionalize etched aluminum.

All the roughness and wettability properties are summarized in Table 7.2 along with RMS roughness, R_a values. By comparing the R_a it is evident that the as-received aluminum surface is about 3 times smoother than the as-received brass surfaces. Etching has similar roughness increasing effect on both the brass and aluminum surfaces and has increased the R_a values 2 and 4.4 times, respectively. The larger change from bare to etched roughness for the aluminum case is expected founded on a relatively smoother base. The functionalization however had an increasing effect on roughness for aluminum case (1.5 increase in R_a compared to the etched aluminum surface), but a decreasing effect for the brass case and has decreased the R_a of functionalized etched brass to the same value as bare brass. This difference matches with the observed nano-micro

sized structures added to the etched brass by functionalization as well as the reported wettability properties.

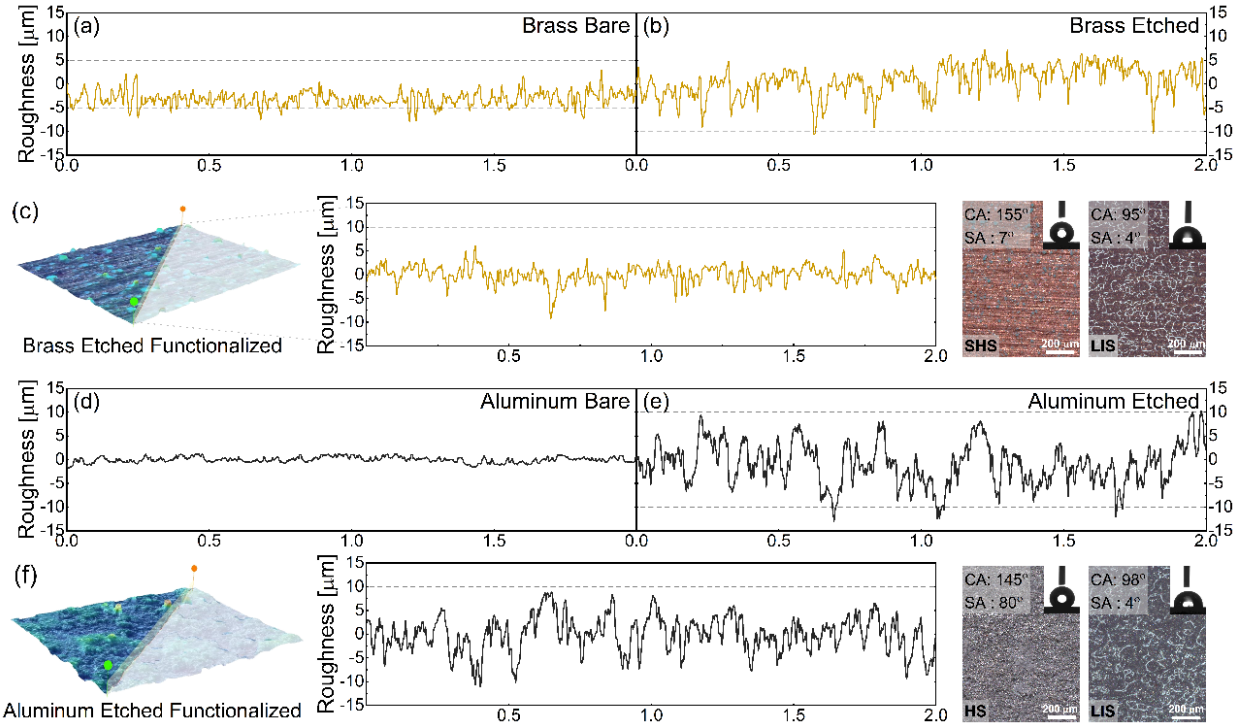

Figure 7.4. Roughness profilometry scans of (a) as revived bare brass surface; (b) etched brass; (c) functionalized etched brass along with surface optical images of brass superhydrophobic surface (SHS) and lubricant infused surface (LIS) with insets showing water contact angle (CA) and sliding angles (SA). Roughness profilometry scans of (d) as revived bare aluminum surface; (b) etched aluminum; (c) functionalized etched aluminum along with surface optical images of aluminum hydrophobic surface (HS) and LIS with insets showing CA and SA.

7.4.2. **Effect of Reynolds number**

The described drum setup was used to perform a series of parametric tests to investigate the effect of rotation rate on mineral fouling on the modified along as received metallic surfaces. Rotation rate was varied at three levels of 100, 200, and 400 rpm. Based on the rotational-Couette flow regime, Equation 7.1, Reynolds number associated with the three chosen levels of rotation rates are 49×10^3, 99×10^3, and 198×10^3. (0.5×10^5, 1×10^5, and 2×10^5). In a typical power plant with 23 mm internal diameter condenser pipe and working fluid speed of 1.8 m/s (2.5 m/s), the Reynolds number is 44×10^3 (62×10^3). Therefore, all the rotation rate parametric

studies chosen levels corresponds to Reynolds numbers above 40×10^3 which is the threshold for turbulent flow in pipes and matches the condition in the environment of application.

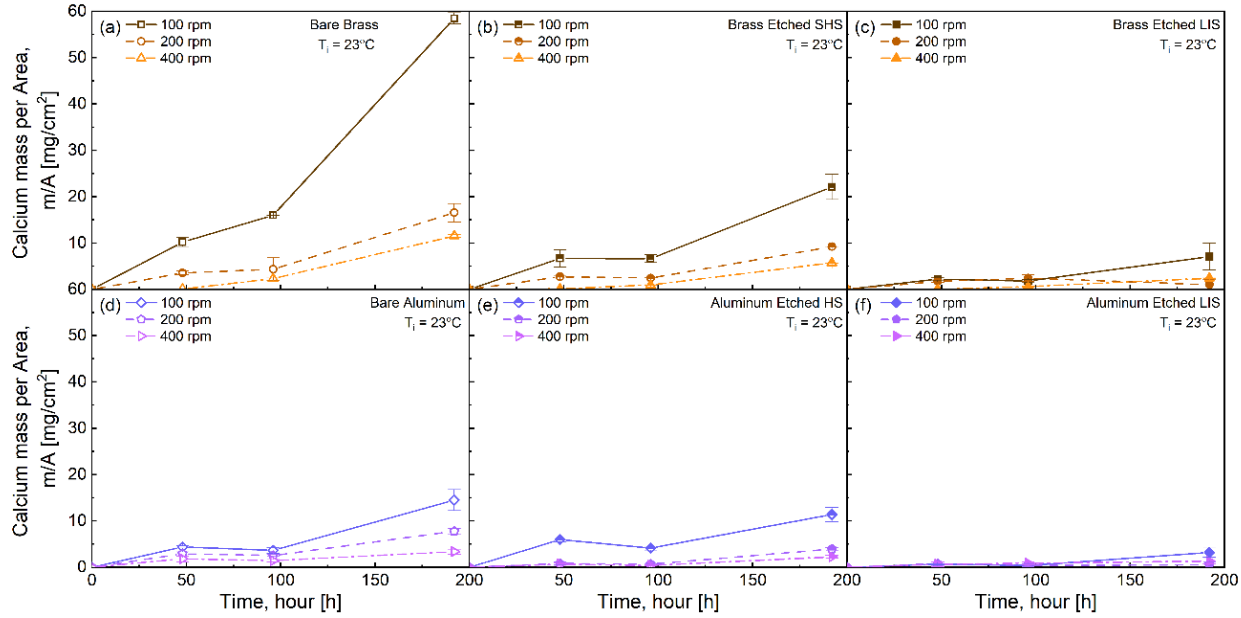

Figure 7.5. Effect of rotation rate versus time on fouling mass per unit area of (a) bare brass; (b) etched brass superhydrophobic surface (SHS); (c) brass lubricant infused surface (LIS); (d) bare aluminum; (b) etched aluminum hydrophobic surface (HS); (c) aluminum lubricant infused surface (LIS). The fouling solution was supersaturated calcium sulfate hemihydrate at room temperature.

Figure 7.5 plots the result for a parametric test showing the effect of rotation rate on calcium mass deposition per area versus time on brass-based and aluminum-based surfaces at room temperature. Regardless of based metal and surface modifications, increasing rotation rate had a decreasing effect on deposited fouling mass. Increasing rotation rate increases Reynolds number and hence the shear stress which increases the removal rate of deposited fouling and/or decreases the calcium crystal nucleation rate by removing the nuclei before reaching to critical radius for stable growth. Increasing rotation rate from 100 rpm to 200 rpm had shown a bolder effect compared to the change from 200 rpm to 400 rpm for all the cases except lubricant infused cases in Figure 7.5(c) and (f). For example, the mass of deposited fouling at 192h on bare brass at 200 rpm to the 100 rpm is 0.3 while the similar ratio for 400 rpm to 200 rpm is 0.7, Figure 7.5(a). This is attributed to the Reynolds number at 100 rpm which is just above the turbulent regime transition Reynolds number while at 200 rpm and 400 rpm the Reynolds number is well above the turbulent

threshold. The difference in the effect of change in Reynolds number on lubricant infused cases is attributed to the slipperiness characteristics of such surfaces where the shear forces even at low Reynolds number was high enough for removal of deposited fouling and/or preventing nuclei to grow. The deposited fouling mass on brass-based surfaces in Figure 7.5(a-c) compared to aluminum-based surfaces in Figure 7.5(d-f) shows a lower deposited mass for aluminum-based surfaces at each rotation rate level. For instance, the deposited mass per area on bare brass is 4, 2, and 3.5 times higher than on bare aluminum surfaces at 100, 200, and 400 rpm, respectively. This could be investigated in the difference between the chemical affinity of calcium to these two metallic surfaces and is beyond the scope of this article.

7.4.3. **Effect of temperature**

A series of parametric tests were done to explore the effect of temperature on fouling deposition. All parameters in Table 7.1 were fixed to selected values except temperature which varied at two levels of 23 °C and 50 °C. The rotational speed was set fixed to 200 rpm as a reasonable representation of turbulent conditions. The concentration of calcium sulfate was set fixed based on the experimental temperature. Calcium sulfate hemihydrate is among compounds that have inverse solubility with temperature, therefore less amount is needed to reach saturation concentration at a higher temperature compared to a lower temperature.

Figure 7.6 juxtaposes the deposited fouling mass at higher temperature and lower temperature on both the brass-based and aluminum-based surfaces. The as-received bare brass and bare aluminum surfaces have shown an increasing trend in the deposited fouling mass at both temperature levels. Moreover, at each time slice, the coupon at a higher temperature had shown significantly higher fouling mass deposited on the surfaces compared to the lower temperature. This is due to two mechanisms: first, a faster nucleation rate, and second, a faster crystallization growth rate at the higher temperature. The ratio of average deposited fouling mass at 50 °C over the average deposited fouling mass at 23 °C at 192h immersion time for bare brass is ~1.12, Figure 7.6(a), while the similar ratio is 1.45 for bare aluminum, Figure 7.6(d), this indicates that the effect of change in temperature was bolder for bare aluminum compared to bare brass. This goes along with the difference in the roughness of these two surfaces. Temperature has shown lesser effect in

increasing fouling deposited mass for Brass-SHS, Figure 7.6(b), compared to the effect of temperature for the bare brass. This was observed to be true for aluminum-HS as well, Figure 7.6(e), compared to its bare case. Regardless of base material, temperature had a rather bolder effect on lubricant infused surfaces in comparison with bare and HS/SHS when the deposited fouling mass after 192 h immersion at 50 °C is compared to similar condition at 23 °C, Figure 7.6(c) and (f). this could be attributed to the effect which temperature has on lubricant viscosity. Despite all, LIS yet exhibited lower deposited fouling mass and superior anti-scaling property compared to the other tested surfaces. Similar to the room temperature at higher temperature of 50 °C, regardless of surface modification, aluminum-based surfaces have shown lower fouling compared to the brass-based surfaces. Both HS/SHS and LIS successfully withstood the higher temperature condition of the tests and exhibited anti-scaling properties at 50 °C with lower deposited fouling mass compared to bare control samples at similar temperature conditions (and even compare to bare control case at 23 °C).

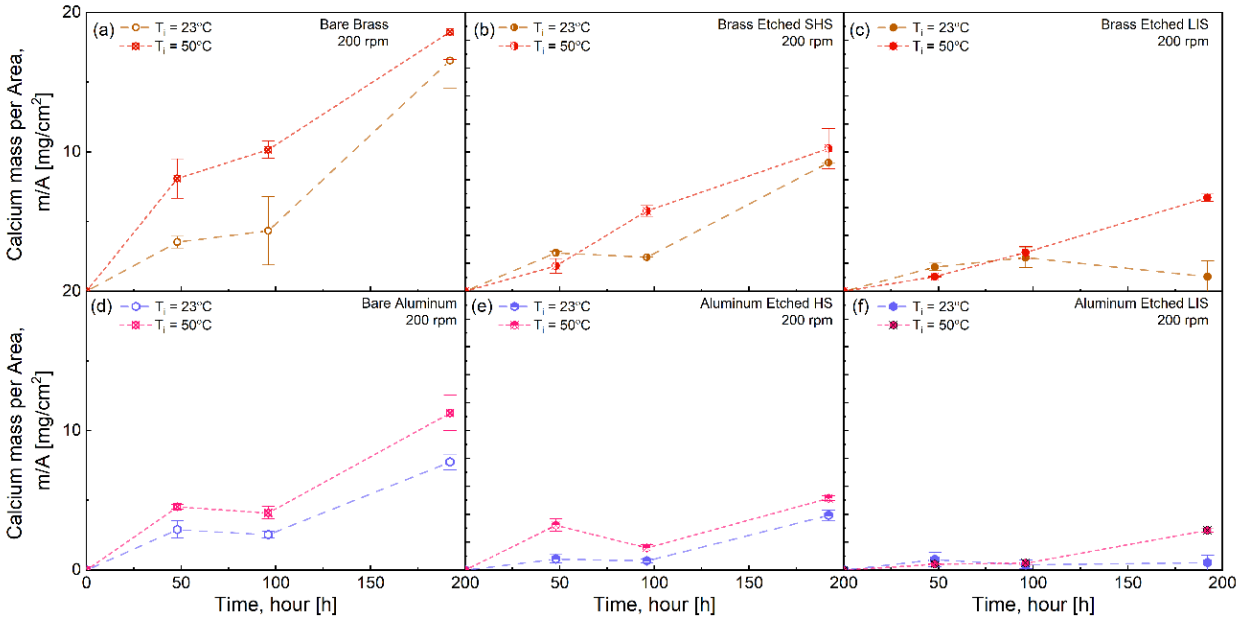

Figure 7.6. Effect of temperature versus time on fouling mass per unit area at 200 rpm drum dynamic test for (a) bare brass; (b) etched brass superhydrophobic surface (SHS); (c) brass lubricant infused surface (LIS); (d) bare aluminum; (b) etched aluminum hydrophobic surface (HS); (c) aluminum lubricant infused surface (LIS).

7.4.4. **Effect of surface modification**

So far parametric test has shown the effect of shear stress as well as temperature on calcium fouling deposition. It is of further interest to scrutinize the effect of surface modifications, namely functionalization and lubricant infusion. This can be investigated by comparing the deposited fouling mass on modified surfaces to the bare control cases. In this lieu, Figure 7.7 plots this ratio for cases of 200 rpm for both brass-based and aluminum-based modified surfaces as well as two temperatures of 23 °C and 50 °C. In general, functionalization has shown to be able to cut the fouling to about 50% of the control sample at the shear stress condition of 200 rpm. This is phenomenon reduction and is regardless of temperature or the base material. Nevertheless, lubricant infused surfaces have shown a superior anti-scaling property as well with over 90% decrease in deposited fouling mass at 23 °C and 200 rpm compared to the bare control case for both brass and aluminum. At 50 °C and 200 rpm also lubricant infused surfaces had over 65% less deposited fouling mass compared to the bare control sample at similar conditions. This expresses that LIS yet excelled HS/SHS even at 50 °C.

As an instance, Figure 7.8(A) illustrates the difference in the physical appearance of the brass-SHS and brass-LIS compared to the bare brass after different immersion times at 200 rpm and 23 °C, via optical images. Even though the thickness and density of the deposited fouling cannot be explored in this figure, which is believed to be higher for the control bare sample, images clearly show less surface area covered with fouling in the case of modified surfaces compared to the bare case. To explore the deposited calcium fouling morphology, SEM images were taken after the fouling experiment. Figure 7.8(B-b) shows bare brass surface which is almost fully covered with calcium crystals (48 hours at 23 °C and 200 rpm) while at the similar test condition brass-LIS has shown significantly less deposited crystal in Figure 7.8(B-e). Elemental analysis was done via EDX area scan of clean bare brass before test beside bare brass, and brass-LIS after scaling, Figure 7.8(B-a,b,e), respectively. Higher coverage and/or higher density of scaling would mask the surface and will attenuate the EDX signal from the base material. Figure 7.8(B-d) EDX areal scans show almost zero detected elemental copper for bare brass after scaling and a high calcium content compared to the brass-LIS. This asserts the hypothesis that fouling deposited on an unmodified surface has a higher density and larger coverage area compared to non-wetting modified surfaces.

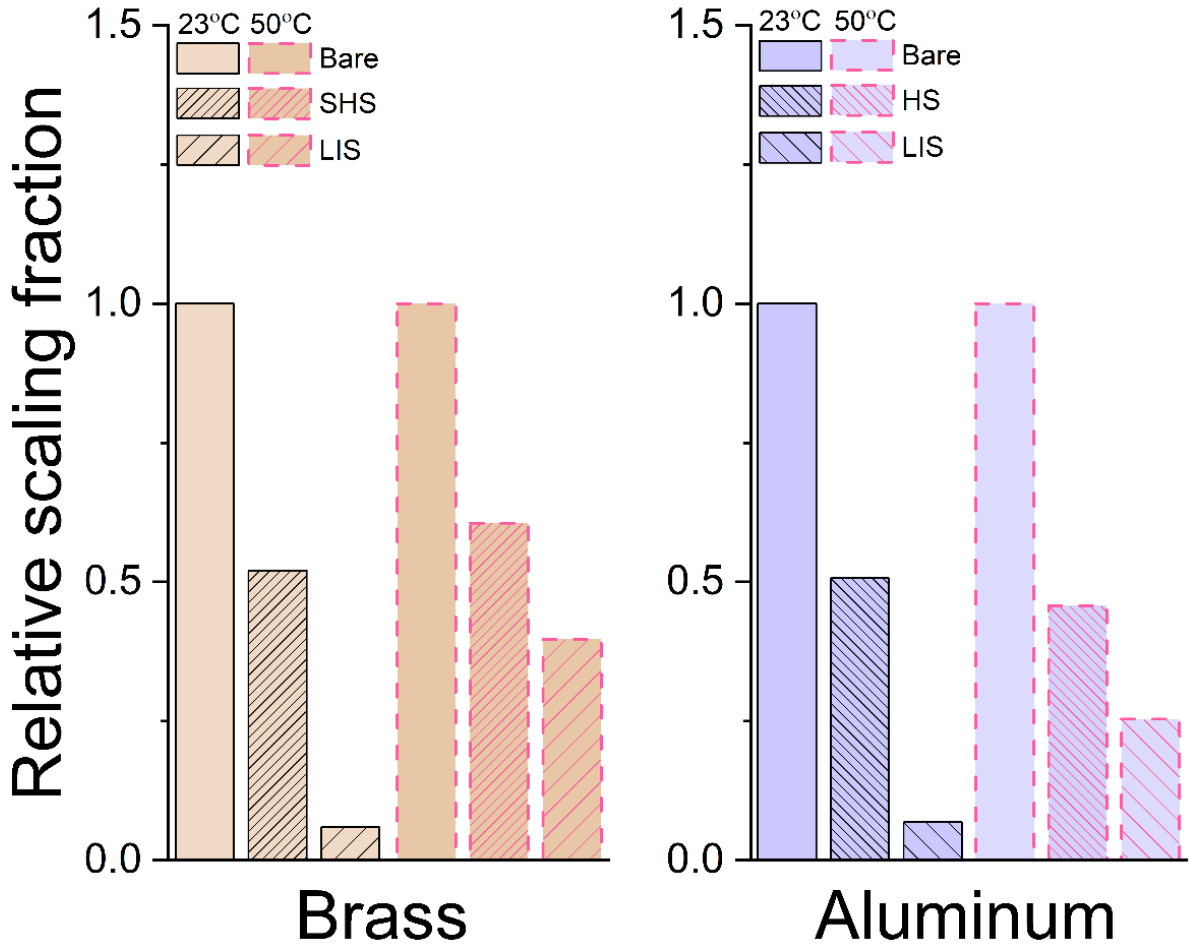

Figure 7.7. Relative scaling fraction showing the effect of surface modification for brass superhydrophobic surface (SHS), brass lubricant infused surface (LIS), aluminum hydrophobic surface (HS), and aluminum LIS after 192 h dynamic scaling tests at 200 rpm at 23 °C and 50 °C.

Higher magnification SEM images of the deposited calcium crystals were taken to further explore the crystal structure of the fouling. Figure 7.8(B-c) shows Rhombohedral crystal units grew and aggregated on the stepped and kinked faces (S and K faces) and formed 2D leaflike flakes along forming needlelike gypsum crystals with rhombohedral shape and hexagonal plane on bare brass. Similar structures were observed for fouling deposited on the modified surface (brass-LIS) with less of the leaflike and more of the long needle-like crystals.

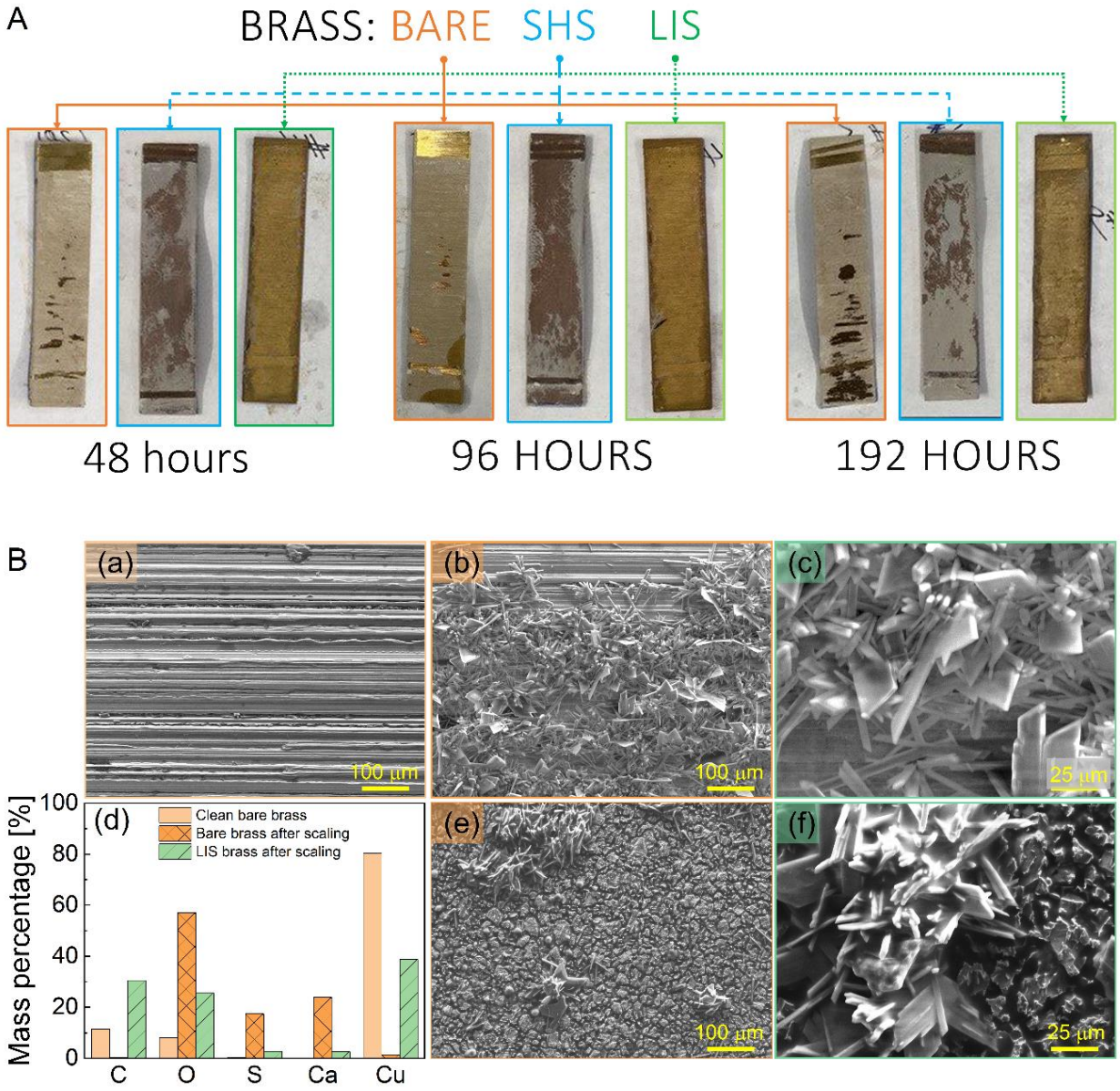

Figure 7.8. Optical and SEM image of surfaces after calcium dynamic fouling test at 200 rpm and room temperature. (A) Illustrates the brass bare surface, superhydrophobic surface (SHS), and lubricant infused surface (LIS) after 48 h, 96 h, and 192 h dynamic scaling experiment. (B) SEM and EDX spectra of brass-based surfaces after 48 h dynamic fouling experiment at 200 rpm and room temperature. (B-a) SEM image of clean bare brass; (B-b,c) bare brass after scaling; (B-e,f) superhydrophobic brass after scaling. (B-d) areal EDX spectra of surfaces in B(a), (b), and (e).

Figure 7.9 illustrates SEM image of calcium crystal grown on aluminum surfaces after 96 hours dynamic scaling test at 200 rpm and 23 ºC. Figure 7.9(a) displays a lush calcium crystal jungle

covered almost the whole aluminum surface, followed by Figure 7.9(b) where hydrophobic aluminum surface shows a few crystals grown in the form of spikes. Figure 7.9(c) imaged aluminum-LIS surface and showed scant and small calcium crystals deposited on its surface. Overall, The SEM images and EDX analysis of the as fabricated non-wetting surfaces verifies the results discussed in previous sections and had provided insight on the crystal morphology.

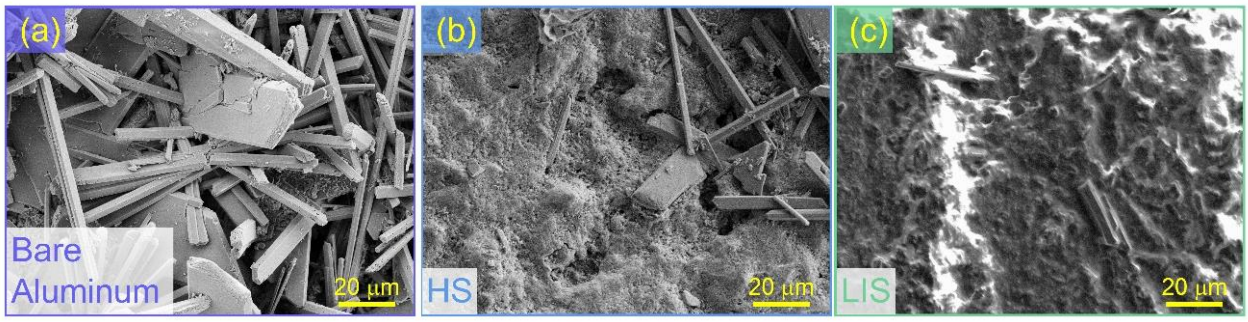

Figure 7.9. SEM image of aluminum-based surfaces after 96 h calcium dynamic fouling test at 200 rpm and room temperature. (a) Bare aluminum surface; (b) aluminum hydrophobic surface (HS); (c) aluminum lubricant infused surface (LIS).

7.4.5. **Comprehensive analysis of modified surface against scaling**

To this end effect of shear stress (rotation rate) at 23 °C, as well as the effect of temperature at 200 rpm was explored for bare and modified brass and aluminum surfaces. Besides brass and aluminum that are widely used, copper is another ubiquitously used material in different applications. Therefore, data were collected from literature where similar dynamic fouling tests were performed on bare, electrodeposited-SHS, etched-SHS, electrodeposited-LIS, and etched-LIS copper surfaces.

Additionally, in order to get a more conclusive perspective, the higher temperature experiments in section 3.3 were expanded to 100 rpm and 400 rpm. Next. the fouling mass data for 192 h were extracted for all the cases and relative scaling fraction was calculated for each individual modified surface and testing condition over its corresponding bare control case. After that, all the collected data points were categorized only by base metal and surface modification type namely functionalized low surface energy surfaces (SH/SHS) and slippery lubricant infused surfaces (LIS) and leaving the other parameters aggregated (rotation rates and temperatures). This has provided a unique higher perspective view to the anti-scaling properties of modified surfaces and is plotted

in Figure 7.10. The analysis reveals that regardless of the base metal, the low surface energy surfaces (SH/SHS) exhibits an excellent anti-scaling property with a median and average of below 0.5 corresponding to more than 50% reduction in deposited fouling mass compared to their bare control cases. On top of that, the slippery lubricant infused surfaces, regardless of the based metal, exhibited a superior anti-scaling property with an average relative scaling fraction below 0.4 (60% reduction) and median below 0.3.

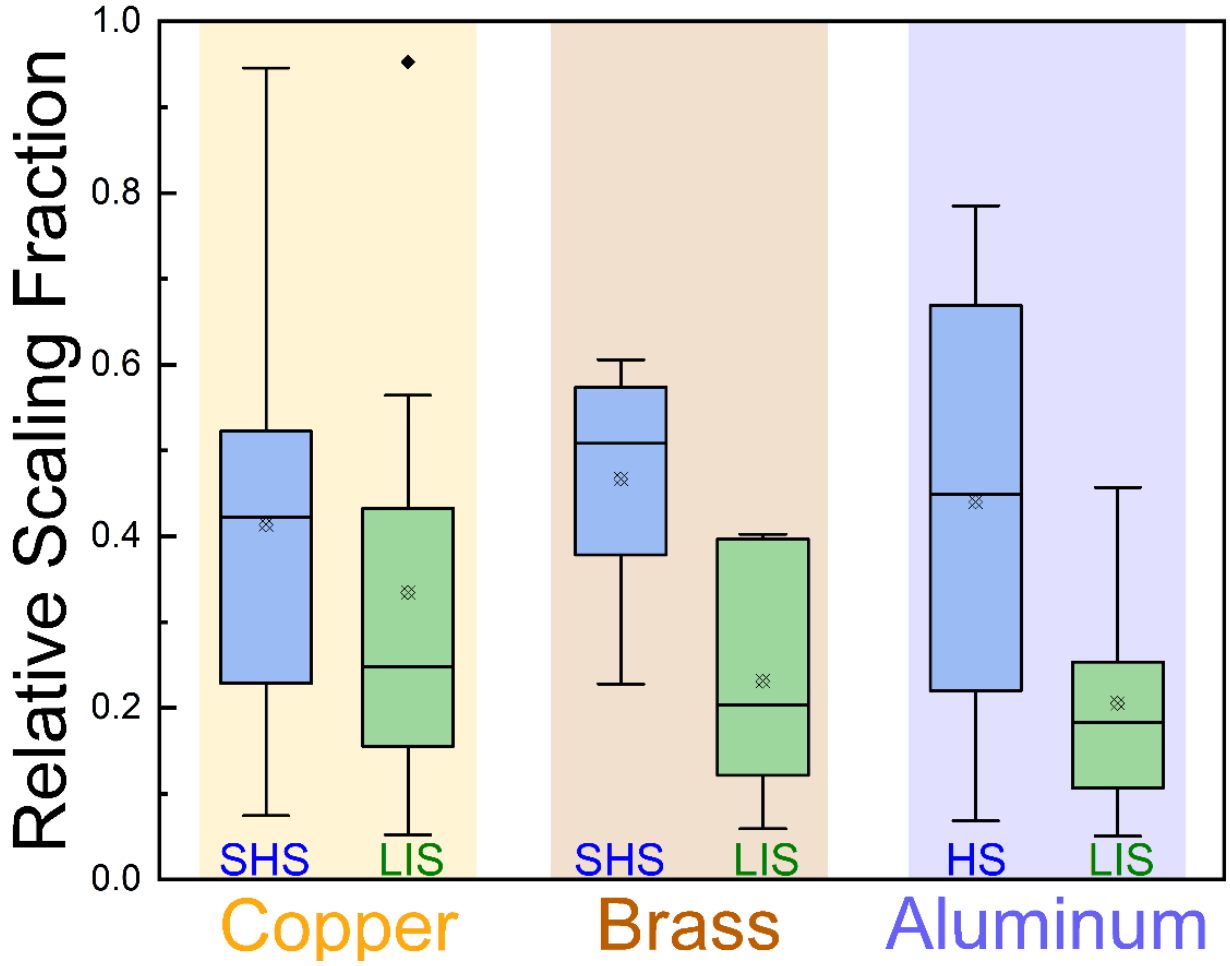

Figure 7.10. Pooled dynamic scaling data and aggregated on rotation rates and temperatures showing relative scaling fraction versus based material and surface wettability. (Summary of the full matrix of dynamic scaling tests showing the mass of calcium scaling versus the mass of calcium scaling on the bare control sample at the corresponding test condition. The tests were done on 72 different conditions including Two different temperatures (25 ℃ and 50 ℃); three flow speeds (100, 200, and 400 rpm); three different based materials (copper, brass, and aluminum); and 4 different surface modifications (Bare/no modification, hydrophobic (HS), superhydrophobic (SHS), and liquid infused (LIS). Besides the etching method, additional SHS and LIS surface fabricated via electrodeposition method is included for copper cases.)

The results in this article focused on the parametric studies on the effect of flow condition (Reynolds number/rotation rate), temperature, and surface modification of metallic surfaces against calcium scaling. The perspective provided points out the effectiveness of hydrophobicity and slipperiness together. The effect of surface chemistry for low-surface energy surfaces and lubricant physical/chemical properties for lubricant-infused surfaces on fouling are important aspects to be further explored by the community.

7.5. CONCLUSIONS

A comprehensive approach to nucleation theory was adopted toward a detailed study of ant-scaling performance of wetting and non-wetting surfaces. Two different metallic substrates were selected, one to represent a smooth surface (Aluminum), and one with 3 times higher RMS roughness value (Brass) to represent rough surfaces. The selected metallic substrates are also materials that are ubiquitously used in different domestic and industrial applications. Hydrophobic, Superhydrophobic, and slippery lubricant-infused surfaces were fabricated by facile chemical etching methods followed by functionalization with an environmentally friendly material. The performance of the as-received and enhanced modified surfaces was evaluated in a simulated calcium scaling environment through a designed dynamic test condition. The comprehensive scaling tests included three levels for dynamic flow condition, two levels for temperature, three levels of immersion time, and five levels of surface properties with 3 repetitions at each unique condition corresponding to a total of 324 tested coupons. The following are the major findings of this study:

I) *Effect of Reynolds number*— The tests spanned at three low, medium, and high Reynolds numbers. The low level was set at the turbulent regime threshold and had a Reynolds number of 49×10^3. The increase in Reynolds number had a non-linear decreasing effect on fouling deposition. Increasing Reynolds number from the lower level of 49×10^3 to medium level of 99×10^3 had shown a bolder effect compared to the change from the medium level to the highest level of 198×10^3 for all the cases except lubricant infused surfaces. The lubricant infusion of LIS has endowed these

surfaces a slipperiness such that the shear forces even at lower Reynolds number was high enough for removal of deposited fouling and/or preventing new nuclei to grow.

II) *Effect of temperature*—When the deposited fouling mass at the end of the experiments at 50 °C is compared to the same condition at 23 °C, it was found that temperature had a greater effect on lubricant infused surfaces in comparison to HS/SHS and bare surfaces, independent of the base material. This could be attributed to the effect that temperature has on the viscosity of the lubricant in question. Yet, despite all of this, LIS demonstrated lower fouling mass deposition and superior anti-scaling properties when compared to the other tested surfaces at higher temperatures.

III) *Effect of surface modification*— Regardless of temperature, at medium Reynold number corresponding to 200 rpm, brass, and aluminum HS and SHS has shown a 50% reduction in fouling mass compared to the control sample. Nonetheless, lubricant-infused brass and aluminum surfaces have demonstrated remarkable anti-scaling properties, with over 90% and 65% reduction in deposited fouling mass at 23 °C and 50 °C, respectively. Pooled data from all the experimented Reynolds number and temperature levels from this study together with data from copper-based surfaces in literature demonstrates that low surface energy surfaces (SH/SHS) have outstanding anti-scaling properties independent of the base metal, with a median and average relative scaling fraction of less than 0.5 (equivalent to more than 50% reduction in deposited fouling mass). Furthermore, regardless of the underlying metal, the slippery lubricant-infused surfaces displayed excellent anti-scaling properties, with an average relative scaling fraction of less than 0.4 (over 60% reduction in fouling) and a median of less than 0.3 (over 70% reduction in fouling).

The results of the study provide valuable insight, for the first time, into the interactive effects of flow condition, temperature, and different non-wetting surface types (HS, SHS, and LIS) on calcium crystallization fouling. With the help of the comprehensive analysis on different based material and test conditions, the study provides a unique overview for the community and future works.

ACKNOWLEDGMENT AND DISCLAIMER

The material reported in this publication is based upon work supported by the U.S. Department of Energy under Award Number DE-FE0031556. This publication was prepared as an account of work sponsored by an agency of the United States Government. Neither the United States Government nor any agency thereof, nor any of their employees, makes any warranty, express or implied, or assumes any legal liability or responsibility for the accuracy, completeness, or usefulness of any information, apparatus, product, or process disclosed, or represents that its use would not infringe privately owned rights. Reference herein to any specific commercial product, process, or service by trade name, trademark, manufacturer, or otherwise does not necessarily constitute or imply its endorsement, recommendation, or favoring by the United States Government or any agency thereof. The views and opinions of authors expressed herein do not necessarily state or reflect those of the United States Government or any agency thereof.

REFERENCES

[1] J. Berce, M. Zupančič, M. Može, I. Golobič, A Review of Crystallization Fouling in Heat Exchangers, Process. 2021, Vol. 9, Page 1356. 9 (2021) 1356. https://doi.org/10.3390/PR9081356.

[2] C. Shen, C. Cirone, A.M. Jacobi, X. Wang, Fouling of enhanced tubes for condensers used in cooling tower systems: A literature review, Appl. Therm. Eng. 79 (2015) 74–87. https://doi.org/10.1016/J.APPLTHERMALENG.2015.01.014.

[3] A. Zaza, N.E. Laadel, E.G. Bennouna, Y. El Hammami, The influence of the cooling system fouling on the thermal performance of a CSP plant: Recent research updated, AIP Conf. Proc. 2307 (2020) 020061. https://doi.org/10.1063/5.0032965.

[4] I.S. Azmi, M.N. Murat, Fouling of heat transfer surface in industry: A review, AIP Conf. Proc. 2347 (2021) 020114. https://doi.org/10.1063/5.0052054.

[5] I. Merino-Garcia, S. Velizarov, New insights into the definition of membrane cleaning strategies to diminish the fouling impact in ion exchange membrane separation processes, Sep. Purif. Technol. 277 (2021) 119445. https://doi.org/10.1016/J.SEPPUR.2021.119445.

[6] A. Abdel-Karim, S. Leaper, C. Skuse, G. Zaragoza, M. Gryta, P. Gorgojo, Membrane cleaning and pretreatments in membrane distillation – a review, Chem. Eng. J. 422 (2021) 129696. https://doi.org/10.1016/J.CEJ.2021.129696.

[7] I. Shahonya, F. Nangolo, M. Erinosho, E. Angula, Scaling and Fouling of Reverse Osmosis (RO) Membrane: Technical Review, (2021) 41–47. https://doi.org/10.1007/978-981-16-3641-7_7.

[8] L. Schnöing, W. Augustin, S. Scholl, Fouling mitigation in food processes by modification of heat transfer surfaces: A review, Food Bioprod. Process. 121 (2020) 1–19. https://doi.org/10.1016/J.FBP.2020.01.013.

[9] M. Saget, C.F. de Almeida, V. Fierro, A. Celzard, G. Delaplace, V. Thomy, Y. Coffinier, M. Jimenez, A critical review on surface modifications mitigating dairy fouling, Compr. Rev. Food Sci. Food Saf. (2021). https://doi.org/10.1111/1541-4337.12794.

[10] K. Pourabdollah, Fouling formation and under deposit corrosion of boiler firetubes, J. Environ. Chem. Eng. 9 (2021) 104552. https://doi.org/10.1016/J.JECE.2020.104552.

[11] D.K. Singh, A. Villamayor, L. Lacheheb, Shell and tube heat exchanger progression fouling and its mitigation using chemical cleaning process, AIP Conf. Proc. 2317 (2021) 030003. https://doi.org/10.1063/5.0036112.

[12] R. Prasad, S. V. Dalvi, Sonocrystallization: Monitoring and controlling crystallization using ultrasound, Chem. Eng. Sci. 226 (2020) 115911. https://doi.org/10.1016/J.CES.2020.115911.

[13] X. You, J. Teng, Y. Chen, Y. Long, G. Yu, L. Shen, H. Lin, New insights into membrane fouling by alginate: Impacts of ionic strength in presence of calcium ions, Chemosphere. 246 (2020) 125801. https://doi.org/10.1016/J.CHEMOSPHERE.2019.125801.

[14] L.D. Tijing, M.H. Yu, C.H. Kim, A. Amarjargal, Y.C. Lee, D.H. Lee, D.W. Kim, C.S. Kim, Mitigation of scaling in heat exchangers by physical water treatment using zinc and tourmaline, Appl. Therm. Eng. 31 (2011) 2025–2031. https://doi.org/10.1016/J.APPLTHERMALENG.2011.03.011.

[15] Z. Xu, Y. Zhao, J. He, H. Qu, Y. Wang, B. Wang, Fouling characterization of calcium carbonate on heat transfer surfaces with sodium carboxymethyl cellulose as an inhibitor, Int. J. Therm. Sci. 162 (2021) 106790. https://doi.org/10.1016/J.IJTHERMALSCI.2020.106790.

[16] S.C. de Morais, D.F. de Lima, T.M. Ferreira, J.B. Domingos, M.A.F. de Souza, B.B. Castro, R. de C. Balaban, Effect of pH on the efficiency of sodium hexametaphosphate as calcium carbonate scale inhibitor at high temperature and high pressure, Desalination. 491 (2020) 114548. https://doi.org/10.1016/J.DESAL.2020.114548.

[17] K.H. Teng, A. Amiri, S.N. Kazi, M.A. Bakar, B.T. Chew, A. Al-Shamma'a, A. Shaw, Retardation of heat exchanger surfaces mineral fouling by water-based diethylenetriamine pentaacetate-treated CNT nanofluids, Appl. Therm. Eng. 110 (2017) 495–503. https://doi.org/10.1016/J.APPLTHERMALENG.2016.08.181.

[18] C.S. Ong, P.S. Goh, W.J. Lau, N. Misdan, A.F. Ismail, Nanomaterials for biofouling and scaling mitigation of thin film composite membrane: A review, Desalination. 393 (2016) 2–15. https://doi.org/10.1016/J.DESAL.2016.01.007.

[19] H. Li, S. Yu, J. Hu, X. Yin, Modifier-free fabrication of durable superhydrophobic electrodeposited Cu-Zn coating on steel substrate with self-cleaning, anti-corrosion and anti-scaling properties, Appl. Surf. Sci. 481 (2019) 872–882. https://doi.org/10.1016/J.APSUSC.2019.03.123.

[20] Junyang Tan, Junjie Hao, Zhenqiang An, Changsheng Liu, Superhydrophobic surfaces on brass substrates fabricated via micro-etching and a growth process, RSC Adv. 7 (2017) 26145–26152. https://doi.org/10.1039/C7RA03308G.

[21] G. Azimi, Y. Cui, A. Sabanska, K.K. Varanasi, Scale-resistant surfaces: Fundamental studies of the effect of surface energy on reducing scale formation, Appl. Surf. Sci. 313 (2014) 591–599. https://doi.org/10.1016/J.APSUSC.2014.06.028.

[22] M. Forster, M. Bohnet, Modification of molecular interactions at the interface crystal/heat transfer surface to minimize heat exchanger fouling, Int. J. Therm. Sci. 39 (2000) 697–708. https://doi.org/10.1016/S1290-0729(00)00229-5.

[23] T.P. Melia, Crystal nucleation from aqueous solution, J. Appl. Chem. 15 (2007) 345–357. https://doi.org/10.1002/JCTB.5010150801.

[24] P. Ragesh, V. Anand Ganesh, S. V. Nair, A.S. Nair, A review on "self-cleaning and multifunctional materials," J. Mater. Chem. A. 2 (2014) 14773–14797. https://doi.org/10.1039/c4ta02542c.

[25] M.J. Kreder, J. Alvarenga, P. Kim, J. Aizenberg, Design of anti-icing surfaces: Smooth, textured or slippery?, Nat. Rev. Mater. 1 (2016) 1–15. https://doi.org/10.1038/natrevmats.2015.3.

[26] T. Zhang, Y. Wang, F. Zhang, X. Chen, G. Hu, J. Meng, S. Wang, Bio-inspired superhydrophilic coatings with high anti-adhesion against mineral scales, NPG Asia Mater. 2018 103. 10 (2018) e471–e471. https://doi.org/10.1038/am.2017.224.

[27] K. Kant, R. Pitchumani, Laminar drag reduction in microchannels with liquid infused textured surfaces, Chem. Eng. Sci. 230 (2021) 116196. https://doi.org/10.1016/J.CES.2020.116196.

[28] Z. Xiao, R. Zheng, Y. Liu, H. He, X. Yuan, Y. Ji, D. Li, H. Yin, Y. Zhang, X.M. Li, T. He, Slippery for scaling resistance in membrane distillation: A novel porous micropillared superhydrophobic surface, Water Res. 155 (2019) 152–161. https://doi.org/10.1016/J.WATRES.2019.01.036.

[29] Y. Zhu, H. Li, M. Zhu, H. Wang, Z. Li, Dynamic and active antiscaling via scale inhibitor pre-stored superhydrophobic coating, Chem. Eng. J. 403 (2021) 126467. https://doi.org/10.1016/J.CEJ.2020.126467.

[30] M. Villegas, Y. Zhang, N. Abu Jarad, L. Soleymani, T.F. Didar, Liquid-Infused Surfaces: A Review of Theory, Design, and Applications, ACS Nano. 13 (2019) 8517–8536. https://doi.org/10.1021/acsnano.9b04129.

[31] E. Yildirim, Improvement of lubricant-infused surfaces for anti-icing applications, Http://Dx.Doi.Org/10.1680/Jsuin.16.00026. 4 (2016) 214–217. https://doi.org/10.1680/JSUIN.16.00026.

[32] S. Sett, X. Yan, G. Barac, L.W. Bolton, N. Miljkovic, Lubricant-Infused Surfaces for Low-Surface-Tension Fluids: Promise versus Reality, ACS Appl. Mater. Interfaces. 9 (2017) 36400–36408. https://doi.org/10.1021/ACSAMI.7B10756.

[33] S.B. Subramanyam, G. Azimi, K.K. Varanasi, Designing Lubricant-Impregnated Textured Surfaces to Resist Scale Formation, Adv. Mater. Interfaces. 1 (2014) 1300068. https://doi.org/10.1002/ADMI.201300068.

[34] J. Meng, S. Wang, Advanced Antiscaling Interfacial Materials toward Highly Efficient Heat Energy Transfer, Adv. Funct. Mater. 30 (2020) 1904796. https://doi.org/10.1002/ADFM.201904796.

[35] M.F.B. Sousa, H.C. Loureiro, C.A. Bertran, Anti-scaling performance of slippery liquid-infused porous surface (SLIPS) produced onto electrochemically-textured 1020 carbon steel, Surf. Coatings Technol. 382 (2020) 125160. https://doi.org/10.1016/J.SURFCOAT.2019.125160.

[36] M.F.B. Sousa, G.F. Barbosa, F. Signorelli, C.A. Bertran, Anti-scaling properties of a SLIPS material prepared by silicon oil infusion in porous polyaniline obtained by electropolymerization, Surf. Coatings Technol. 325 (2017) 58–64. https://doi.org/10.1016/J.SURFCOAT.2017.06.038.

Chapter 8. Summary and Future Work

The essential contribution of this work was to bring our understanding of metallic superhydrophobic surfaces (SHS) and lubricant infused surfaces (LIS) for anti-corrosion and anti-scaling application one step closer to the real-world practical conditions, which despite decades of research on such surfaces, was not explored in-depth due to the difficulties that such practical environment might incur on the applicability of these surfaces.

In the fabrication of part, the author of this dissertation suggests that a closer look into natural leaves and the human body can inspire new fabrication techniques that overcome current facing limitations like lubricant retention on LIS. For instance, the human body is a complex system full of wet and lubricated surfaces such as our lungs, smooth surface of our eyes, porous joints, intestine, hairy breathing and hearing passages; all working seamlessly with anti-fouling and self-repairing properties. This work has shown successful offline rejuvenation of SHS and LIS, however, online rejuvenation will be a game-changing property for such surfaces. The author suggests engineering metallic surfaces (and pipes) with such lubrication channels inspired by the human body or veins of leaves; to always have a passage to replace the surface with a fresh functional agent or lubricant. In this regard, another suggestion is to approach online rejuvenation by using working fluid mixed with a functional agent or lubricant. A future work could be toward investigating the possibility of lubricant infusion by flowing a two-phase flow, a mixture of a solution and lubricant. This could be further detailed into the level of infusion and systematic study for optimization of the rejuvenation solutions mixture.

This study for the first time scrutinized the possible anti-corrosion mechanisms on copper superhydrophobic surfaces to reveal the crucial role of air cushion for this matter. A survey in related literature revealed no report to unify the parameters involved in the corrosion process into one parameter for readily any material. Therefore, the author suggests future work on an effort to characterize the air cushion, for example in terms of thickness and homogeneity of the layer, and relate the status of that layer to corrosion of the substrate regardless of any other factors such as material or surface roughness. The homogeneity of the air cushion can be investigated via impedance spectroscopy circuit analysis that was explained in detail in this work.

Based on the fundamental study on surface properties that was explored in this dissertation, it is expected that the fabricated non-wetting surfaces to show superior de-icing and biofouling properties as well which are to be explored in future works. Moreover, exploring anti-fouling against minerals other than calcium such as magnesium is of interest. Additionally, the author suggests a much-needed in-depth work dedicated to exploring a variety of surface roughness and features and their effect on the performance of SHS and LIS. It was seen that there is not a consensus among the literature on the effect of roughness. The common belief is that a rough superhydrophobic surface to be better than a smooth or rough hydrophilic surface for applications like anti-scaling while few studies showed the opposite. However, roughness quantification was done for the surfaces in this work, but the author suggests that the term "roughness" needs much more delineation in the field and need to be divided into specific roughness levels with specific qualitative parameters, which in light of that, one might be able to explain the contradictions in the literature. Such dedicated future study is believed to benefit the whole community in further improving the non-conformal design of non-wetting surfaces.